THE UNIVERSITY *of* EDINBURGH

Begin codeEnd code

Development of Novel High Pressure Instrumentation

Xiao Wang

A thesis submitted for the degree of Doctor of Philosophy.
The University of Edinburgh.
December 2014

Abstract

The application of pressure to chemical substances can change their physical properties (optical, magnetic, and electrical) and it can also be used to alter some chemical reactions. The need for compatible pressure generating instruments is constantly growing in various high pressure (HP) researches. The work described in this thesis is focused on development, construction, testing of several high pressure cells of novel design. These designs were developed to meet the requirements of different research collaborations. The main objective of this project is to develop high pressure cells for magnetic studies in the magnetic properties measurement system known as MPMS, which is the most popular commercial magnetometer nowadays. Three high pressure cells were designed and tested for different type of magnetic measurements.

The first design presented in this thesis is a cylinder type pressure cell which is specially designed to measure the magnetic susceptibility of the pressure-sensitive material under pressure. The cell is driven by compressed helium gas which allows the internal pressure to be adjusted with small increments (1 MPa) through the regulator of the external gas cylinder. The cell was made of non-magnetic beryllium copper alloy and designed to work up to 100 MPa at 400 K temperature. The design was verified with finite element analysis (FEA) simulation and its sample volume was optimised to provide large sample capacity which allows high quality data to be collected in the MPMS.

Modified from the earlier turnbuckle magnetic diamond anvil cell (TM-DAC) reported in Konstantin V. Kamenev (KVK) group, the second high pressure cell presented in this thesis is an opposed diamond anvil pressure cell. The working mechanism of this cell is based on the turnbuckle principle. The cell was specifically developed for iHelium3 system which is a add-on cryostat of the MPMS. The cell was coded TM-3He-DAC to distinguish with the original TM-DAC. The cell is 6 mm in diameter and 7 mm in length, which are smaller than the dimensions of the predecessor (TM-DAC). Copper titanium alloy was used in building the cell to further reduce the magnetic background from the cell. The cell is capable of achieving close to 5 GPa sample pressure in the loading test and the magnetic background is significantly lower than the TM-DAC. The development of this cell enables high pressure magnetic measurements to be performed at extreme low temperature (0.5 K) in the iHelium3 system.

The third high pressure cell developed for the MPMS is also a turnbuckle diamond anvil cell, however, all the material used in the cell is non-metallic to enable high-pressure ac magnetic measurement to be performed. An advanced high strength polymer was assessed using finite element analysis and experimental testing. The performance and failure modes for the key components of the cell working in tension and in compression were evaluated and the ways for optimising the designs were established. The cell is coded PTM-DAC in this thesis and the composite gasket was also developed and tested for the PTM-DAC. The cell is approximately 14 mm long, 8.5 mm in diameter and was demonstrated to reach pressures of 5.6 GPa. Ac susceptibility data collected on Dy_2O_3 and U_6Fe demonstrated the performance of the cell in magnetic property measurement and confirmed that there was no screening of the sample by the environment which typically accompanies used of conventional metallic high pressure cells in oscillating magnetic fields.

Based on the experience of from the development of above two turnbuckle diamond anvil cell, a turnbuckle sapphire anvil cell (T-SAC) was developed in this project for high-pressure neutron scattering. Commercial spherical sapphire were used as anvil in the cell as they are much more cost effective if compared to the diamond anvil. The developed T-SAC can generate and maintain sample pressures above 6 GPa with a sample volume 6×10^{-2} mm^3 which is 6 times that of conventional diamond anvil cell (DAC). Failure analysis was performed on the sapphire anvil to gain a better understanding of the failure mechanism of the spherical sapphire anvil. The cell had been used in measuring the crystal structure of single crystal niobium at 1.6 GPa through small angle neutron scattering (SANS) technique. The cell is less than 16 mm in length and 14 mm in diameter, it is the smallest sapphire anvil cell to date. The miniature feature allow it can be fit into most cryostat of modern scientific instrument without difficulties.

Lastly, two piston-cylinder type high pressure cells were developed for high-pressure chemistry studies. These cells were designed to pressurise large amount of liquid sample (particular for water-based sample) up to 800 MPa in a controllable manner. Each design is presented separately with stress analysis in FEA and a description of the working mechanism. Hoop strain at the external surface of the cell was measured and then the internal pressure was calculated through the Lamé equation. After that, the load and attainable internal pressure was calibrated for the users. These cells have been used in the high-pressure study of salicylaldoximes process, bio-diesels decomposition and crystallization, material polymerisation and pharmaceutical experiments.

Declaration of originality

This thesis has been composed by myself and it has not been submitted in any previous application for a degree. The work reported with was executed by me, unless otherwise stated.

Xiao Wang

Acknowledgements

First of all, I would like to express my sincere appreciation to Professor Konstantin Kamenev who has supervised my work over the last four years. In this PhD project, I had experienced many difficulties to achieve success. He has always been willing to devote time to guide me with encouragement and patience. I would not be able to finish this PhD thesis without his motivation and supervision.

I also would like to thank my second supervisor Professor Euan Brechin who is a knowledgeable scientist. He was very supportive of my work. A special thank-you goes to Dr. Matthew Jacobsen and Dr. Martin Misek who had offer a great help in testing the plastic turnbuckle cell. In addition, I would like to thank Professor Giovanni Hearne who offered assistance on different occasions.

I am also grateful to my friends in CSEC. they are Dr. Weiwei Wang, Dr. Junwei Fang, Dr. Artur Bocian, Dr. Suresh Narayanaswamy, Dr. Gaetan Giriat and Mr. Chris Ridley.

I would also like to thank the workshop technicians Mr. Robert Louden, Mr. David McCabe, Mr. Paul Aitken and Mr Andrew Downie. They are very professional in manufacturing the instrument and always finish my work in time. Sometimes, their also provide me very useful suggestions to improve my design.

I am most grateful to my family. Their support is so generous and vital and my gratitude is beyond the words. While I was studying in the UK, my parents have supported me throughout the whole period both spiritually and financially. I wish I would be able to spend more time with them in future. I love and thank my dear wife Jingying Wang, I would have never got this far without her support. Finally, I thanks to my son, Zicheng Wang, who gives me countless joy and motivation.

Contents

List of figures

List of tables

Acronyms and abbreviations

HP	High Pressure
DAC	Diamond Anvil Cell
MPMS	Magnetic Properties Measurement System
SQUID	Superconducting Quantum Interference Device
TM-DAC	Turnbuckle Magnetic Diamond Anvil Cell
FEA	Finite Element Analysis
SANS	Small Angle Neutron Scattering
FEM	Finite Element Method
DSA	Direct Stiffness Method
DOF	Degrees of Freedom
BC	Boundary Condition
SCO	Spin-crossover
SCONPs	Spin-crossover Nanoparticles
TM-3He-DAC	Turnbuckle Magnetic ^{3}He Diamond Anvil Cell
PTM-DAC	Plastic Turnbuckle Magnetic Diamond Anvil Cell
T-SAC	Turnbuckle Sapphire Anvil Cell
WC	Tungsten Carbide

Nomenclature

P	Pressure
T	Temperature
H	Magnetic field
T_c	Superconducting transition temperature
σ_t	Hoop stress
σ_r	Radial stress
σ_a	Axial stress
σ'	Equivalent stress
σ_Y	Yield stress
D	Internal diameter of the thin-walled cylinder
t	Wall thickness of the thin-walled cylinder
r	Internal radius of a element in the thick-walled section
φ	Anlge fo the element
u	Radial displacement
ε_t	Hoop strain
ε_r	Radial strain
ε_a	Axial strain
ε_e	Elastic strain
ε_p	Plastic strain
S_t	Tensile strength
S_y	Yield strength
S_{ys}	Shear yield strength
E	Young's modulus
ν	Poisson's ratio
τ	Shear stress
α_v	Thermal expansion coefficient
ρ	Density

Magnetism unit

Most magnetism units used in this thesis are Gaussian cgs system, which stands for 'centimeter, gram, second'. As SI (*Systèm Internationale d'Unités*) units are the official units of measure agreed upon by most nations, the following table provides the conversion between the cgs and SI units.

Symbol	Quantity	cgs unit	Conversion factor (C)	SI unit
M	Magnetisation (magnetic moment)	electromagnetic unit (emu)	10^{-3}	A·m^2
H	Magnetic field strength	oersted (Oe)	$10^3/4\pi$	A/m
B	Magnetic flux density	gauss (G)	10^{-4}	tesla (T)
χ	(Mass) susceptibility	emu/g	$4\pi \times 10^{-3}$	m^3/kg
Multiply a number in cgs unit by the factor C to convert it to SI unit				

Chapter 1
Introduction

This first chapter provides a general introduction of high pressure instrumentation and a brief description of high-pressure magnetic measurement. In addition, the methodologies used in the instrumentation are introduced. The aims of this PhD project and the thesis structure are described at last.

1.1 High pressure instrumentation

In our daily life, pressure (P) is as important as temperature (T) among thermodynamic parameters. We use pressure cookers in our kitchen to fasten the cooking speed and use gas cylinders to contain liquefied petroleum gas as fuel or store liquefied gases at high pressures. High pressure air is filled in the tyre of our bicycle and cars to absorb shock during the journey. Apart from that, pressure processes the greatest range of magnitude among the thermal dynamic parameters, 60 orders from the highest vacuum in space to the pressure in the centre of a neutron star. With the modern diamond anvil cell (DAC) technique, the maximum static pressure obtainable in the laboratory was reported 460 GPa [1]. The achieved magnitude is probably higher than the pressure at the core of our earth, which was estimated to be 360 GPa [2].

There are two methods of generating high pressure: static and dynamic. This thesis concentrates on static high pressure which provides scientist with a powerful tool for tuning in a controllable manner the volume of the sample and, therefore, the properties of that sample. The terminology, high pressure, in this thesis is referred to static high pressure. Since the application of high pressure can produce many interesting phenomena (e.g. structural, electronic, magnetic and other phase transitions, polymerisation of organic substance), high pressure instrumentation become more and more important and a variety of high pressure cells are constantly reporting in the high pressure community. Most of these instruments are designed to be used in the study of physical properties of material under pressure, such as X-ray diffraction, neutron diffraction/scattering, Raman scattering, optical spectroscopy, electrical resistivity measurement and magnetic measurement. From the perspective of the construction layout, these high pressure cells can be divided to two general categories, piston-cylinder and opposed anvil type. The difference of these two types of high pressure cell will be demonstrated in Chapter 2.

1.2 High-pressure magnetic measurement

Magnetisation (M) is a fundamental physical property characterising the response of a material to applied magnetic field. The dependence of magnetisation and temperature (T), field (H) and pressure (P) could be used to investigate the nature of magnetic interactions, the value of the exchange parameters, the critical T, H, and P of magnetic phase transitions. The intrinsic spin and orbital angular momentum of a material can be revealed through magnetic property measurement. For those strongly magnetic materials, such as the ferromagnetic material used

in electric motors or the material used in hard disk drive, determining a magnetisation curve over a range of applied magnetic fields will help establish its commercial value in application. For other materials, those that might be categorised as non-magnetic, a similar magnetic research might reveal information about the electronic structure, interactions between neighbor molecules or the character of a phase transition of the material. Apart from that, magnetic measurements at high pressure can pave the way to developing materials with optimised properties for application. The main objective of this project is developing high pressure cells to carry out high-pressure magnetic measurement in the magnetic properties measurement system (MPMS®) [3], manufactured by Quantum Design and using superconducting quantum interference device (SQUID) technology [4]. More specific introduction of this commercial magnetometer will be introduced in the two following chapters.

1.3 Turnbuckle technique

Limited space available in sample chambers of the MPMS SQUID magnetometer is the main constraint on the dimensions of high pressure cells. Other constraints will be further discussed in Chapter 2 and Chapter 3. The dimension constraint is also very common for many cryogenic instrument which is required to thermalise the sample in the sample chamber efficiently. To overcome the dimension constrain, the novel turnbuckle opposed anvil technique pioneered by S. W. Tozer [5–9] is an extremely effective solution to size down the dimensions of the high pressure cell and the layout of such cells can be very simple. Figure 1.1 shows the turnbuckles which are widely used for bracing or losing the guy wires or cables in construction sites. Force can be created and maintained by rotating the body of the device while restriction the counter threaded ends to translational movement. The self lock mechanism of the turnbuckle was firstly introduced in fabricating DAC by S. W. Tozer [10] for pulse magnetic study at low temperature.

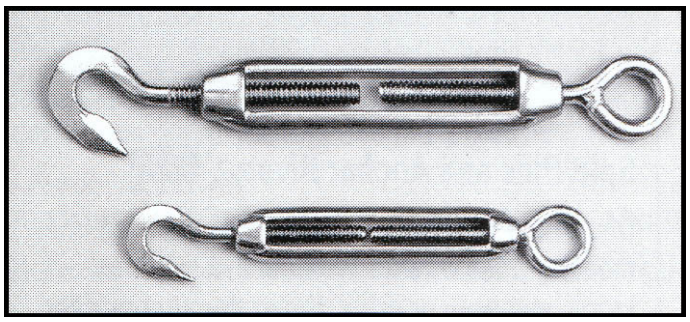

Figure 1.1: *Commonly used stainless steel turnbuckles.*

As shown in Figure 1.2, the turnbuckle DAC can be made to only three moving parts, the buckle and the two rods entering the buckle with one having a reverse thread. The rods could be made shorter and the diamond anvils could sit on the ends of the rods. External load pushes the anvils together to squeeze the sample inside the gasket to generate pressure and creates a small clearance between the threads which allows the turnbuckle body to rotate and lock the anvils advance. This thesis will present three new types of turnbuckle opposed anvil cells which are based on the existing *turnbuckle magnetic diamond anvil cell* (TM-DAC) [11] as shown in Figure 1.2. The specification of the TM-DAC will be further introduced in Chapter 4.

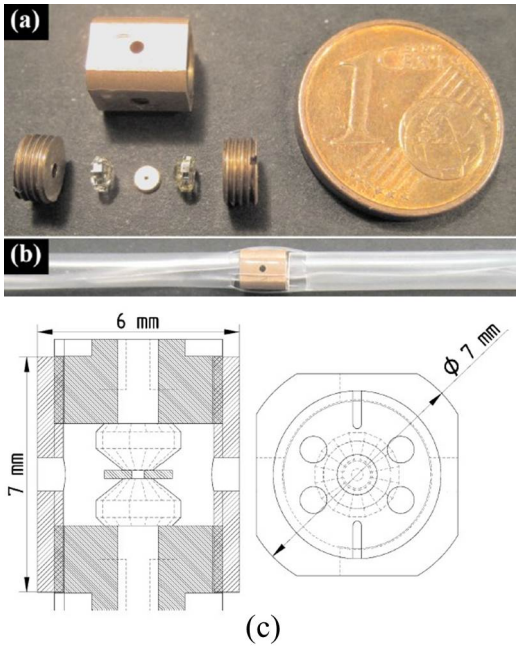

Figure 1.2: *TM-DAC: (a) parts; (b) the assemble TM-DAC in the standard plastic straw holder of MPMS; (c) drawing of the cell with key dimensions. [11]*

1.4 Finite element method

Instrument design is the core of this project and Finite Element analysis (FEA) was used extensively in this project to assess/optimise the designs. FEA is a computational approximation method which enable engineer to analyse the mechanical quantities (such as stress, strain, deformation ect.) of a part in a fast, inexpensive and non-destructive way. The fundamental concept of finite element method is that the volume of a continuum part can be divided into a finite set of contiguous, discrete elements and solve a set of simultaneous equations, each of which applies to an elements and to the nodes that connect the elements. The FEA was firstly codified

in 1956 [12] and now there are numerous highly developed commercial FEA codes available. FEA technique become essential for many engineers who work in the engineering sector because it can effectively reduce the product developing time. This technology was used in high pressure instrumentation since 1980s and was proof an efficient tool in designing/optimising the high pressure cells. To fasten the engineering decision in this project, all the presented high pressure cells were developed/optimised through finite element method. The methodology and technique will be further introduced in Chapter 5.

1.5 Objectives

The overall objective of this project was to develop instrumentation and methodology for measuring properties of materials at the extremes of pressures, temperatures and magnetic fields where such techniques did not exist. The following were the areas of focus:

- To develop a helium gas pressure cell for magnetic susceptibility measurements on pressure sensitive materials.
- To develop a miniature diamond anvil cell for the ^{3}He insert into MPMS SQUID magnetometer; it should enables the measurement of magnetic susceptibility at high pressure and at extremely low temperatures (down to 0.5 K).
- To develop a miniature non-metallic diamond anvil cell for high-pressure ac susceptibility measurement in MPMS SQUID magnetometer.
- To develop a compact opposed-anvil cell with spherical sapphire anvils.
- To develop a couple of large-volume piston-cylinder pressure cells for chemical reactions.

1.6 Thesis outline

The thesis consists of eleven chapters outlined below:

Chapter 1: Introduction

General introduction of high pressure instrumentation and high-pressure magnetic measurement, methodologies, and aims of this project are described.

Chapter 2: Literature Review

First part of the Chapter 2 is devote to chronologically review the existing designs of high pressure cells for the MPMS SQUID magnetometer. Then two types of sapphire high pressure cell are reviewed, sapphire anvil cells with spherical sapphire anvil and the sapphire cells developed for small angle neutron scattering (SANS). The final part of the review describes the the publications and past projects that are related to FEA application in high pressure engineering.

Chapter 3: Magnetic Properties Measurement System

As the MPMS SQUID magnetometer is one of the most popular modern commercial magnetometers, this chapter is dedicated to introduce the system layout and the measurement technique of this system. The two different measurement technique in MPMS, direct current (dc) and alternative current (ac), are described in detail. A ^{3}He cryostat add-on system (iHelium3) for the MPMS is described at last in this chapter.

Chapter 4: High Pressure Experimental Methods

This chapter gives a review of theory and common methods for high pressure cell design. The first part of this chapter focus on the piston-cylinder cell. The second part describes the opposed anvil technique which includes the diamond anvil cell and sapphire anvil cell. The final section introduces several commonly used pressure transmitting medias used in high pressure experiment.

Chapter 5: Finite Element Analysis

As FEA was used in the design process of all the pressure cells developed in this project, this chapter provide a brief introduction and information of the technique of the finite element method.

Chapter 6: Helium Gas Pressure Cell for MPMS SQUID Magnetometer

A helium gas pressure cell is presented in this chapter, which is used for magnetic susceptibility measurements on pressure sensitive material at high temperature. The design and testing process are demonstrated and discussed. The measurements data for a newly developed spin-crossover nanopaticles is attached at last to demonstrate the data quality.

Chapter 7: Turnbuckle Diamond Anvil Cell for Sub-K Low Temperature Magnetic Measurement

This chapter presents the development and testing of a miniature, turnbuckle diamond anvil cell for the iHelium3 system. The design was modified from the TM-DAC and the material of the

cell was replaced to CuTi alloy which was reported with lower magnetic signal. The performance of the cell was confirmed in a FEA package and fully tested. The magnetic background of the cell was measured and presented. Several future possible improvements are discussed at the end of the chapter.

Chapter 8: Non-metallic Turnbuckle Diamond Anvil Cell for Ac Magnetic Measurement
The cell presented in this chapter is based on turnbuckle principle and constructed with totally non-metallic components to enable high pressure ac magnetic measurement. The material selection and design process is described in detail including material magnetic background measurement, gasket preparation, pressurisation testing and optimisation. FEA was used extensively for design, failure analysis and optimisation. Ac magnetic measurement data of Dy_2O_3 and U_6Fe is presented to demonstrate that the cell avoids the screening issue which usually accompanies conventional metallic high pressure cells during ac measurement.

Chapter 9: Turnbuckle Sapphire Anvil Cell with Spherical Sapphire Anvils
This chapter is set to build a turnbuckle high pressure cell to contain more sample for neutron scattering. Commercial spherical sapphire are used for anvil as the cost is much lower than the diamond anvil while more sample space. Two designs were tested and the second version was found able to generate and maintain sample pressure above 6 GPa with a sample volume 6 times larger than the conventional diamond anvil cell. Failure analysis was perform on the sapphire anvil to gain a better understanding of the failure mechanism of spherical sapphire anvil. The settle design had been used in measuring the crystal structure of single crystal niobium at 1.6 GPa through small angle neutron scattering (SANS) technique.

Chapter 10: Large Volume Piston-Cylinder Pressure Cells
This chapter presents two piston-cylinder type high pressure cells for chemistry studies. These cells are designed to pressurise large amount of liquid sample up to 800 MPa with controllable manner. Each design and its working mechanism are presented separately. Strain gauge method are used to estimated the internal pressure then the pressure was calibrated with the applied load. The auxiliary tools for the cells are presented at last in this chapter.

Chapter 11: Conclusions and Future Developments
The conclusion and significant outcomes form this project are summarised in this chapter. Furthermore, the future works of each cell developed in this project are outlined at the end of this thesis.

Chapter 2
Literature Review

This chapter is divided to three sections. The first section of this chapter focuses on reviewing the existing high pressure cells for MPMS. The second part concentrates on two types of sapphire high pressure cell, the sapphire anvil cells with spherical sapphire anvils and sapphire cells particular developed for SANS. As FEA method is widely used in the instrumentation work in this project, the recent high pressure engineering involve FEA method are presented at last. All the literatures in each section are reviewed chronologically.

2.1 High pressure cells for the MPMS, Quantum Design

Magnetisation (M) is a fundamental physical property characterising the response of a material to applied magnetic field. The dependence of temperature (T), field (H), and pressure (P) could reveals the nature of magnetic interactions, the critical T, H, and P of magnetic phase transitions, ect. A. A. Galkin has been one of the pioneers of magnetic properties measurements at high pressure. Using a piston-cylinder cell with a built-in solenoid for generating high pulsed magnetic fields, the group led by him mapped and investigated the P-T-phase diagram of MnAs [13].

As the modern magnetometers [3, 14] can provide precise control in temperature and magnetic field change, high pressure instrumentation for the magnetometer became an important field of magnetisation study in past two decades. The main target of this project focuses on developing or modifying high pressure cells for the Magnetic Property Measurement system (MPMS®) from Quantum Design [3], which is the one of the most popular commercial magnetometer as the sensitivity of this magnetometer reaches 10^{-8} emu over a wide range of temperature and magnetic fields. As the excellent sensitivity of this instrument is based on the integrated superconducting quantum interference device (SQUID), this system is usually referred as SQUID magnetometer or MPMS magnetometer for abbreviation. The working principle and operation of this system will be introduced in next chapter.

This section mainly covers existing high pressure cells for the MPMS SQUID magnetometer from 1996 to date. Design constraints and suitable materials for building the cell are discussed first. Then two types of high pressure cells for the SQUID magnetometer, cylinder and opposed anvils are described separately with chronological order. All the existing high pressure cells are only compatible with dc measurement technique, and for ac measurement, the high pressure cells must equipped with built-in coils and most of them are based on DAC design. The difference between dc and ac techniques, the high pressure cells with built-in coils, will be introduced separately in next chapter.

2.1.1 Design challenge of high pressure cells for SQUID magnetometer

The size limitation is the first challenge for designing a high pressure cell for MPMS as the diameter of sample chamber in MPMS is only 9 mm diameter, which means external diameter of the cell must smaller than 9mm to be fit in. Therefore, the published cell designs were

usually described as miniature due to the dimensions of such cells are much smaller than conventional high pressure apparatus. Material selection is another important consideration in design. Magnetic measurements normally involve high magnetic field (0.1 tesla to 7 tesla) and low temperature (200 K to 0.5 K). The material used in construction of a high pressure cell needed to be carefully considered in such extreme environment.

There are three fundamental requirements for material. First, the material strength needs to be high enough to withstand high pressure. Second, the magnetisation of the material is desired to be small and insensitive to the applied magnetic fields, the sensitivity of the cell can be increased if it was made of lower magnetic background material. Last, the mechanical and magnetic property of the material is desired to be stable for a broad temperature particular in extremely low temperature. Apart from three constraints above, sometimes other factors will matter such as commercial availability and price. There are a few suitable materials from the existing publication so far [15–17]. None of these materials listed here is absolute perfect, the instrument scientists need to find their own balance among these considerations such as high pressure range, high sensitivity, budget, material availability etc.

Figure 2.1 and Figure 2.2 shows the magnetic susceptibility of three candidate materials for the magnetic cell. BeCu alloy is the most popular material for pressure cells in the magnetisation measurement at present. The magnetic susceptibility is low as Be and Cu are both diamagnetic element. The ultimate tensile strength can achieve 1.4 GPa after fully hardening at 315 °C for 2 hours. It is commercially available as standard rod or sheet in the market which is convenient and economical to purchase. As shown in Figure 2.1, the magnetic susceptibility of BeCu increases noticeably at low temperature due to impurity containment of nickel or cobalt. The commercial BeCu alloy normally contains Ni and Co with the rates of 0.2-0.5% to avoid the toxic beryllium oxide appears on the alloy surface [18]. The magnetisation of BeCu depends on the added impurity of Co and Ni and the amount. Ni is preferred to Co as its magnetic moment is smaller [19–21]. Apart from that, the mechanical properties of BeCu are very stable at low temperature, the plasticity even increase [17]. This is a unique advantage for constructing low temperature cell as BeCu cells would less likely to have a brittle failure at low temperature.

NiCrAl is a promising alloy for high pressure cell due to the non-magnetic and high strength characteristic. The heat treated alloy is with tensile strength 2.2 GPa [16]. However, the main issue of this alloy is the availability. It is called Russian alloy as it was only available in former USSR region with small quantity [22]. It was not commercially available until successfully

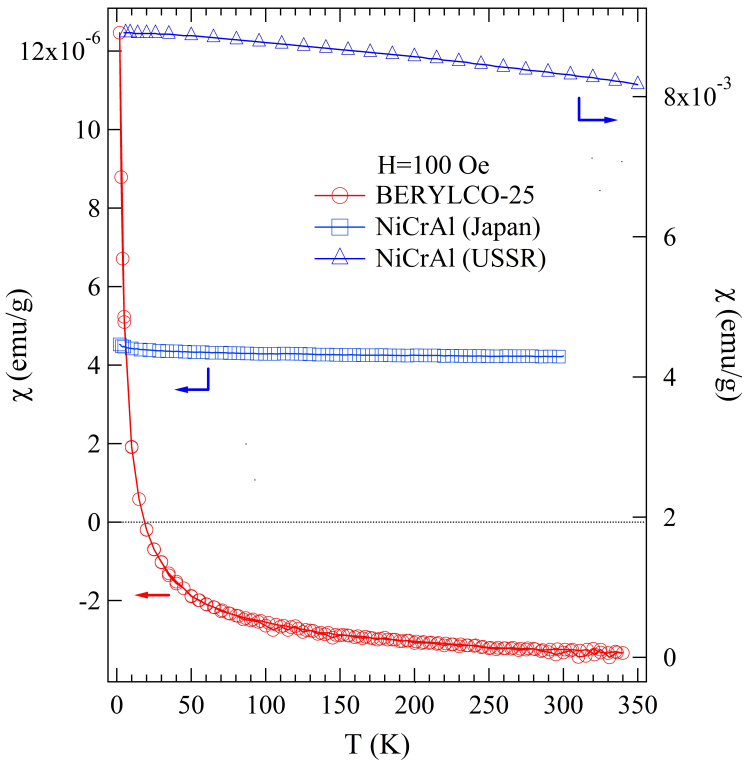

Figure 2.1: *Temperature dependence of the magnetic susceptibility of BeCu alloy (BERYLCO-25) from NGK [15], and NiCrAl alloy from Japan [16] and the USSR region [17]. The BERYLCO-25 is with 0.2% Co and 0.6% Ni+Fe impurity. The arrows indicate which scale the data is associated with. The susceptibility was measured in 100 Oe field over the temperature range from 300 to 2K. It is clear that the NiCrAl from Japan is much lower than the one from former USSR region, the purity control is improved significantly in the Japanese NiCrAl [16].*

reproduction in Japan on 2002 [16], the magnetic background of the alloy was improved significantly as shown in Figure 2.1. Apart from the alloys mentioned above, there is another high strength non-magnetic alloy Co-Ni-Cr-Mo (MP35N) [22] with 1.79 GPa yield strength, which had been used to fabric piston-cylinder high pressure cells [22] for use at 3.5 GPa pressure. However, the magnetic susceptibility of MP35N alloy is much higher than other non-magnetic alloy [16], which made it less favorable in construction a cell for SQUID magnetometer.

High purity CuTi alloy with 3 wt% was reported with lowest magnetic susceptibility among the candidate alloys so far [21]. The susceptibility of diamagnetic copper component and paramagnetic component titanium almost cancel out in the alloy. The definitions of diamagnetic and paramagnetic are explained in chapter 3. The susceptibility of this alloy is reported with 3×10^{-9} emu/g at room temperature, 8×10^{-8} emu/g at 1.8 K [18]. The susceptibility of this

alloy increase at low temperature was believed caused by the impurity. The tensile strength is between 680∼1000 MPa based on mechanical treatment. Again, availability issue is the main disadvantage as this alloy is not widely commercialised as BeCu. The strongest and most pure CuTi alloy seems only available in Japan so far.

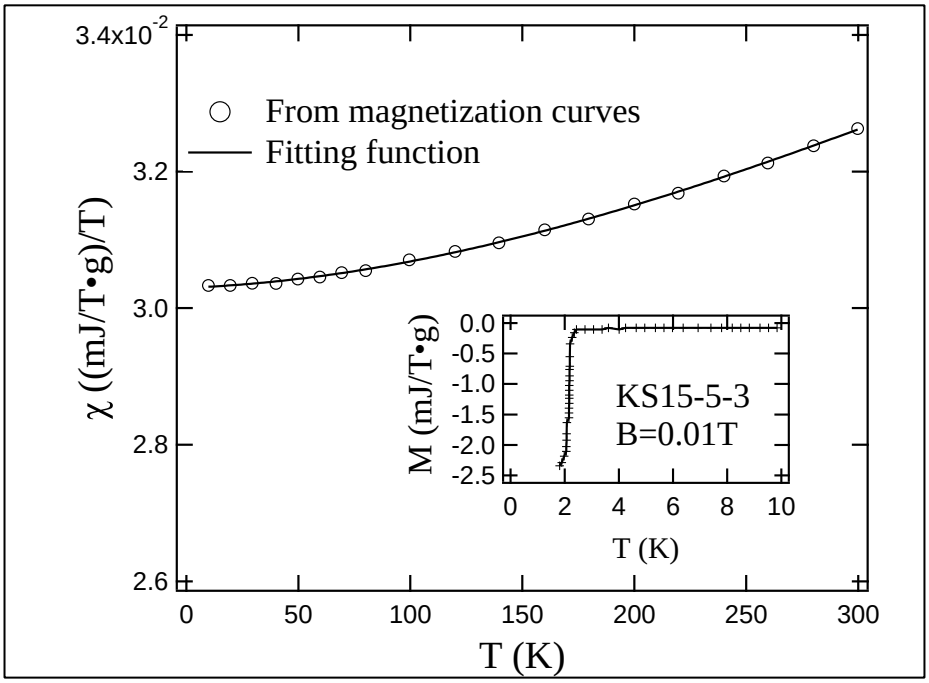

Figure 2.2: *The magnetisation of KSI5-5-3 for several temperatures, the inset shows the temperature dependence of the magnetisation at B=0.01T, superconducting phase transition occurs at 2.5K. [18]*

A β phase titanium alloy KS15-5-5-3 reported by Kamishima and co-workers [18] is a good candidate material because this alloy is extremely pure without ferromagnetic component. The magnetic susceptibility is closed to 3.03×10^{-2} (mJ/Tg)/T at 3 K and almost featureless at broad temperature range (Figure 2.2). For convenience, the magnetic unit is converted to 'emu/g' then the number is 3.03×10^{-6} emu/g. The tensile strength is 1.76 GPa after mechanical rolling and heat treatment, which is higher than harden BeCu alloy. The main problem is that the material experiences a superconducting phase transition at 2.5 K when external magnetic field is applied. Therefore, this alloy is unable to use for magnetic measurement below 2.5 K. In addition, the common shortcoming of Titanium alloy is that the alloys tend to be brittle at low temperature, which makes the titanium alloy less favorable for cryogenic instrumentation.

Recently, high strength engineering plastic material start to be used for building high pressure cells [8, 23]. Engineering plastic is a valuable potential material for high pressure engineering

in magnetic measurement. Particular in diamond anvil cell which does not require much load to applied high pressure on tiny sample. Chapter 7 presents our progress in constructing a DAC from engineering plastic which enable the high pressure ac susceptibility can be measured in the SQUID magnetometer directly.

2.1.2 Cylinder type high pressure cells for SQUID magnetometer

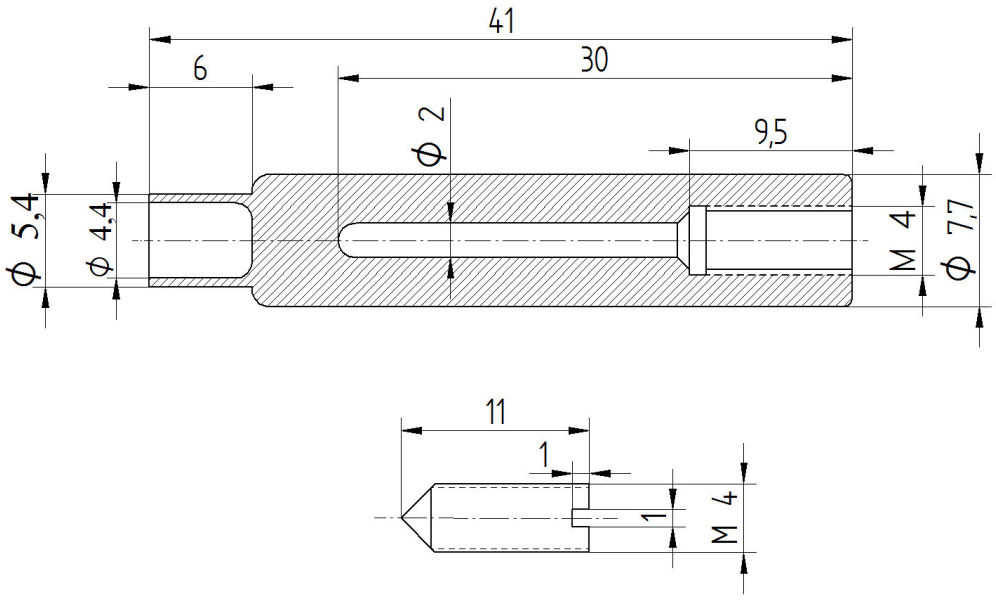

Figure 2.3: *The design of the pressure cell reported by Reich and Gordin [24]. Sample and a Pb manometer was loaded into the cell and immersed in the liquid gallium pressure medium, the dimensions are in mm. Figure was redrawn, not to scale.*

Early pressure cells for SQUID magnetometer were built as cylinder type. This type of pressure cell is very simply to fabricate and with large sample volume. Most of cells were with pressure limit no higher than 1.2 GPa. The first high pressure cell made for the MPMS SQUID magnetometer was reported by Reich and Godin [24] in 1996. The cell was made of titanium alloy (Ti-6Al-6V-2Sn) and only simply consists of two parts, a single cylinder cell body and a closed nut (See Figure 2.3). It is named as miniature cell as the overall diameter is 7.7 mm and overall length is only 41 mm. The maximum pressure was reported about 0.4 GPa by solidifying the pressure medium liquid gallium at liquid nitrogen temperature. This cell had been used to investigate the influence of the pressure on ceramic superconductors $HgBa_2Ca_2Cu_3O_{8+x}$(1223) compound. The superconducting temperature of this material was found increased from 133 K at ambient pressure to 136 K at 0.4 GPa pressure. The pressure was measured by spotting the

superconducting transition temperature T_c of Pb manometer. The manometer technique was proposed by Eiling and Schilling [25], which used the shift of superconducting transition temperature T_c of Pb, Sn and In to calibrated the sample pressure. These elements are widely used in the high pressure cell for magnetic measurement because of the accuracy and convenience, therefore they are often called manometer in the high pressure society. The detail of this technique is further explained in chapter 4, equation 4.25. As the pressure generation of Reich's cell is uncontrollable by this setting, piston-cylinder cell are more commonly used in the following designs.

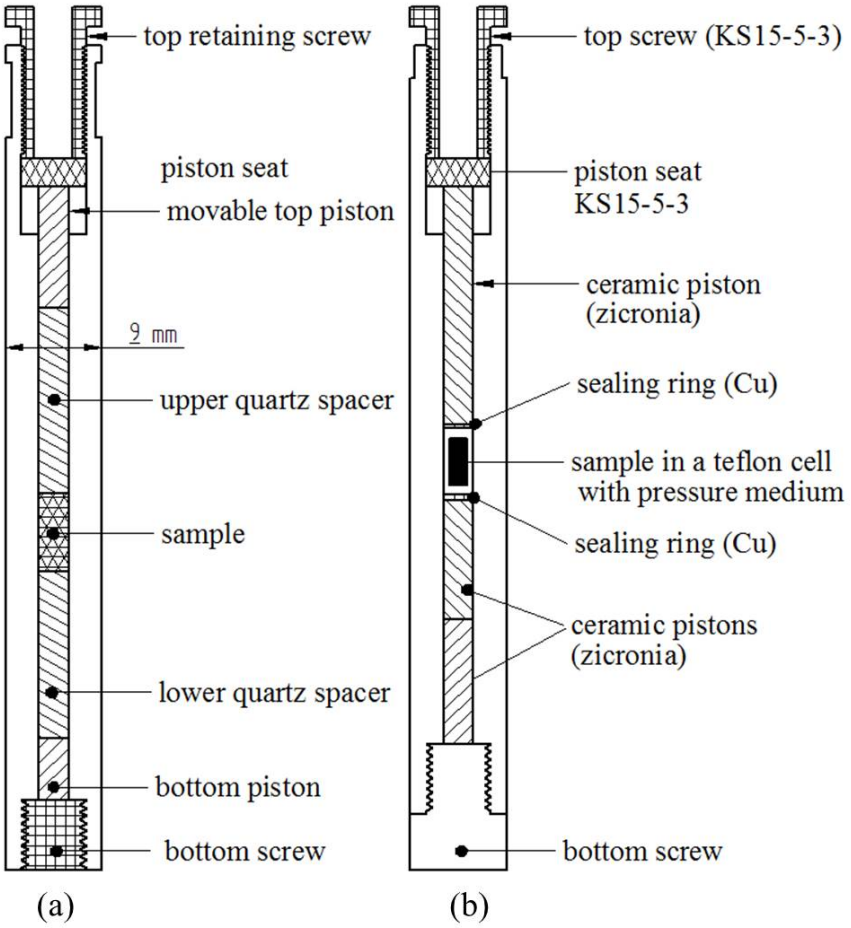

Figure 2.4: *(a) Schematic of the cell reported by Diederich et al [26], which is made of BeCu alloy with 210 mm overall length; (b) Kamishima's cell [18], made of KS15-5-3, overall length is 120mm. (Figures were redrawn, not to scale).*

Figure 2.4(a) shows a typical piston-cylinder high pressure cell developed in 1996 for SQUID by Diederichs *et al.* [26]. The pressure of this cell is created by applying the load to the pusher which is inserted into cell through the hole on top. The load is transfered to the piston seat then

finally to the sample. External load is generated a hydraulic press. In the meantime, the hollow retaining screw is tightening into the cell body to lock the advance of the piston to lock the pressure. When desired pressure is achieved, the cell can be removed from the press and insert into the SQUID magnetometer for measurement. The body of the cell is a long cylinder which is made of BeCu alloy. The highest attainable pressure was reported 1 GPa with Flourinert FC 75 pressure transmit medium. A pair of quartz spacers are used to pressurised the sample directly. This layout keeps the sample away from the ends of the cell. which yields a more symmetric distribution of the magnetic background signal. Sealing mechanism of this cell was not mentioned in the paper. The pressure was found able to be calibrated by measuring the extension of the overall length of the cell through an optical micrometer at room temperature. Combining with the T_c measurement of a Pb manometer, the pressure and the extension of the cell body is liner related as 42.2 μm/GPa, which enables the pressure can be approximated at room temperature through measuring the extension of the cell body only. The cell was used to measure the magnetic susceptibility of Rb_3C_{60} sample under pressure in the SQUID magnetometer. The magnetic susceptibility of this material was found decrease under pressure both at 50 K and room temperature.

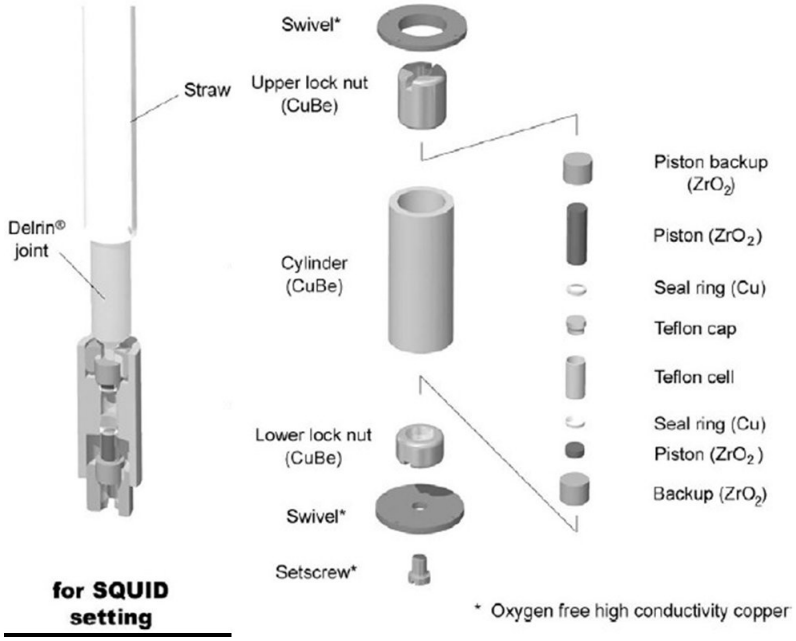

Figure 2.5: *Schematic drawings of micro high pressure cell [27, 28].*

Figure 2.4(b) shows an improved design reported in 2000 [18]. The cell was made of titanium alloy (KS15-5-3) which shows desirable temperature-independent magnetisation curve as

shown in Figure 2.2. This alloy is with low magnetisation and high material strength in comparison to BeCu alloy. The ceramic (Zirconia) piston is with lower magnetic background if compare to quartz piston used in the earlier design [26]. Therefore the sensitivity of this cell is increased with these measures. PTFE capsule was used to contain sample and liquid pressure medium. Cu rings were used for extra seals to prevent leakage and extrusion. The pressure range of this cell is 1 GPa and Sn manometer is used for pressure calibration. The cell had been used in measuring the pressure effect on the one-dimensional antiferromagnet Ni (333-tet) (μ-NO_2)×(ClO_4) which is with small magnetisation. The main shortcoming of this cell is that it is unable to use at temperature below 2.5 K which is the superconductivity temperature of the titanium alloy in used. A similar BeCu version piston-cylinder cell for MPMS was commercial available from easyLab [29] since 2004, the working principle of the cell is the same with cells reviewed above but pressure capability was increased to 1.2 GPa. Researchers can purchase this pressure cell commercially rather than manufacturing in-house.

A series of short version of piston-cylinder cells were reported by Umehara *et al.* [27] in 2004 and Uwatoko *et al.* [28] in 2005 (Figure 2.5). These cells were designed to measure the magnetisation of CeAg sample in MPMS and the specific heat of the sample through standard adiabatic method. These cells were named as micro high pressure cell due to the length of the cell was minimized to 21 mm which is the shortest piston-cylinder cell to date. These cells were made of harden BeCu alloy and the highest pressure was achieved 2 GPa in one cell with 2.5 mm diameter bore. Sn manometer was used for pressure measurement.

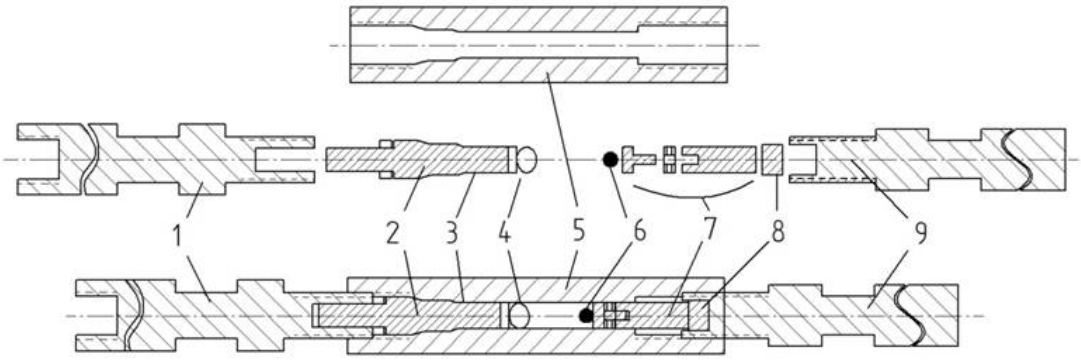

Figure 2.6: *Schematic drawing of high pressure cell for MPMS designed by Kamarád and co-workers [30]. The cell is with 2.5 mm bore and outer diameter 8.6 mm; (1) upper clamping bolt, (2) plug, (3) seals, (4) sample on holder, (5) cell body, (6) Pb manometer, (7) piston with Bridgeman mushroom-type seal, (8) piston backup, (9) lower clamping bolt. The figure was redrawn, not to scale.*

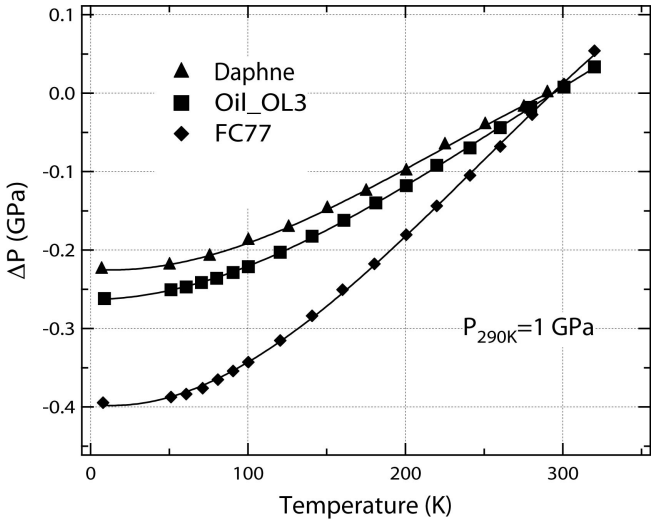

Figure 2.7: *Temperature induced pressure variation in the clamped cell reported by Kamarád et al.[30].*

Figure 2.6 shows the schematic drawing of different piston cylinder cell reported by Kamarád *et al.* [30] in 2004. The cell was made of BeCu alloy with 2.5 mm internal diameter and 8.6 mm external diameter with pressure limit up to 1.2 GPa. Hydraulic press was not needed in this design as pressure is generated by tightening the clamp screws manually. The sample and pressure medium can be loaded directly into the cell without capsule as the Bridgman mushroom seals are used to seal the moving piston at high pressure. The Bridgman mushroom seals will be further described in Chapter 4. As there is no magnetic signal from the PTFE capsule, the sensitivity and sample volume of the cell can be increased. Lamé equations were found can be used to approximate the pressure inside cylinder body at room temperature by measuring the radial expansion of the cell body and calibrated the Pb manometer. The cell had been used to study the temperature induced pressure changes from 350 K down to 5 K using different pressure transmitting media like Daphine, Oil OL3 and FC77 as shown in Figure 2.7. Pressure variation at low temperature is a common senario for low temperature measurement and can be significant for piston-cylinder cell due to the difference in thermal expansion coefficients of the alloy and the pressure transmitting media.

Kamenev *et al.* [31] reported a long symmetric high pressure cell (Figure 2.8) for high pressure magnetic measurements on a molecular antiferromagnet compound $[N(C_2H_5)_4][FeCl_4]$ up to 1 GPa. The cell body is made of BeCu and the pre-stressed technique (double layer with interference fit) was used in constructing the cell to improve the stress distribution on the cell body. The working principle of this cell is similar to the last design [30]. Pressure is generated

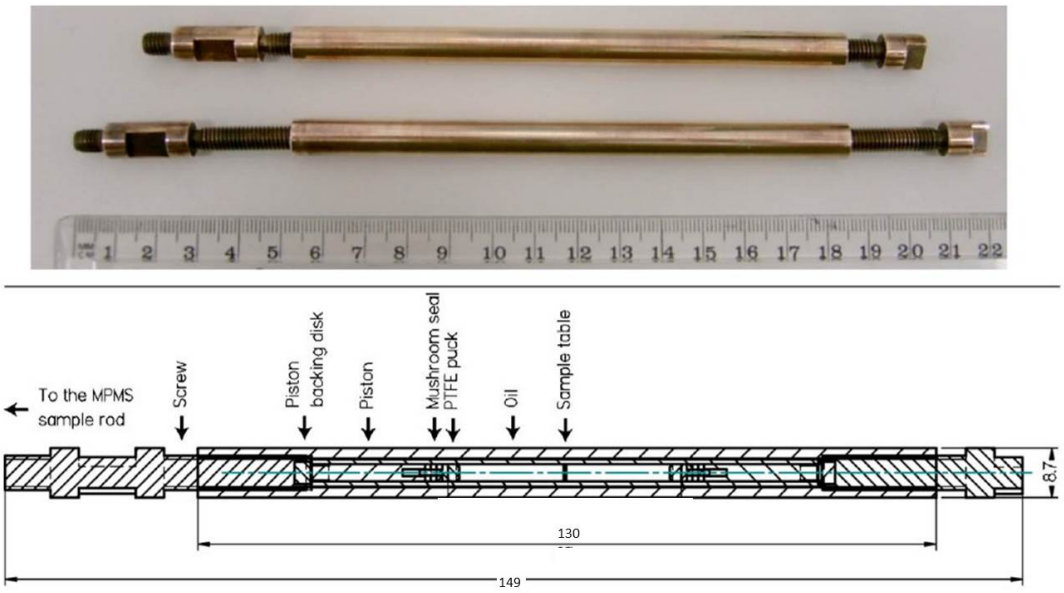

Figure 2.8: *(a) photograph of the high-pressure cell at ambient pressure (bottom) and top pressure (top); (b) Drawing of the cell with the distance between the pistons shown for the top applied pressure. Figures from Kamenev et al. [31]*

by tightening the clamp screws to applied load to the sample. However, the sample volume is greater than Kamarád's cell as the cell was made much longer. The fully symmetrical layout of the cell was turned out to be very beneficial on the background correction and improve the sensitivity of the measurement, which allows sample with low magnetic susceptibility to be measured under high pressure. As the sample has a transition into an antiferromagnetic (AF) phase at T_N=3.0 K, which is lower than the temperature of the superconductive transition of manometer Pb (T_c=7.20 K), Sn (T_c=3.20 K), or In (T_c=3.40 K), using the manometer for pressure measurement will create significant background and and screens the sample signal. Therefore, Lamé equations were used to calculate the pressure at room temperature then the pressure was further calibrated with manometer Pb to obtain the pressure variation information at low temperature.

In 2008, Sanchez-Benitez *et al.* [32] reported a piston-cylinder cell with a plug for in situ pressure measurements with feed-through wires connected to a manganin pressure sensor which has a known pressure dependence of electrical resistivity (Figure 2.9). It provided a mean to monitor pressure continuously during magnetisation measurements in MPMS. The true pressure can always be established in the range of temperature in this cell.

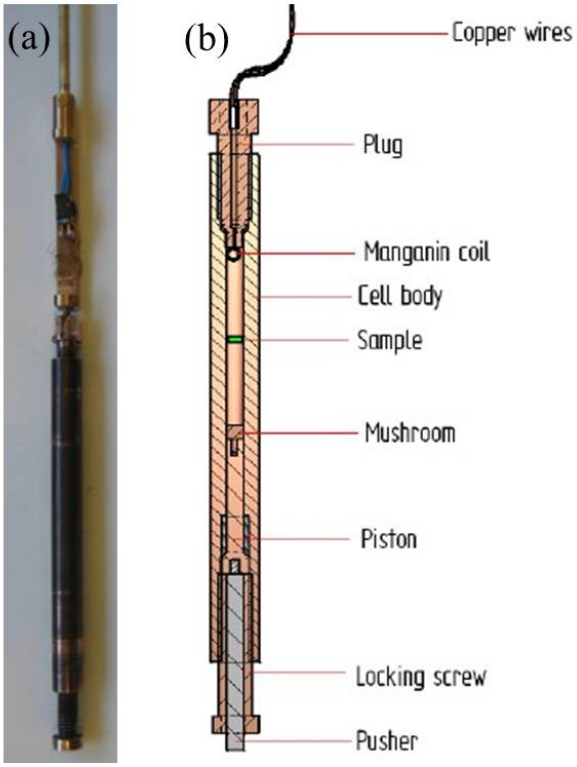

Figure 2.9: *(a) Assembled pressure cell attached to the MPMS sample rod through and adapter with a 4-pin socket mounted on it; (b) cross sectional view of the assembled pressure cell. Figures from Sanchez-Benitez et al. [32]*

2.1.3 Opposed anvil cells for SQUID magnetometer

Because of the strength limitation of the non-magnetic materials, higher pressure range (greater than 2 GPa) requires the use of opposed anvil cells which was pioneered by P W Bridgman [34]. This opposed anvil technique will be further introduced in Chapter 4 and DAC is one of the most popular opposed anvil cell. Limited sample volume in the opposed anvil cells is the major disadvantage for magnetisation measurement in the MPMS. To employ this type of high pressure cell in magnetic measurement, efforts is required on minimising the magnetic background of the cells as much as possible. Accordingly, increasing the sample volume to contain more sample is another development direction. Progress is started at beginning of 21st century by Mito *et al.* [33]. They developed the first miniature diamond anvil cell (mDAC) for the MPMS in 2001 as shown in Figure 2.10. The cell was made from BeCu alloy with tilt adjustments of the anvil. Pressure in this cell was calibrated by measuring the T_C of Pb and ruby fluorescence method [35]. This cell had been used to perform a high pressure research on f-electron ferromagnetic compound $GdZn_2$ up to 4.9 GPa at 20000 Gauss magnetic field. The sensitivity of

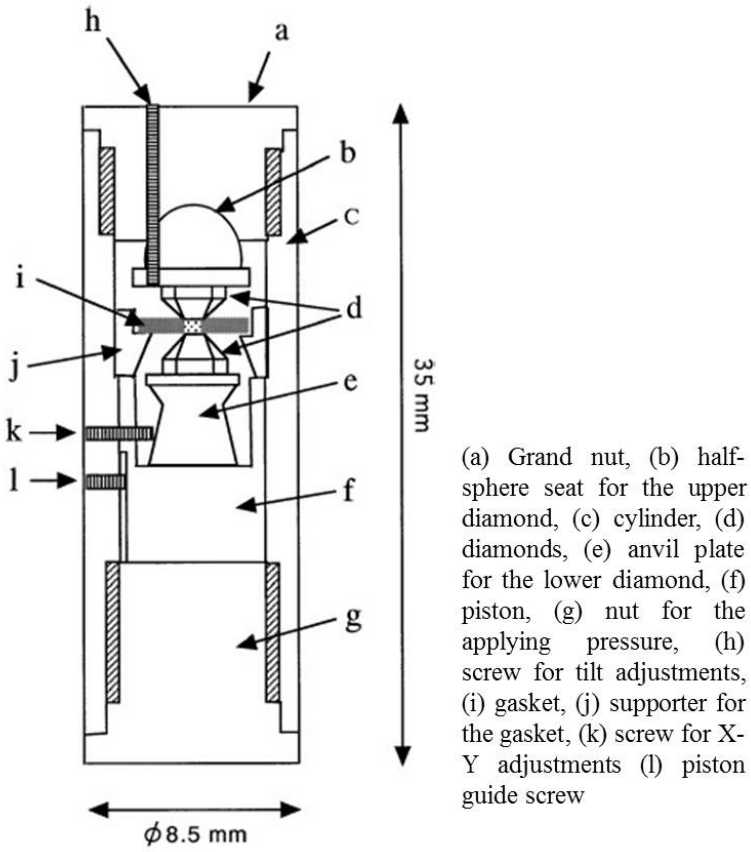

Figure 2.10: *Schematic drawing of the mDAC [33]*

this cell is around 10^{-6} emu.

Kobayashi *et al.* [36] developed a ZrO_2 (Zirconia) opposed anvil cell for SQUID magnetometer in 2007 (Figure 2.11). The cell seems like a combination of piston cylinder cell and opposed anvil cell. The cell body was machined from BeCu alloy. Zirconia anvils were used in the cell as its magnetisation is negligible if compared the the measured sample. Thick gasket was used and it was made of NiCrAl. The high strength gasket enables the cell to contain greater initial sample volume with 1 mm in diameter and 1 mm in thickness, the sample volume reaches 0.3 mm^3 which can compensate the strong background signal from the NiCrAl gasket. As background signal from the gasket cannot be overlooked, the background correction of the measurement is necessary for this cell. The magnetisation of the NiCrAl alloy was found depends on the aging temperature and time. $700\,^{\circ}\mathrm{C}\times 2$ h was recommended the optimal aging condition because this heat treatment provides the alloy with a small, linear magnetisation which is preferable for the background subtraction. The major shortcoming of using ceramic

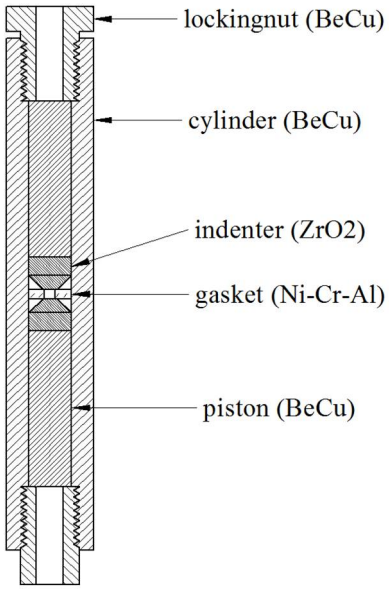

Figure 2.11: *Cross-sectional view of the Kobayashis cell [36]. (Redrawn, not to scale)*

anvil is that the pressure measurement method is limited to the manometer method as of the anvil is not transparent. Therefore, pressure inside the cell is only measured by superconducting transition of the manometer inside the sample. This cell had been used to gather high pressure magnetisation measurement data of UIr sample up to 4 GPa.

NdRhSn single crystal was found with huge anisotropy of magnetic interactions, Kamarád *et al.* [37] had designed two miniature uniaxial pressure cells for magnetic and neutron-diffraction studies of this crystal in a SQUID magnetometer and in a neutron diffractometer respectively. The schematic drawing of the uniaxial pressure cell for SQUID magnetometer is showed in Figure 2.12. The oriented sample is closed by two ZrO-ceramic anvils. The uniaxial force applied on the sample is produced from a set of CuBe bellville springs. Each set of the springs is inserted into a thin-wall tube and fixed to the cell-squeezing screw. This springs system was calibrated by compressing it using a precision load transducer in advance. Users can determine the actual force acing in the cell directly from the calibration curve and a measured elastic compression of the springs system inside the cell when tightening the squeezing screw.

A break through DAC design was reported by Alireza and Lozarich [38] on 2009. This DAC (Figure 2.13) can be considered as a modified version from the previous ceramic anvil cell [36]. Instead of ceramic anvil, diamond anvils were used. The DAC was made from high purity CuTi alloy which has ultra low magnetic susceptibility. Pressure is generated by tightening the screw

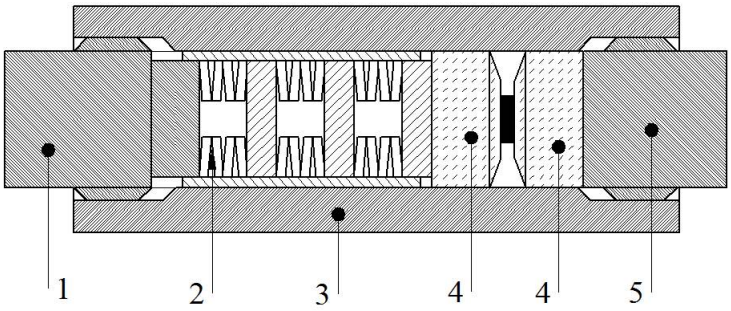

Figure 2.12: *Schematic drawing of uniaxial pressure cell for MPMS designed by Kamarád et al. [37]. (1) CuBe squeezing screw, (2) set of the Belleville springs, (3) cell body, (4) ZrO anvils, (5) CuBe fixing screw. (Redrawn, not to scale)*

so the hollow pistons push the anvils toward each other to compress the sample in the gasket. The hollow piston provides an optical access for pressure measurement by ruby fluorescence. Alignment mechanism is highly depends on the machine quality of the cell and the anvils surface. The cell material around the sample is removed to further reduce the magnetic background signal from the cell. Apart from that, the cell body was electro polished and kept free as possible of magnetic containment. As a result, the sensitivity of this cell reach as high as 10^{-7} emu in the experiment. The cell is capable to detect the magnetic features of phase transitions in the weakly magnetic samples based on its extremely low magnetic background. The ferromagnetic transition of $Cu_2Ru_2O_4$ and CoS_2 were seen clearly at high pressure even without background subtraction. In addition, antiferromagnetic transition of the $CePdGa_6$ material was detected at 4.5 GPa with the background subtraction and a pair of diamonds with larger culet diameter of 900 μm were used to increase sample volume. In the experimental test, the cell was capable to achieve above 14.2 GPa at room temperature with a pair of 800μm culet diamond, and the sample size is $\sim 200\times180\times60\mu m^3$.

An extremely small turnbuckle magnetic DAC (TM-DAC) for MPMS was developed in our group [11] in 2010. As shown in Figure 1.2, the cell is 7 mm long and 7 mm in diameter and weight only 1.5 g. The cell is made of BeCu alloy and only consisting of a counter-threaded cylindrical body and two anvil supports which are identical but with external threads cut in opposite direction. The load on the diamond anvils and the sample between them is generated using a hydraulic press. The load is then locked by rotating the buckle cell body with respect to the anvil supports. No particular holder is needed for the cell as it can be loaded into a standard plastic straw holder (as shown in Figure 1.2). It is capable of achieving

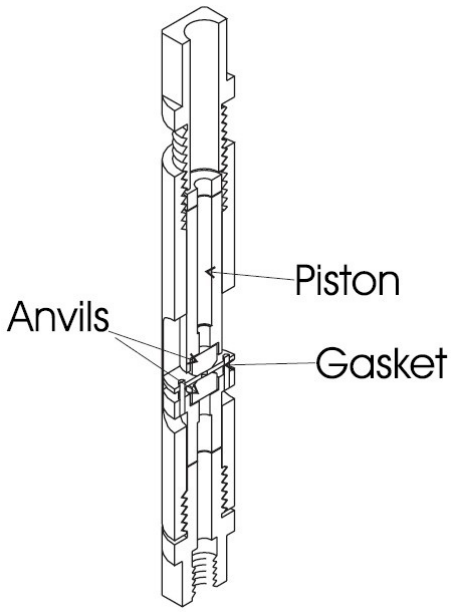

Figure 2.13: *Schematic drawing of the diamond anvil cell designed for MPMS reported by Alireza and Lozarich [38]. The cell is 8.4 mm in diameter and 64 mm in length.*

pressure in excess of 10 GPa while allowing measurements to be performed with the maximum sensitivity (10^{-8} emu) due to the tiny size of the cell and the symmetric layout. The cell had been successfully used to perform high pressure magnetic study on $Mn_3[Cr(CN)_6]_2{\cdot}H_2O$ Prussian blue analog up to 10.3 GPa.

Most recently, during 2011 and 2013, a serial of cells called miniature ceramic anvil high pressure cell (mCAC) were developed by Tatewia and co-workers [39–41]. As shown in Figure 2.14, these cells are based on the previous cell reported by Kobayashi et al. [36] with several improvements. The unique feature of this cell is that the anvil was made of non-magnetic composite ceramic (FCY20A) [42]. This material is a mixture of Y_2O_3-partially stabilized zirconia (ZrO_2) and alumina (Al_2O_3) synthesized under high temperature and high pressure. The magnetization of this newly develop ceramic is comparable to the conventional zirconia but with 2 times higher fracture toughness (6.5MPa $m^{1/2}$). The excellent property of this material allows the cell can be machined without an anvils alignment mechanism. The latest version type C is shown in the Figure 2.14, the BeCu piston was gradually replaced by the ceramic piston to further reduced the magnetic background from the cell. BeCu gasket was used for lower magnetic background in comparison to Kobayashis cell [36]. The main advantage of such cells is the cost effectiveness. The cost of the ceramic anvil was claimed 10 times lower than diamond

anvil but with the same pressure performance. Maximum pressure was reported up to 13 GPa with 500 μmm culet anvils and a rhenium gasket. The sample volume can be increased with cupped ceramic anvils (1 mm culet) and pressurised up to 5 GPa.

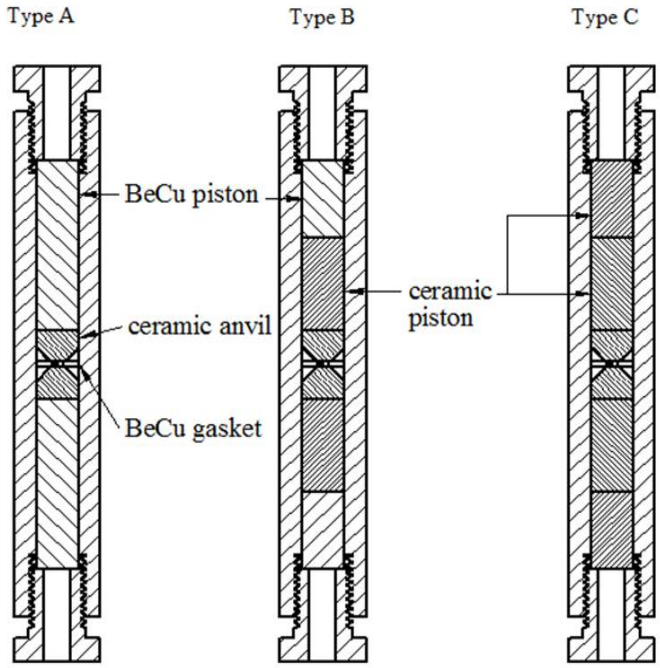

Figure 2.14: *Cross-sectional views of the miniature ceramic high pressure cells [39–41]*

2.1.4 Discussion

After reviewing all existing high pressure cells developed for magnetic measurements in the MPMS SQUID magnetometer, there is a trend that the opposed anvil cell (mostly DAC) are become more and more popular in this field based on the following reason. The DAC is three to four orders of magnitude smaller but able to generate static pressure much higher than the piston-cylinder cell. In most scenarios, the excellent sensitivity of the SQUID magnetometer can pick up the sample signal even though the available sample volume is very limited in a DAC. Apart from that, the DAC is much easier in design, fabrication and operate. More importantly, in the event of failure the DAC is completely safe to the users. In contrast, great attention must be paid to the safety protection for massive hydraulic pressure cylinder.

There are three aspects listed below that the existing high pressure instrumentation for MPMS SQUID magnetometer had not been involved. First, the minimum controllable pressure of the

piston cylinder type cell is above 100 MPa for piston cylinder cell. The conventional piston-cylinder cells are very inconvenient for investigating the materials which are extremely sensitive to pressure. Such as the magnetisation of the material can be tuned greatly by the pressure in 10 MPa scale. Second, the lowest temperature limit of the MPMS SQUID magnetometer is 2 K. There is a recently developed add-on ^{3}He system [43] to extend the temperature range of the SQUID magnetometer to further down to 0.05K. However, the space inside this add-on system is even more limited (diameter smaller than 6 mm). Because of this, there is no high pressure instrumentation work have been carried out for this system so far. Therefore, high pressure magnetic measurement at sub-K temperature range in the MPMS is still very difficult. Last, even though the SQUID magnetometer is capable to measure ac susceptibility, all the high pressure cells reviewed so far are only compatible with dc magnetic measurement because the conventional cells are made of metallic materials which are not usable in ac magnetic field. The solution of these issues are provided in this document, and the progressive works will be presented specifically from Chapter 5 to Chapter 7. All the developed instruments were tested extensively and their effectiveness have been proven in magnetic measurements.

2.2 Sapphire cell

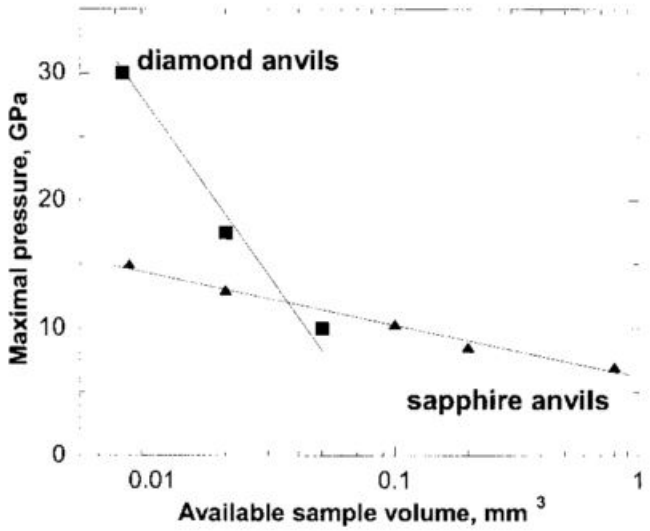

Figure 2.15: *Maximal pressure versus available sample volume in Diamond and sapphire anvils cells [44]*

The nomenclature of sapphire cell is divided to two categories in this section, the opposed

sapphire anvil cell and sapphire window cell, which are both related to the high pressure cell presented in Chapter 9. Sapphire have been used in fabrication of high pressure instrument because of the following advantages. Sapphire is transparent in wavelength range from ultra-violet to the infrared (144 nm - 6 μm) [45], which is a very welcome characteristic for optical measurement. Apart from that, sapphire is preferable for neutron scattering due to the fact that large gems (typically 10 mm diameter) are commercially available with trivial cost [46] if compare to diamond. For opposed anvil cell, the larger sapphire anvil allow more sample volumes which can be orders of magnitude larger than traditional diamond anvil cell. The disadvantages of sapphire is also very clear, it is brittle and fragile which limit the pressure capability. Therefore, for the opposed anvil cell with pressure capability below 10 GPa, sapphire anvil cell is very cost effective. There are vast number of sapphire anvil cells and sapphire window cells, which have been reported during the past two decades. This section would only review two types of sapphire cells, the sapphire anvil cell with spherical anvils and the recently developed high pressure cells for SANS experiment. These high pressure cells specifically developed for the SANS experiment are called SANS cell in this document.

2.2.1 Spherical sapphire anvil

The pressure performance of sapphire anvil cell and diamond anvil cells are mainly rely on the sample volume (or culet size) as shown in Figure 2.15. The pressure performance generally decreases when sample volume is increased. Highest pressure in sapphire anvil cell was reported up 15 GPa for a sample volume less than 0.01 mm^3 [44]. In most sapphire anvil cell, the anvil is ground from a cylindrical sapphire to formed conical head with a small culet based on traditional Bridgman anvil shape. Spherical sapphire anvil was found a much more economic and convenient to be used as anvil because the sapphire ball is a standard industrial product which has been massively produced. As a result, the price is almost negligible, the largest standard size 3/8 inch (9.53 mm) cost less than 30 pounds. In addition, the sapphire ball can be formed to anvil very fast by polishing a small compression face (culet) on it. A parallel face can be polished at the opposite size for observation. The pressure performance of the spherical anvils can be comparable to the conical anvil, the highest pressure of spherical sapphire anvil was reported 12 GPa [45].

Self-alignment is an another advantage of spherical anvil based on the spherical backing support [45]. One anvil can glued into the spherical support with approximate alignment from

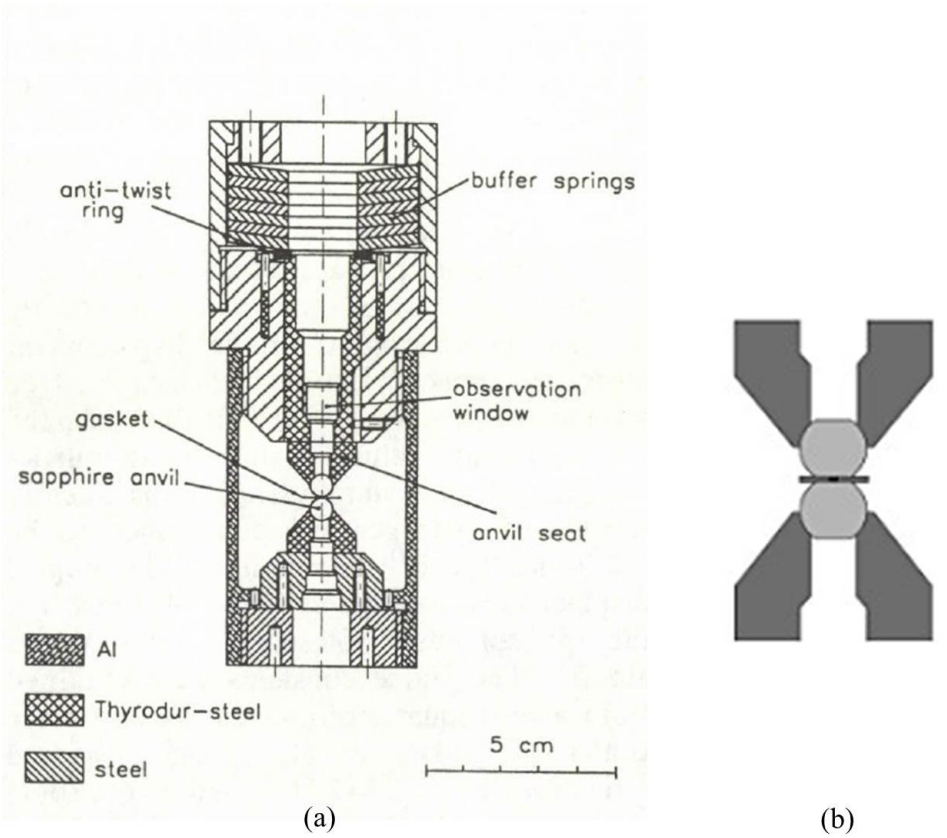

Figure 2.16: *(a)Schematic drawing of the cell reported by Kuhs and co-workers [47–49]. (b) The enlarged view of the anvils and support.*

the cell, the other anvil was then inserted and culets were broght into contact. This process would rotates the second anvil and the culet face will be parallel aligned by its own. Impurity of Cr^{3+} in the commercial standard sapphire ball could lead to interference if ruby fluorescent method [35] was used in pressure measurement. High focalised laser beam is needed to avoid the interference.

Figure 2.16 shows the first high pressure cell equipped with spherical sapphire anvils reported by Kuhs *et al.* [47] in 1989. The cell was designed for work on four-circle diffractometers equipped with an Eulerian cradle and the cell had been test with pressure up to 2.5 GPa. The central optical assess through the cell allows users observing the sample during the high pressure experiment and measure the pressure by ruby fluorescence method. The cell is loaded manually by turning the screws on the top of the cell which had not been shown in the figures. The cell had been used in high pressure in neutron diffraction on normal and deuterated ice VI. Later in 1996, the cell with an improved data collection software was tested in both X-ray

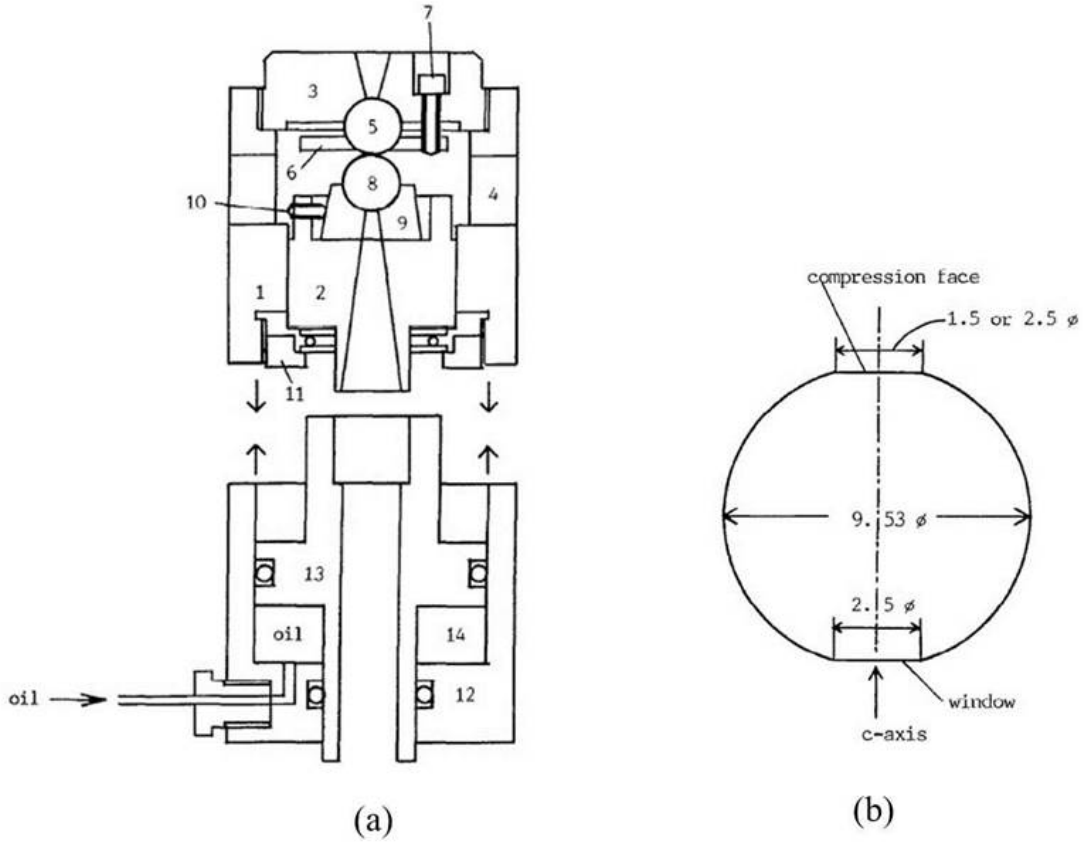

Figure 2.17: *(a) The construction of the cell and a hydraulic actuator; (b) The spherical sapphire anvil with a flat compression face and an optical window face on top. Figures from [45].*

and neutron diffraction up to 3 GPa [48] under the temperature range from room temperature to a few K. The quality of test data is comparable to the existing Merrill-Bassett cells system. The cell had been further used in single crystal experiments on H_2O and D_2O ice VI and KDP (KH_2PO_4). The measurement data of KDP sample within this cell was published in 1998 [49].

As shown in Figure 2.17, a more compact sapphire anvil cell with spherical sapphire anvils was reported by Takano and Wakatsuki [45] in 1991. The operation of the cell is more delicate as a hydraulic system was incorporated into the cell. The load applied on the anvils can be monitored in the hydraulic system. This cell is specifically developed for the optical and spectroscopy study which is less demanding for sample volume. Therefore, the pressure performance of this cell was much higher based on the smaller culet and thin gasket. The highest sample pressure was achieve 12.6 GPa with 1.26 ton load and the sample volume was approximately 0.01 mm^3 (as shown in the Run No.1 in Figure 2.18). The pressure is the highest record in the existing

sapphire anvil cells with spherical anvil. There was a simple sapphire ball cell developed for ultraviolet study in 1992 by Daniels *et al.* [50]. As the pressure range of that cell is limited, the construction would not be further reviewed.

Run no.	Diameter of compression face (mm)	Gasket: External diameter (mm)	Gasket: Diameter of hole (μm)	Gasket: Thickness (μm) initial	Gasket: Thickness (μm) final (t_f)	Cell load (ton)	Average pressure (GPa)	Attained pressure (GPa)	$t_f/2a$	Efficiency	Pressure medium
1	1.5	10	350	100		1.26	7.10	12.6		1.80	silicone oil (1)
2	1.5	2.5	250	100	70	0.90	5.10	10.5	0.046	2.06	"
3	2.5	2.5	250	300	120	2.50	5.09	10.7	0.048	2.10	"
4	2.5	10	1000	100		1.43	2.90	5.4		1.90	KI
5	1.5	2.5	250	250		1.24	7.00	8.4		1.20	Et-Me[a]
6	1.5	10	250	200	100	1.11	6.30	11.8		1.90	silicone oil[b]

[a] A mixture of 4:1 ethanol and methanol.
[b] Shin-Etsu Chemical Co., Ltd., KF96-50cs.

Figure 2.18: *The test data from Takano and Wakatsuki [45].*

2.2.2 SANS cell

Small-angle neutron scattering (SANS) is an experimental technique that uses elastic neutron scattering at small scattering angles to investigate the structure of various substances at a mesoscopic scale of about 1 - 100 nm. For example, SANS can be used for observation of vortices in superconductors [51], combining extreme sample environment of high pressure and magnetic field. The pressure-dependent studies of material through SANS is increasing recently. However, only a few pressure cells had been developed for SANS so far. Most experiments are within this subjects as soft condensed matter research or biology system, which normally required moderate pressure environment (100 MPa to 1 GPa). Instead of pressure capability, sample volume is the main requirement for most SANS experiment. Traditional piston-cylinder cell had been used for the SANS experiment [52], but the sample signal was found not satisfactory because the neutron beam needs to go through the cell body for scattering. The micro structure of the alloy such as precipitations, grain boundaries can interfere the measurement result greatly. To avoid the problem, most existing SANS cells are used large sapphire window in the pressure cell fabrication [53–58]. The maximum pressure of these sapphire windows can hardly achieve beyond 500 MPa which is the major shortcoming of the window cell. Figure 2.19 shows the basic working principle of these cells. The sample is located between two sapphire window, and pressure is generated by an external pressure generator. The incoming neutron beam would go through the windows and hit the sample then scatter with a small an-

gle. A detector on the opposite side would collect the scattering data for further analysis. As these designs are conceptually similar, only the most recently build sapphire window cells are reviewed [57, 58].

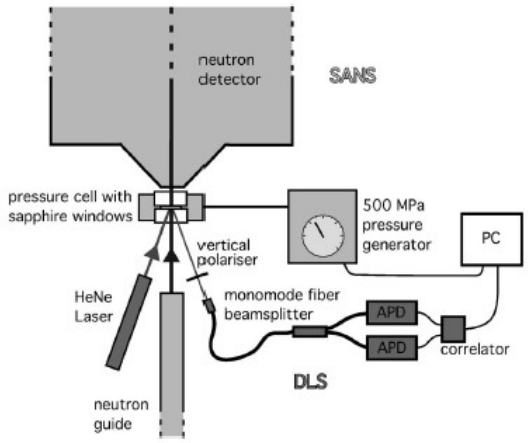

Figure 2.19: *Schematic diagram of common setup of high pressure sapphire window cell for SANS [58].*

Figure 2.20 shows a window cell reported by Gabke *et al.* [57] in 2005, which follows the typical layout of the sapphire window cells. Two 10 mm thick sapphire windows are enclosed in the cell to form a disk-liked sample chamber and windows are locked in the position by two backing nuts with central holes, these holes is for the incoming and scattering neutron beam. The sample is injected into the sample chamber through a side hole and pressurised by an external hydraulic compressor. Maximal pressures of about 300-400 MPa were reported in this cell. A circulating water system is included to control the temperature of the cell.

Figure 2.21 shows a bigger window cell built by Kohlbrecher *et al.* [58], which is with a more sophisticated set up. The sapphire windows are much larger than earlier version, 62 mm in diameter and 35 mm thick. The sample volume can be 1.5 cm^3 which is highest in the existing SANS cells. In addition, the pressure performance was increased to 500 MPa. The fluid sample is pre-loaded in a sample container which consists of two smaller sapphire plates and a pair of Viton O-ring. By this setting, sample and hydraulic fluid from the external compressor are separated during the pressurisation. This measures can effectively prevent the contamination issue which is important in Biology research.

Apart from the sapphire window cell, there is only one SANS cell [59] adopted the opposed anvil technique. Figure 2.22 shows the section view of the cell. Anvils are 30 mm in base

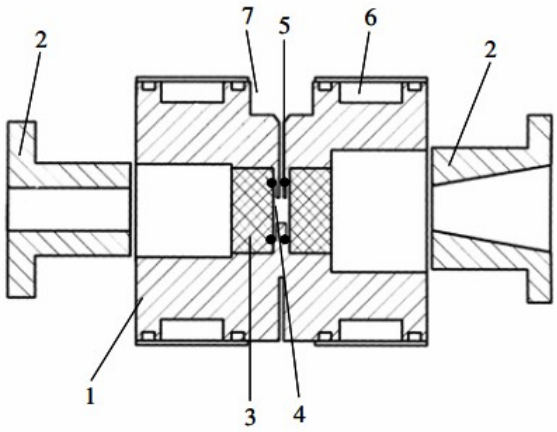

Figure 2.20: *Gabke's SANS cell, (1) body, (2) closure nut, (3) sapphire windows, (4) sample, (5) Vilton O-ring seal, (6) water circuit, (7) high-pressure [57].*

diameter and 20 mm high, both are shaped in to a truncated cone with a large culet (14 mm in diameter). Thick and large gasket were used to increase the sample volume as much as possible. A hydraulic system was incorporated in the design for applying load. The pressure performance of the cell was slightly higher than the window cell. Highest pressure was reported 530 MPa by applying 15 tonnes load on a BeCu gasket with 1.8 mm thick and a 4 mm diameter sample hole. The pressure rang of this opposed anvil cell is obviously much lower than the conventional sapphire anvil cell because of the sample volume is the main consideration. The thick gasket and large culet would cause the pressure generation efficiency much lower and the anvil would failed before pressure reached higher value.

2.3 Finite element analysis for high pressure engineering

This section introduces the existing literatures of high pressure instrumentation involving FEA method. FEA method was firstly developed in 1956 [12] and stared to be used in high pressure instrumentation since 1980s following the developing of computer science. At the beginning, FEA is mainly used to optimising the geometry of diamond anvil to improve its pressure performance and extend its working life time. The FEA method allows the researchers to assess the anvil in a fast, economic and non-destructive way. The stress and deformation patterns of the anvil under load can be simulated in a computer without risking the real diamonds in a actual failure test. It is used more widely in the high pressure community in all sorts of high pressure cell development nowadays. This section starts from the FEA on DAC and then move

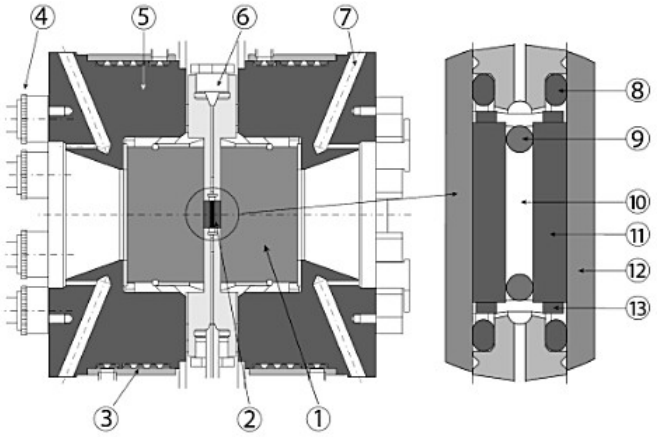

Figure 2.21: *Kohlbrecher's SANS cell [58], (1) sapphire window, (2) sample cell, (3) colling jacket, (4) tie rods, (5) cell body, (6) hydraulic oil inlet, (7) heater holes, (8) metal seal, (9) Viton ring, (10) sample chamber, (11) sapphire plate, (12) sapphire window, (13) brass ring with holes. Figure from [46].*

to other high pressure cell developments which involve FEA method. All the literatures are review chronologically. The methodology of the FEA is further introduced in Chapter 4.

2.3.1 Finite element analysis on DAC

Adam and Shaw [60] performed the first FEA study in diamond anvil cell on 1982. The authors considered three stress tensors can originate the failure based on simulation result and the observed failure mode in high pressure experiments. First, the largest compressive and shear stresses around the culet caused the plastic flow starts there, as had been observed. Apart from that, the largest tensile stresses at the base, above the unsupported light port are vital as brittle material is liable to fracture in tension which was called basal radical crack. On the other hand, ring crack on the diamond is caused by the tensile radial stress. The study also showed two feasible ways to reduce the basal tensile stress, using bigger height to base ratio and harder support. Based on the this simulation result, optimisation study of the cell was carried on by Adam *et al.* [61] later in 1992, basal tensile stress can be minimized if the support conical light port is made with semi-angle between 25 and 30 degree.

One shortcoming of these early FEA studies [60, 61] is that the models were over-simplified. The FEA models was simplified to two parts: diamond and support in a axi-symmetric manner. Various loads depicted in Figure 2.23 were used to mimic actual pressure distribution. The

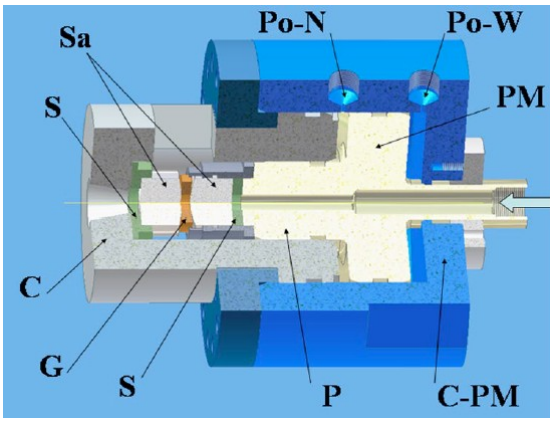

Figure 2.22: *Partial cross section of the Bonetti's SANS cell. C: steady cylinder; P: piston supporting the moving anvil; SA: sapphire anvils; G: gasket; S: anvil seat; PM:piston of the pressure intensifier;C-PM: cylinder housing of the piston PM; Po-W: port for pressurized water; Po-N: port for pressurized nitrogen. (Figure from [59])*

tensile stress at the base was turned out to be insensitive to the changes in the stress distribution at the culet in the view of that the basal region under tension are far from the culet, which is consistence to Saint-Venants principle in theory of elasticity [62]. The limitation of this FEA model is clear, the stress distribution on the culet would not be accurate enough to analysis the failure on the culet area because the effect of the plasticity flow of the gasket and sample were not considered. As a result, shear stress induced by gasket flow was unable to be accounted in the simulation. Therefore, these studies only limited to analyses of the destructive tensile stress at the bottom of the diamond anvil.

In the application of DAC, beveled diamond anvil was found outperforming the non-beveled ones. To investigate this, Bruno and Dunn [63] create a FEA model as shown in Figure 2.24 to study the stress pattern of the beveled diamond anvil. The model included a diamond and a metal gasket. A uniform pressure of 2.07 GPa is applied on the table of the diamond to mimic the load which corresponds to a pressure on the centre of the culet around 20 GPa. Different stresses on the culet of the anvil were studied, including axial compressive stress, compressive radial stress, compressive hoop stress and shearing stress. The author considered that the high shear stress was the main reason of chipping at the edge of the anvil. The use of beveled angle can effectively moderate the shear stress concentration and the optimised bevel angle was considered to be around 15 degree. The loading conditions of this FEA model is much closer to the reality as gasket was included in the model. However, there are two settings in this model which can result in unrealistic stress pattern. First, all the materials in the FEA model were

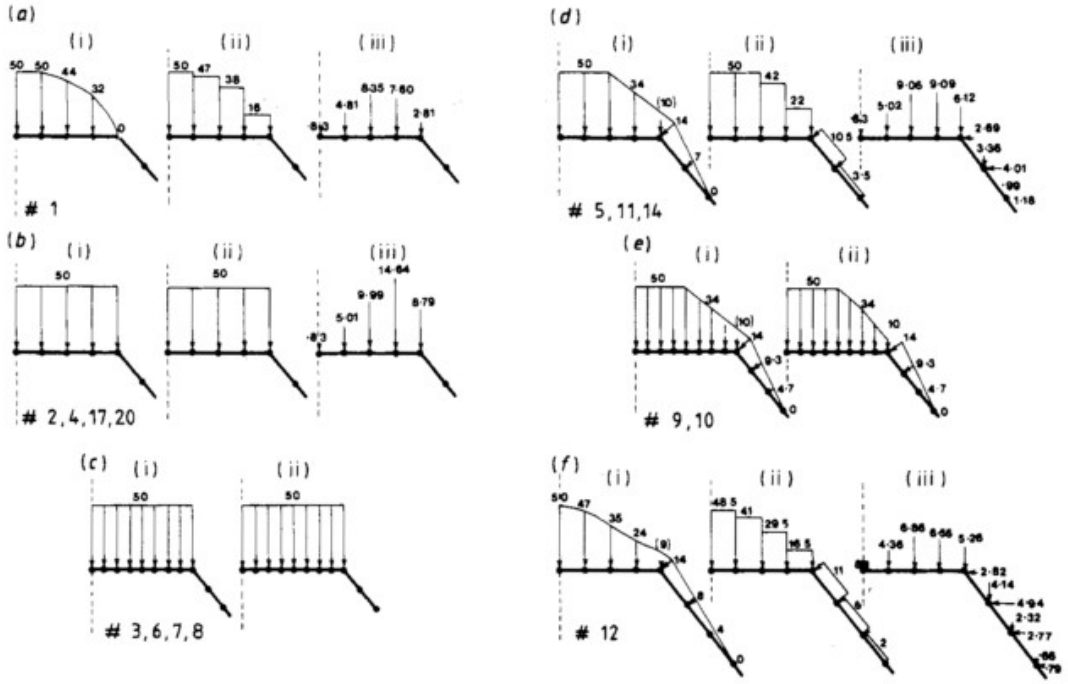

Figure 2.23: *Different loading scenario in the FEA model created by Adam and Shaw [60]. In each diagram (a), (b), (d) and (f) is shown: (i) the chosen applied pressure; (ii) the actual applied pressure; and (iii) the load (kN) assigned to each node by the programme. For (c) and (e), the point loads are not shown. The detail of these load types are listed in ref [60].*

presumed to be perfectly elastic. This presumption is only justified for the diamond as diamond is extremely hard without obvious plasticity under load. On the other hand, the metal gasket doesn't possess the same characteristic as diamond. The plastic deformation of the gasket would be significant during the pressurisation stage. Secondly, perfect cohesive interface was applied between the anvil and gasket, which is not close to reality as the gasket could flow and the surface of the gasket can move. The frictional contact should be more reliable for simulation. The main reason of these two simplification is that the early FEA program cannot cope with the material non-linear calculation. The absent of accurate modeling of the gasket behaviour would result in the shear stress caused by gasket flowing is not taken in account, which could lead to shear analysis from the model is not reliable.

Later in 1986, another FEA study on the diamond anvil was reported by Moss *et al.* [1]. The study focused on investigating the stress pattern of the diamond anvil which was tested under ultra high pressure range (above 100 GPa to 450 GPa).The model is shown in Figure 2.25 which includes a diamond and a gasket. Sample was not considered in the FEA model as in the high

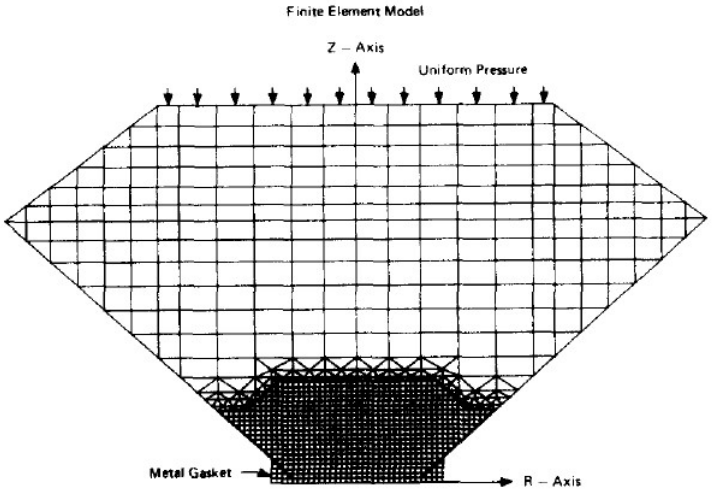

Figure 2.24: *Finite element model of diamond anvil and metal gasket [63]. It is comprise of quadrilateral and triangular axisymetric elements in the r-z plane defining the cross section of a brilliant-cut diamond anvil and a metal gasket. A uniform pressure is applied along the top surface of the diamond.*

pressure experiment, no sample was loaded apart from tiny ruby powder was spread on the culet to measure the pressure distribution. The solid gasket was equivalent to a hard sample. The FEA model was constructed as axi-symmetric and a symmetry boundary was applied on the neutral plane of the gasket. Both plasticity of the gasket and frictional interaction between anvil and gasket was considered in the model because the authors used a more advanced FEA codes called NIKE2D [64]. This finite element code is capable to solve highly non-linear simulation in both static and dynamic condition. For large deformation simulation, the included re-zoning function can automatically re-mesh the over-distorted elements which usually terminates the calculation in common FEA codes.

To demonstrate the important of the gasket material definition in FEA simulation, Moss *et al.* [1] compared the experimental data to the simulation results from a model with elastic properties only (elastic model) and a model with elastic-plastic and frictional contact properties (improved model). As demonstrated in Figure 2.26, the calculated axial stress distribution from improved model is close to the experimental data. In contrast, the elastic-model was less accurate as the axial stress was change much more abruptly. This result proved that the gasket (plasticity) has an critical effect on the stress state on the culet area. The gasket plasticity can smooth the axial stress and would affect the shear stress significantly. Also, symmetric model was proof an effective way to provide simulation result with high accuracy and can save calculation time. The study indicated two ways to improve the pressure performance of a DAC.

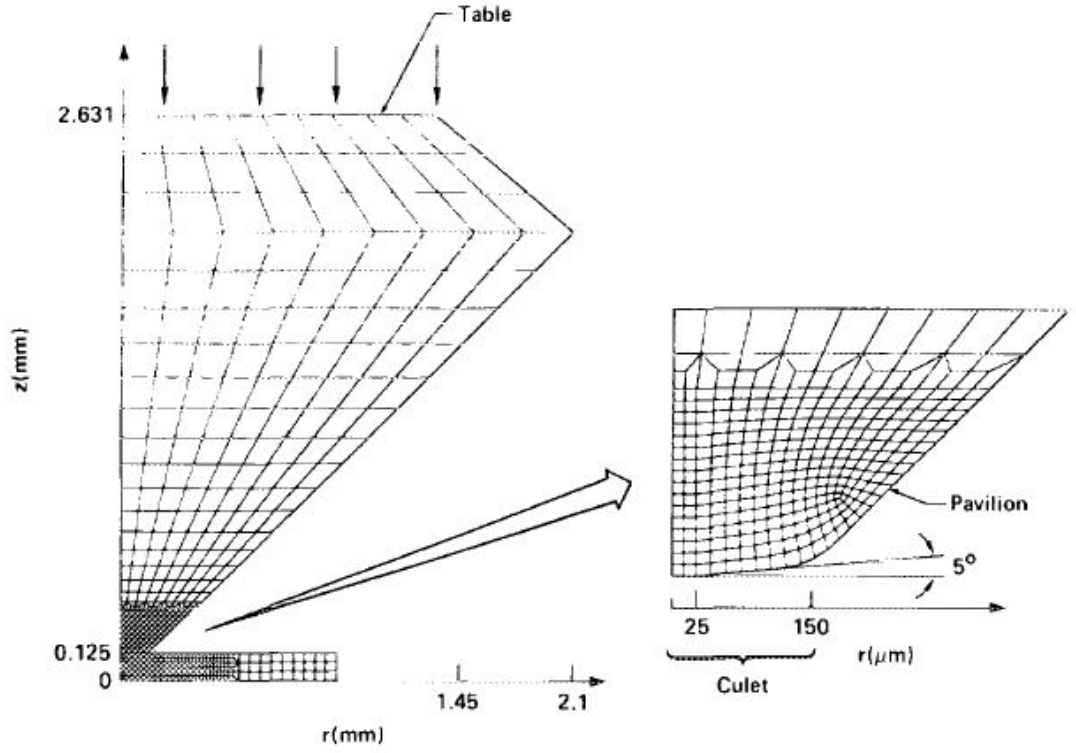

Figure 2.25: *The computational mesh for the diamond with follow culet geometry, 25 μm radius central flat, 5° bevel angle and 150 μm radius culet [1].*

First, using a gasket made of high yield strength alloy and with good ductility. Second, applying double bevel angle on the culet. These measures were proved experimentally in a successful 460 GPa ultra-high pressure testing in which a gasket made of tool steel with 2.5 GPa yield stress and double beveled anvils were used.

In the later analysis of anvil failure [65] in 1987, the authors considered the diamond anvil failure was related to the 'cupping' deformation. Sample was included in the FEA model for the failure analysis in this study. They found the culet of the diamond deformed in a 'cupping' manner after the bevel was flatten on the working area at high pressure (See Figure 2.27). The diamond tips would eventually contact at the annulus of the outer culet edge then failed. Apart from that, the simulation showed the beveled angle on the culet can delayed this cupping deformation which is believed the main reason of beveled anvil outperforming at higher pressure. The cupping deformation of diamond anvil was verified experimentally by synchrotron X-ray imaging on 1997 [66]. A follow FEA stress analysis carried by Merkel *et al.* [67] in 1990s also confirmed the cupping profile on the culet of the diamond anvil in ultra high pressure condition.

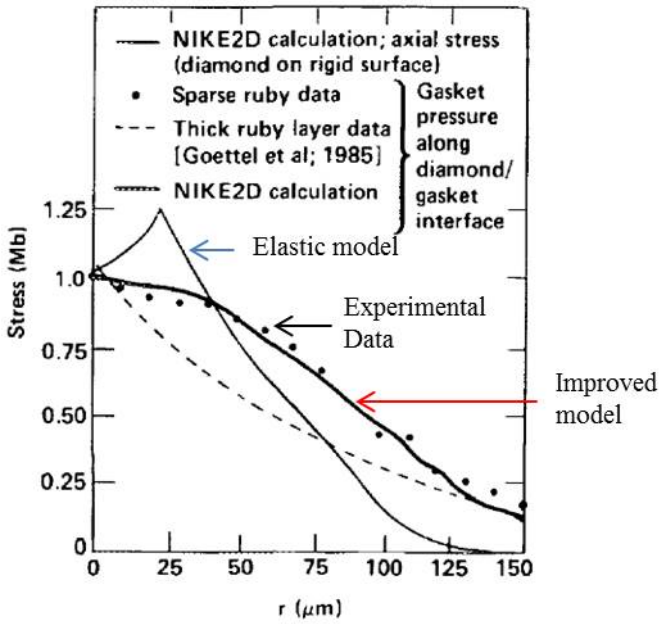

Figure 2.26: *Comparison of the computational result of the elastic model and the improved FEA model, and the experimental measurement. [1].*

2.3.2 Other studies

Apart from the diamond anvil, FEA started to be used to analyse the toroidal anvil from 1980s. Toroidal anvil cell was invented in former soviet high pressure community and became a preferential anvil type for neutron study after it was introduced into the western Europe. The most significant feature of this type of anvil is that it allows large amount of sample can be pressurized to 25 GPa routinely with relative small applied load. Levitas and Dushinskaya [68] from USSR first computationally calculated the stress distribution in the deformable gasket used in toroidal anvils. The computer program was coded Ductility which was based on constructing slip line fields in plasticity instead of finite element method. To improving the pressure performance of the toroidal anvil, stress analysis through FEA method had been performed by many researchers [69–72]. In addition, FEA has been used to analyse the multi-anvils pressure cell recently [73–75].

For the conventional piston cylinder cell, even though the thick wall theory can be used to calculate the stress of the cell, the design process still can be tiresome particular for the case of pre-stressed method. The FEA method can help shorten the design process as the design can be virtually tested before manufacture. For example, a large volume two layered piston-cylinder pressure cell was recently developed for neutron scattering experiment [76]. The FEA

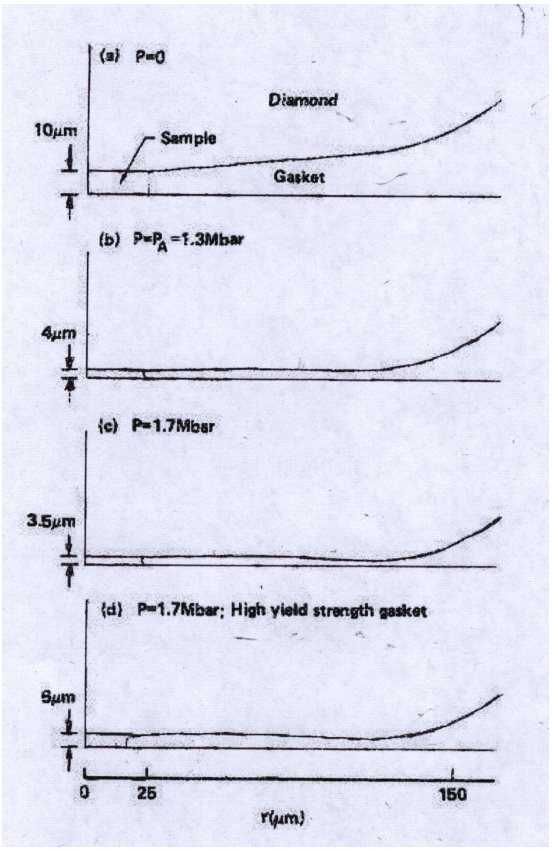

Figure 2.27: *Figure (a–c) is calculated deformation of the double bevel culet diamond anvil from a FEA model with follow parameters, 25 μm radius central flat, 5° bevel angle and 150 μm radius culet. (a) Configuration at P=0; (b) deformation at the onset of cupping P=130 GPa; (c) cupped culet at P=170 GPa. (d) The experimental culet deformation at P=170 GPa using a high yield strength gasket, the final gasket is slightly thicker than the simulation result (c) at the same pressure. [65].*

method had been used in designing and optimising the cell, the stress distribution was much more intuitive as shown in Figures 2.28.

In 2012, Ma and co-workers [77] introduced FEA method in a study of the elastic plastic interfaces of autofrettaged thick-walled cylindrical aluminum high pressure vessels. Neutron diffraction technique was used to obtain the residual strain magnitude and the depth of the plastic region to verify the previous analytical theory and the FEA model. The neutron experimental results agree well with both the analytical and FE simulation result. The FEA method was proven to be a practical and effective design tool in high pressure instrumentation work.

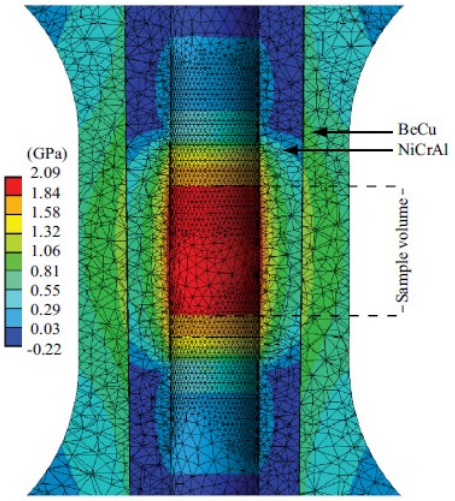

Figure 2.28: *Section view of the 3D FEA double cylinder model [76].*

Chapter 3
Magnetic Properties Measurement System

This chapter is dedicated to introduce the MPMS SQUID magnetometer in a more detail manner to provide basic understanding of the layout and working principle of this commercial magnetometer. The two different measurement technique in MPMS, direct current (dc) and alternative current (ac), are described in detail. A ^{3}He cryostat add-on system (iHelium3) for the MPMS is described at last. This introduction is based on the model MPMS-XL which was used to verify our designs in this project.

3.1 Introduction

As stated in Chapter 1, temperature (*T*), magnetic field (*H*), and pressure (*P*) are the three fundamental physical parameters in the investigation of the nature of magnetic interactions. The intrinsic spin and orbital angular momentum of a material can be revealed through its magnetic property measurement. Magnetic Property Measurement System (MPMS®) from Quantum Design [3] is the most popular commercial magnetometer at the moment, its sensitivity can reach 10^{-8} emu over a wide range of temperature (*T*) and magnetic fields (*H*). The high sensitivity is based on the integrated superconducting Quantum Interference Device (SQUID). The configuration of the system will be demonstrated in Section 3 in this chapter.

3.2 Magnetic susceptibility

The word 'magnetic' is usually used to refer to something that attract a piece of iron or a permanent magnet. In fact, every material possess some kind of magnetic behaviour. The 'magnetic' behaviour described above is a particular type of magnetism called ferromagnetism and it is only one of the many types of magnetism. The MPMS SQUID magnetometer can be sued to measure the magnetisation (amount of magnetism) of a sample. By studying how the magnetisation changes with temperature and how it changes with the magnitude of the magnetic field which is applied to the sample, one can determine the type of magnetism and important related parameters.

There are two main types of magnetic measurement. One is measuring the magnetisation of a sample as a function of applied magnetic field, which is commonly referred as $M(H)$. H is the applied magnetic field which is the magnetic field applied to the sample. An $M(H)$ measurement is carried out by fixing the temperature T and measuring M at a series of H value. The other type of measurement is measuring the the magnetisation of a sample as a function of temperature, which is called $M(T)$. An $M(T)$ measurement is made by fixing the applied field H and measuring M as a series of T value.

Magnetic susceptibility is the key parameters in the study of magnetic properties of materials. The magnetic susceptibility χ represents the degree of magnetisation of an atom in an applied field which is usually given by

$$\chi = M/H \tag{3.1}$$

Where M is the magnetisation of an atom (the magnetic moment per volume), and H is the external magnetic field. However, the equation 3.1 is only correct with certain types of magnetism, paramagnetism and diamagnetism. Paramagnetism is the simplest form of magnetism, this kind of materials are attracted by an externally applied magnetic field, and form internal, induced magnetic fields in the direction of the applied magnetic field. The most obvious feature of paramagnetic material is that their magnetisation induced by the the applied field is linear and reversible in the field strength and the magnetisation doesn't retain when the field is removed. The magnetic moment of the magnetised paramagnetic sample is normally weak and typically need to be measured in the MPMS SQUID magnetometer. The paramagnetic sample have a small, positive susceptibility to the magnetic field. In contrast with the paramagnetic behaviour, diamagnetic materials are repelled by magnetic fields and form induced magnetic fields in the direction opposite to that of the applied magnetic field. Therefore, a $M(H)$ plot of diamagnetic sample is linear and reversible but has a negative slope, its susceptibility χ is negative.

For ferromagnetic material, as the relationship between M and H is no linear, its susceptibility χ must be represented with a general definition of differential susceptibility as below:

$$\chi = \frac{\partial M}{\partial H} \tag{3.2}$$

The units of magnetisation (or magnetic moment) are various in science community. The MPMS reports the magnetic moment M in SI cgs (centimeter-gram-second) unit, emu (electromagnetic unit) which is used in this thesis. The mass magnetic susceptibility would be the magnetic moment of material divided by a product of mass in gram and magnetic field in Oe, which is expressed as emu/g·Oe. For molar magnetic susceptibility, it would be the magnetic moment divided by the product of number of mole (in mole) and magnetic field in Oe, the unit is emu/mole·Oe.

3.3 The MPMS-XL system

Figure 3.1 shows the main components of the MPMS-XL which consists of 5 systems as follow:

- Temperature Control System. The sample temperature can be precisely controlled in the range 1.8 K ($-271\,^{\circ}\mathrm{C}$) to 400 K ($127\,^{\circ}\mathrm{C}$). Liquid helium and liquid nitrogen are used

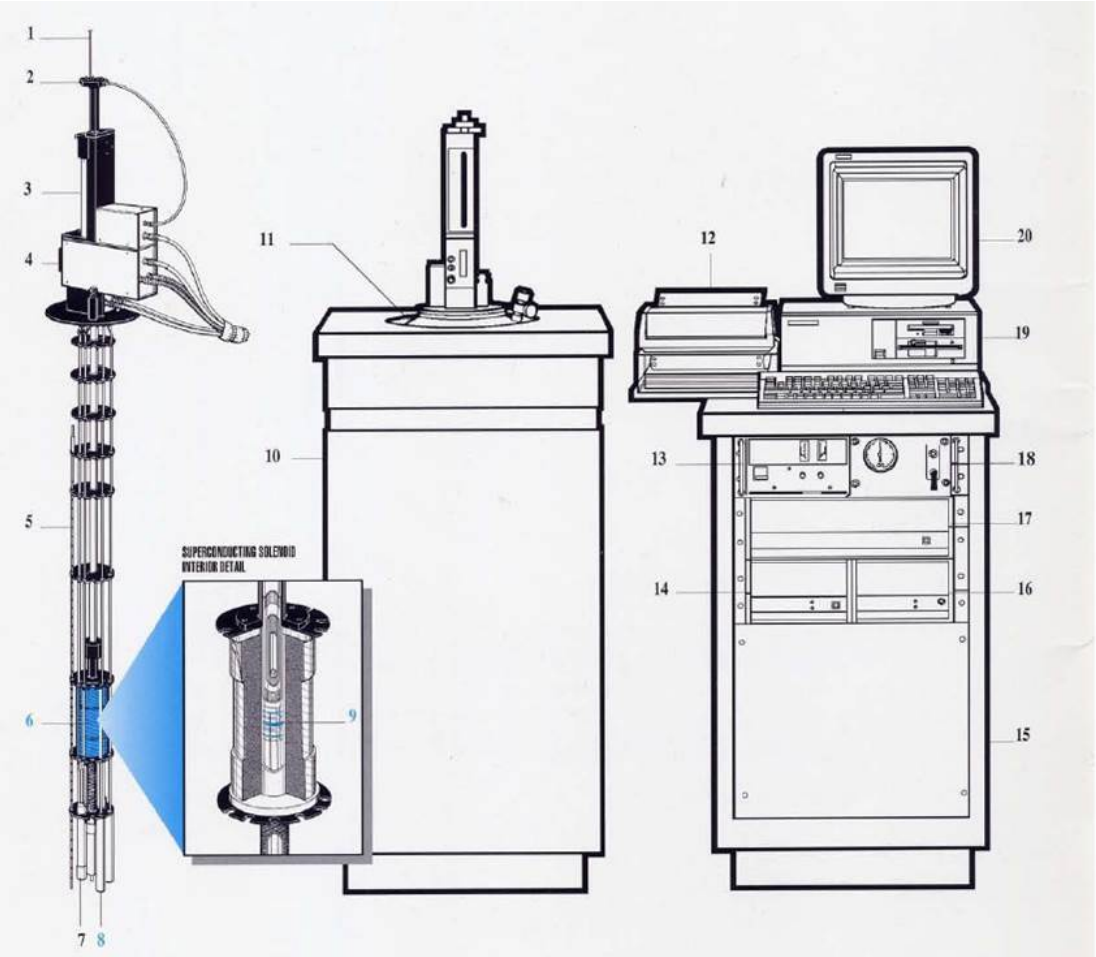

Figure 3.1: *System components of MPMS-XL. 1, Sample rod; 2. Sample rotator; 3. Sample transport; 4. Probe assembly; 5. Helium level sensor; 6. Superconducting solenoid; 7. Flow impedance; 8. SQUID capsule with Magnetic shield; 9. Superconducting detection coil; 11. Dewar; 13. Magnet power supply; 14. Temperature controller. [4]*

for cooling the system.

- Magnet Field Control System. Current from a power supply is used to charge to the superconducting solenoid for magnetic fields generation, the magnetic field can be increase up to 7 tesla.

- Magnetic measurement system with SQUID sensor. This facility is the heart of the instrument as shown in Figure 3.1, the part No.6, 8, 9. This subsystem will be further introduced later.

- Sample Handling System. This system can transmit and rotate the sample smoothly

through the detection coils, and allows for varied scan lengths.

- Computer Operation System. All operation of the MPMS are automated, computer controlled. The sample environment (temperature and magnetic field) is controlled via a GPIB connection using the Graphical User Interface (GUI).

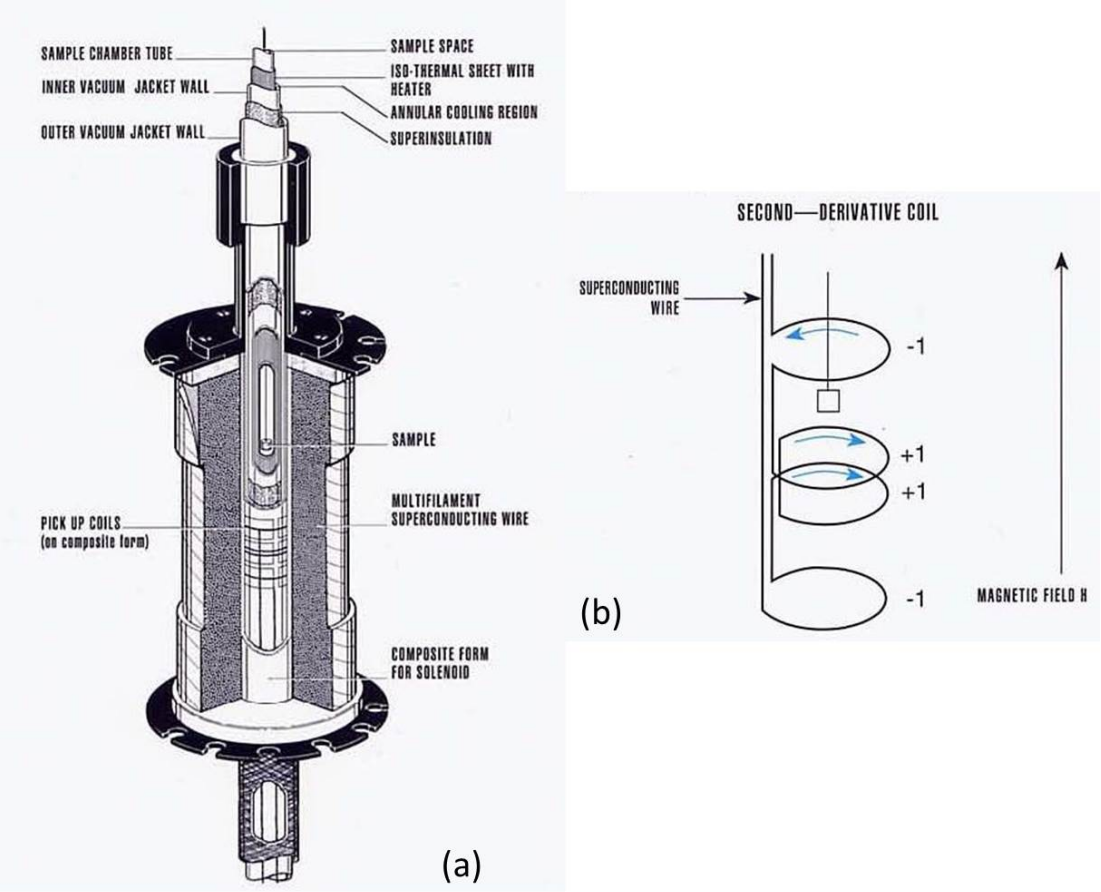

Figure 3.2: *(a)The core of the MPMS; (b) the configuration of second derivative coil (Pick-up coil). [4]*

Figure 3.2(a) shows the configuration of the core in the MPMS. Figure 3.2(b) shows the winding direction of the superconducting detection coil. The upper coil is a single turn wound counter-clockwise, while the center coil consists of two clockwise turns, and the bottom coil is a single turn wound counter-clockwise. The superconducting detection coil are used to probe the change in the magnetic flux density produced by a sample. When the magnetic flux change, electric current is induced in the detection coil. The detection coils are connected to the input of a superconducting quantum interference device (SQUID) with superconducting wires, allowing the current to inductively couple to the SQUID sensor (as shown in Figure 3.1, No.8). As an

extremely sensitive current to voltage converter, the SQUID element would produce an output voltage which is proportional to the current flowing in the SQUID input. The MPMS determines the magnetic moment of the sample by measuring the output voltage of the SQUID sensor. The SQUID sensor itself is shielded in a superconducting shield to prevent any interference caused by magnetic field fluctuation from both laboratory and superconducting solenoid. The sensitivity of this instrument can reach 10^{-8} emu.

3.4 Dc and ac magnetometry

The MPMS-XL model used in this project is capable to measure material magnetisation in both dc and ac modes which are two entirely different techniques to investigate magnetic properties. Both techniques rely on detection coils to pick up the variation in the magnetic flux from the magnetised sample. The fundamental difference between dc and ac techniques is how to create the flux variation. In a dc magnetic measurement, a sample is subject to and magnetised by a constant dc magnetic field which is generated by the superconducting solenoid (the part No.6 in Figure 3.1 and Figure 3.2). Then the sample is moved relative to the detection coil. The variation in the magnetic flux density induces a current in the detection coil due to the movement of the magnetised sample. As a result, the induced current in the detection coil can be measured and related to the material magnetisation.

Instead of moving sample, the sample is centered within a solenoid statically in ac measurement. A small ac drive magnetic field is superimposed on the dc field, causing a time-dependent moment in the sample. The field of the time-dependent moment in the sample induced a current in the pickup coils, allowing measurement of the ac moment without sample motion. Because the induced sample moment is time-dependent, ac measurements yield information about magnetisation dynamics which cannot be obtained in dc measurement, where the sample moment is constant during the measurement time. The detection circuitry is configured to detect only in a narrow frequency band, normally at the fundamental frequency (that of the ac drive field). The detail of the difference between dc and ac magnetometry is further explained as follow.

Dc magnetic measurement is straightforward as it determines the equilibrium value of the magnetisation in a sample. The sample is magnetised by a constant magnetic field and the magnetic moment of the sample is measured, producing a dc magnetisation curve $M(H)$. In a ac magnetic measurements, a small ac drive magnetic field is superimposed on the dc field. In order

to understand what is measured in ac magnetometry, first consider very low frequencies, where the measurement is close to dc magnetometry. In such case, the magnetic moment of the sample follows the $M(H)$ curve that would be measured in dc measurement. As long as the ac field is small, the induced ac moment is shown as follow:

$$M_{ac} = (\frac{dM}{dH}) \cdot H_{ac} sin(\omega t) \tag{3.3}$$

Where H_{ac} is the amplitude of the driving field, ω is the driving frequency, and $\chi = dM/dH$ is the slope of the $M(H)$ curve, is the susceptibility. The susceptibility is the quantity of interest in ac magnetometry.

As the dc applied magnetic field is changed, different parts of the $M(H)$ curve are assessed, giving a different susceptibility. The advantage of the ac measurement is clear: the measurement is highly sensitive to small change in $M(H)$. Because the ac measurement is sensitive to the slope of $M(H)$ and not to the absolute value, small magnetic shift can be detected even when the absolute moment is large.

At higher frequencies than those considered above, the ac moment of the sample does not follow along the dc magnetisation curve due to dynamic effects in the sample. For this reason, the ac susceptibility is often known as the dynamic susceptibility. In this higher frequency case, the magnetisation of the sample may lag behind the driving field, an effect that is detected by the magnetometer circuitry. Thus, the ac magnetic susceptibility yields two quantities: the magnitude of the susceptibility, χ, and the phase shift, φ (relative to the drive signal). Alternately, one can think of the susceptibility as having an in-phase, or real, component χ' and an out-of phase, or imaginary, component χ''. The two representations are related by

$$\begin{aligned} \chi' &= \chi cos\varphi \\ \chi'' &= \chi sin\varphi \end{aligned} \tag{3.4}$$

The representations can be rewritten as

$$\begin{aligned} \chi &= \sqrt{\chi'^2 + \chi''^2} \\ \varphi' &= arctan(\chi''/\chi') \end{aligned} \tag{3.5}$$

In the limit of low frequency where ac measurement is most similar to a dc measurement, the real component χ' is just the slope of the $M(H)$ curve discussed above. The imaginary component, χ'', indicates dissipative process in the sample. In conductive samples, the dissipation is due to eddy currents. Relaxation and irreversibility in spin-glasses give rise to a non-zero χ''. In ferromagnets, a nonzero imaginary susceptibility can indicate irreversible domain wall movement or absorption due to a permanent moment. Also, both χ' and χ'' are very sensitive to thermodynamic phase changes, and are often used to measure transition temperatures. Ac magnetometry allows one to probe all of these interesting phenomena. Typical measurements to access this information are χ vs. temperature, χ vs. driving frequency, χ vs. dc field bias, χ vs. ac field amplitude, and harmonic measurements [78].

Despite the commercial MPMS SQUID magnetometer can provide both measurement techniques to the users, all the high pressure magnetic measurements in SQUID were limited in dc mode as the cell material issue. The metallic cell body can interfere the measurement result greatly due to the induced Eddy current in ac field. The magnetic signal from the sample is virtually impossible to 'see' in high frequency ac field. So far, the high pressure magnetic measurement with ac techniques can only be performed through high pressure cell with built-in coils such as those shown in Figure 3.3. Several papers [36, 79–89] were published regarding to this kind of systems, however the complexity of these systems limits their application.

3.5 Sample preparation

Sample for magnetic measurement in SQUID magnetometer can be liquid form which need to be sealed in a capsule or solids (both powder or polycrystalline form). A powder sample must be loaded into a non-magnetic container such as a gelatin capsule to prevent contamination. A single crystal can be mount on a sample table using non-magnetic adhesive like GE varnish. In most cases, sample is in powder form which needs to be loaded into the gelatin capsule first then positioned in the middle to a plastic straw. A few holes in the upper end of the straw need to be punctured for letting air in and out during the air evacuation in the sample transport chamber. The straw in attached to the sample rod and then insert into the sample transport chamber for air evacuation, air is evacuated by a vacuum pump and purged with helium gas. After the air evacuation, the sample can be fully inserted in to sample chamber inside the superconducting detection coil. The sample must be centred in the second-order gradiometer pick up coil before measurement carried out, this is a compulsory step in both dc

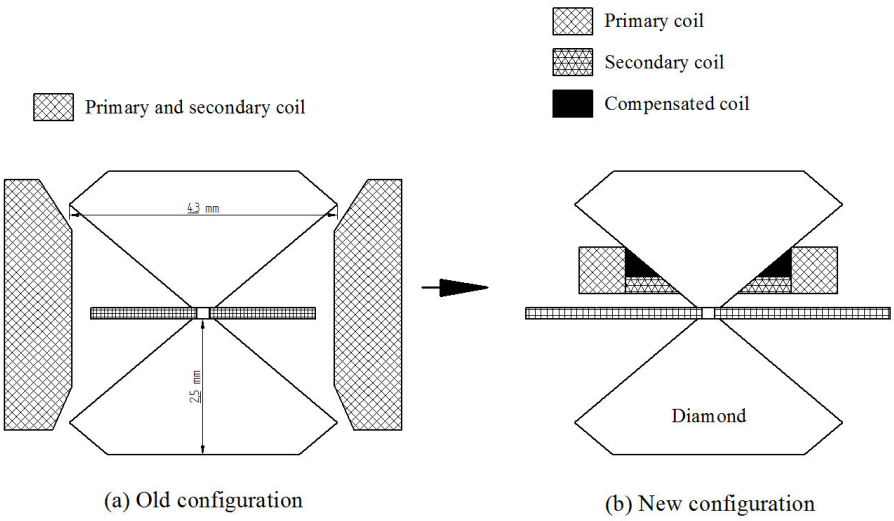

Figure 3.3: *The geometrical configuration of (a) the first diamond anvil cell with built-in coils for ac magnetic measurement [79, 81, 82]; (b) a later improved version [83]. Figures are redrawn, not to scale*

and ac measurement. This procedure insures that the sample will be magnetised uniformly and the centering can be performed by the system command.

3.6 iHelium3 system

As stated at the beginning of this chapter, the cooling system in the MPMS SQUID magnetometer is capable of providing sample temperature as low as 1.8 K. Recently, however, the study of material magnetic properties at even lower temperature (T<2 K) attracts considerable research interest. To achieve such temperatures, Shirakawa *et al.* [90] developed a ^{3}He cryostat add-on refrigeration system which can be inserted into the standard MPMS SQUID magnetometer without modification to the original machine (as shown in Figure 3.4). This system extends the minimum temperature of magnetic measurement down to 0.5 K and has been used to measure superconducting transition of single-crystal Sr_2RuO_4 at 1.5 K [90] and the magnetism of an organic ferromagnet β-*p*-NPNN at 0.48 K [91].

As shown in Figure 3.5, the ^{3}He cryostat consists of a sample rod, a main pipe, bellows, and a box. A sample and a thermometer plus a heater for temperature control are attached to the

Figure 3.4: *iHelium3 system from IQUANTUM [43].*

lower end of the sample rod. The system is designed to soak the sample in the liquid ^{3}He for low temperature cooling. The main pipe is a liquid ^{3}He container with a vacuum jacket at the bottom end so that the liquefied ^{3}He is thermally insulated. The main pipe is slim enough ($<$8.6 mm) to fit into the sample chamber of the MPMS SQUID. The measurement principle is as the following. After loading the sample rod from the top, the main pipe is suspended at its neck in the sample chamber of the MPMS. the whole cryostat, including the sample, are moved up and down and scanned through the pick-up coils. An RSO (Reciprocating Sample Oscillation) servo motor unit are used to drive the movement. On the top, a box was mounted on the RSO drive as a sample-space airlock which is used to keep the sample chamber of the MPMS sealed. A bellows inside the box interconnects between the ^{3}He cryostat and a flange, which is the port to a external gas-handling system. The vertical small figures in Figure 3.5 shows how the cryostat is installed. The sample chamber of the MPMS needs to warm up to room temperature and venting with He gas at first. Then the airlock box is mounted on the top of the RSO unit. After that, the ^{3}He cryostat is installed into the sample chamber of the MPMS and connect the electric wires and the bellows. Finally the system is ready to be cooled downed after the box needs is covered and the cryostat is evacuated.

The cryostat uses ^{3}He gas as heat-exchange medium for cooling. First the sample chamber of the MPMS is cooled down to around 4.2 K. Then the auxiliary rotary pump will be switched

on to cool down and maintain the temperature of the sample chamber at 1.6 K, at which ^{3}He gas is condensed inside the cryostat. Finally, the liquefied ^{3}He is pumped out for cooling the sample to below 0.5 K. The system was reported that it can reach 0.48 K within 30 minutes after starting to pump the liquefied ^{3}He, the base temperature can last for 10 hours as long as no heater power is applied.

Figure 3.6 shows the vacuum jacket of the cryostat, which is scanned in the MPMS during the measurement. This part is called ^{3}He insert as it needs to be inserted to the MPMS. The internal diameter of the insert is 6.4 mm which allow the standard MPMS to be used for sample mounting. The sample needs to be wrapped in a thermal conducting sheet then inserted into the straw. Since the sample is thermally insulated form the outside of the cryostat, the temperature has to be measured in situ. There is a low magnetic background thermometer is adopted for temperature measuring. It is accommodated in a polyimide tube and placed just above the sample. A heater is mount on top of the ^{3}He insert for temperature controlling. The drawback of this set-up is that background signal is increased inevitably. Shirakawa and Tamura [91] reported that the total background is about 6×10^{-4} emu at 0.5 K and 1 T. For most magnetic measurements, the background is small enough to be neglected. However, background subtraction is required for the sample with low magnetic susceptibility. This ^{3}He cryostat has been commercialized and coded iHelium3 system in Japan recently [43].The system is only compatible to the dc measurement mode at present. To this point, there is no high pressure instrument that has been developed for use with the iHelium3 system as the space of the ^{3}He insert is too limited (OD$<$6.4 mm) for all existing high pressure cell designs.

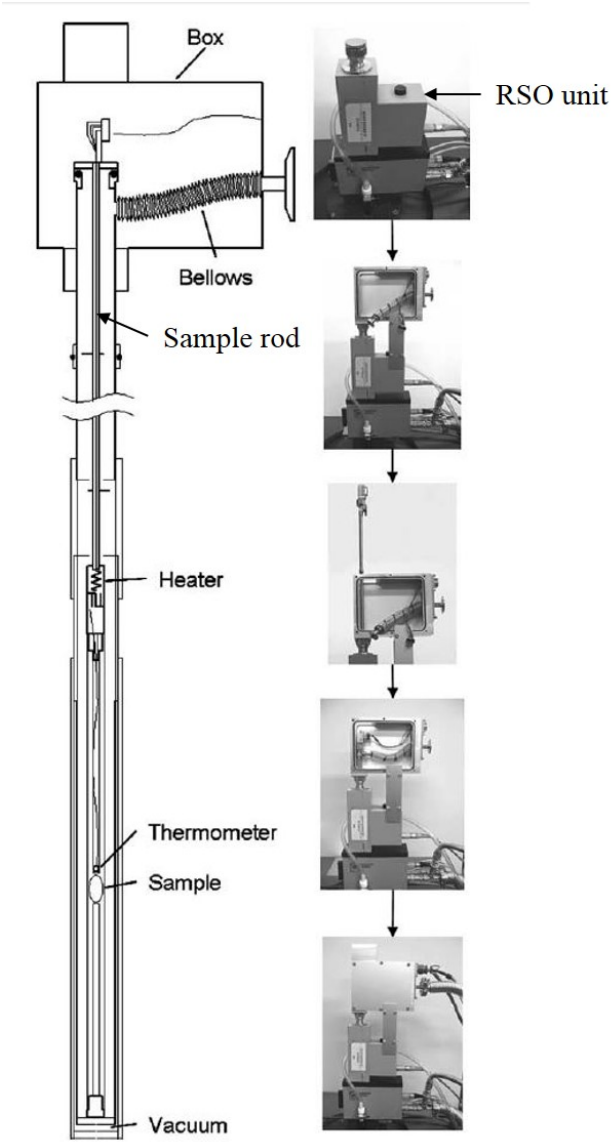

Figure 3.5: *(Left) Schematic drawing of the ^{3}He cryostat. (Right) Figures showing the set-up procedure of the ^{3}He cryostat [91].*

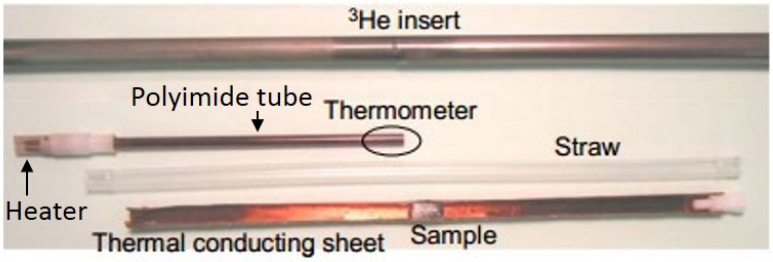

Figure 3.6: *The ^{3}He insert of the ^{3}He cryostat [43].*

Chapter 4
High Pressure Experimental Methods

This chapter gives a review of theory and common methods for high pressure cell deign. The first part of this chapter focus on the piston-cylinder cell. The second part describes the opposed anvil technique which mainly covers the diamond anvil cell and sapphire anvil cell. The final section introduces several commonly used pressure transmitting medias used in high pressure experiment.

4.1 Piston-cylinder cell

The piston-cylinder system is the most obvious method of pressure generation. This type of cell consists of at least one cylinder and one piston. The cell body can be categorised to closed-end configuration or open-end configuration as shown in Figure 4.1. When the load is applied on the piston to press the sample, the wall of the cylinder will subject to two dimensional applied stress, radial and hoop (tangential) stress. If the cell is equipped with self-clamp thread to maintain the advance of piston, three dimensional applied stresses will occur, axial or longitudinal stress will be presented in the wall as well.

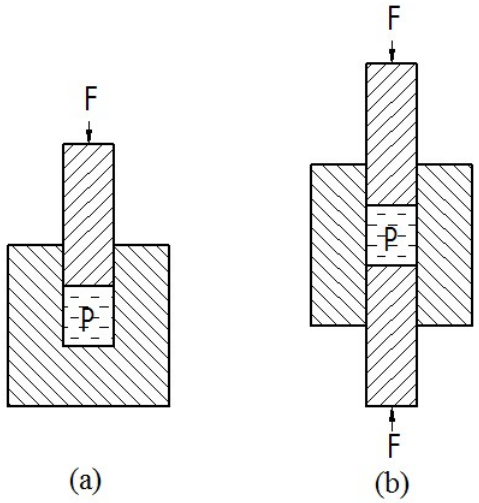

Figure 4.1: *(a) closed-end cylinder and (b) open-end cylinder.*

Because the design and fabrication of piston cylinder cell is simple and the sample volume can be large, it has a wide application in high pressure research such as high pressure electrical resistivity, thermoelectric power, optical studies, studying the compressibility of fluid ect. However, the main shortcoming of this type of cell is that the highest pressure capability is limited below 4 GPa [16]. Because heavy load is required to press the large amount of sample in piston cylinder cell, the cell must be reliable and safe. The major part of this type of cell, the cylinder body, needs to be calculated carefully before manufacture. The analytical calculation is well documented based on Lamé theory which was developed for thick wall cylinder calculation. The theory is explained in the following subsection to provide a in-depth understanding of the behavior of the cylindrical cell body at high pressure.

4.1.1 Analytical stresses calculation for cylinders

4.1.1.1 Thin-walled cylinder

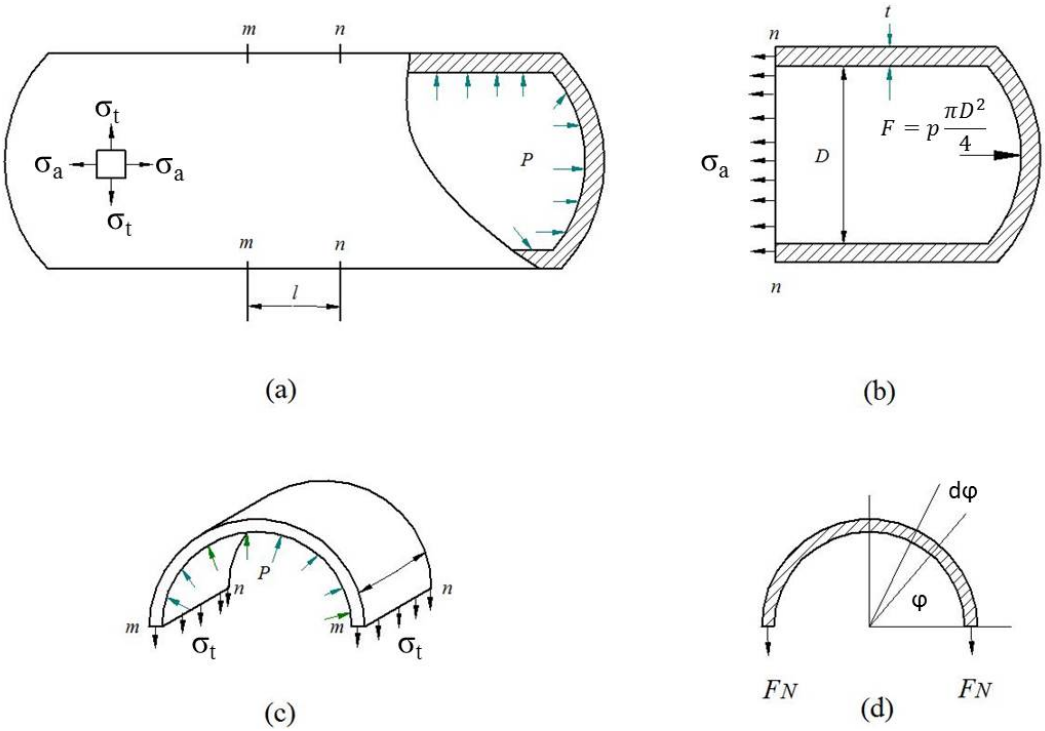

Figure 4.2: *A thin-walled cylinder subject to internal pressure.*

As shown in Figure 4.2, when the wall thickness of the cylinder is less than about 1/20 of the diameter, the cylinder can be considered thin-walled. When a thin-walled cylinder is subject to internal pressure P, the classical theory assumes that the infinitesimal element on the cylinder body subject to two dimensional principle stresses, the hoop stress σ_t and axial stress σ_a. The radial stress is ignored based on the assumption that there is no pressure gradient across the wall. The stresses can be calculated with follow equation [92].

$$\sigma_t = \frac{PD}{2t} \tag{4.1}$$

$$\sigma_a = \frac{PD}{4t} = 0.5\sigma_t \tag{4.2}$$

Where D is the internal diameter of the thin-walled cylinder, t is the wall thickness of the thin-walled cylinder.

The calculation of thin-walled cylinder is very straightforward but the equations are only valid

when the wall thickness and diameter ratio is smaller than 1/20. If the ratio is larger than 1/20, the radial stress σ_r becomes significant and cannot be ignored. Lamé equation [93] for thick-walled cylinder must be used for calculation. Since most cell bodies of piston-cylinder cell are thick-walled cylinder, the development of the Lamé equation is further introduced as followed.

4.1.1.2 Development of the Lamé theory

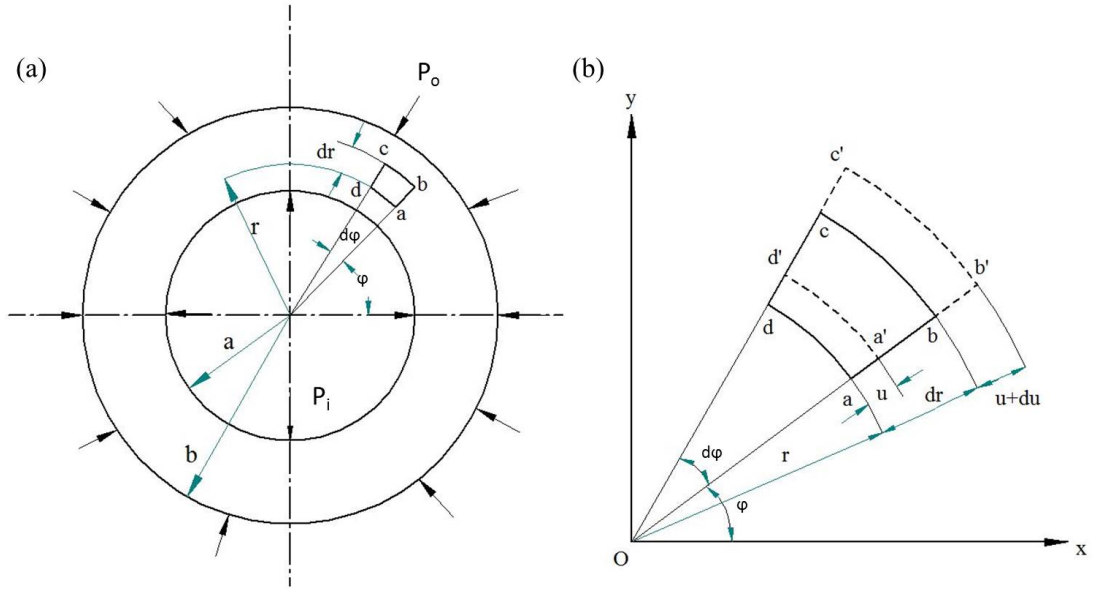

Figure 4.3: *(a) an infinitesimal element abcd on a thick wall cylinder. (b) the enlargement view of the element abcd and the deformed shape a'b'c'd'.*

Strain

Thick cylinders are concerned with sections remote from the ends. The development of the theory is based on the follow assumptions. The central sections of a thick cylinders are symmetrical and all points on an annular element of the cylinder wall will be displaced by the same amount, this amount only depends on the radius of the element. As a result, there are no shearing stress set up on transverse planes and the applied axial stress is one of the principle stresses. Similarly, because of the uniformly distributed pressure as shown in Figure 4.3 (a), the shape of element a'b'c'd' is maintained without distortion. As a result, there are no shears on radial or tangential planes, the radial an hoop stresses are both principle stresses. These three stresses are mutually perpendicular, tri-axial and termed radial, hoop (also called tangential or circumferential), and axial (longitudinal) stress in this thesis.

Figure 4.3 shows a thick-walled cylinder subject to both internal and external pressure. An

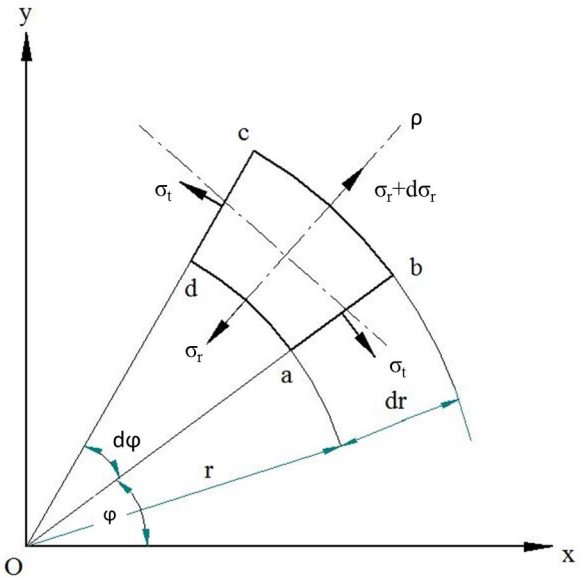

Figure 4.4: *The stress diagram of the unit length element*

infinitesimal element with unit length was cut from the wall as depicted, the internal radius of the element is r and external radius is $r + dr$, the annual angle is dφ. Because the cylinder is axisymmetric, all the nodes in the cylinder only deform radially, and the displacement u only relates to the radius r, independent to the angle φ. The edge of the element ad moves to $a'd'$, therefore the hoop (tangential) strain can be calculated as

$$\varepsilon_t = \frac{\widetilde{a'd'} - \widetilde{ad}}{\widetilde{ad}} = \frac{(r+u)d\varphi - rd\varphi}{rd\varphi} = \frac{u}{r} \tag{4.3}$$

Since u is a function of r, along the edge of ab, if the displacement of point a is u, then the displacement on the point b is $u + du$. The radial strain is

$$\varepsilon_r = \frac{\overline{a'b'} - \overline{ab}}{\overline{ab}} = \frac{[dr + (u + du) - u] - dr}{dr} = \frac{du}{dr} \tag{4.4}$$

Because the section plane remain plane, the axial (longitudinal) strain ε_a is independent to the radius r and φ, it is constant across the all of the cylinder.

Static equilibrium equation

As shown in Figure 4.4, the element subjects to a normal radial stress σ_r and normal hoop stress σ_t. Because the axisymetric feature, the stresses are independent to the angle φ and only related to the radius r. No shear stress on the element thus all the normal stresses are principle stress. The stresses on surface cd and ab are equal with opposite direction. There is

an increment $d\sigma_r$ on the surface cb. Based on force equilibrium principle, if one projects all internal forces on the axi ρ, then a equilibrium equation can be constructed as

$$(\sigma_r + d\sigma_r)(r + dr)d\varphi - \sigma_r r d\varphi - 2\sigma_t dr \cdot sin\frac{d\varphi}{2} = 0 \tag{4.5}$$

For small angles:

$$sin\frac{d\varphi}{2} \simeq \frac{d\varphi}{2}$$

Neglecting second-order small quantities, the Equation 4.5 can be reduce to

$$r d\sigma_r + \sigma_r dr = \sigma_t dr$$

Then we have

$$\sigma_t - \sigma_r = r\frac{d\sigma_r}{dr} \tag{4.6}$$

General Hook's law

In linear elasticity condition, the stress and strain relation follows the general Hook's law

$$\begin{aligned} \text{Hoop strain} \quad & \varepsilon_t = \frac{1}{E}[\sigma_t - \nu(\sigma_r + \sigma_a)] \\ \text{Radial strain} \quad & \varepsilon_r = \frac{1}{E}[\sigma_r - \nu(\sigma_t + \sigma_a)] \\ \text{Axial strain} \quad & \varepsilon_a = \frac{1}{E}[\sigma_a - \nu(\sigma_r + \sigma_t)] \end{aligned} \tag{4.7}$$

The axial strain ε_a is constant across the wall of the cylinder based on the assumption that the plane sections remain plane. It is also assumed that the axial stress σ_a is constant across the cylinder walls at points remote from the ends. Then,

$$\varepsilon_a = \frac{1}{E}[\sigma_a - \nu(\sigma_r + \sigma_t)] = \text{constant}$$

$$\sigma_r + \sigma_t = \text{constant} = 2A \qquad \text{(assigned)} \tag{4.8}$$

Lamé equations

Substituting equation 4.8 to equation 4.6 to eliminate the σ_t, then we have

$$2A - 2\sigma_r = r\frac{d\sigma_r}{dr}$$

Multiplying through by r and rearranging,

$$2\sigma_r r + r^2 \frac{d\sigma_r}{dr} - 2Ar = 0$$

$$\frac{d}{dr}(\sigma_r r^2 - Ar^2) = 0$$

Therefore, integrating,

$$\sigma_r r^2 - Ar^2 = \text{constant} = -B \qquad \text{(say)}$$

$$\sigma_r = A - \frac{B}{r^2}$$

Then, solving the equation 4.8, we have the general form of the Lamé equations

$$\begin{aligned} \sigma_t &= A + \frac{B}{r^2} \\ \sigma_r &= A - \frac{B}{r^2} \end{aligned} \tag{4.9}$$

where the A and B are usually refereed as Lamé constants.

Substitute the follow boundary conditions to equation 4.9 to determined the Lamé constants A and B. Note that both internal and external pressure are considered as negative radial stress based on the sign convention in elasticity which take normal compression stress as negative and tensile as positive.

$$\text{at} \quad r = a, \;\; \sigma_r = -P_i$$

$$\text{at} \quad r = b, \;\; \sigma_r = -P_o$$

the constant A and B is

$$\begin{aligned} A &= \frac{P_i a^2 - P_o b^2}{b^2 - a^2} \\ B &= \frac{(P_i - P_o)a^2 b^2}{b^2 - a^2} \end{aligned} \tag{4.10}$$

Substituting A and B back to the general form of the Lamé equation 4.9, the hoop stress and radial stress can be stated more specifically:

$$\begin{aligned} \sigma_t &= \frac{P_i a^2 - P_o b^2}{b^2 - a^2} + \frac{(P_i - P_o)a^2 b^2}{b^2 - a^2}\frac{1}{r^2} \\ \sigma_r &= \frac{P_i a^2 - P_o b^2}{b^2 - a^2} - \frac{(P_i - P_o)a^2 b^2}{b^2 - a^2}\frac{1}{r^2} \end{aligned} \tag{4.11}$$

Axial stress

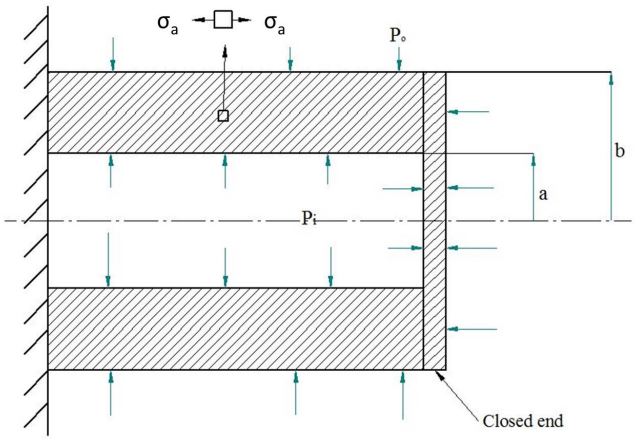

Figure 4.5: *Cylinder longitudinal section*

Consider the cross section of a thick cylinder with closed ends subjected to both external and internal pressure as shown in Figure 4.5. For longitudinal equilibrium,

$$P_i \pi a^2 - P_o \pi b^2 = \sigma_a \pi (b^2 - a^2)$$

Then rearrange the equation then the axial stress can be calculated as follow:

$$\sigma_a = \frac{P_i a^2 - P_o b^2}{b^2 - a^2} = A \tag{4.12}$$

It is clearly that the axial stress σ_a is constant and equal to the lamé constant A as shown in equation 4.10.

Radial displacement

From equation 4.3 and General Hook's law (equation 4.7), we have

$$\varepsilon_t = \frac{u}{r} = \frac{1}{E}[\sigma_t - \nu(\sigma_r + \sigma_a)]$$

The radial displacement of any point in the cylinder can be computed as

$$u = \frac{r}{E}[\sigma_t - \nu(\sigma_r + \sigma_a)]$$

Substitute the Lamé equation 4.9 and equation 4.12, then the displacement function can be rewritten with the Lamé constants A and B.

When the axial stress exist,$\sigma_a = A$ the displacement u is:

$$u = \frac{r}{E}[A + \frac{B}{r^2} - \nu(A - \frac{B}{r^2} + A)]$$

$$u = \frac{r}{E}[A(1-2\nu) + \frac{B}{r^2}(1+\nu)]$$

$$u = \frac{1-2\nu}{E}\frac{P_i a^2 - P_o b^2}{b^2 - a^2} \cdot r + \frac{1+\nu}{E}\frac{a^2 b^2 (P_i - P_o)}{b^2 - a^2} \cdot \frac{1}{r} \tag{4.13}$$

In the case of the axial stress is absence, $\sigma_a = 0$. then

$$u = \frac{1-\nu}{E}\frac{P_i a^2 - P_o b^2}{b^2 - a^2} \cdot r + \frac{1+\nu}{E}\frac{a^2 b^2 (P_i - P_o)}{b^2 - a^2} \cdot \frac{1}{r} \tag{4.14}$$

4.1.2 Thick-walled cylinder loaded with internal pressure

In this case, substituting $P_o = 0$ into equation 4.11 and 4.12, we have the three principle stresses in the wall of the cylinder.

$$\begin{aligned} \sigma_t &= \frac{P_i a^2}{b^2 - a^2}(1 + \frac{b^2}{r^2}) \\ \sigma_r &= \frac{P_i a^2}{b^2 - a^2}(1 - \frac{b^2}{r^2}) \\ \sigma_a &= \frac{P_i a^2}{b^2 - a^2} \end{aligned} \tag{4.15}$$

According to the sign convention of the principle stress in elasticity, algebraically largest=σ_1, algebraically smallest=σ_3, and other=σ_2. As $b \geq r \geq a$, it is clear from the equation 4.15 that the hoop stress is with highest positive value and the radial is with the highest negative value, then .

$$\sigma_1 = \sigma_t,\ \sigma_2 = \sigma_a,\ \sigma_3 = \sigma_r \tag{4.16}$$

both σ_t and σ_r exceed σ_a in magnitude and the greatest value occurs at the internal diameter a as plotted in Figure 4.6.

4.1.2.1 Failure theory

In many scenarios in machine design, material in a part must works and deformed within the elastic region. Material yielding is unacceptable and should be consider failure. This failure criterion can be quantified as the stress in two failure theories, the maximum shear theory (or

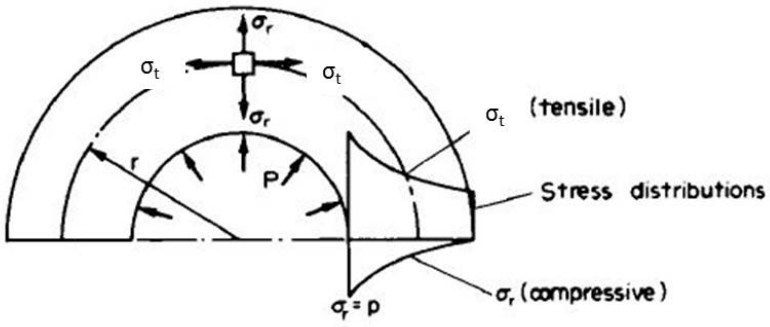

Figure 4.6: *The Hoop stress and radial distribution of a thick cylinder when subjected to internal pressure [17].*

so-called the Tresca-Guest theory) and the Distortion-energy theory (the Von Mises-Hencky theory). These two theory are widely used for the failure criterion of metallic material.

Maximum shear-stress theory

The maximum shear-stress theory states that failure occurs when the maximum shear stress in a part exceeds the shear stress in a tensile specimen at yield (half of the tensile yield strength S_y). This predict that the shear yield strength (S_{ys}) of a ductile material is

$$S_{ys} = 0.5S_y \tag{4.17}$$

The failure criterion is

$$\tau_{max} = S_{ys} = 0.5S_y \tag{4.18}$$

The maximum shear stress at any point of the wall is

$$\tau_{max} = \frac{\sigma_1 - \sigma_3}{2} = \frac{\sigma_t - \sigma_r}{2} \tag{4.19}$$

$$\tau_{max} = \frac{1}{2}[(A + \frac{B}{r^2}) - (A - \frac{B}{r^2})]$$

$$\tau_{max} = \frac{B}{r^2} \tag{4.20}$$

Because B is constant, in the internal pressure only case, the greatest value of τ_{max} occurs at

the internal diameter a as

$$\tau_{max} = \frac{b^2}{b^2 - a^2} P_i \tag{4.21}$$

Therefore, from the failure criterion Equation 4.18, the pressure limitation of a thick wall cylinder cell can be roughly estimated based on the material yield strength S_y, and the geometry dimension a and b.

$$P_i = \frac{b^2 - a^2}{b^2} \frac{S_y}{2} \tag{4.22}$$

This analytical result shows that even in a very thick cylinder ($b \to \infty$), the $P_i \leq S_y/2$. The limitation of a single cylinder is clear limited by and highly related to the material strength. Increasing the wall thickness is not effective and waste of material.

Distortion-energy theory

The distortion-energy theory is a more accurate to predict material yielding because it is based on three dimensional stresses calculation. The theory states that the material in a part would yield when its equivalent stress (Von-mises stress) $\sigma^{'}$ exceed the material yield strength S_y. The equivalent stress can be calculate by 3 principle stress as followed,

$$\sigma^{'} = \sqrt{\frac{1}{2}[(\sigma_1 - \sigma_2)^2 + (\sigma_2 - \sigma_3)^2 + (\sigma_3 - \sigma_1)^2]} \tag{4.23}$$

As the three principle stress in the thick-walled cylinder is already shown in Equation 4.16. The equivalent stress of any point of the wall can be calculated straightforward. Though the distortion-energy theory had been widely accepted as that it can provide a more accurate result, the maximum shear stress theory was still popular in high pressure instrument design because it is easier to calculate and more conservative [92], which can be preferable for some designers as it would provide an extra safety margin.

4.1.2.2 Change of cylinder dimensions

From general Hook's law in equation 4.7 and the Lamé constant A and B, the dimension changes of a cylinder cell under internal pressure can be calculated directly and vise versa. As shown in Chapter 2, the internal pressure of some piston cylinder cells [30, 31] was estimated by measuring the geometry change based on the general Hook's law and Lamé equation. This measure is conveniently to be used for pressure estimation. The numerical process is shown in

this section as follow.

Change of diameter

The most common way to measure the deformation of a cylinder is measuring the hoop (circumferential) strain at the external wall of the cylinder, which relate to the original radius based on the equation 4.3 as

$$\varepsilon_t = \frac{u}{r} = \frac{\Delta R}{R} = \frac{\Delta D}{D}$$

From general Hook's law, we have

$$\varepsilon_t = \frac{1}{E}[\sigma_t - \nu(\sigma_r + \sigma_a)]$$

$$\Delta D = \frac{D}{E}[\sigma_t - \nu(\sigma_r + \sigma_a)]$$

The equation can be solved by substitute equation 4.13. One thing must be aware about is that the existence or absence of axial stress σ_a affects the diameter change ΔD and hoop strain ε_t significantly.

Change of length

Similarly, the change of length of the cylinder is given by

$$\Delta L = \frac{L}{E}[\sigma_a - \nu(\sigma_r + \sigma_t)]$$

4.1.3 Pre-stressed techniques

As shown in Equation 4.22, the pressure capacity of the single cylinder is limited. Pre-stress techniques including multi-layered cylinders and autofrettage had been widely used to strengthen the cylinder and those method would be introduced briefly here. The analytical processes of this two pre-stresses techniques had been fully developed and available [17], these analytical processes are not included in this thesis because of the limited space.

4.1.3.1 Double-layered cylinder with interference fit

Figure 4.6 shows that hoop stress mainly concentrates at the bore of the thick-walled cylinder and reduce gradually along the radius. Increasing the wall thickness has little effect on the pressure performance as shown in equation 4.22. The material of the cylinder is not therefore used to its best advantage as the external portion is almost not loaded. There are two methods to

increase the pressure limit. The most popular method is introducing double or multiple layers cylinder. For the double layers technique (Figure 4.7), the outer diameter of the inner cylinder is slightly bigger than the bore of the outer cylinder. The inner cylinder is forced into an outer cylinder and the interference fit δ would introduce a pressures P_c applied on both inner and outer cylinders. As shown in the Figure 4.8, the induced pressure P_c can introduce a large amount of compressive hoop stress on the internal bore. The compressive stress can partially cancel out the tensile hoop stress when the cylinder body subject to internal pressure. As shown in equation 4.19, the hoop stress is the main stress tensor contributes to the maximum shear stress. Therefore, reducing the hoop stress can effectively decrease the maximum shear stress then the pressure limit of the cylinder can be increased.

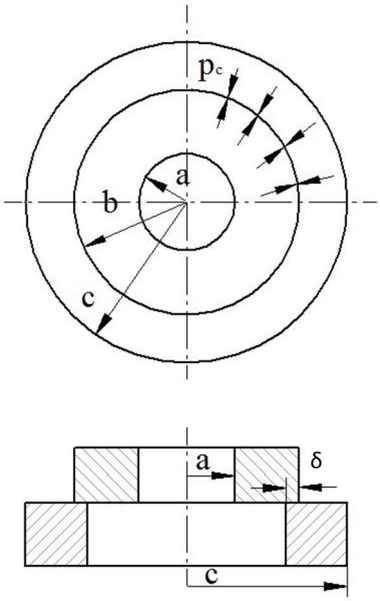

Figure 4.7: *Double cylinder with interference fit δ*

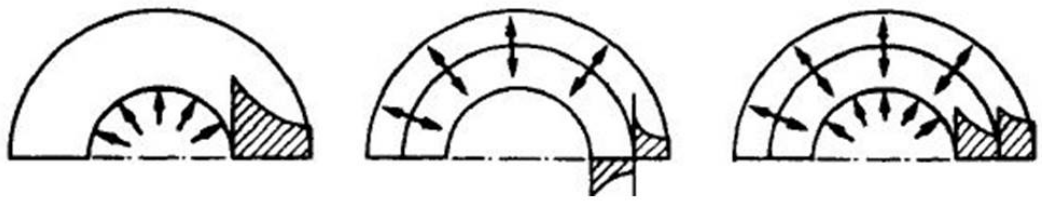

Figure 4.8: *Superposition of hoop stresses distribution caused by internal pressure and interference fit δ.*

4.1.3.2 Autofrettage

Apart from the double cylinder method, autofrettage method is another widely used technique to pre-load compressive hoop stress to the bore of the cylinder [77]. In this method, the single cylinder is preloaded with an enormous pressure to produce plastic deformation at the internal portions of the cylinder. The bore would be work hardened with the pressure, but the primary mechanism of the strengthen is based on different deformation stage of the inner and outer portion of the thick wall cylinder. With the pre-load pressure, the inner portion is deformed plastically and outer portion remains in elastic region. When the pre-load is released, the outer portion of cylinder tries to return to the original position whereas the inner cylinder maintains at the deformed position. This resulting in compressive residual stress on the inner portion of the cylinder, which is similar to the scenario of double-cylinder with interference fit.

In autofrettage procedure, the preload pressure must be high enough to yield the internal layer of the thick wall cylinder. Theoretically, the cylinder will not subject to plastic deformation if the working pressure does not exceed the preload pressure. There are several ways to pre-load the cylinder. Most convenient way is pressurising soft and incompressible medium such as lead or indium in the sample bore and only simplest seal is required to seal the piston. Another method of autofrettage is to force an oversized conical mandrel through the bore of the cylinder to achieve the necessary deformation.

The autofrettage method is more effective than the double cylinder method as it can pre-load higher compressive hoop stress on the inner layer of the thick wall cylinder. However, the autofrettage method comes with high risk of fracture during the pre-load. This is because the most high strength alloy are brittle, such as the fully harden BEREYCO25 can only elongate 2% in tensile test [15]. The double layer technique is much safer as all the deformation in the pre-stressed treatment is within elastic region.

4.1.4 Seals

Apart from the stresses calculation, seal is extremely important for piston cylinder cell. Sealing the cylinder can become difficult when pressure inside the cell get higher which results the clearance between the piston and bore increased under pressure. Therefore, successful pressurisation is highly rely on the quality of the seals, particular the seal on the moving piston. This section introduces some several well-tested sealing mechanisms.

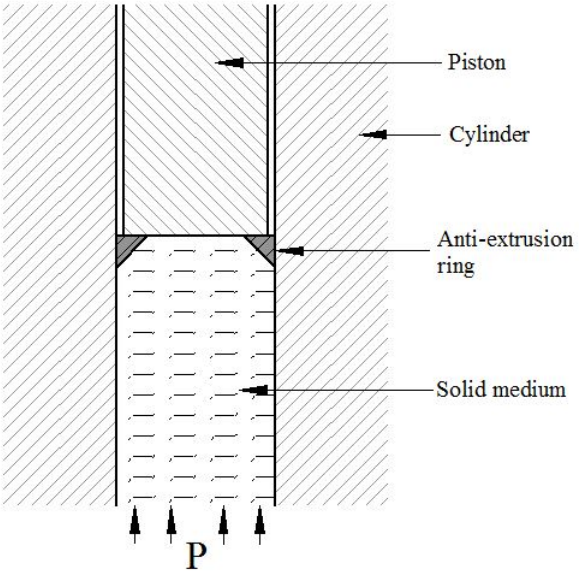

Figure 4.9: *Anti-extrusion ring seal.*

The simplest seal is the anti-extrusion ring method as shown in Figure 4.9. It is dedicated to seal solid pressure medium (sample) or serve as a supplementary seal in a complex sealing system to prevent extrusion of soft material. The seal material can be different metal based on the pressure requirement but the metal must be with certain degree of plasticity so that the ring can deform under pressure to fill the clearance. Conventionally, copper or aluminum are used for low pressure, hardened BeCu alloy for moderate pressures and steels for highest pressure.

Another classical example for sealing liquids and gases is mushroom-type seal which was invented by P. W. Bridgman as shown in Figure 4.10. The pressure in the seal P_s is always automatically higher than the pressure P in the medium since the cross-section of the seal is less than the area of the bore. Based on empirical value, the P_s needs to be 10-15% more than P to be effective. The central washer in the seal is made from soft material like nylon, rubber or indium. When the pressure in the cell exceeds the yield strength of this material, the seal starts effectively to plug the pressure medium. With increasing pressure, the rest of anti-extrusion washers starts to flow and seal the soft washer and the pressure medium. There is a final back-up ring to provide further seal at high pressure environment to stop the washers flow. Even though the mushroom-type seal had been test effective up to 3 GPa pressure, some drawbacks of this type of seal were found as well. The whole sets of seals is complicated and the existence of friction is very high (can take up to 20% of the load). In addition, retrieving the sample after high pressure experiment is inconvenient as the seal would usually stuck in the bore.

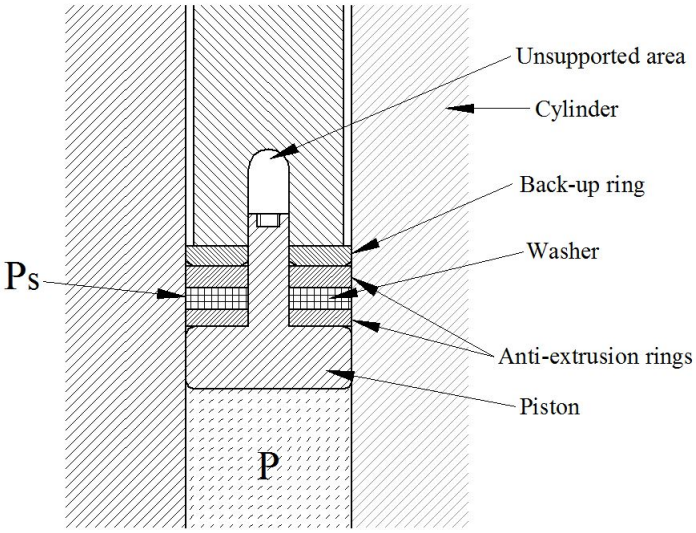

Figure 4.10: *Mushroom-type seal.*

Another type of seal called wedge seal developed by Whalley and Lavergne [94] becomes popular (as shown in Figure 4.11). The initial seal is made with an rubber O-ring. The metal wedge seal does not operate until the pressure reaches a few hundred mega-pascals. As the contact surface of the seal and the bore is much smaller than the mushroom-type seal, the friction is much smaller as a result. The friction can be further reduced by coting the metal ring with a thin layer of soft metal.

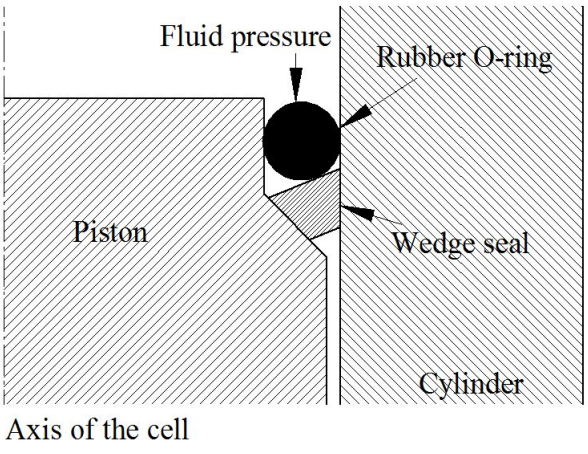

Figure 4.11: *Wedge-type seal.*

For open-ended piston cylinder cell, extra immobile seals are needed to close the gap between

the plug and the sample bore at other side of the cell as shown in Figure 4.12. This seal is simple and takes small place based on unsupported area principle.

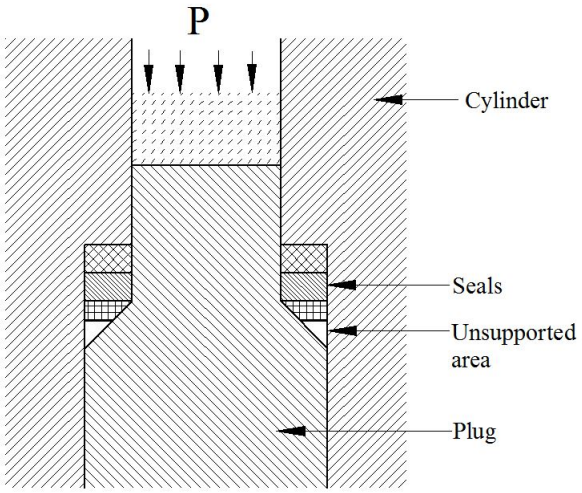

Figure 4.12: *Immobile seal for plug.*

4.1.5 Pressure calibration

Presently, manganin pressure gauge offers the most accurate pressure measurement in the piston cylinder cell. As the resistance change of the manganin coil is related to the pressure, the relation of resistance and pressure chage is given [95],

$$P - P_o = \Delta P = \alpha \Delta R + \beta \Delta R^2 \tag{4.24}$$

To measure the resistance, an integrated electrical feed-through is needed for the cell. However, this method is not always feasible. Such as if the pressurised sample is reactive which can contaminate the experiment. To avoid such problem, the deformation change of the cell in diameter or axial elongation can be used to calculated the internal pressure through Lamé equation. This method had been used in several existing piston cylinder cells [26, 30, 31].

For magnetic measurement, the pressure in the piston-cylinder cell can also be determined by using the superconducting properties of lead, tin or indium [25]. These superconductors are usually called manometer as their critical temperature T_C (where the superconductive transitions occurred) are linearly related to the pressure. For example, the transition temperature of

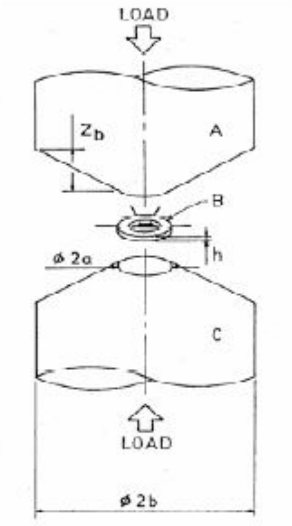

Figure 4.13: *Schematic layout of the first opposed anvil cell. A: upper WC anvil, B: gasket, C: lower WC anvil.*

lead changes as a function of pressure P as ,

$$\frac{\Delta T_C(K)}{\Delta P(GPa)} = 0.405(K/GPa) \tag{4.25}$$

4.2 Opposed anvil cell

The opposed anvil device works on the principle of massive support. The principle is a laboratory analogue of the tapered foundation design, to support the large loads of huge structures by the comparatively softer earth. The taper reduce the large working stresses quickly to tolerable level. The opposed anvil technique was invented by P W Bridgman, therefore, the first opposed anvil cell was called Bridgman anvils. As shown in Figure 4.13, the first opposed anvil cell was loaded by applying force on the loading face of the anvils, a large stress is generated at the working face (culet). A non-metallic gasekt was used to contain the sample and the pressure transmitting media, and to convert the stress into hydrostatic pressure in the sample region. Pyrophyllite ($Al_4Si_8O_{20}(OH)_4$) was used as the gasket material and steatite (hydrous magnesium silicate), AgCl, talc or petroleum jelly were used as the pressure transmitting medium for generating quasi-hydrostatic pressure. The Bridgman anvils were made of cemented tungsten carbide (WC) and the pressure can reach up to 18 GPa. The following improved version can go even higher to 25 GPa.

Comparing to the conventional piston cylinder cell, opposed anvils cell have smaller sample volume, but have higher pressure capability. Since the first Bridgeman cell, there are many types of opposed anvil cells that have been developed for all sorts of high pressure research. Such as DAC, multiple anvil cells, belt apparatus ect. The Belt apparatus and multiple anvils cell had been used extensively in material synthesis and for monitoring electrical resistivity, thermoelectric power, X-ray diffraction, etc. High temperature up to 2500 K can be available in these apparatus by incorporating suitable heating system. As these apparatuses are beyond the range of this article, detail information would not be introduced here. The Diamond anvil cell (DAC) is discussed in the follow section as it is the main research interest in this article.

4.2.1 Diamond anvil cell

DAC technique was invented by Valkenburg and co-workers [10] in 1958 and developed rapidly in 1970s based on the following advantages. As shown in Figure 4.14, the DAC is mainly consist with three critical parts, a pair of diamond anvils and a gasket. This simplicity allows the DAC can be built easily. The transparent feature of diamond allows optical access to the sample, so scientist can observe the sample under high pressure directly. The most important advantage of DAC is that it can achieve very high pressure up to 450 GPa [1]. Failure of the DAC is safe to users in spite of the cost which could be heartbroken. The working mechanism of DAC is straightforward. External force is applied on the back of the anvil and the pressure transmitting medium and a sample in the hole of the gasket is squeezed to generate high pressure. The pressure obtained form DAC mainly rely on the diameter of a diamond culet (compression face). The smaller the culet is, the higher pressure can be achieved.

4.2.1.1 Diamond anvil

Diamond is the hardest material known so far. The mechanical properties of diamond had been reported as, tensile strength S_t=2.8–2.9 GPa, Young's modulus E=1050 GPa, ν=0.11 [61]. As the DAC is popular in the high pressure research, the diamond anvil had been standardised and available commercially as shown in Figure 4.15 and Table 4.1. The standard anvil can be polished with single bevel or double bevels on the culet based on requirements. The diameter of the culet can be varied depending on the requirement maximum pressure and sample volume, the limit of maximum pressure can be roughly estimated with the Equation 4.26 which is based

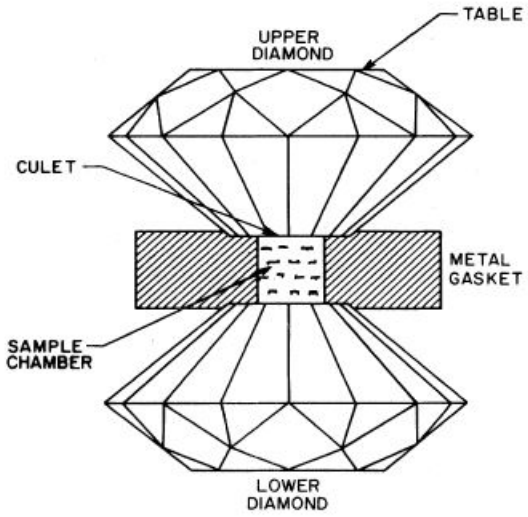

Figure 4.14: *The configuration of DAC, with a metal gasket for sample confinement in a pressure medium. These three parts are the critical parts in a DAC [96].*

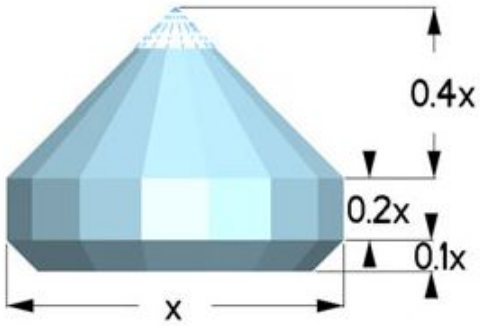

Figure 4.15: *Type Ia standard diamond design in Almax·easyLab [29], x stand for the table diameter in mm.*

on empirical application [97].

$$P_{max}(GPa) = 10/d(mm) \tag{4.26}$$

Where d is the diameter of the culet in mm.

4.2.1.2 Gasket

In conventional DAC application, the gasket is normally a thin metal which can be stainless steel, beryllium copper or other high strength metal based on the pressure requirement. The main function of the gasket is to provide a high pressure chamber for the sample. The gasket

x (mm)	Approximate weight (carats)
2.50	0.09
2.75	0.12
3.00	0.16
3.25	0.21
3.50	0.26
3.75	0.32
4.00	0.38
4.25	0.46
4.50	0.55
4.75	0.64

Table 4.1: *The available dimensions of the standard diamond in Almax·easyLab [29], 1 carat=0.2 g.*

is comparatively softer than the diamond anvil, it deforms plastically during the pressurisation. The load transmit from the anvil cause the gasket flow inwards and outwards. Therefore, the deformation of the gasket rely on the yield strength of the material. Two factors needs to be considered, the diameter of the sample hole and the thickness of the gasket. In the theory of gasket in DAC proposed by Dunstan [98], the gasket can hold high pressure inside the sample hole based on massive support principle, the pre-indentation of the gasket can increase the massive support factor which result the achievable pressure inside the gasket can reach higher. Apart from that, the sability of the sample hole is increased if the gasket was pre-indented.

There are two empirical ways to guarantee the gasket will be in the thin status [98], (a) the initial thickness of the gasket is made only a little greater than the final thickness obtained in previous runs to similar pressures; (b) pre-indentation is carried out using a force nearly as great as the force that will be applied in the experiment to generate the highest pressure. Though thiner gasket works better in DAC, the smaller sample volume is the main shortcoming. This can be unacceptable particular in magnetic measurement as larger sample volume is preferable. Based on our previous DAC experience in magnetic measurement, the balance is that a half-hardern BeCu gasket needs to be pre-indented to 100 μm initial thickness. Under this setting, the sample pressure can achieve 10 GPa routinely and the magnetic signal from the sample can still be detected. To insure the sample hole is stable at high pressure stage, the initial diameter of the sample hole should be made no greater than 1/2 and preferable 1/3 of the diameter of anvil culet.

4.2.1.3 Pressure calibration

Ruby fluorescence method is the most widely used technique to determine pressure in DAC. This technique is first introduced by Forman et al. [99] in 1972 and then was further investigated by his co-workers [35]. The principle of this method is that when a ruby atom is excited by a high intensity light such as laser, it emits double fluorescent peaks which is R_1 at at 6942 Å and R_2 at 6828 Å at ambient pressure respectively. Later in 1975, Piermarini and Block [100] found the emission line, R_1 of the ruby atom shifts approximately linearly with the pressure up to 30 GPa with coefficient $d\lambda/dP = 0.365$ Å/kbar. It was further calibrated up to 172 GPa by Mao and Bell [101] in 1978 as following equation.

$$P = 380.8[(\frac{\Delta\lambda}{694.2} + 1)^B - 1] \tag{4.27}$$

Where P is pressure in GPa, $\Delta\lambda$ is the ruby R_1 line wavelength shift in nanometer and B is equal to 5 for non-hydrostatic conditions and 7.665 for quasi-hydrostatic conditions.

As stated before, in magnetic measurement, superconductors Pb, Sn and In can be used to calibrate the pressure as well. It is usual for DAC in magnetic measurement, both ruby fluorescence method and the superconductor method are used to probe the pressure changes when the DAC is cooling down.

Another technique for calibrating pressure inside the pressure cell is using the equation of state (EOS). If the EOS $V = V(P, T)$ of some substances is obtained, then pressure can be determined because the lattice parameters of substance can be measured accurately by means of neutron or X-ray diffraction measurements. NaCl is the most common substances which has been used as a high pressure gauge due to its known principle terms in lattice energy [102]. As this method is not applied in this thesis, further detail information is not included here.

4.2.1.4 TM-DAC design

The turnbuckle technique is the main design approach in this thesis. Three high pressure cells developed in this project is based on the TM-DAC [11]. The working mechanism of this cell is introduced here in detail. As shown in Figure 4.16, TM-DAC was specially developed to be used in MPMS SQUID magnetometer in 2010. It has been successfully used in many high pressure magnetic studies in SQUID magnetometer since published. The operation of the cell is simple. Once the sample is loaded into the cell, the pressure cell is placed into a specially

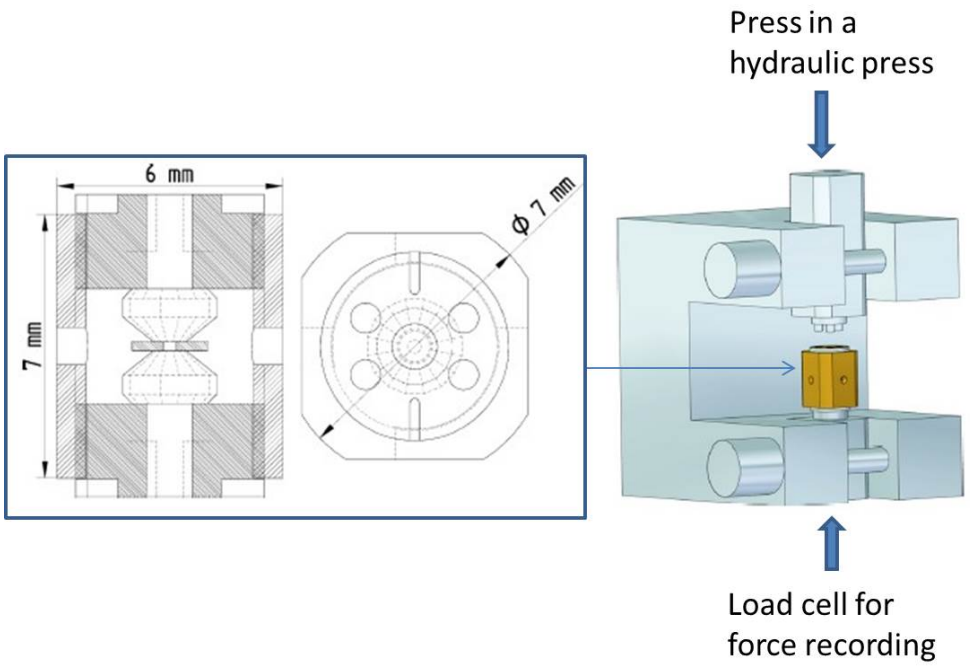

Figure 4.16: *TM-DAC [11] assembly. A special bracket was design for pressurising the cell, a load cell needs to be placed under the bracket for recording the force applied on the cell.*

designed bracket with for pins engaging into the four holes in both end-nuts as shown in Figure 4.16. The part of the bracket with top pins can slide vertically allowing the pressure cell to be put into the bracket and also to adjust the height of the pins to ensure that they engage fully into the guide holes in the end-nuts.

Once the pins are engaged they can only slide up and down when the body of the cell is rotated. While it is possible to generate some initial pressure by turning the turnbuckle body held inside the bracket, at higher loads the friction between the thread becomes large. For further pressurisation, the bracket needs to be placed into a hydraulic press and the load, monitored by a sensitive load cell, is applied in small steps. This process relaxes the threads which enables the users to lock load by turning the body of the cell with respect to end-nuts. The pressure inside the gasket can be checked by using ruby fluorescence. Once the desired pressure is achieved, the pressure cell can be removed from the bracket and load into the SQUID magnetometer for measurement. As the cell is so small, it can be loaded into the standard plastic straw recommended for use with the SQUID magnetometer as show in Figure 1.2. The cell is made of hardened BeCu alloy (BERYLCO 25 from NGK [15]) to allow pressure capability up to beyond 10 GPa (sample volume$<$0.01 mm^3).

4.2.2 Sapphire anvil cell

Sapphire anvil cell has got fundamentally the same layout as diamond anvil cell but the anvils are made from sapphire. However, sapphire anvils are not just a cheap substitute for diamond anvils working at lower pressures. Sapphire is transparent in the ultraviolet region much further than diamond (down to 140 nm). It enables the studies of emerging wide-band-gap materials.

Apart form that, sapphire cell is very useful for Raman scattering measurements as the luminescence background is much lower than for diamond anvils. Another important advantage of sapphire anvil is that the anvil can be much lager than diamond anvil with ignorable cost and therefore the sample volume can be scale up. For pressure range below 10 GPa, sapphire anvil is much more cost effective than diamond anvil, particular in neutron scattering experiment, in which the sample volume is the prior consideration.

The main disadvantage of sapphire is the weak material strength if compare to diamond. The brittle anvil can be broken easily during the high pressure experiment if they were not implemented properly. In previous literature [17], the sapphire can work reliably up to 12–16 GPa with culet smaller than 1 mm in diameter and 6–8 GPa with 2–4 mm culet. Though it's pressure performance cannot compete with DAC, it is much higher than the piston cylinder cell.

The mechanical properties of sapphire varies with its crystallographic direction because its single crystal structure. The measured tensile strength distributes between 275 to 400 MPa, Young's modulus (E) varies between 494 to 322 GPa and the value of Poisson ratio ν is between 0.27-0.3 [103]. Based on empirical application, there are some general advices for using sapphire anvil.

1. The gasket material must be soft material such as Copper, CuNi alloys, unhardened BeCu alloy etc. Strong gasket usually resulted in surface cracks appear earlier. Eremets [17] explained the reason is that the shear stress τ on the surface of the anvil is equal to the shear yield stress of the gasket material when "sticking" conditions are fulfilled. The edge of the sapphire anvil is apparently the weakest area and the use of soft gasket reduce the shear stress. One disadvantage of using soft gasket is that the final thickness can be thin which might cause some problem in certain sample.

2. It is essential to smoothen the edges of the culet to improve the pressure distribution and reducing chipping. The rounded form of the edge of the anvil results lower gradients in

the pressure distribution.

3. The strength of sapphire can be increased by surface treatment to remove the surface layer saturated with nuclei stretches. The disturbed layer can be completely removed by ion etching. One of the best chemical methods is etching in melted borax with 25% Al_2O_3 at 1000 °C. High temperature etching is also another way to improve the polished surface. Eremets [17] found that heating an anvil at 1850 °C for 20 minutes can improves the surface significantly the disturbed layer caused by polishing can be evaporated. However, if heating longer than that would cause the surface rough. A another high temperature treatment (1200 °C for 1 hour) was proposed for improving surface. The high temperature treating have not been studied so far.

4. In the application of sapphire anvil in the past decades, whether the anvil strength is related to the crystallographic direction is still controversial. From the point of view of crystallographic structure, the compression face of the sapphire anvil perpendicularly to the crystallographic c-axis was believed the strongest face as it is with the highest harness [17, 45]. However, several tests result from Furuno *et al.* [104] and Klotz [46] showed that the crystallographic orientation of sapphire with respect to the compression face had no influence on the pressure performance, particular for spherical sapphire.

4.3 Pressure transmitting media

Pressure transmitting media are normally used in piston cylinder cells to create a hydrostatic pressure environment for the sample. There are several media that had been used for high pressure experiments. The 4:1 methanol-ethanol mixture was first used in 1973 [105] for high pressure experiment and it was found stay hydrostatic up to 10 GPa. One shortcoming of this media is that it is not ideal for low temperature environment due to solidification. Pressure would vary (normally drop) due to the solidification of the pressure media. To overcome the issue, another media, Daphne 7373 [106], is becoming widely used today for high pressure experiment at low temperature because it remains liquid at low temperature. However, the Daphne 7373 starts to solidified at 2 GPa [107].

For opposed anvil cell, the pressure in is far more higher than piston cylinder cell. The pressure transmitting media used in DAC can be either gas, liquid or solid. That mainly depends on the experiment requirement. If the sample is a liquid or gas, it can be load into the gasket without

any pressure medium. If it is a single crystal, a fluid transmitting medium can be used to generate hydrostatic pressure environment. Apart from the The 4:1 methanol-ethanol mixture, commercial silicon oil can be used as well. If the sample is in a powder form, it can be loaded into the gasket hole directly. However, if the sample is very compressible, other powder as MgO, Al_2O_3 or NaCl can be loaded in to the gasket as pressure transmitting medium.

Chapter 5
Finite Element Analysis

As the Finite Element method (FEM) was widely used in this project, this chapter provide a brief introduction of this method. In addition, the main modeling techniques are introduced in this chapter, which are important to obtain good simulation result from the finite element method.

5.1 Introduction

Since the geometry of the machine parts become more and more complex, such as the propeller, gear, and crankshaft. The stress, strain and deflection calculation of these parts through classical anaysis can be complicated and time consuming. Instead, finite element method become a widely used engineering tool to solve these problem based on enhanced computer performance and commercial FEA codes nowadays. The finite element method is not only limited to structural analysis but also able to cover the calculation of fluid mechanics, heat transfer, acoustics, electromagnetic, and other specialised problems. This chapter only introduces its use in structural mechanics which is the major aspect in high pressure cells design.

The fundamental concept of finite element method is that the volume of a continuum part can be divided into a finite set of contiguous, discrete elements and solved as a set of simultaneous equations, each of which applies to an elements and to the nodes that connect the elements. Several different mathematical formulations have been reported since 1956. The main approach used for structural analysis is Direct Stiffness Method (DSM) [12] that uses element stiffness to compute the nodal displacements and internal forces that result form a set of applied external loads and boundary conditions. Strains are computed from the displacements and stresses using Hooke's law. The concept is easy to understand, however, the mathematical processes of most FEA models are computationally intensive and require the solution of large matrices. The mathematical process is beyond the theme of this thesis and would not be further described.

5.2 Element types

As shown in Figure 5.1 and 5.2, Elements can be categorised as line, surface, solid and some special purpose elements. Apart from that, they may be of different "order" where it refers to the order of the function (usually a polynomial) that describes the distribution of displacement across the element. In most cases, the simplest elements that will give the desired information will be much more welcome for FEA engineer as the computation time becomes costly for elements with higher dimension or order.

Element Type	None	Shape	Number of Nodes	Applications
Line	Truss		2	Pin-ended bar in tension or compression
	Beam	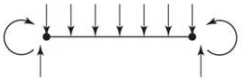	2	Bending
	Frame	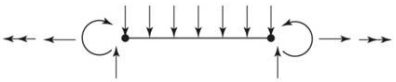	2	Axial, torsional, and bending. With or without load stiffening.
Surface	4-node quadri-lateral		4	Plane stress or strain, axisymmetry, shear panel, thin flat plate in bending
	8-node quadri-lateral		8	Plane stress or strain, thin plate or shell in bending
	3-node triangular		3	Plane stress or strain, axisymmetry, shear panel, thin flat plate in bending. Prefer quad where possible. Used for transitions of quads.
	6-node triangular		6	Plane stress or strain, axisymmetry, thin plate or shell in bending. Prefer quad where possible. Used for transitions of quads.

Figure 5.1: *Commonly used element types in structural analysis, Figure from [108]*

5.2.1 Element dimension and degrees of freedom (DOF)

A node in finite element possess degrees of freedom (DOF). Degrees of freedom are the independent translational and rotational motions that can exist at a node. A node can posses up to three translational and three rotational degrees of freedom in 3 dimensional simulation. Line element can be used to modeling structure such as truss (1-D line), beam (2-D line) and shaft (3-D line). The 1-D line element for truss structure can only transmit force along its length because it only has 2 DOF. 2-D line element has 3 DOF per node so it can support a moment and forces in two directions which can use to represent a beam in simulation. A 3-D line element are more complicated as has 6 DOF per node, which can model shaft-beam structure with moments and torques at each node in additional to forces in three directions. Elements with more complicated geometry like triangle, quadrilateral, solid type (tetrahedral, and hexahedral) have more DOFs.

In the FEA simulation, solid element can provides most accurate element. However, the cost of computing a 3-dimensional problem can be expensive and the unbearable. If a 3-dimensional structure can be considered as plane stress or plain strain case (zero magnitudes in the third

Element Type	None	Shape	Number of Nodes	Applications
Solid†	8-node hexagonal (brick)	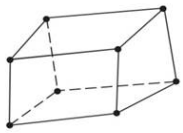	8	Solid, thick plate
	6-node pentagonal (wedge)	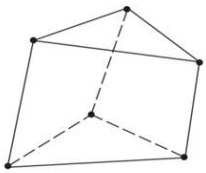	6	Solid, thick plate. Used for transitions.
	4-node tetrahedron (tet)	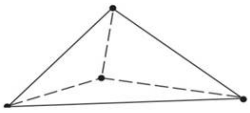	4	Solid, thick plate. Used for transitions.
Special purpose	Gap		2	Free displacement for prescribed compressive gap
	Hook		2	Free displacement for prescribed extension gap
	Rigid		Variable	Rigid constraints between nodes

Figure 5.2: *Commonly used element types in structural analysis 2, figure form [108]*

dimension), the analysis of this type of structure can be simplified by using two-dimensional surface elements. Additionally, the axi-symmetric structure can also be simplified to 2D simulation by using axi-symmetric boundary and axi-symmetric surface element. This model technique was widely used in this article as most designs presented in this thesis are axi-symmetric structure. The main advantage of 2D axi-symetric surface element is that it can provide an accurate simulation result with less computing time. Surface element (shell) can be used in 3 dimensional simulation if the structure belongs to thin-walled structure, where the stress gradient along the thickness can be ignored.

5.2.2 Element order

As shown in Figure 5.1, high order elements (such as 8-node quadrilateral, 6-node triangular surface element) can have curved boundaries, while linear elements (such as 4-node quadrilateral, 3-node triangular surface element) must have straight boundaries. The former have better ability to conform to geometric contours of complex parts and can handle steeper stress gra-

dients. However, higher element order is more computationally expensive. It is reasonable to try modeling a part with linear elements initially to acquire the approximate stress pattern, then optimised the model with higher order elements in the critical area.

The linear triangular or tetrahedral element has a limitation. Strain is computed by differentiating the displacement function in the element. The displacement function across the linear triangular element is a straight line and the strain is constant. Because this would lead to the stresses calculation is less accurate, linear triangular or tet element should be avoided to be used in the critical area of the FEA model. The better estimation of stress is using a 4-node quadrilateral (quad) or 8-nodes hexahedral (brick) element, which has a linear strain across the elements. However, sometime it can be difficult to mesh a part entirely with quads and bricks elements only, particular for some odd-shaped parts. If triangular or tet elements are unavoidable in the critical area, higher order elements (with more nodes) such as 6-node triangular element (quadratic triangles) and 10 nodes tet element can be used. These higher order elements can give better stress approximation than their lower-order counterparts and have been shown to be as good as linear 4 node quad and 8-node brick.

5.3 Meshing

Nowadays, most commercial FEA packages include automesher function which make the meshing process much more easier than the early FEA codes. For a part with complex shape, many FEA packages can import the part geometry from a solid modeling CAD program and then mesh the part automatically. For 2D modeling, automesher could mesh the part dominated by linear quads elements to assure the simulation accuracy. For 3D modeling, many automeshers can only mesh the models with tetrahedral elements. As this type of element might not be satisfactory in some case, high order tets should be consider or FEA engineer can manually mesh the part with a combination of 8-node bricks and 6-node wedges. Manual meshing requires more effort and time than the automeshing but may be essential to obtain good result.

Ordinarily in the early stage of the product development, automesher is used initially due to the faster speed of process. Though the absolute numbers may be less accurate, one can compare the alternate designs based on automeshed FEA result. Early in a design process, it is better to get less accurate information rapidly in order to determine if the design is feasible before spending a lot of time to found that the concept is not viable. When a design settle down, more

effort can be spent on generating a better mesh and getting more accurate simulation for the final design.

To minimise the computation time, coarse mesh can be assigned to the insignificant region where the stress gradient in the part is small. The coarse mesh can yield adequate result for such region. In the regions where the stress gradient is high, such as the stress concentration area, loading area, or boundary conditions, a finer mesh is needed to capture the stress variation. Varying the mesh density over the model is called mesh refinement which is essential technique for the stress concentration problem.

5.4 Boundary conditions

Boundary conditions (BC) are used to constrain the DOF of the specified nodes in FEA model, which realistically represents the constraints on a real part. It is important to define the boundary condition as it can significantly affect the simulation outcome. The nodes of a 2-D plane stress quad each have 2 translational DOF, and those of 3-D brick has 3 translational DOF. Shell or line elements can also have rotational DOF at their nodes. External constraints are applied to nodes of the model. At minimum, enough constraints must be applied to remove all the kinematic DOF of the part and put it in static equilibrium. In addition, the physical connections of the part to its neighbour in the assembly must be modeled as closely as possible.

BCs should neither over-constrain the model nor allow deformations that would not occurred in reality. A physical constraint will never have infinite stiffness, however, when a node is specified that it cannot move in an FEA model, it becomes infinitely stiff in the computation. This introduces an exaggerated error in the simulation result on the nodes where inappropriate boundary conditions were applied. If too few BC are applied, the system will be under-constrained and the computation would be terminated. If too many BC are applied, the system is over-constrained and the stress value would not be correct as the model would be too stiff.

5.5 Applying loads

Properly applying loads to a FEA model is a similar problem to that of applying boundary conditions correctly. In a classic closed-form calculation, load is usually simplified as a force applied at a point. This could be done but not recommended in FEA as a load applied at a single

node would result in local infinite stress which is not reliable. Distributing a specified load with loading function is a more reasonable approach to prevent the stress singularity.

5.6 Verification and explicit solver

The application of FEA has became relatively easy because of the availability of commercial packages. It is easy to obtain FEA result that looks reasonable but result still needs to be verified. The verification can be performed by comparing the simulation result with the experimental observation. Alternatively, hand calculation can be used to assess the FEA model. The approximation can be improved by using more elements of smaller size at the expense of increased computing time. With present computer speeds (which will continue to increase in future) this is less of a problem than in the early days of FEA.

Part of the analyst's problem is to optimise the trade-off between accuracy and computation time. Most linear simulation can be solved by the standard FEA code presented at the beginning of this chapter with high accuracy if the model is build properly. This kind of standard code is also named implicit solver which is capable to analyse linear and nonlinear static problem. However, for some complex FEA problems especially nonlinear and large deformation simulation, using implicit solver can still result in long computing times even on powerful computers. The computation usually terminated due to the nonlinearity. For larger deformation and non-linear problem, explicit solver had been shown effective to prevent convergence issue (as shown in Figure 2.25 in Chapter 2). The explicit solver has following advantages [109]:

- It has been designed to solve highly discontinuous, high-speed dynamic problems efficiently.
- It has a very robust contact algorithm that does not add a additional degrees of freedom to the model.
- It does not require as much disk space as standard solver for large problems, and it often provides a more efficient solution for large deformation analysis.
- To develop a compact opposed-anvil cell with spherical sapphire anvils.
- It contains many capabilities that make it easy to simulate quasi-static problems.

The explicit solver is often used when efficient solution is difficult/impossible to obtain by standard (implicit) solver if there are significant discontinuities in the FEA model. This circumstance occurred in this PhD project, which is presented in chapter 9, section 6.

Chapter 6
Helium Gas Pressure Cell for MPMS SQUID magnetometer

This chapter presents the development of a high pressure cell for magnetic susceptibility measurements on pressure sensitive materials at high temperature (300-400 K) in a MPMS SQUID magnetometer. Unlike to the conventional piston cylinder cell, the pressure inside this cell is driven by compressed helium gas to obtain precision pressure control. As the operation of compressed gas poses a potential safety hazard, this chapter focuses on the engineering design of the gas pressure cell with detailed stress calculations to assure safety. Measurement data for a newly developed spin-crossover nanoparticles (SCONPs) material is attached to demonstrate the data quality.

6.1 Design motivation

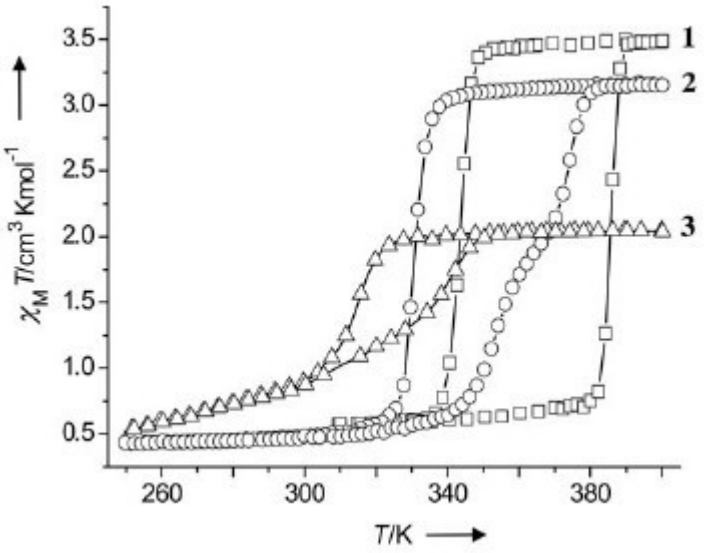

Figure 6.1: *Plots of magnetic moment χ_M versus temperature for (open squares) refer to the pure sample without any Zn^{π} doping [110].*

The motivation for this cell was provided initially by research collaborators in the School of Chemistry, with the aim of performing high temperature magnetic measurements on new synthetic ferromagnetic material $[FE(HTrz)_2(Trz)](BF_4)_n$ [110],which is an example of a spin-crossover (SCO) material. These octahedral coordination compounds with electronic configuration from d4 to d7 have received much attention in recent years due to this unique transition between the high-spin (HS) and low-spin (LS) state [111] . The spin state, and consequently the apparent colour, dimensions, and magnetic properties of these SCO systems can be tuned through external stimuli such as temperature, pressure, exposure to radiation, magnetic fields, and the absorption of auxiliary materials. Some SCO compounds exhibit abrupt transitions with hysteresis (magnetic memory) effects, offering some promising opportunities for applications in information processing, data storage, molecular switches, and display devices [112]. SCO materials usually need to be prepared at the nanometer scale for integration into functional devices, such materials are referred to as spin-crossover nanoparticles (SCONPs). The sample considered here, $[FE(HTrz)_2(Trz)](BF_4)_n$, is a recently developed SCONPs material synthesised by Titos-Padilla and co-workers [110]. It was found to exhibit an abrupt transition with large thermal hysteresis centred close to room temperature as shown in Figure 6.1 curve No.1. The magnetic hysteresis loop is found between 300 K and 400 K in ambient pressure. However, the pressure dependence of this hysteresis loop as yet to be characterised, partly due

to lack of instrumentation. The pressure cell presented here was designed to allow this pressure dependence to be understood.

6.2 Design

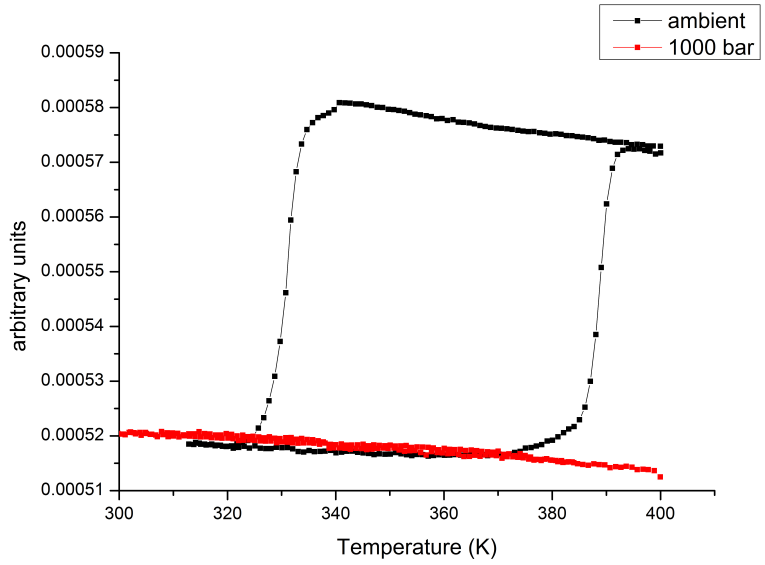

Figure 6.2: *The measurement result of the [FE(HTrz)$_2$(Trz)](BF$_4$)$_n$ sample in a piston-cylinder cell. Magnetic moment versus temperature, black line is before pressurisation, red line is the result of the pressurization data at 1 Kbar (100 MPa). The sample experiences temperature cycle from 300 K to 400 K, then cool down from 400 K to 300 K. From the figure, the hysteresis loop is totally suppressed at 1 Kbar (100 MPa).*

The sample was loaded into a TM-DAC [11] and a piston cylinder cell for magnetic measurement under pressure in MPMS®. However, the measurement result in Figure 6.2 shows that this material is extremely sensitive to pressure and the magnetic hysteresis loop was totally suppressed even with the minimum controllable pressure (100 MPa) in the piston cylinder cell. The traditional piston cylinder cell is not workable for this specific sample. A specially designed cell with more precise pressure control below 100 MPa is required for an accurate measurement of the transition.

As the pressure range expected to be needed for this type of experiment is relatively low ($<$100 MPa) and the controlled application is of the utmost concern, a gas pressure cell is the ideal option. Such a cell can be connected to an external gas pressure system or regulator through a long capillary. The internal pressure can be adjusted and monitored carefully through

such a setup. However, because liquid helium is used for cooling the SQUID, it is best to use helium gas as the medium in the cell as if leakage occurs, the leaked helium gas would not contaminate the sample chamber of the SQUID. Apart from that the pressure applied on the sample is hydrostatic.

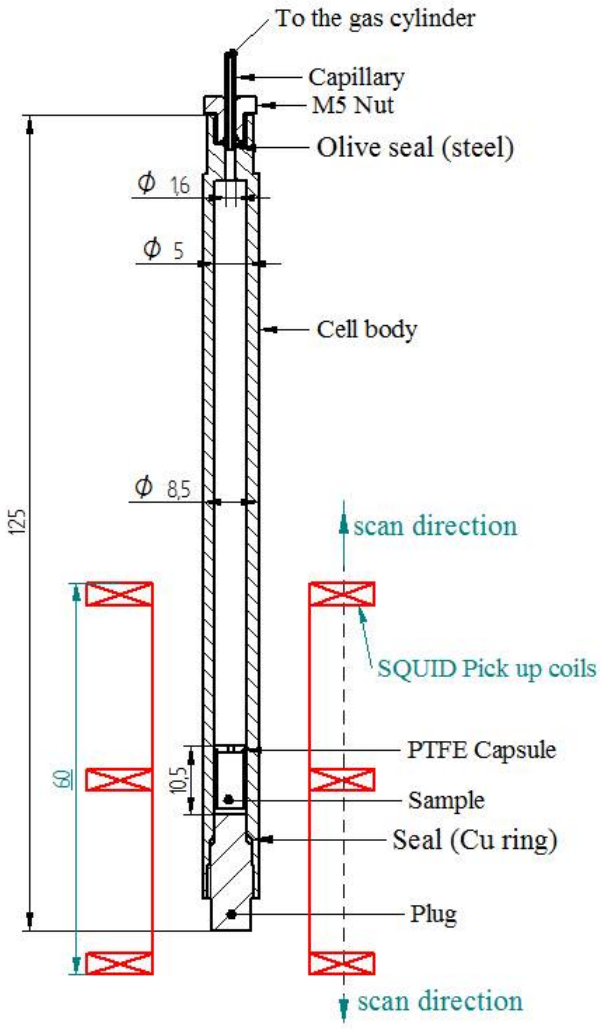

Figure 6.3: *The configuration of the helium gas pressure cell with key dimensions. The red diagram represents the pick-up coils in SQUID.*

The design is shown in Figure 6.3, the cell is a long cylindrical body with 125 mm length and 8.5 mm diameter to fit the sample chamber of the SQUID magnetometer. The cell consists of two main components, a cylindrical body and a plug, both of which are made of fully hardened BeCu alloy (BERYLCO 25, yield strength 1.2 GPa) from NGK [15]. A soft copper ring is placed between the plug and the cell body as immobile seal. The plug needs to be turned

forcibly to deform the copper ring and create a sealed environment. The cell is connected to an external compressor or pressure regulator by means of a steel capillary. An olive shape seal is used between the cell and the capillary not shown in Figure 6.3. The M5 nut on the top is used to deform the olive and create a seal. For fast fabrication, the capillary, olive seal and the M5 nut are commercial standard products and made from steel. The sample is contained in a PTFE capsule for easy loading. In order to avoid interference when measuring, the cell body is designed to be a long cylinder with the sample placed at the bottom of the cell. With this setting, only the sample area of the cell can be scanned in dc measurement. The effect of an asymmetric layout can be ignored if the sample is a strong ferromagnet. The wall thickness of the cell is much thinner than conventional piston cylinder cell, partly due to the low pressure range requirement. In addition, a thinner wall enables the cell to include more sample volume, which is beneficial for magnetic measurements. However, the thickness of the wall needs to be carefully examined because the use of compressed helium gas increases the operational risk. Therefore, to insure safety for the user and the SQUID magnetometer, the design is verified in FEA simulation as shown in following section.

6.3 Stress analysis through FEA

The classical closed-form analysis presented in Chapter 4 has shown that the internal bore of the cell is the most concerned area. The finite element method can calculate the stress not only limited to the internal bore but also cover all the the other areas included the potential stress concentration areas, in location such as the neck of the cell body and the thread. The stress contour is more intuitive then the classical closed-form calculation. Apart from that, thermal effects on the cell can be simulated in the FEA package together. Finite element analysis is used here to calculate the static stresses and thermal effects together. The distortion-energy failure theory (Von Mises-Hencky theory) [92] is used as failure criterion for the bore which means that any yield at the bore is not acceptable and will be considered failure. Therefore, equivalent stress on the cell is examined when the cell is load to 100 MPa pressure.

6.3.1 FEA model

First of all, the model is as shown in Figure 6.4. As the geometry of the cell is symmetric and rather simple, a 3D assembly model including the three main parts of the cell (M5 nut, body and

plug) is created in SolidEdge® [113] and then introduced in ANSYS [114] for Finite element analysis. Due to the extreme computing resources needed for a 3D model with contacts, half of the model is simulated to save computing time and symmetric boundary conditions are applied at the cutting plane as shown in Figure 6.4. Both M7×0.5 and M5×0.5 threads are modeled in the analysis. A100 MPa internal pressure is applied to the bore of the cell and the two surfaces on the plug. The axial movement of model is constrained by fixing the axial displacement on the curved surface of the M5 nut (the stress on this surface is not likely to be accurate due to this boundary conditions). The mesh of the model is shown in Figure 6.5, sweep mesh technique is used to mesh the model with hexahedron element as much as possible to improve the accuracy. Only the areas with irregular geometry are meshed with tetrahedron elements but with higher mesh density.

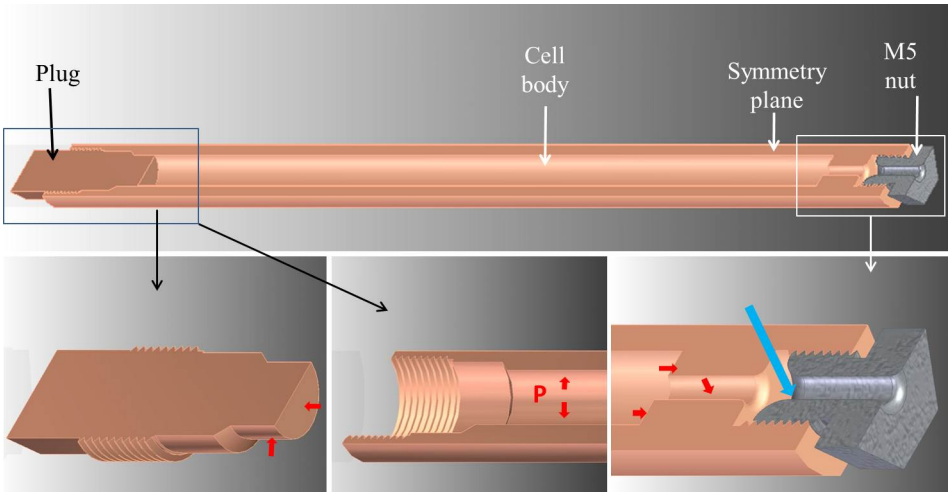

Figure 6.4: *The section view of the helium gas cell (top) and the enlarge views of the specific areas (bottom). Red arrows point to the areas where the loading (pressure) is applied. The curved surface (the area indicated by the blue arrow) on the M5 nut is fixed with a fixed boundary condition to constraint the movement of the cell in the FEA simulation. Apart from that, the symmetrical section surface is also defined with a symmetry boundary condition.*

Bilinear model as shown in Table 6.1 is defined to the mechanical properties of the BERYLCO 25 and stainless steel, strain hardening is not considered here as the cell is strictly designed to work in elastic region. The thermal expansion coefficient and density of the materials are also defined in the FEA codes to calculate the stress at 400 K temperature.

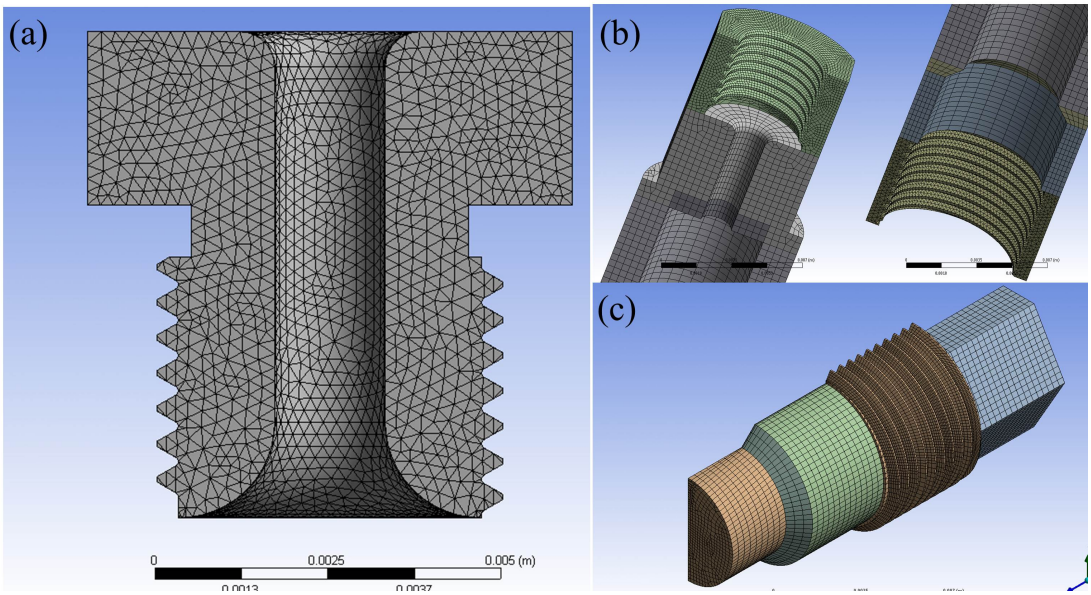

Figure 6.5: *The meshed model of (a) M5 nut, (b) cell body and (c) plug.*

	Young's modulus E (GPa)	Poisson's Ratio ν	Yield strength S_y (MPa)	Thermal expansion coefficient $\alpha_v(1/^\circ C)$	Density ρ (kg/m^3)
BERYLCO 25	123	0.3	1200	9.7	8250
Stainless Steel	200	0.3	250	12	7850

Table 6.1: *The mechanical properties of stainless steel [114] and BeCu alloy [15].*

6.3.2 Stress analysis

Figure 6.6 and Figure 6.7 show the equivalent stress of the cell when the cell subjects to 100 MPa internal pressure at room temperature conditions (300 K). The equivalent stress on the plug as shown in Figure 6.6 is concentrated on the first two screw thread and the maximum value is between 259 to 292 MPa which is far below to the yield strength of BERYLCO 25. On the M5 nut, the peak value 61.9 MPa is likely an artifact of the sharp edge in the model because of the applied symmetry boundary conditions. Instead, the maximum value is more likely to be around 37 MPa which is also below than the yield point of stainless steel.

Figure 6.7 shows the equivalent stress distribution on the cell body. The equivalent stress at the bore is around 265 MPa which is in a safe level. The stress rises up to 320–423 MPa at the neck corner due to the abrupt geometry change. The stress level on the M5 thread is trivial, whereas the stresses in the M7 thread rise up to 295 MPa at the first turn of the thread. The

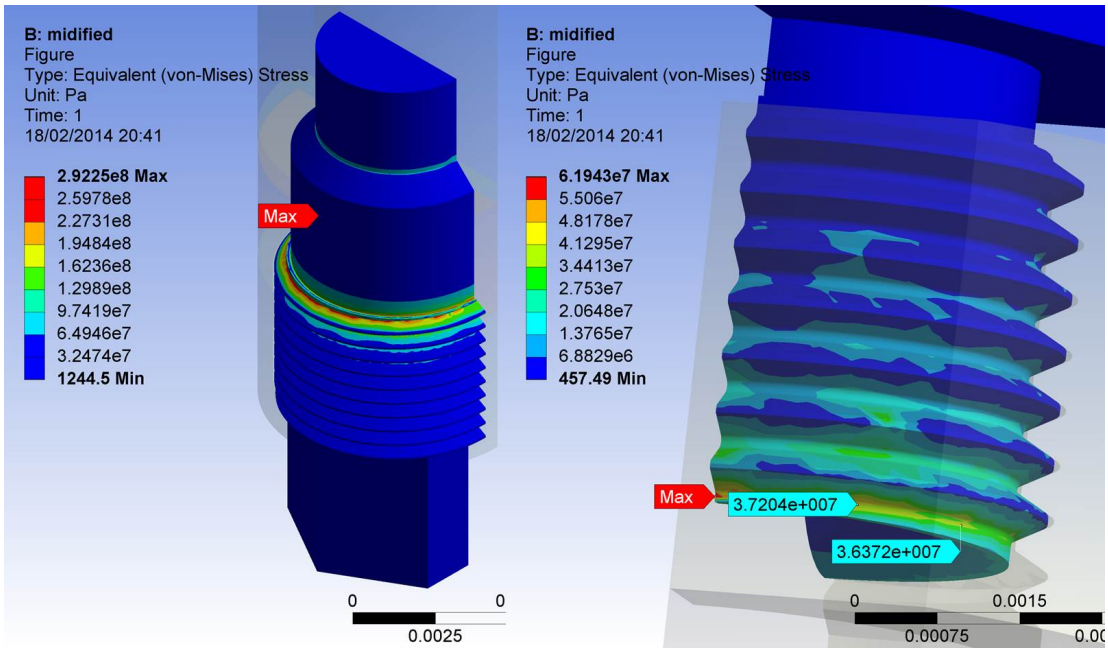

Figure 6.6: *Equivalent stress of Plug (left) and M5 nut (right) at 300 K.*

overall design factor of this cell is 2.8 which calculated by dividing the material yield strength of BeCu (1.2 GPa) to the maximal equivalent stress (423 MPa) at the neck corner.

The FEA model can be verified with a hand calculation based on Equation 4.15. When the thick-walled cylinder subjects to 100 MPa internal pressure, referring to Equation 4.15, gives

$$\sigma_t = \frac{P_i a^2}{b^2 - a^2}(1 + \frac{b^2}{r^2})$$

$$\sigma_r = \frac{P_i a^2}{b^2 - a^2}(1 - \frac{b^2}{r^2})$$

$$\sigma_a = \frac{P_i a^2}{b^2 - a^2}$$

Substituting the following values to the above equations, a=2.5 mm, b=4.25 mm, P_i=100 MPa, r=a=2.5 mm, the 3 principle stresses on one point of the internal surface, the three stress tensors are available as: σ_t=205.82 MPa, σ_r=-100 MPa, σ_a=52.91 MPa
According to the sign convention of the principle stress in elasticity, algebraically largest=σ_1, algebraically smallest=σ_3, and other=σ_2. then

$$\sigma_1 = \sigma_t,\ \sigma_2 = \sigma_a,\ \sigma_3 = \sigma_r$$

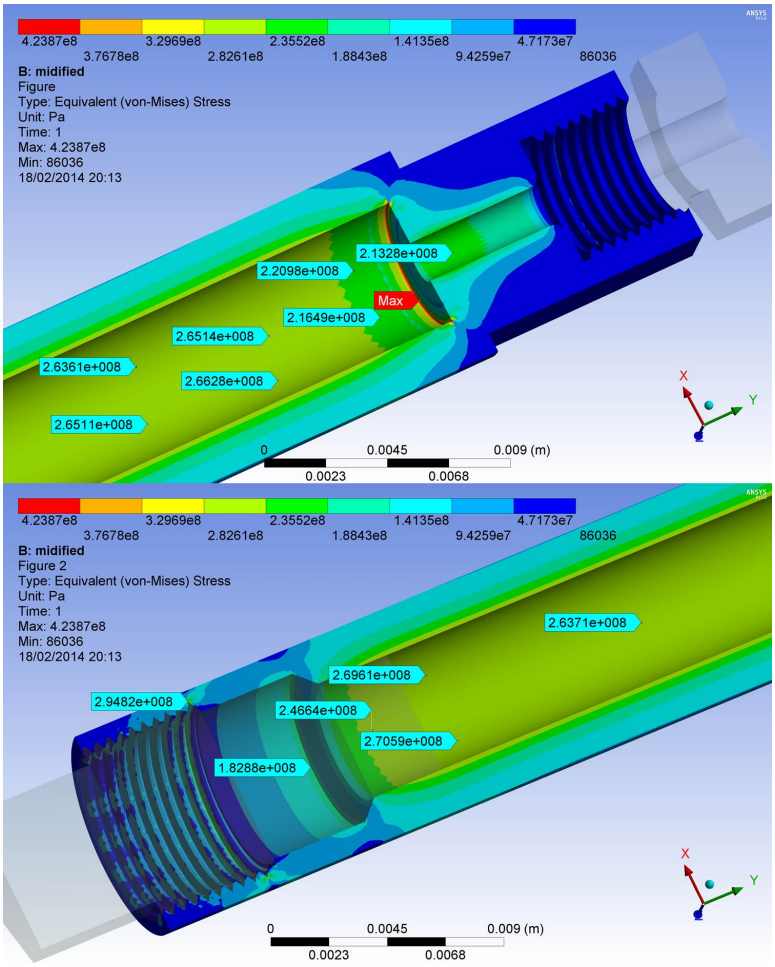

Figure 6.7: *Equivalent stress distribution of the cell body at 300 K.*

The equivalent stress (Von-mises stress) is calculated with Equation 4.23 based on the distortion-energy failure criterion.

$$\sigma^{'} = \sqrt{\frac{1}{2}[(\sigma_1 - \sigma_2)^2 + (\sigma_2 - \sigma_3)^2 + (\sigma_3 - \sigma_1)^2]}$$

$$\sigma^{'} = 264.848MPa$$

The calculated the equivalent stress agrees well with the simulation result shown in Figure 6.7, which shows the FEA model is very reliable and accurate.

Equivalent stress at 400 K

The temperature is raised from 300 K to 400 K in the simulation to investigate if any thermally induced stress could affect the stress distribution. The stress distribution of the plug and cell

body was hardly affected at high temperature (400 K) as shown in Figure 6.8 and Figure 6.9. Since both cell body and plug are both made of the same material with identical thermal expansion coefficient, the equivalent stress nearly remain as in room temperature. A couple of stress points on the M5 thread on the cell body are increased to 62-74 MPa, which is believed to be caused by the different thermal expansion coefficient of steel and BeCu. However, the stress level on this area is still insignificant.

The stresses on the M5 nut (Figure 6.8) change substantially particular at the curve suface, which is conspicuous and unreliable because the fix boundary conditions was applied on this area. The thermal expansion at this nodes would result high thermal-induced stress due to the constrains. This is the main pitfall of this FEA model which needs to be addressed in future work. Apart from the area with fixed boundary condition, the thread on the M5 nut is free to deform under high temperature. While the stress change on the M5 thread is considerable and reliable, it is still far lower than the yield strength of stainless steel.

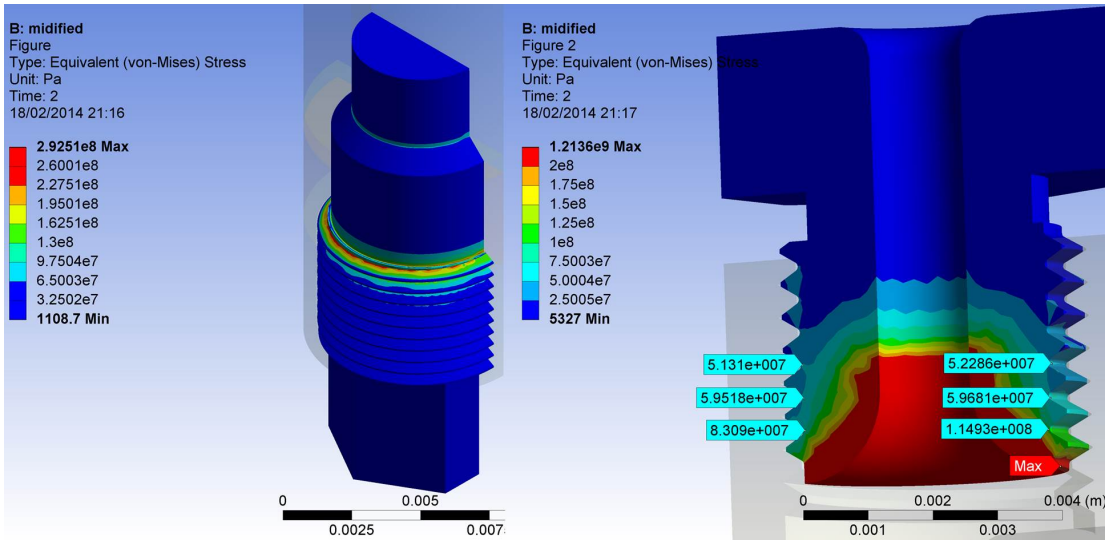

Figure 6.8: *Equivalent stress of Plug (left) and M5 nut (right) at 400 K.*

6.4 Magnetic measurement

Figure 6.10 (a) shows the assembled cell and sample rod of the MPMS SQUID magnetometer. The SCONPs powder sample is loaded in to a PTFE capsule which is punched with holes to allow passage for the pressure medium. After sample is prepared, it is loaded into the bottom of the cell. Finally, the M5 nut is screwed to deform the olive seal to fill the gap between capillary

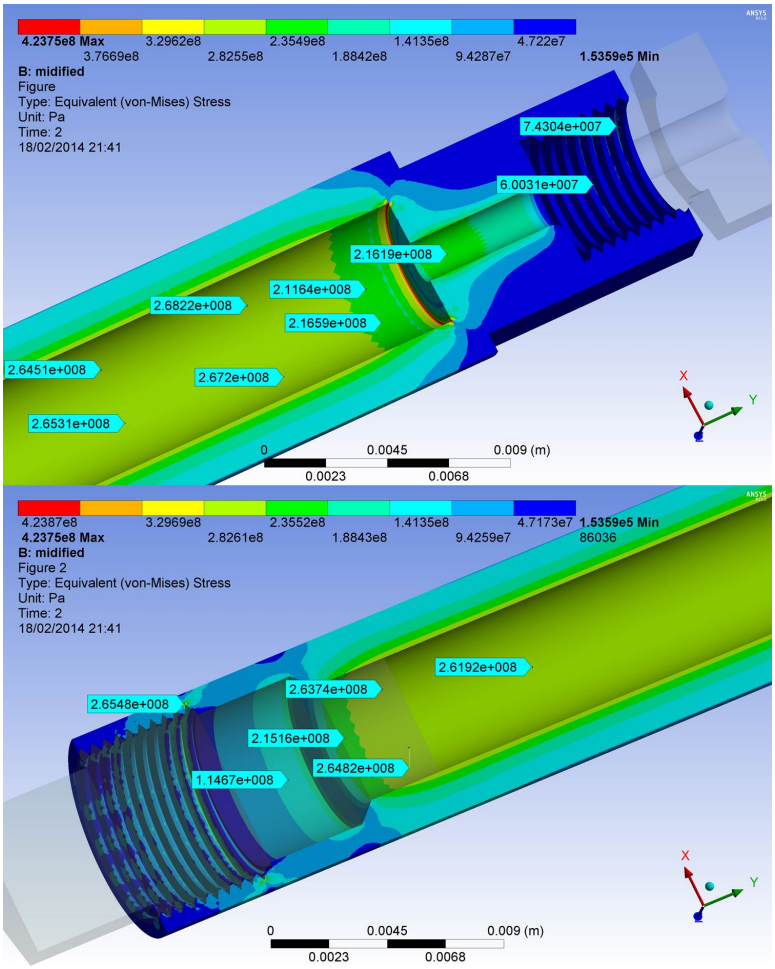

Figure 6.9: *Equivalent stress distribution of the cell body at 400 K.*

and the cell body. The cell needs to be pumped in with helium gas at low pressure and released several times to purge air from the cell assembly. After all preliminary measures are completed, the cell can be pressurised by a helium gas cylinder through a pressure regulator, which is used to apply and monitor gas pressure. The cell, at the desired pressure, is then inserted into the magnetometer for dc measurement, as described in Chapter 3.

The measurement data is shown in Figure 6.10 (b). The pressure study was limited to less than 180 bar (18 MPa) which is the maximum output of the regulator. As a large amount of sample was loaded into the cell and due to the strong sample magnetic signal, background correction was not needed in this measurement. Even though the full pressure capacity of the cell had not been reached, the high pressure magnetic measurements have shown the pressure effect on the sample very clearly. At ambient pressure, the cell and the sample were heated from room temperature to around 400 K, the magnetic signal at 390K dramatically rose, indicating spin-

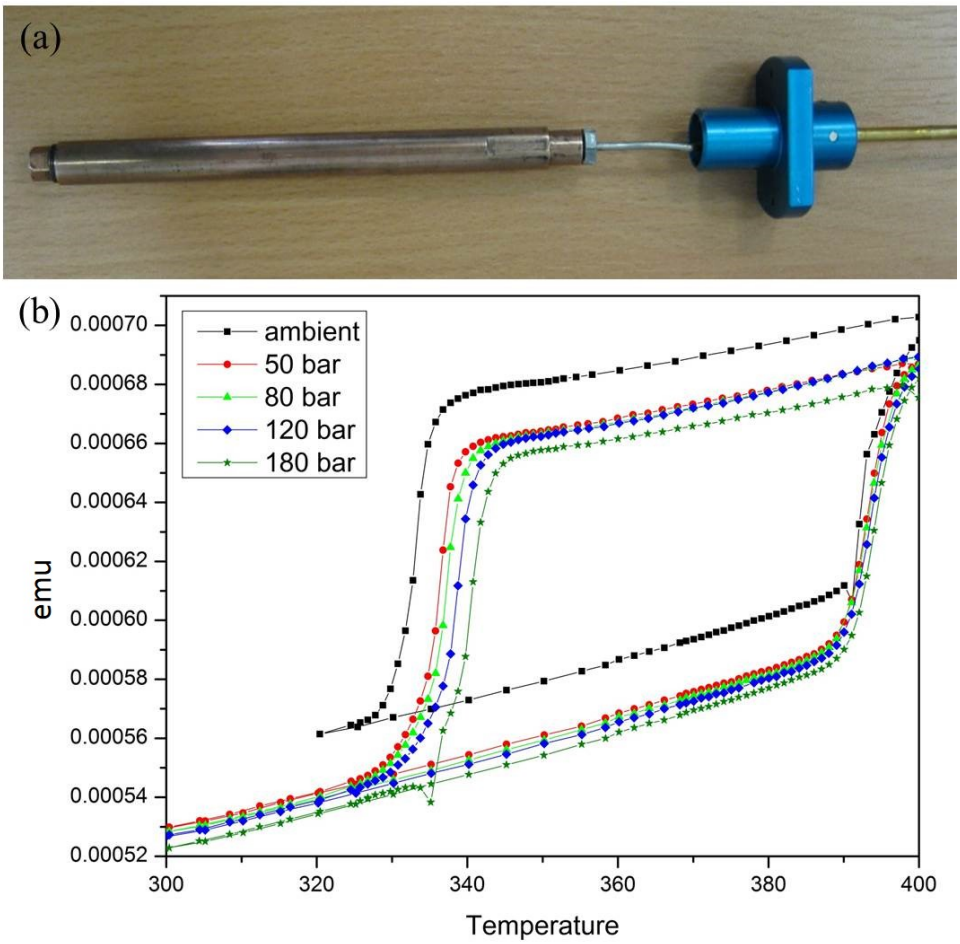

Figure 6.10: *(a) The assemble of the cell before insert into the SQUID magnetometer, (b) pressure effect on the hysteresis loop up to200 bar (20 MPa).*

crossover behaviour. Then the sample were cooled down to 320 K gradually, with the magnetic signal dropping abruptly at 335 K and further decreasing to room temperature. The thermal cycle was repeated with 5 increasing pressure steps at 50 bar (5 MPa), 80 bar (8 MPa), 120 bar (12 MPa), and 180 bar (18 MPa). The thermal hysteresis loop was found to move right-down and shrank as pressure increased. As a result, it was determined that the spin state of this material can be tuned in a controllable manner through application of pressure.

6.5 Future work

A helium gas pressure cell has been developed for magnetic measurements on pressure sensitive materials. The pressure capacity of the gas cell was confirmed in commercial FEA package

at room temperature and 400 K high temperature condition. The external gas driven design can provide precision pressure control inside the cell, which is particular suitable for magnetic study of pressure-sensitive material. In addition, high quality data can be collected from the cell because of its large available sample volume. A helium gas compressor with higher pressure output close to 100 MPa is needed if user requires higher gas pressures in future.

Several further improvements can be made. The magnetic parts of the cell (the steel capillary, steel seal and steel nut) can be replaced by non-magnetic material to avoid interference and make the centering process of this cell easier. In FEA stress analysis, the maximum pressure capability of the cell is around 300 MPa, determined by the point where the internal surface starts to yield. The pressure capability and safety of the cell can be increased with conventional cylinder cell methods as shown in Chapter 4, such as increased wall thickness, double cylinder layers or autofrettage. However, these techniques will reduce the internal diameter of the cell and the sample volume will be decreased as consequence. From the point of view of safety consideration, if user requires pressure higher than 100 MPa, it seems that a conventional piston cylinder cell may be a better solution. These piston cylinder cells have been fully developed for SQUID magnetometer and have been described in Chapter 2.

Chapter 7
Turnbuckle Diamond Anvil Cell for Sub-K Low Temperature Magnetic Measurement

In this chapter, the development of a turnbuckle diamond anvil cell is presented to enable high pressure magnetic measurements in a iHelium3 system, which is a sub-system of MPMS SQUID magnetometer allowing temperatures close to 0.5 K to be achieved. Based on turnbuckle principle, this diamond anvil cell design is an further development of the existing TM-DAC which has been described in Chapter 2 and Chapter 4. The external diameter of the cell is reduced to 6 mm, overall length remain 7 mm. The cell is probably the smallest diamond anvil cell to date. This chapter presents the engineering design process associated with this cell and preliminary magnetic measurements for which it was applied. Possibilities for further improvements are discussed at the end of the chapter.

7.1 Design motivation

The development of this cell is collaborated with Hearn's research group in University of Johannesburg to develop a high pressure cell for extreme low temperature (below 1 K) magnetic measurement in the iHelium3 system. As described in Chapter 3 (Figure 3.4), the system is capable to extend the minimum temperature of the SQUID magnetometer down to 0.5 K and has been used to measure several magnetic samples with superconducting transition below 2 K. Because the extreme limited space inside the ^{3}He insert (OD<6.4mm) , there is no high pressure instrument that has been developed for use with the iHelium3 system so far.

Apparently, the idea of TM-DAC is an optimal solution to address the challenges in the iHelium 3 system. However, the cell needs to be made even smaller to fit the ^{3}He insert which could compromise the strength of the cell body and pressure performance. Apart from that, the BeCu alloy used in TM-DAC contains impurities of Ni, Co and Fe which contribute to the rising background signal from the cell at low temperature (as shown in Figure 2.1 in Chapter 2). This magnetic background signal would increases more dramatically as temperature decreases further below 2 K in the ^{3}He system. Lower background alloy is preferable for the cell.

7.2 Design

7.2.1 Cell Design

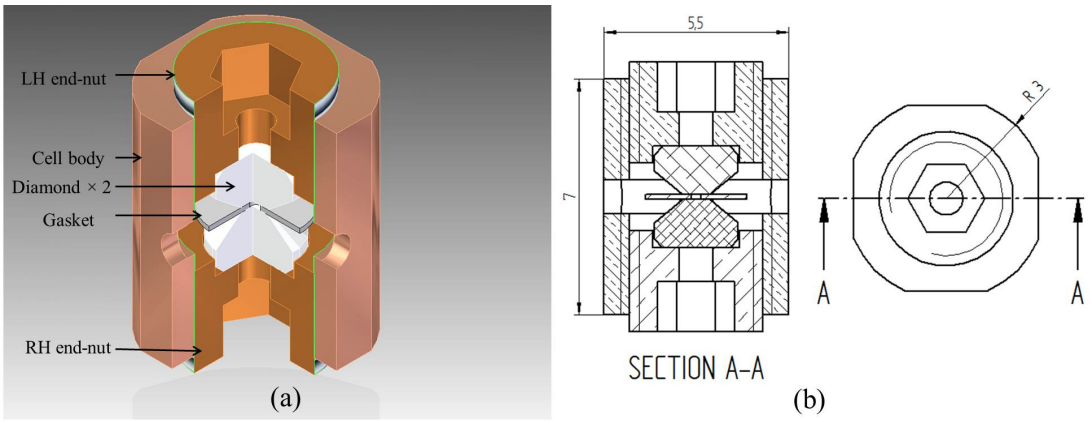

Figure 7.1: *(a) Quarter-section view of TM-3He-DAC; (b) the CAD drawing with main dimensions*

The modified turnbuckle diamond anvil cell developed in this project is coded as TM-3He-DAC to distinguish with the origin of TM-DAC [11]. In order to fit the cell into the limited

space in the ^{3}He insert and reduce magnetic background from the cell as much as possible, the dimensions of the cell are minimised as shown in figure 7.1, the external diameter of the cell is reduced to 6 mm, overall length remain 7 mm. Hexagonal counter bores are milled on the end-nut to remove as much material as possible to reduce the magnetic background. The end-nuts are identical apart from having the external M4.5×0.5 fine threads cut in opposite directions. An observation hole with 1 mm diameter is drilled on the end-nuts for observation and pressure measurement at room temperature. The four side holes are used to observe the lateral anvils alignment. Standard 2.5 mm diameter diamond anvils with 800 μm culets from Almax·easyLab [29] are used in the cell. High purity BeCu alloy was considered to make the cell but abandoned because high purity BeCu alloy is toxic. Instead, non-magnetic alloy CuTi is used in fabrication, as it had been seen to have lower magnetic background and good mechanical properties. However, the pressure capability of this cell is likely to be lower as the dimension of the cell is smaller and the strength of the CuTi alloy is lower than the hardened BeCu.

7.2.2 Clamp design

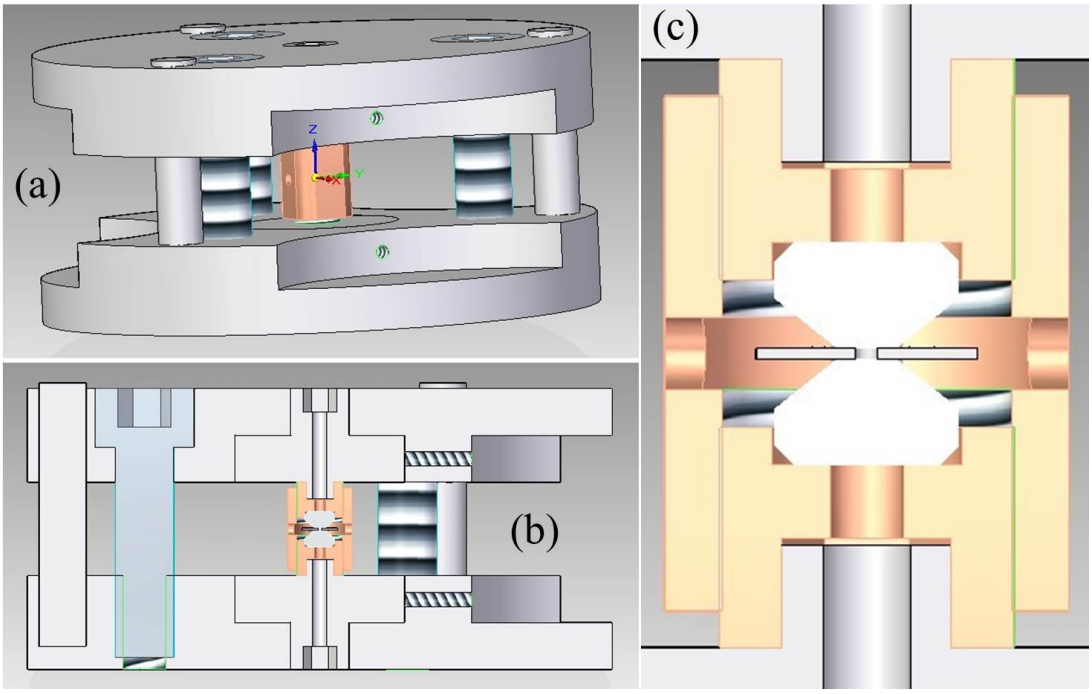

Figure 7.2: *Virtual assemblies of the TM-3He-DAC and the accessory screws-clamp, (a) overall view, (b) section view, (c) enlarged-section view of the cell.*

This cell is operated the same way as the TM-DAC described in Chapter 4, but it is also designed to work with a specially designed clamp for those users who doesn't have a hydraulic press and a load cell. As shown in Figure 7.2, a screw-clamp device was designed to applied load to the TM-3He-DAC. This auxiliary device is inspired by conventional Merrill-Basset cell design [115] and enables the user to apply load through turning the screw by allen key. After the cell is loaded with sample and placed between the plates, the compression on the end-nuts is generated by turning each screw one by one gradually followed by the turnbuckle cell body being tightened to lock the pressure. The holes on the clamp provide optical access to the sample and enable monitoring of the pressure by ruby fluorescence directly. This design is much more compact and a hydraulic press is no longer needed. However, if user intends to use hydraulic press and a load cell to record the actual compressive force on the cell, the screws can be removed and the load can applied on the clamp directly as it is working as a bracket as the old bracket system with a load cell underneath.

7.3 Stress analysis through FEA

7.3.1 Mechanical Properties of CuTi alloy

As described in Chapter 2, CuTi alloy has proved an ideal alloy for high pressure instrumentation for magnetic measurement due to its extremely low magnetic background [21, 38]. The tensile strength of this alloy is around 680 MPa-1000 MPa [21, 38, 116]. However, the material strength is determined by the supplier. The CuTi alloy for our cell was provided by Testbourne Ltd (UK) [117] and its tensile strength is around 680 MPa based on our hardness testing, which is comparable to the literatures result [21, 38, 116]. The alloy was not fully hardened to ideal strength (1000 MPa) by cold rolling hardening [116]. Another disadvantage of this alloy is the price of this alloy is much higher then BeCu alloy because it is not commercialised at the moment.

Based on our previous experience of TM-DAC, distortion energy theory is too conservative for the failure criterion in this type of cell. This mainly because plastic deformation is foreseeable due to the sharp angle of at the back of the diamond. This geometry would inevitable lead to high stress concentration on the anvil support area and indentation mark usually occur. As most of cell still hold the pressure even with minor indentation on the end-nut, this kind of permanent deformation is not considered failure. However, as the CuTi alloy is weaker than

BeCu alloy, the indentation on the end nut would be more obvious than the TM-DAC. To have better simulation result, tri-linear stress-strain model as shown in Figure 7.3 is used to defined the CuTi material in FEA. This strain hardening idealisation is based on experimental tensile test data from Nagarjuna *et al.* [116]. The material is expected to strain harden up to 680 MPa with 0.2164 plastic strain. Based on this strain hardening idealisation, the equivalent stress in the simulation will not be higher than 680 MPa.

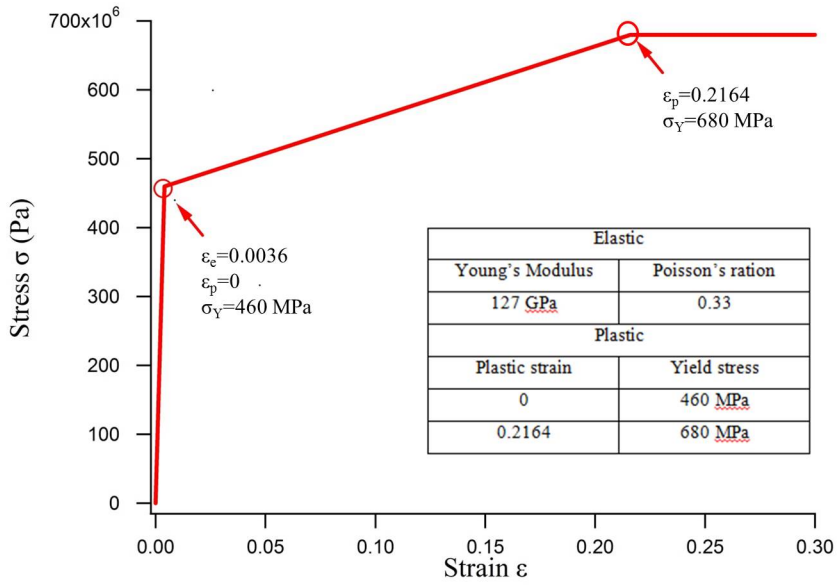

Figure 7.3: *Mechanical properties of CuTi in FEA simulation*

7.3.2 FEA model

Diamond failure is very rare from previous experience in TM-DAC due to its superior strength, which makes it an ideal anvil material. Therefore, the mechanical properties of diamond is defied as elastic, E=1208 GPa, ν=0.07 [60]. The meshed FEA model and the boundary and loading conditions are shown in Figure 7.4. Since the cell is fully symmetric, the FEA model is simplified to a 2D axis-symmetry problem to save computing time with the following boundary condition and loading. A symmetry BC (U_Y=0) is applied on the symmetry surface as shown in the figure. In addition, a compressive force is applied to the culet of the anvil to represent the reaction force from the squeezed sample and the deformed gasket. Quadrilateral elements are meshed in the model to increase mesh quality, whilst the mesh density is increased at the threaded area which is the main concerned area.

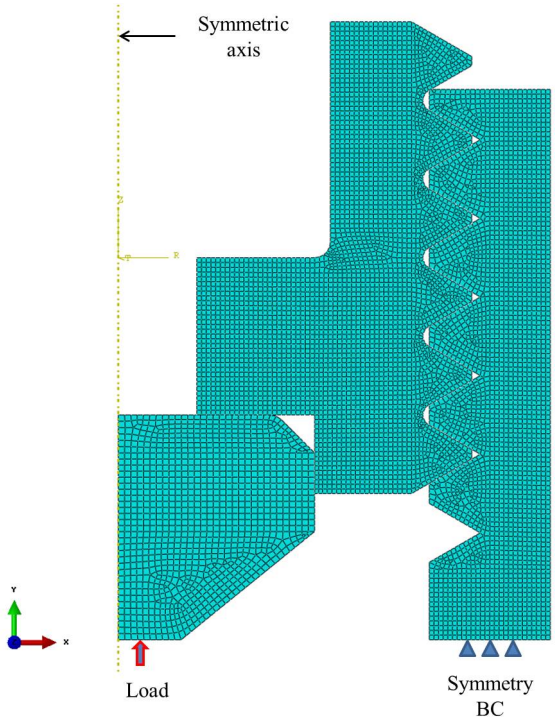

Figure 7.4: *FEA model of TM-3He-DAC*

7.3.3 Stress analysis

In the simulation results shown in Figure 7.5, the cell structure starts to have structural issues when the anvil is subject to 3 kN load. On the end-nut, appreciable plastic deformation is present on the area supporting the diamond anvil and is mainly caused by the sharp edge on the taper of the standard diamond. The analysis result indicates 3 dangerous areas on the cell when the load reaches 3 kN. The girdle edges of the diamond lead to insufficient support and sharp geometry change, which produces excessive equivalent stress concentrated on the end-nut (area A in the Figure 7.5) or alternately, the anvil indents into the end-nut. Shear failure modes could occur here potentially based on the deformation trend. However, the stress concentration on this area seems unavoidable if the standard 2.5 mm diamond geometries are used. In the meantime, the back of the anvil support (B) bulges significantly and the tensile stress accumulation can potentially lead to cracking. In addition, cracking could also occur at the root of the first two turns of the thread on the cell body (area C) as the tensile stress level on this area reaches critical value. The most possible fatal area is B as if this area fail, the anvil can possibly lose support and will not retain pressure. Area A is less likely to fail instantly based on the ductile feature of the material, the material could elongate 30% before fracture in the tensile test. On the other

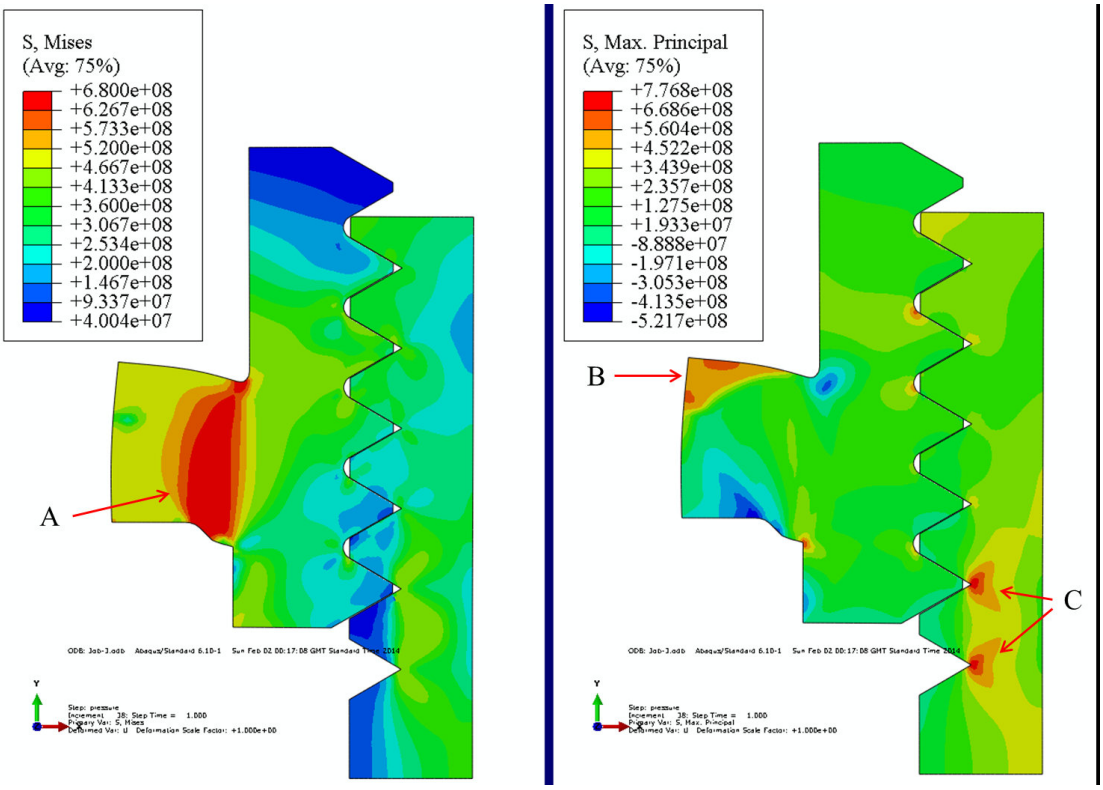

Figure 7.5: *Equivalent stress (left) and max principle stress (right) distributions on the structure of the cell when the anvil subject to 3 kN load.*

hand, failure on area C is less dangerous because the rest of thread will take up the load if first turn of the thread yield or shears off. Therefore, the deformation on the end-nut needs to be checked carefully during pressurisation. 3 kN here is considered the maximum load the cell structure can bear and is equivalent to average pressure 6 GPa on the anvil with 800μm culet. However, the attainable pressure is not consistent with this rough calculation. The actual attainable pressure highly relies on the gasket material, sample hole, pressure medium, which needs to be assessed in a prototype test.

7.4 Pressurisation test

The prototype of both cell and clamp are made as shown in Figure 7.6. The cell is constructed from Cu-Ti 97/3 wt % rod [117] and most of the clamp components are made of steel. The only major exception to this is the backing discs which is made of BeCu alloy. Because these backing discs contact the cell directly, it is necessary to prevent the cell from contamination by ferromagnetic substances. Three standard M6 bolts are used for load application. A 5.5 mm

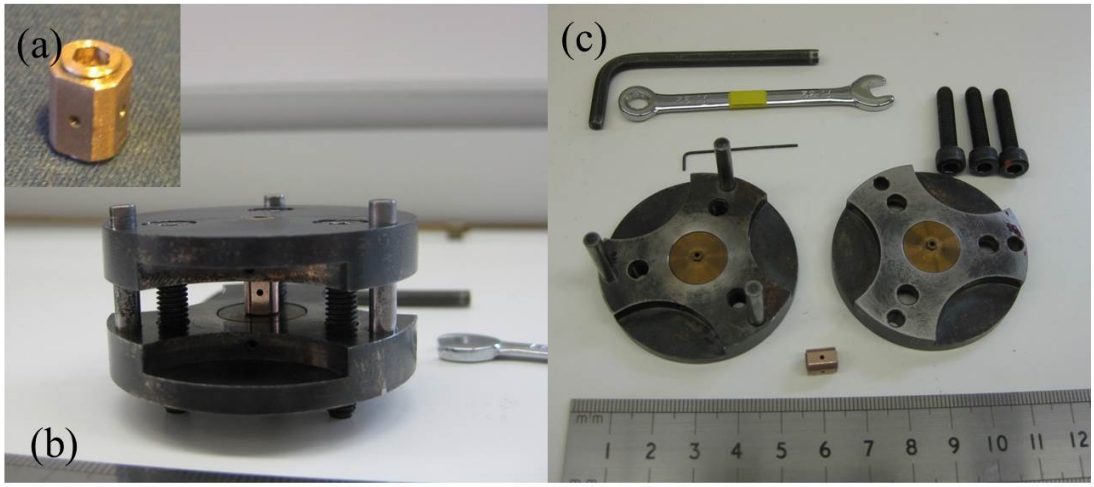

Figure 7.6: *(a) TM-3He-DAC; (b) the full assembly of the cell; (c) disassembly*

small spanner is used to turn the cell body and lock the pressure after the loading is complete. Even though this loading procedure is designed to avoid a hydraulic press, it is still workable in a hydraulic press as a bracket if screws are removed. In addition, the cell design is also compatible to the old loading system with a hydraulic press and load cell as shown in Figure 4.16.

In pressurisation test, the cell was tested with two pressure cycles to assess the pressure performance. In the first pressure cycle, the cell was pressurised using the clamp with a hydraulic press and a load cell to record the load and investigate the pressure variation at low temperature. The second pressure cycle was tested with the screw-driven concept for verification.

In the first test, the clamp is loaded with a hydraulic press instead of screws. The cell is pressurised at room temperature (300 K), as shown in Figure 7.8, ruby and Pb manometer are loaded into the sample hole of a BeCu gasket with Daphne 7373 oil used as the pressure transmitting medium. The maximum pressure was tested up to 3.8 GPa with 3.2 kN load in the first pressure cycle. Based on the result of the first test, the relation of load and accessible pressure is plotted in Figure 7.7, which shows that the load and pressure are almost linearly related. Then the pressure was released and the cell was disassembled for damage checking. No crack failure was found on the thread, and no sign of failure on the anvil backing area of the end-nut.

The first four pressure points (ambient, 1.5 GPa, 2.5 GPa, 3.5 GPa) at room temperature were measured by ruby fluorescence as shown in Figure 7.8. The pressure is determined by the shift of the R_1 fluorescent peak, the wavelength of the peak was converted by the Lab-Ram program based on the Equation 4.27. At each pressure point, the pressure was calibrated at

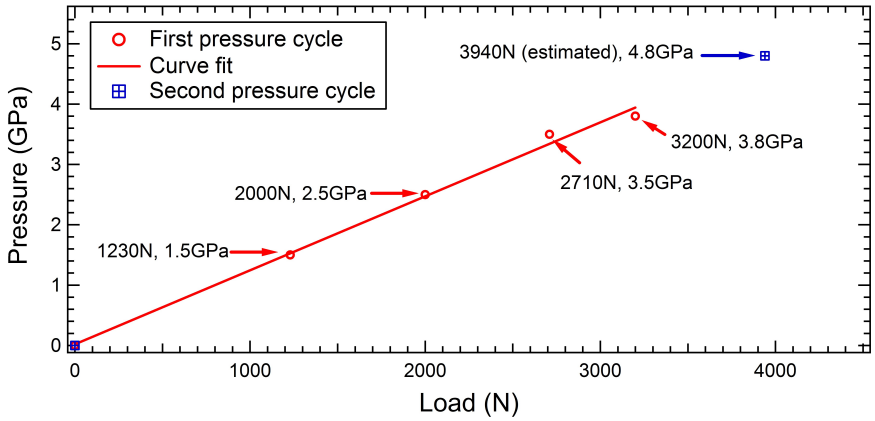

Figure 7.7: *The load and accessible pressure line.*

low temperature to investigate the variation of pressure at low temperature. The pressure at low temperature was measured through the MPMS SQUID magnetometer. Low temperature pressure was determined by measuring the critical temperature (T_c) of Pb manometer. As shown in Figure 7.9, the magnetic phase transition of Pb at low temperature can be seen even without the background correction. The mid-point of the temperature transition was chosen to be the T_c. The corresponding pressure at low temperature can be calculated based on the Equation 4.25. Based on the calibration line in Figure 7.10, the pressure variation within four pressure point is trivial and can be neglected.

In the second pressure cycle, a new gasket was replaced for second pressurisation test with the screw-driven concept as shown in Figure 7.6 (b) to verify the screw loading. The main disadvantage with the screw loading is that the force could not be recorded with such set up. In the second presssurisation test, maximum sample pressure achieved 4.8 GPa in which the corresponding load can be estimated around 3940 N based on the linear relation of the force and pressure (Figure 7.7). In this test, the cell was overloaded to 130% of the maximum allowable load and without any catastrophic failure occur such as crack. After pressure was released, the cell was disassembled and checked under a microscope. Appreciable bulge deformation (Figure 7.11 (a)) and indentation (Figure 7.11 (b-c)) were observed on the end-nut. These deformation agree with the simulation result (Figure 7.5), further loading the cell can accumulate high level of tensile stress on the bulge area, crack can be likely to occur. Because the cell still maintain high sample pressure with the bulge and indentation, these deformation are considered acceptable. On the other hand, the end-nut is expendable and can be replaced if indentation start to affect the performance of the cell.

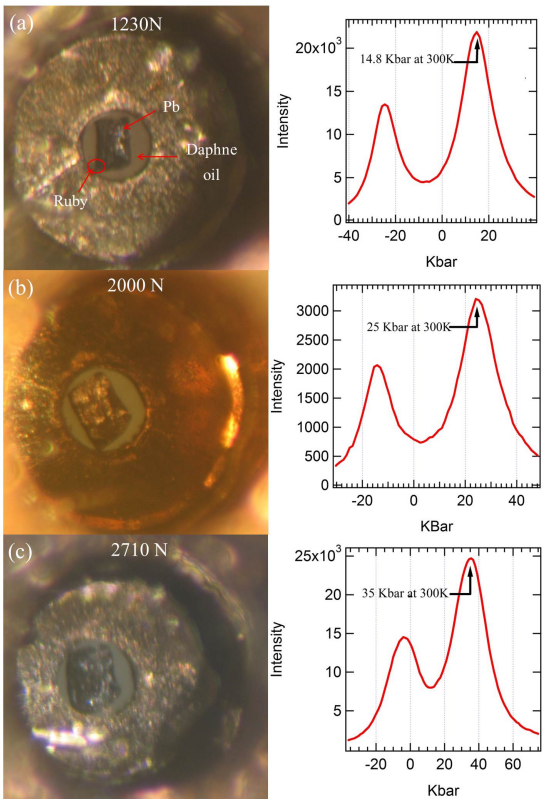

Figure 7.8: *Observation of sample and gasket deformation under loads: (a) 1230 N ; (b) 2000 N; (c) 2710 N. The pressure readings of each load was accuried by ruby fluorescence as shown on the right: (a) 1.5 GPa, (b) 2.5 GPa (c) 3.5 GPa, the wavelengths of R_1 peak were converted to pressure reading by the program on the Raman spectrometer based on Equation 4.27.*

7.5 Background measurements in MPMS SQUID magnetometer and iHelium 3 system

The empty TM-3He-DAC cell was firstly measured in MPMS SQUID magnetometer in order to assess the magnetic background. 100 Oe field was applied on the cell and the measurement was performed from 1.9 K to 300 K to acquire the background signal. The magnetic background of the TM-3He-DAC is compared to the predecessor TM-DAC as shown in Figure 7.12. The magnetic background of the TM-3He-DAC is generally less than the TM-DAC, almost half of the TM-DAC value in the range from 25 K-300 K. Therefore the sensitivity of this cell is higher with its lower background feature. However, both cells shows a low temperature upturn due to the material impurity. The CuTi used for the TM-3He-DAC is reported contain 0.0021% Fe by the supplier. Apart form that, the BeCu gasket in used also contain 0.6% of Co, Ni and Fe element. These impurity contributes the majority of the signal at low temperature. Even though,

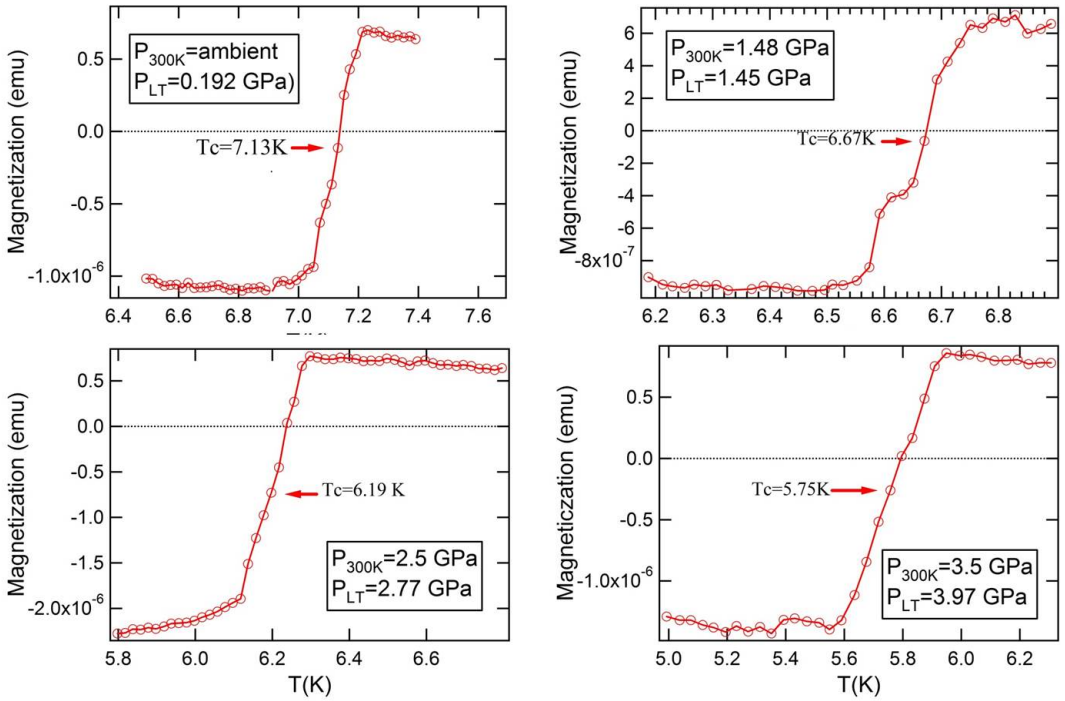

Figure 7.9: *The pressure of the TM-3He-DAC at low temperature was calculated by measuring the superconducting transition temperature T_c of Pb, which is based on the equation 4.25 from Eiling and Schillings publication [25].*

at the lowest temperature available in SQUID magnetometer, the magnetic signal of the TM-3He-DAC still lower than TM-DACs magnetic background signal. Based on the tendency of magnetisation curve, the background of the cell would be more significant at lower temperature range which is displayed in Figure 7.13.

Figure 7.13 shows background signal of the empty TM-3He-DAC at sub-K range (T<2 K) which was measured in the iHelium3 system. With the cell, the ^{3}He system is still capable to stabilised at the base temperature (490 mK). As anticipation, Figure 7.13 shows the magnetic background of the cell was further increased when the cell was cool down below 2 K. However, the magnetisation curve is still very smooth which shows that the cell still capable to probe superconductivity behaviour at the sub-K temperature range. As shown in Figure 7.14, field measurement also carried out on the cell to investigate the magnetic background behavior of the cell. At four isothermal low temperature (0.526 K, 0.552 K, 0.982 K and 1.116 K), the magnetsation of the cell is measured with increasing magnetic field. The magnetisation curve is also smooth and almost temperature independent at high filed environment.

Figure 7.15, Figure 7.16 and Figure 7.17 show how the cell was installed into the ^{3}He insert of

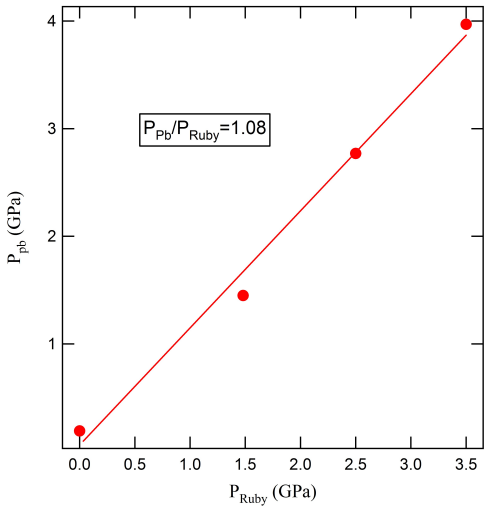

Figure 7.10: *The calibration line of pressure at room temperature and low temperature, which shows P_{Pb}≈1.08 P_{Ruby}, the pressure variation is trivial and can be ignored.*

the iHelium3 system. Figure 7.16 shows how the cell was loaded into the straw. The thermal conducting sheet needs to be cut with several slits in the middle, which allows the cell can be retrieved conveniently. Then the sheet is wrap as a tube and inserted into a standard straw for fixture. The straw needs to be cut open at the middle in advance, which is used to load the cell. After all, the cell is loaded in to the insert from the middle of the straw and two smaller polyimide tube are inserted from top and bottom of the straw to fix the cell in the middle of the insert. The top polyimide tube with a connector head is used to mount the insert on the sample rod (Figure 7.17). A thermal meter is mounted on the bottom of the polyimide tube for temperature recording. Figure 7.16 shows that the cell can be fit in the insert without any difficulties based on its miniature feature.

7.6 Future work

This section presented the design and testing process of turnbuckle diamond anvil cell made for magnetic measurement at extreme low temperature environment. In the loading test, the cell is capable to reach sample pressure close to 5 GPa without failure. The background measurement in MPMS SQUID magnetometer shows that the background signal of the TM-3He-DAC is less then its predecessor TM-DAC, and therefore the sensitivity of this cell is higher than the TM-DAC. This unique feature shows that the cell is ideal to probe magnetic signature of weak magnetic material. In addition, the smooth magnetic signature of the empty cell allows the

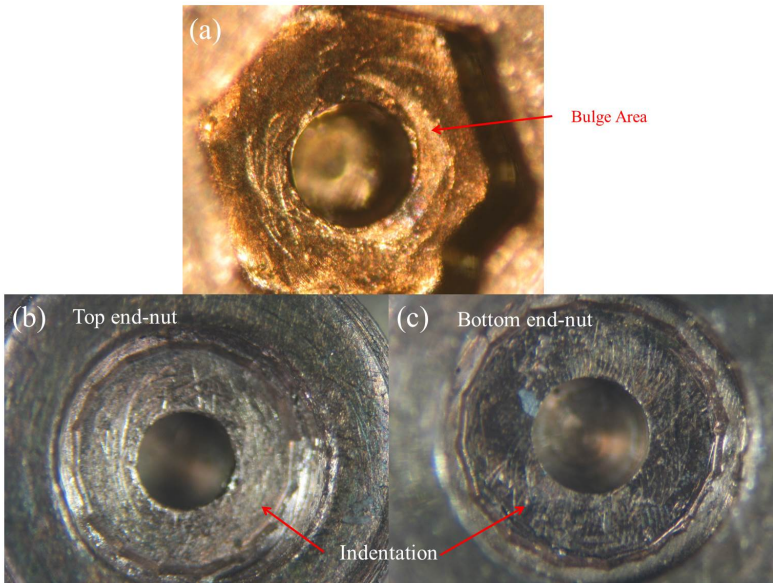

Figure 7.11: *(a) Bulge area of the end-nut; the indentation of the anvil support area on the (b) top end-nut and (c) bottom end-nut.*

cell to be also used to probe high-pressure superconductivity behaviour of material at sub-K temperature.

The rising background at low temperature in the background measurement shows that the impurity level of the CuTi alloy needs to be further reduced in future. The impurity of CuTi alloy currently in use is reported with 0.0021 % Fe contaminant, this impurity can be further reduced to 0.001% with the same supplier in UK [117]. The future version of TM-3He-DAC and the gasket should be made of the CuTi alloy with lower iron contaminant to reduce the background signal.

Apart from the purity perspective, the strength of the alloy as it was reported can be increased more than 30% by cold rolling process [116]. If this was done, the pressure capability of the cell can increase significantly. With the current available material, the indentation and bulge as shown in Figure 7.4, can be mitigated by enlarging the anvil support area, such as grinding off the sharp taper of the standard diamond or using a larger diamond. The cost of this approach will increase substantially. Alternatively, increasing the thickness of the anvil seat could be a more economic way but with the cost of slightly higher magnetic background.To validate this, the original FEA model shown in Figure 7.4) was modified. The thickness of the anvil seat was increased with 0.5 mm as shown in Figure 7.18. Under the same load (3 kN), a 0.5 mm extra thickness (second design shown in Figure 7.18) on the anvil seat can offer a more robust

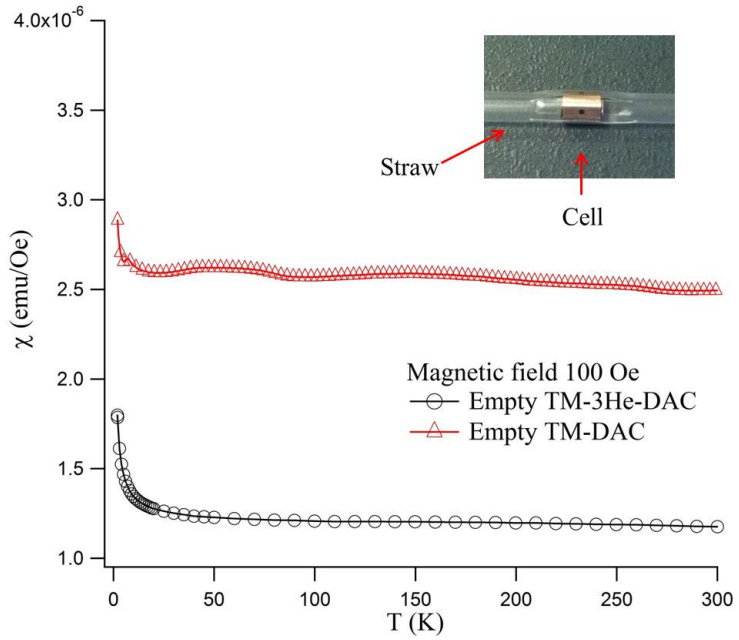

Figure 7.12: *The temperature dependence of the magnetisation of empty TM-3He-DAC and TM-DAC, the magnetisations data of each case is normalised as $\chi = M/H$ for comparison. The small figure at top right shows the cell loaded in to the straw.*

support. The deformation on the end-nut is much less than the original design. However, tensile stress level still high in the first two turns of the thread at the cell body due to shear and bending. Increasing the wall thickness of the cell body by enlarging the cell body could mitigate the stress concentration but is not feasible when the major dimensional constrain of iHelium3 system is considered. Nonetheless, as failure occurrences in this area are less fatal, geometry changes on the cell body are less necessary.

Many commercial FEA packages integrate versatile shape optimisation algorithms [118] nowadays. This optimisation approach can be used to further optimise the end-nut design in future. Shape optimisation is different to the conventional design approach. With conventional design approach, the shape of a part is predefined first, then loads and boundary conditions are applied on the part in FEA. When the simulation is finished, the results (deformation or stress/strain) are checked to see if they meet the design constraints or not. If results are not satisfied, the original design is modified for next simulation. Iteration will continue until the simulation provides the final optimal result. With shape optimisation, the loads, boundary conditions and design constrains of the part are defined first. Then designer can specify what space the part has to fit into before running the simulation. After the simulation finished, the software package can provide the best shape to satisfy constraints like minimum weight or maximum stiffness. In

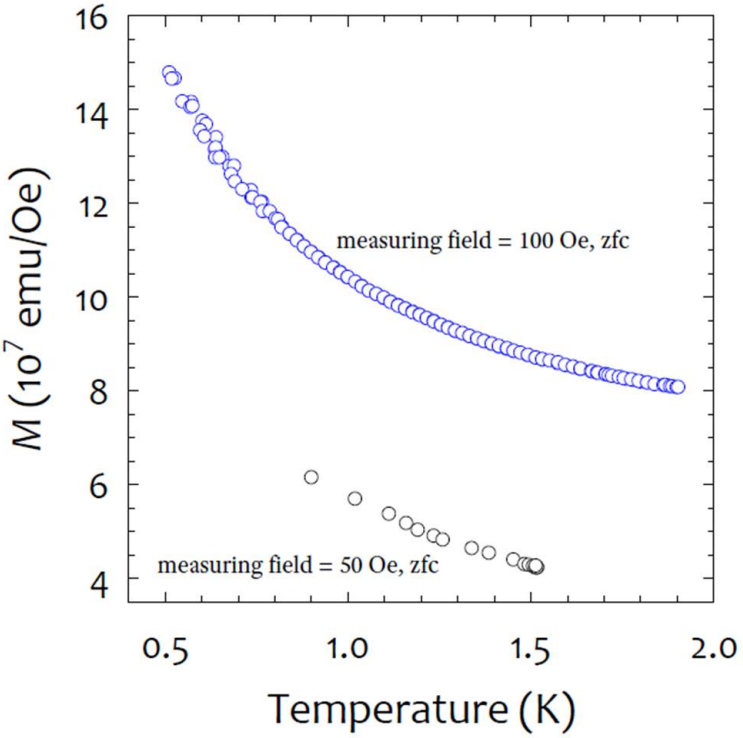

Figure 7.13: *The temperature dependence of the magnetisation of empty TM-3He-DAC in the temperature range 0.5 K to 2 K. 2 different field were applied, the magnetisations data of each case is normalised as* $\chi = M/H$.

the case of the end-nut design, if the maximum allowable deformation of the end-nut can be defined, with the minimum weight constrains, the optimal thickness of the anvil seat end-nut can be obtained through shape optimisation approach.

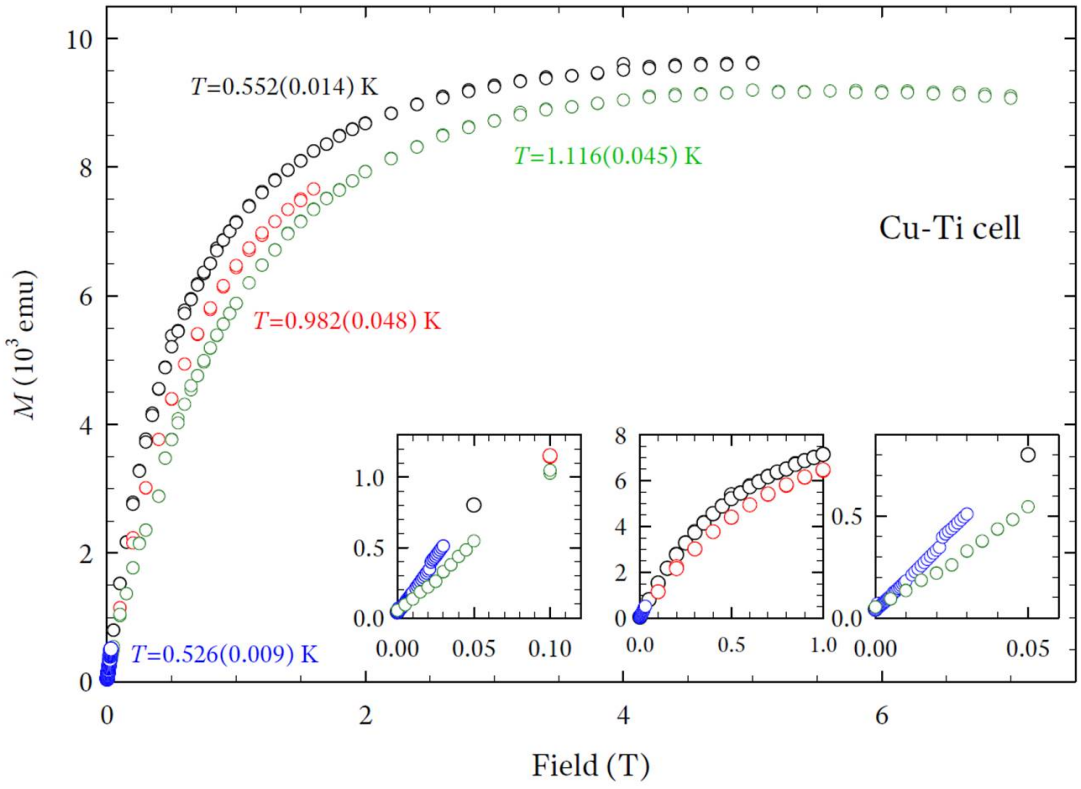

Figure 7.14: *The field dependence of magnetisation of empty TM-3He-DAC at four isothermal temperatures, the value in the bracket is the uncertainty value in temperature.*

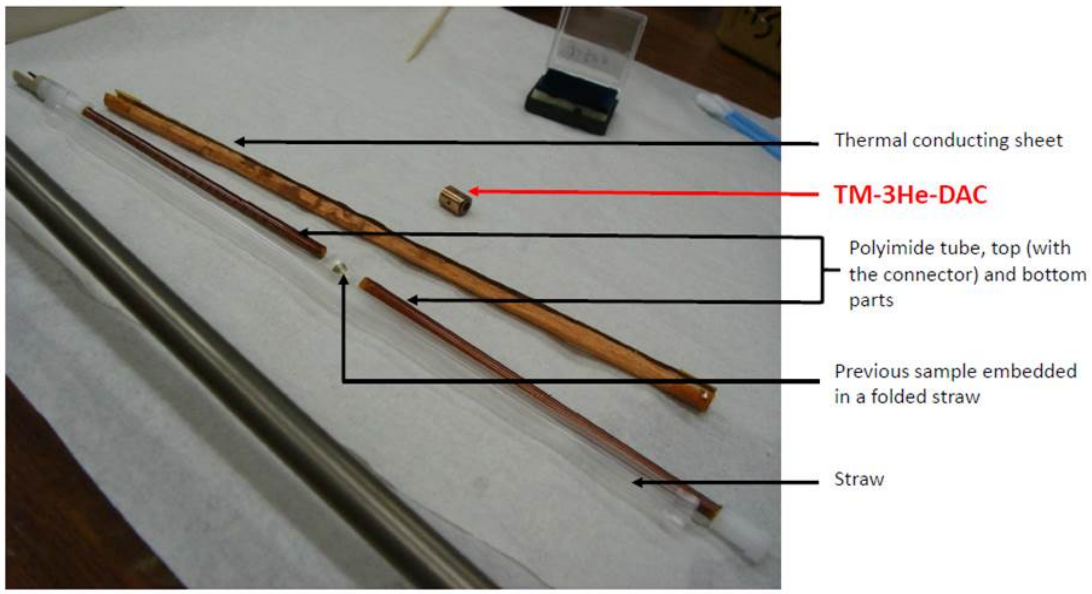

Figure 7.15: *The disassembly of the ^{3}He insert and the TM-3He-DAC.*

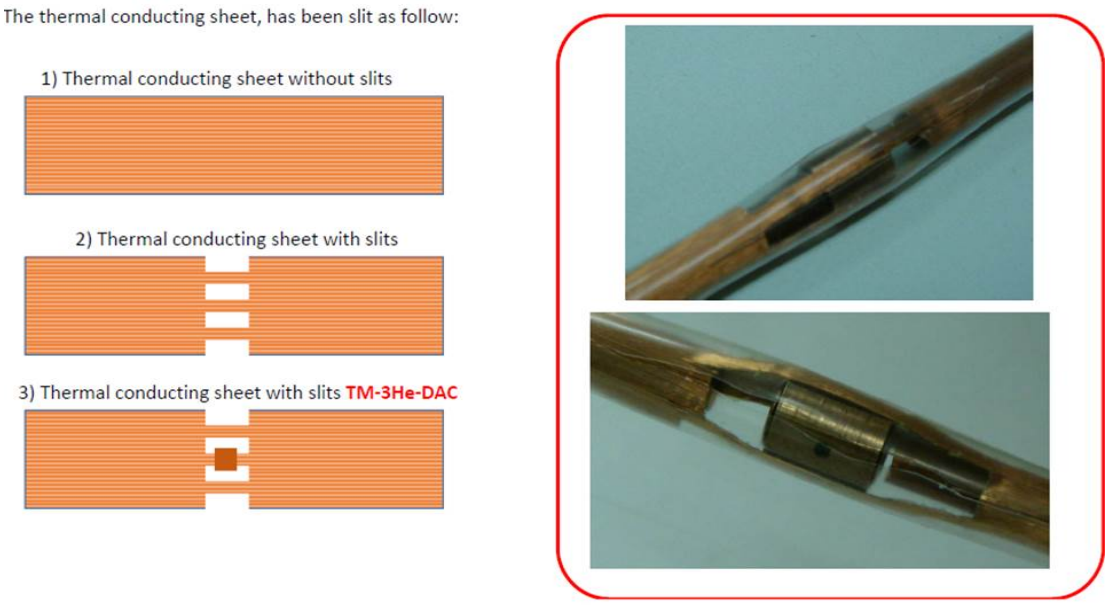

Figure 7.16: *The thermal conducting sheet was cut with several slits which are used to mount the cell and assist in cooling (left); The detail pictures of the loaded cell in the straw (right).*

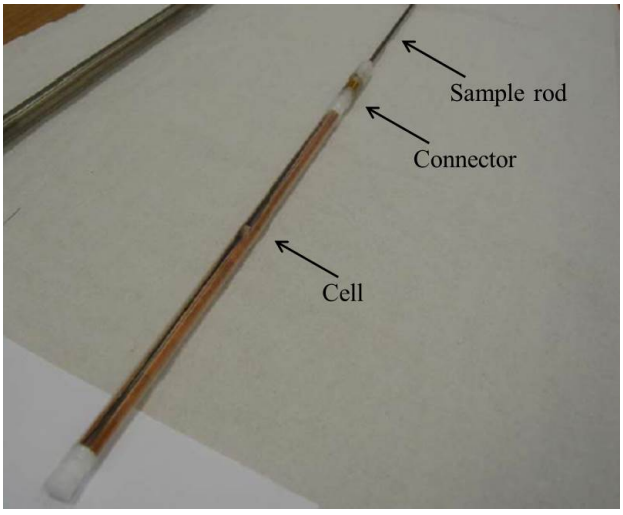

Figure 7.17: *Insert was set up and mount on the sample rod.*

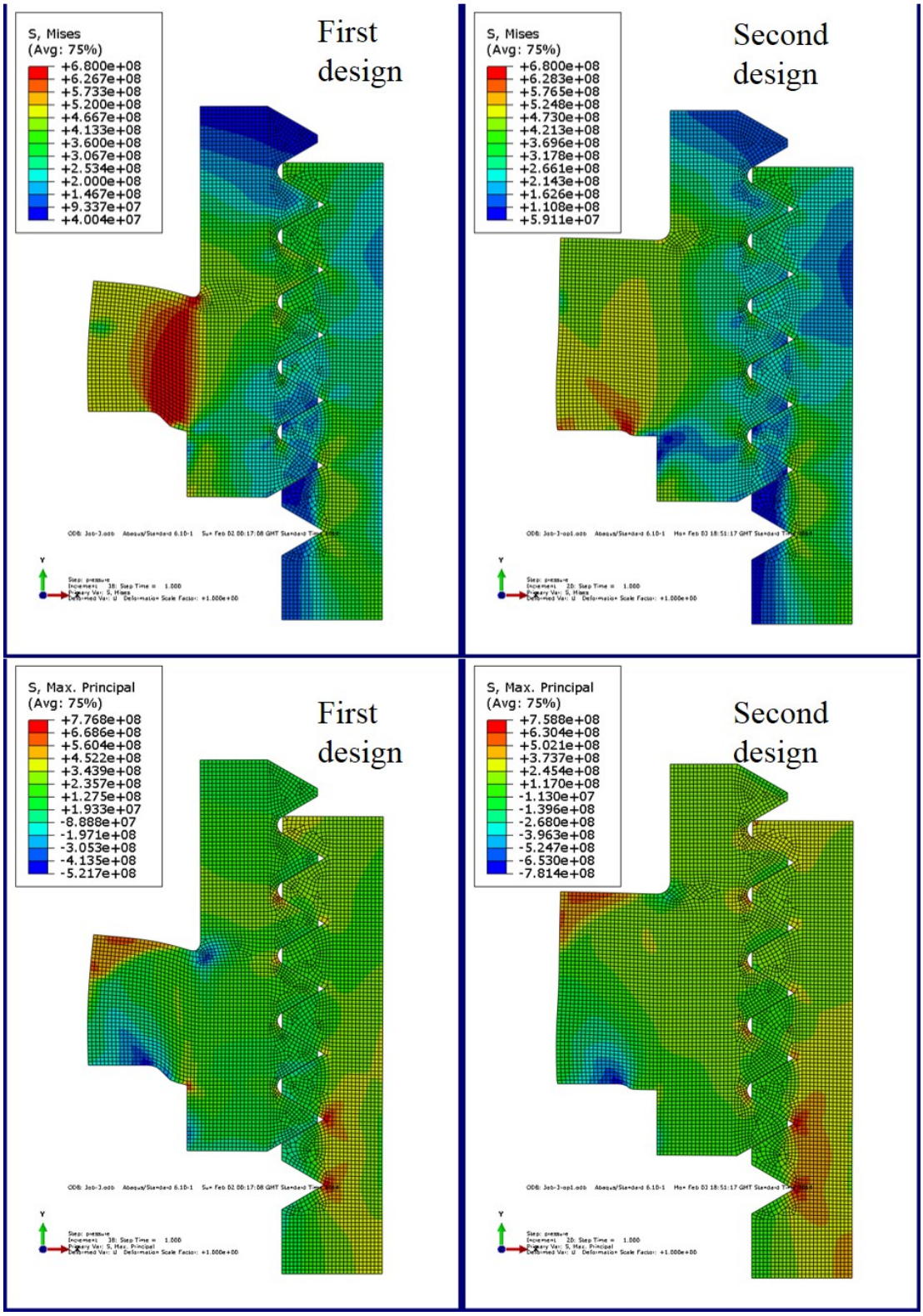

Figure 7.18: *Equivalent stress distributions of the original design and the second design which the thickness of the anvil seat was increased with 0.5 mm.*

Chapter 8
Non-metallic Turnbuckle Diamond Anvil Cell for Ac Magnetic Susceptibility Measurement

The applicability of fibre-reinforced polymers for fabrication of turnbuckle diamond anvil cells was assessed using finite element analysis and experimental testing. Performance and failure modes for the key components of the cell working in tension and in compression were evaluated and the ways for optimising the designs were established. These models were used in construction of a miniature fully non-metallic diamond anvil cell for magnetic ac susceptibility measurements in a Magnetic Property Measurement System. The cell is approximately 14 mm long, 8.5 mm in diameter and was demonstrated to reach pressures of 5.6 GPa. Ac susceptibility data collected on Dy_2O_3 and U_6Fe demonstrate the performance of the cell in magnetic property measurements and confirm that there is no screening of the sample by the environment which typically accompanies use of conventional metallic high pressure cells in oscillating magnetic fields.

8.1 Design motivation

As described in Chpater 2, there are some non-magnetic DACs were designed for use with the SQUID commercial magnetometer [11, 33, 38] recently. Despite the ability of most magnetometers to perform magnetic measurements in both direct current (dc) or alternating current (ac) modes [3, 14], high-pressure magnetic studies with these setups have been primarily limited to dc measurements. The reason for this is that traditional DACs are constructed using metals and alloys, creating issues involving eddy currents and sample screening when coupled with high-frequency ac techniques. At present, the high-pressure ac measurements are only available in cells with built-in pick-up coils [36, 79–89]. In comparison with use of the commercial magnetometer, fabrication of pick-up coils is complicated, time consuming, and can be expensive. Nonetheless, ac measurements can yield information about magnetisation dynamics which cannot be obtained in dc measurement. Thus, the motivation for this study was to address challenges presented by designing an entirely non-metallic high-pressure cell which can be used to perform such measurements in both dc and ac modes.

The presented work describes the development of a non-metallic pressure cell from the concept and design to experimental testing for which a Magnetic Property Measurement System (MPMS®) from Quantum Design [3] is used. The design adapted for the pressure cell is based on the turnbuckle principle which has been pioneered by S. Tozer [5–9]. In this chapter, we investigate magnetic and mechanical properties of advanced composite materials, analyse failure mechanisms of key components of the pressure cell, and optimise the design for ac susceptibility measurements. The name of the cell presented in this article is abbreviated as PTM-DAC for *plastic turnbuckle magnetic diamond anvil cell*.

8.2 Material

The material used in previously reported plastic cells [8, 23] is a high strength polymer referred to as Parmax 1200 in the US. It is the the strongest non-reinforced material to date which exhibits excellent cryogenic performance [119, 120]. The room temperature tensile strength of Parmax 1200 is 203 MPa, with compressive strength of 351 MPa. These values become 170 and 348 MPa at 77 K and 174 and 431 MPa at 4 K, respectively. Elongation is 4, 1.8 and 2.1 % and Young's modulus is 8, 9.7 and 9.8 GPa, respectively, as the temperature decreases from ambient through to liquid nitrogen and then to liquid helium temperatures [119]. Unfortunately,

manufacturing of this material stopped several years ago. It is hoped that the material will be reintroduced as Tecamax SRP® by Ensigner [121] shortly. Currently, only small samples of this material are available. The colour of the Tecamax SRP sample is black which is different to Parmax 1200 (clear brown), which indicates that the composition of the Tecamax SRP might be different from its predecessor. As both Parmax 1200 and Tecamax SRP are not currently available, we focused on finding an alternative material.

Polymer name	Additives	Young's modulus E (GPa)	Tensile strength S_t (MPa)	Compressive strength S_c (MPa)	Elongation %
PARMAX 1200[a]		8	203	351	4
TECAPEEK GF30[b]	30% GF	9.5	180	172	2.5
TECATRON GF40[b]	40% GF	14	185	172	1.9
TECAPEI GF30[b]	30% GF	9.5	165		2
TECAMID 66 CF20[b]	20% CF	13.5	190		2.5
Torlon 4XG [c]	40% GF	6.9	159	275	4
90HMF40[d]	40% CF	45	330	310	1.2

Table 8.1: *Major high-performance polymer materials, their composition and key mechanical parameters at room temperature. The key below indicates the manufacturer, a, Parmax material was originally made by Dow Chemical, then produced by Mississippi Polymer Technology, it is now coded as Tecamax SRP® and manufactured by Ensinger [8, 120, 121]; b, Ensinger engineering plastic [121]; c, Quadrantplastics [122]; d, Victrex Polymer [123] plastics. GF stands for glass fibre and CF stands for carbon fibre additives to the polymer.*

Mechanical properties of several high performance plastics from major engineering polymer manufacturers such as Ensinger [121], Quadrant [122] and Victrex [123], were compared, as shown in Table 8.1. As general grade plastic materials have quite low elastic parameters and material strengths, introduction of glass or carbon fibre additives is a common measure to enhance their properties. The final selection is based on four considerations: high strength, low magnetic background, machinability and availability. Of all candidate materials, the carbon fibre reinforced PolyetherEtherKetone (PEEK) coded 90HMF40 from UK based company Victrex [123] proved to meet these requirements best. It is a high performance thermoplastic made with up to 40% carbon fibre and 60% PEEK. The ultimate tensile strength is reported as 330 MPa with the compressive strength of 310 MPa. The elastic modulus of this material (45 GPa) is substantially higher than that of other materials (Table 8.1). It was also found to have very good machining characteristics. The low temperature performance of this material is yet to be characterised. We measured and compared magnetisation of 90HMF40 and Tecamax SRP, and established that at the maximum in magnetic response the Victrex product has

approximately 40 times lower magnetic (mass) susceptibility, as can be seen in Figure 8.1.

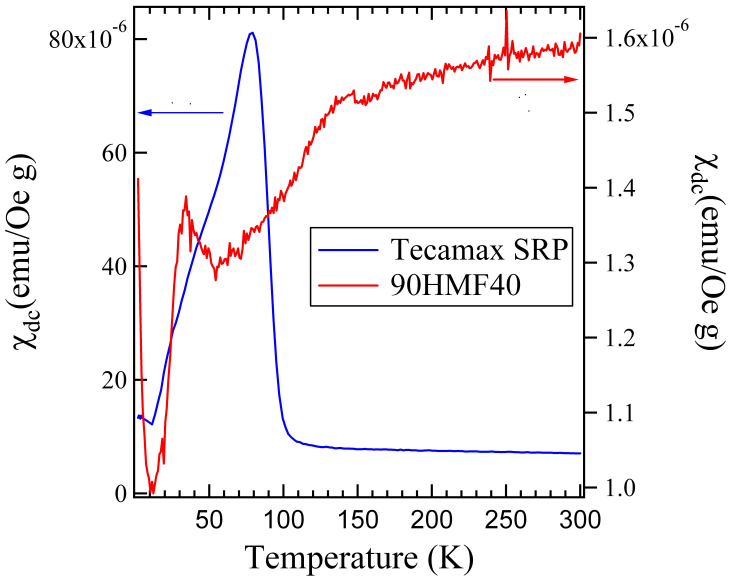

Figure 8.1: *Temperature dependence of magnetic susceptibility for Victrex 90HMF40 and Tecamax SRP. In this figure, the arrows indicate with which axis each dataset is associated. The data were collected in 100 Oe field.*

8.3 Initial design

Our starting point was modifying the existing turnbuckle magnetic DAC (TM-DAC) [11] which is made from BERYLCO 25 and designed for dc measurement in MPMS system. For ac measurement, the metallic material in this design needs to be replaced by non-metallic material. Moreover, unlike to the scenario of TM-3He-DAC in last chapter, the dimensions of PTM-DAC need to be as large as possible to provide sufficient support to diamond anvils. Which is mainly in the view of the 90HMF40 plastic is far weaker than BERYLCO 25 or CuTi alloy. As shown in Figure 8.2, the original design was revised to achieve the maximum allowable dimensions in order to compensate for lower material strength.

The external diameter of the cell is approximately 8.5 mm and the cell body 9 mm long. The end-nut with a hexagonal head and M5$\times$0.5 fine thread is used for this cell with the fit between the internal and external threads made as tight as possible. Stronger coarse threads, such as M6$\times$0.75 had been considered but were found to reduce the cross-sectional area of the cell body which would make it too weak in tension. In addition, because the brittle material is much more sensitive to the stress concentration, side holes for observing anvil alignment in the

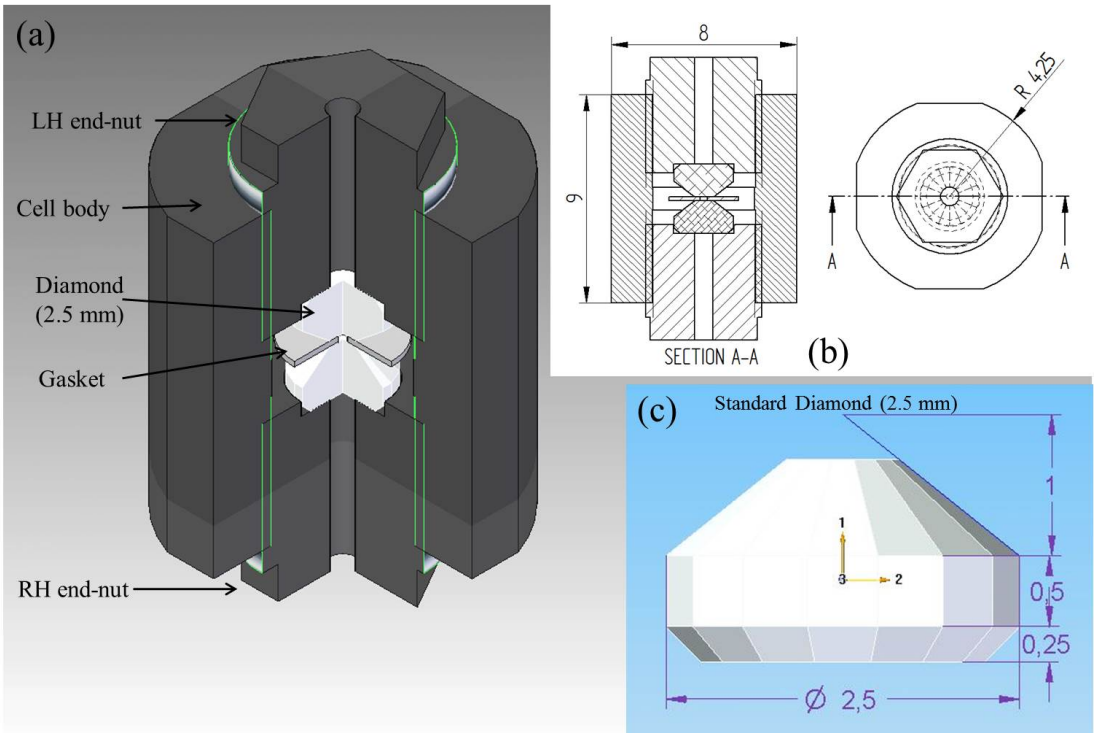

Figure 8.2: *(a) Quarter section view of the initial design of PTM-DAC (LH and RH stand for left-hand and right-hand thread, respectively); (b) engineering drawing with key dimensions; (c) standard cut diamond.*

TM-DAC were removed in this design. Standard-cut 16 facet 2.5 mm diameter diamonds with 800 μm culet from Almax·easyLab [29] were used initially. The anvil alignment is achieved through precision machining of the end-nuts and the cell body. The operation of the cell is as in the case of TM-DAC [11].

8.4 Composite gasket

The last remaining component of the pressure cell that needs to be made non-metallic is the gasket. The gasket we used is based on the one developed by Graf *et al*. [8], however there are some differences in the preparation procedure which will be outlined in this section. Figure 8.3 shows an example composite gasket, which consists of two parts, the internal solid core and the external Zylon® reinforcement. The preparation procedure of the composite gasket has two stages. These involve the preparation of the solid core and then winding the Zylon® fibre around it. In the first stage, one drop of epoxy (Stycast 1266) is blended with two types of powder (1. diamond powder, grain size approx. 1 μm, Logitech Ltd; 2. aluminium oxide pow-

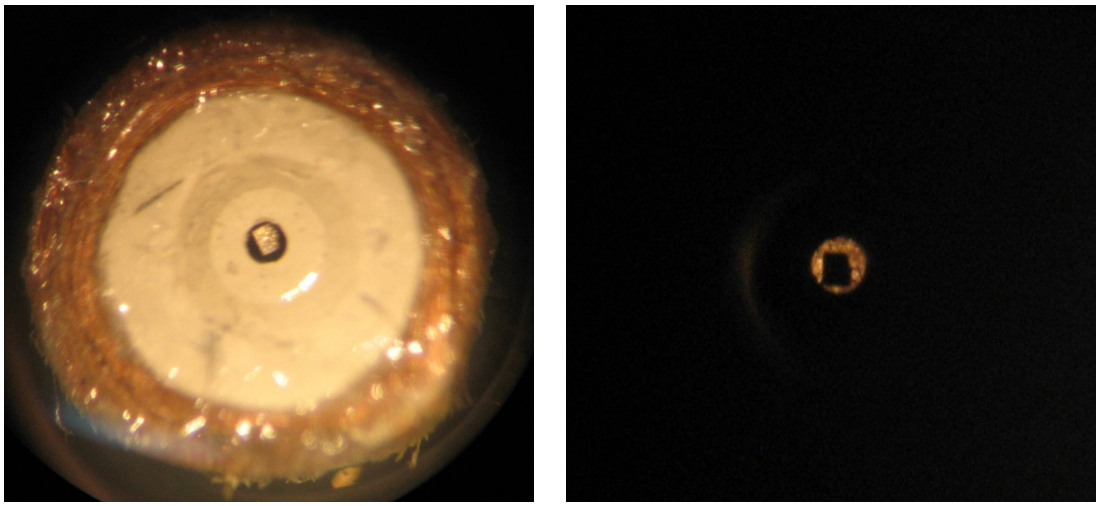

(a) Composite gasket (b) Sample hole deformation at 5.6 GPa

Figure 8.3: *Composite gasket with a sample loaded: (a) the internal core is made of diamond and aluminium powder and reinforced by Zylon® fibre. The internal core was indented with a pair of 800 μm culet diamonds; (b) the shape of the hole at 5.6 GPa pressure.*

der nano-powder, <50 nm, SIGMA-ALDRICH). The powder is continually added and blended until a sticky consistency is reached. The ratio of diamond and aluminium oxide powder is approximately 1:1. After that, a small piece is separated from the mixture and formed into a disk shape. This is heat cured at 70°C for a 15–20 minutes to part-harden. The disk is then compressed to form an indented gasket of the desired thickness (normally around 100 μm) between two opposed diamond anvils. Prior to this, PTFE is sprayed on the culet of the diamonds to ensure the indented gasket can be removed. The gasket is further heat-cured for 1 hour and the indented gasket can be removed for sample hole drilling. A sample hole (normally, with the diameter of 270 μm) is drilled mechanically at the centre of the indented gasket. This then is followed by a final heat-curing for at least 3 hours.

The gasket then requires reinforcement with Zylon® fibre. In the second stage, the outer diameter of the cured gasket must be reduced to approximately 2 mm by manual filing. After that a strand of Zylon® fibre is wetted with Stycast 1266 epoxy and wound around the solid gasket core until the overall diameter becomes approximately 4 mm. When the winding is complete, the gasket must be left for at least 24 hours to cure completely before use.

As shown in Figure 8.3 (a), the gasket needs to be glued on top of the anvil with epoxy or

GE varnish before loading the sample and pressure medium. During the experimental testing, the composite gaskets were found much harder than conventional BeCu gaskets used with the TM-DAC, resulting in a lower pressure generation efficiency. Moreover, the pressure and load are not linearly related in this composite ceramic gasket as in a metal one. Apart from that, we found pre-compression is required if the desired sample pressure needs to be higher than 2 GPa. The characteristics of this gasket are further described in the section of testing (Section 7). The pressure medium used in the test is Daphne 7373 [107], NaCl powder is blended with the medium (mass ration of 2:1) to increase the viscosity and prevent leaking. It was shown experimentally that the sample hole can expand to approximately 350 μm at the highest accessible pressure, as shown in Figure 8.3 (b).

8.5 Loading test and failure analysis

8.5.1 Experimental testing

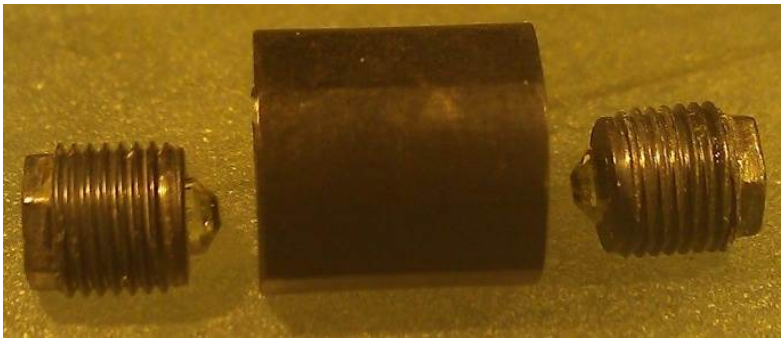

Figure 8.4: *Prototype of initial design.*

The initial design was machined for prototype testing as shown in Figure 8.4. Pressurisation testing was carried out using two different sets of gaskets (BeCu and composite gaskets described above) to assess the pressure performance of the cell and of the composite gasket. For the BeCu gaskets, it was found that the sample pressure readily reached 3 GPa under 2.5 kN external load. However, achieving higher pressures was difficult and higher loads resulted in the failure of the cell as shown in Figure 8.5. The pressure generation efficiency is low due to a lack of support for the table of the diamond anvil which tends to indent the end nut rather than to deform the gasket. For the composite gaskets, the pressure performance of the cell is also limited, with sample pressures reaching 2 GPa under 2.7 kN of external load. As shown in Figure 8.5, the failure pattern of the end-nuts is similar in each failed end-nut, with radial cracks

occurring and propagating quickly through the part. No failures of the body of the cell were observed. One common feature of the failures is the end nuts cracked when the anvil support area indented to a certain depth (see the next section for more detail). The 'sinking' of the anvil shows that the material presents some degree of ductility.

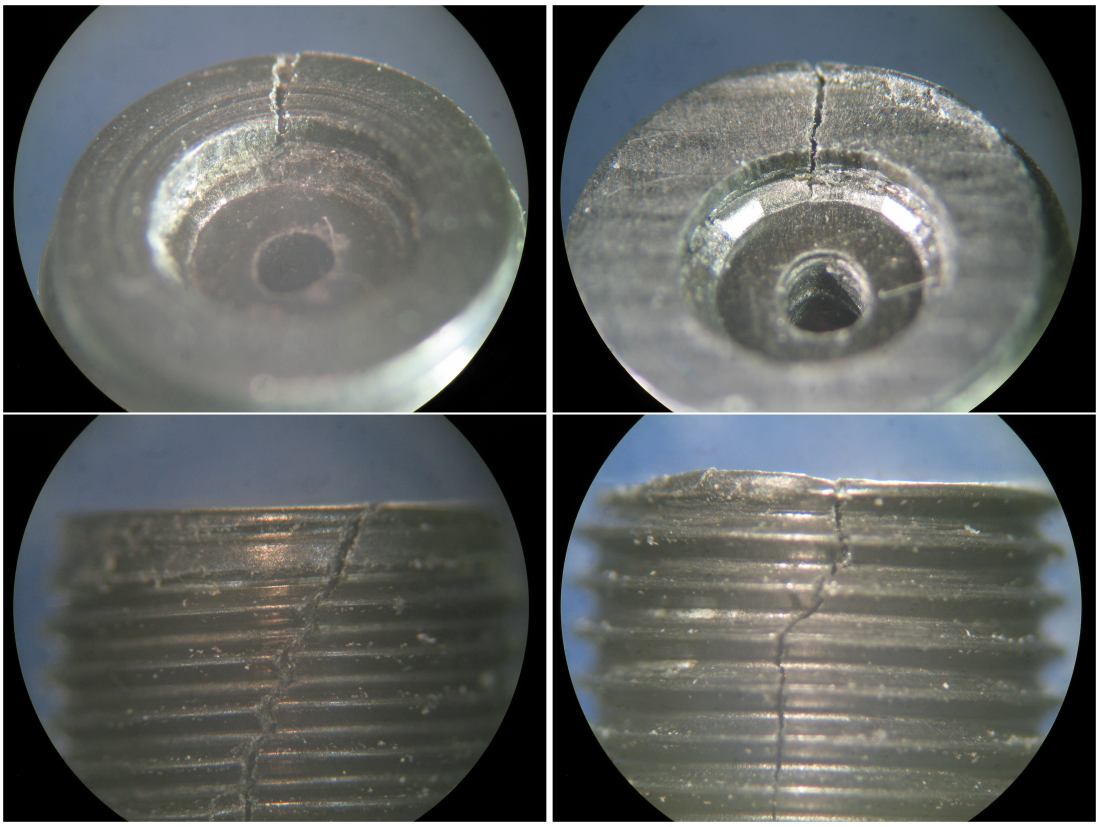

Figure 8.5: *Typical failure pattern (radial crack) in the end-nuts. Note, in the top pictures (left and right) the diamond facet indent marks are clearly visible, demonstrating the deformation of the material. It can also be seen that the crack originates at the sharp edges between the facets of the crown.*

8.5.2 Failure analysis

Evidently, the plastic deformation plays an important role as the cause of the radial cracking. To improve the design, it is essential to understand the mechanism of this failure first. To achieve this, we use commercial finite element analysis package, ABAQUS, to investigate the deformation of the end-nut. 2D axisymmetric model in FEA with symmetric boundary condition as shown in Figure 8.6. In the experiment test, all the end-nuts were failed in the pressurisation stage when the thread between the body and end-nuts was not engage. Thus, to analyse the

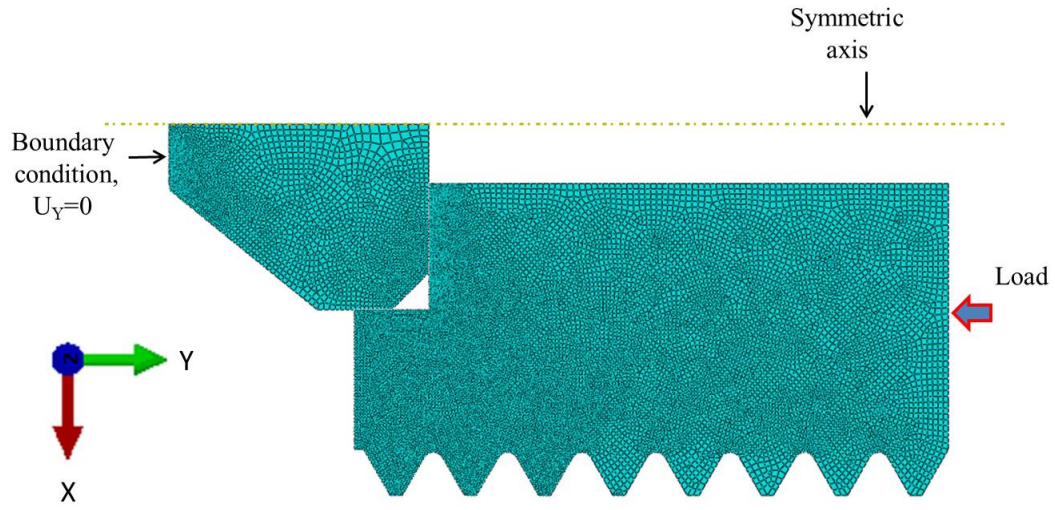

Figure 8.6: *FEA model used to analyse the deformation of end nut in Figure 8.5. The strain-stress relationship of diamond is considered perfectly elastic in the model with the following parameters: Young's modulus E=1208 GPa, Poisson's ratio ν=0.07 [60]. The properties of 90HMF40 material are defined using bi-linear model with the following parameters: E=45 GPa, ν=0.3, yield strain ε_Y=0.012, and yield stress S_Y=310 MPa, no strain hardening. Load is applied on the nodes of elements at the top of the end-nut surface.*

deformation of the end-nut closed to reality, the cell body is not included in this model. Quad elements are used mainly in meshing the model and the mesh density at the area close to the anvil contact area is increased to improve the accuracy of the simulation.

We measured the depth of experimentally observed indentation (250 μm) of the failed end-nut and modelled the corresponding stresses using FEA, as shown in Figure 8.7. The stress pattern shows a high tensile hoop stress accumulation at the outer edge of the end-nut, which can account for the radial crack. This stress is related to the indentation caused by large localised plastic strains located in the anvil support area. The bulge creates a large tensile hoop stress, in turn causing this area to rupture in the circumferential direction.

8.6 Optimisation and final design

8.6.1 Optimisation

Large plastic deformation (indentation) of the end nuts was found to be the main reason of the end-nut failure. The only possible solution is to increase the compression resistance of the end-

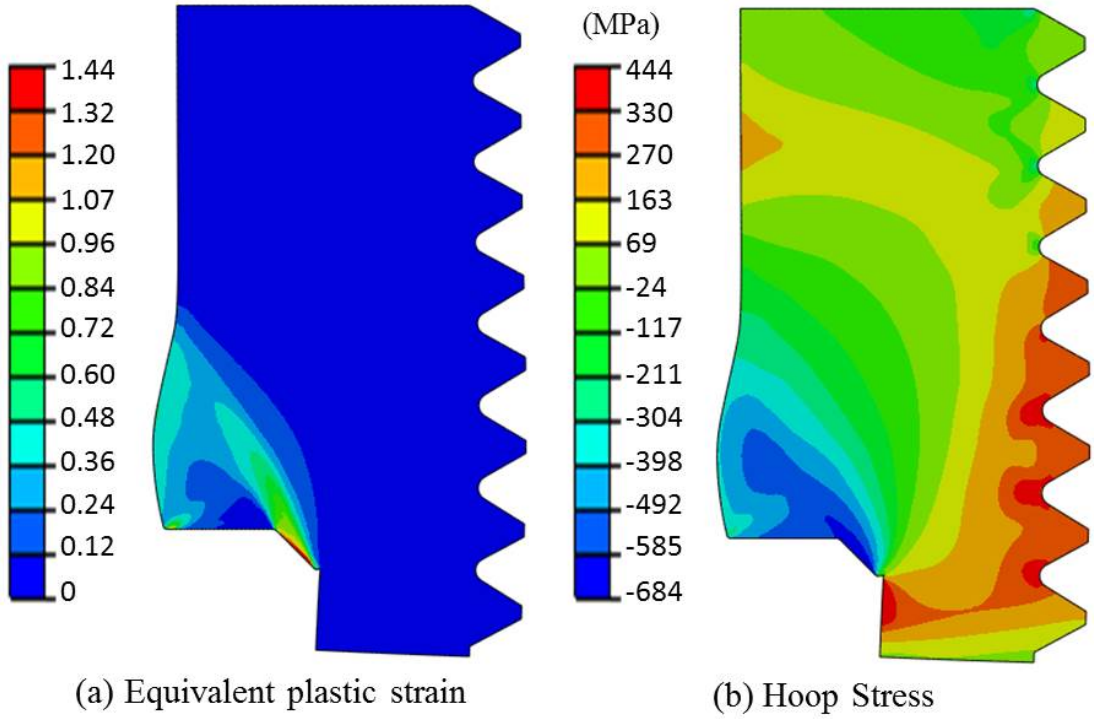

Figure 8.7: *(a) Plastic strain and (b) tensile hoop stress (max principle stress) distribution when the anvil table indented into the anvil support (the deformation modeled here is 250 μm which corresponds to the load of 2.7 kN).*

nut thus reducing its plastic deformation. Enlarging the contact area with the anvil is the most straightforward way to achieve this. A compression test was performed, as shown in Figure 8.8, with a 4 mm diameter dummy anvil made of steel and placed on a flat end-nut to test the failure point using the maximum available support area. This assembly was compressed directly with a load cell with which the actual compression force applied onto the anvil was recorded directly. It was found that the end-nut fractured diagonally under the load of 4.8 kN which is almost double the load achieved in the initial tests described above. There is no visible deformation observed before cleavage which indicates that the observed failure is of a brittle nature.

The compression test is simulated in FEA to investigate the deformation and stress pattern before failure as shown in Figure 8.9. The strain and stress contour demonstrated in Figure 8.10 confirms that little deformation is caused by the load of 4.8 kN near the failure point. The diagonal fracture (Figure 8.8) can be explained by the high shear stress and plastic strain accumulation in the diagonal direction across the end-nut. This is commonly called 'shear band' or 'strain localisation', which usually lead to intense damage and fracture on cylindrical parts subjected to excessive axial compression [124–128]. These destructive stresses and strains are

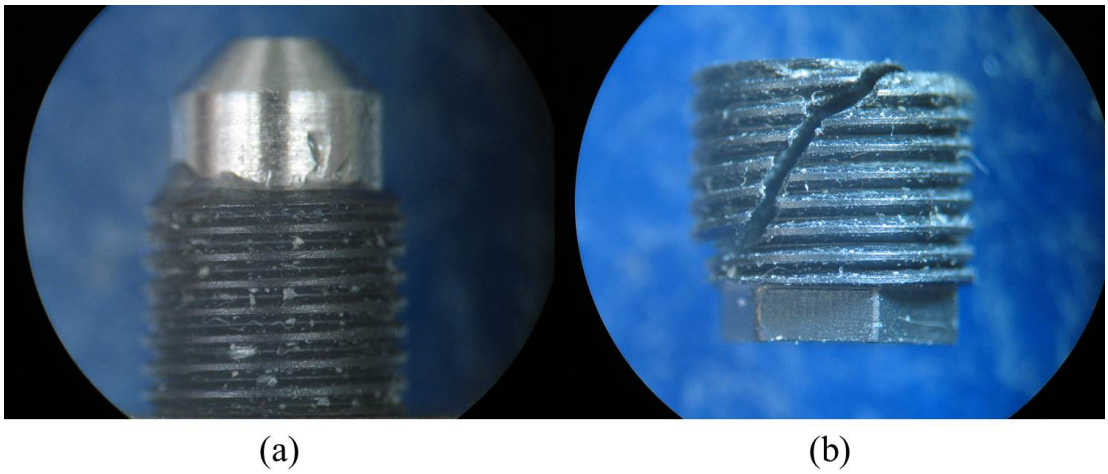

Figure 8.8: *(a) Before test, a dummy anvil was glued on the end-nut, (b) the failed end-nut after test.*

the main cause of the end-nut fracture. In contrast, the hoop stress in the end nut is far smaller than in the previous case of a smaller diameter (2.5 mm) anvil as large plastic strain is prevented. The failure mechanism of the larger diameter diamond anvil on the flat end-nut support is different to that observed in the initial design and it proves that enlarging the contact area is the way to improve the load capacity of the cell.

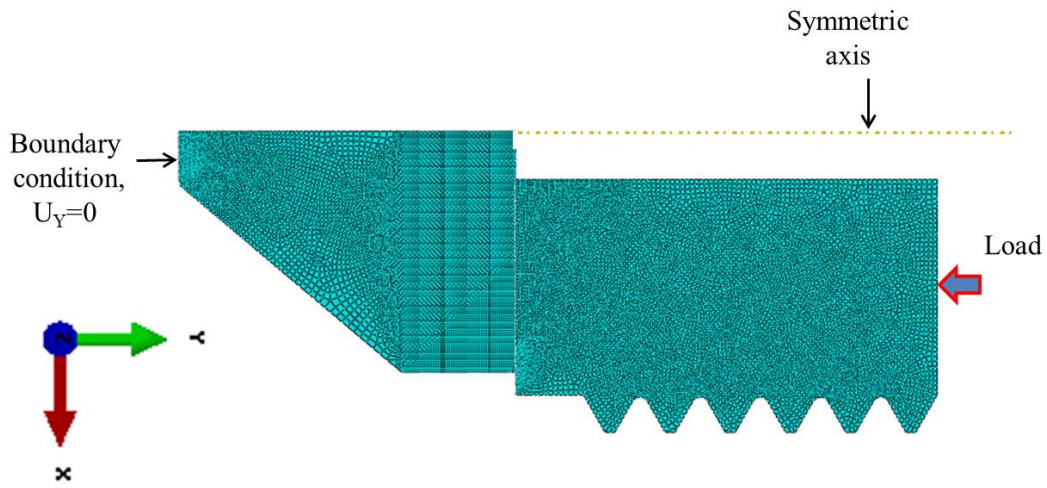

Figure 8.9: *FEA model for the compression test*

Even though the optimised end-nut can withstand 4.8 kN compression force, the same level of load might not be sustained by the assembled pressure cell. This is because there is also the thread on the cell body, which may weaken the cell in tension when it is clamped, and the

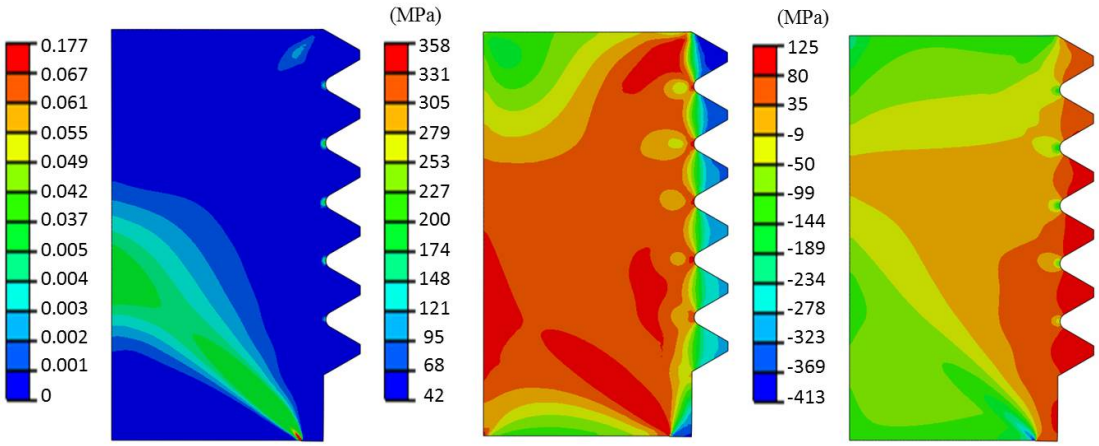

(a) Equivalent plastic strain (b) Maximum shear stress (c) Hoop stress

Figure 8.10: *FEA simulation of the final version end-nut subjected to 4.8 kN load.*

body of the cell takes the reaction force from the end-nuts. The simulation result presented in Figure 8.7 shows that the material is highly sensitive to the tensile stress tensor which could lead to the failure of the thread. To verify this, an FEA model focusing on the thread area was created as shown in Figure 8.11. The cell body, end-nut and the anvil all need to be included in this model to acquire the actual stress pattern when the pressure is clamped by the thread. Figure 8.12 demonstrates that when the cell is loaded at 4 kN and locked, the thread reaches the critical failure stress near the root area. The tensile stress value at the root of the thread starts to exceed the tensile strength of the material (330 MPa) and thus cracking is likely to occur in any turn of the thread. This indicates that the highest loading limit of the cell should be less than approximately 4 kN (as confirmed by the experimental testing described below).

8.6.2 Final design

Obviously, a large customer designed diamond is an ideal approach for the final design. However this approach will increase the cost significantly. Several other methods have also been investigated. A first idea is placing a hard washer under the 2.5 mm diamond, but this will create extra magnetic signal and risk Eddy current heating which are downsides. A more economical approach is using sapphire spherical anvils. However, the maximum allowable size of the spherical sapphire is limited to 4 mm diameter (half ball or full ball) due to the available space in the plastic cell. These small size of the spherical sapphire has been tested and found far too weak to be used.

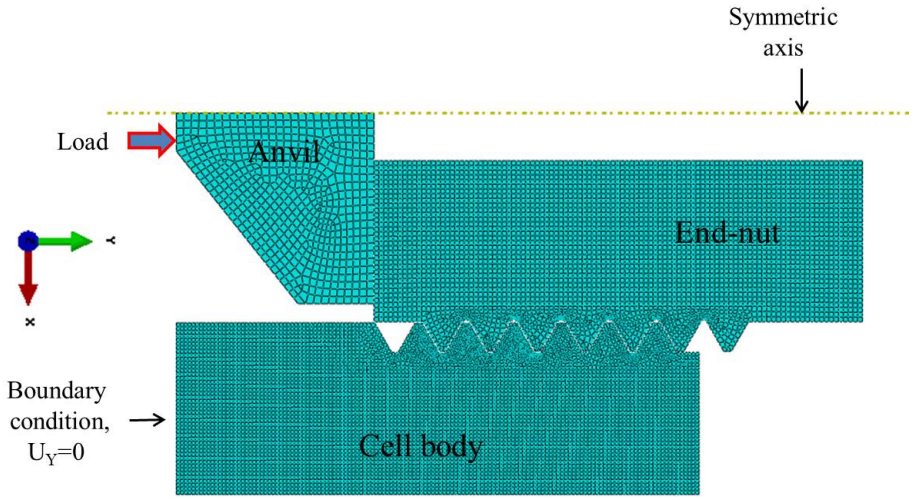

Figure 8.11: *FEA model for tensile testing on the thread*

The final design shown in Figure 8.13 introduces a pair of custom-designed diamonds. The diamond anvils have a 4 mm girdle size with an 800 μm culet. The conventional taper at the table of the diamond is rounded off to remove the sharp corners which could lead to stress concentrations on the end-nut. The girdle of the diamond is rounded as well. The length of the cell body is extended to 11 mm to provide space for taller anvils. In addition, the counter bore used to centre and fix the diamond anvil in the initial design was removed due to the limited space in the cell. This change means the anvils need to be glued to the end-nuts with epoxy (Stycast 1266). The central observation hole on the end-nut can be used to position the first anvil in the centre. An indented metal gasket is then glued on the the top of the first anvil. After that, the second anvil is glued on the other end-nut. Before the epoxy around the second anvil is cured, both end-nuts are screwed into the turnbuckle body until the diamonds are fully engaged into the indentations in the gasket. The cell is then left assembled for the epoxy to cure completely. The indentation on both sides of the gasket has been found to maintain the anvils alignment rather well.

8.7 Loading test of the final design

Experimental pressurization testing was performed on the final design for verification, using the cell, as shown in Figure 8.14. Both BeCu and composite gasket are tested with the final design. For BeCu gasket test, NaCl powder and ruby are loaded into the gasket, with NaCl as

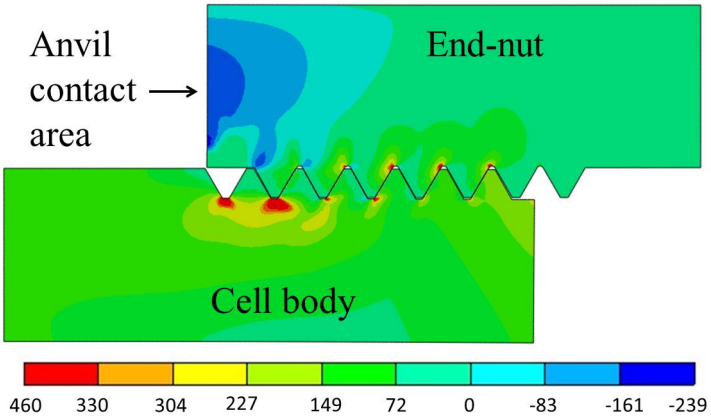

Figure 8.12: *Maximum principle stress distribution in the threaded connection between the body of the cell and an end-nuts under 4 kN load.*

the pressure medium. The cell managed to achieve pressures higher than 6 GPa with relatively low applied load (2.46 KN) as shown in Figure 8.15. At the highest pressure point (6.29 GPa), two ruby fluorescence peaks merged as a broad peak. Even though, the pressure can still be determined by the Raman spectrometer as illustrated. The pressure generation improved significantly as shown in the Table 8.2 because of the anvil gains enough support from the end nut. The pressurised cell was left for a couple of days and checked for possible pressure relaxation, with the pressure remaining stable. The cell was opened up and checked carefully in the critical areas, such as the thread and the anvil support, with no damage observed.

Load (N)	Attainable pressure (GPa)
980	1.5
1720	2.5
1970	3
2210	5.2
2460	6.3

Table 8.2: *Load and attainable pressure of final design in the testing with the BeCu gasket.*

The same cell was tested again with a composite gasket which was loaded with ruby, a piece of lead and pressure medium (mixture of NaCl and Daphene 7373) as shown in Figure 8.3. The load and attainable pressure is shown in Table 8.3. The cell was loaded to 3 kN initially and sample pressure reached 3 GPa. Then the cell was left overnight at room temperature and it was found that the sample pressure dropped to 2.3 GPa. After that, the cell was further loaded and the sample pressure was increased with the load more efficiently than in the initial design. At each pressure point shown in Figure 8.16, we have measured the superconducting transition

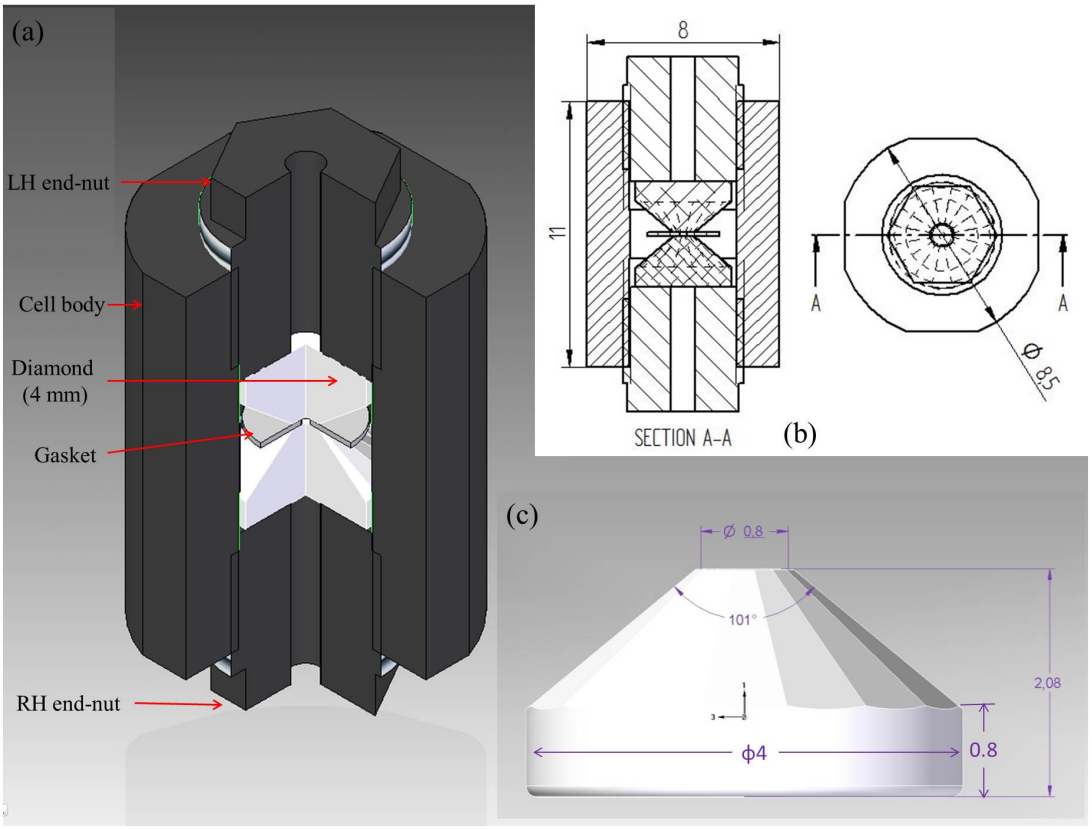

Figure 8.13: *(a) Quarter-section view of the final design of PTM-DAC. (b) Engineering drawing of the final design with key dimensions. (c) 4 mm custom-designed diamond, the culet is 800 μm and bevels up to 900 μm at 9°, girdle ground round with 0.10 mm radius.*

temperature T_c of Pb in the MPMS magnetometer and no pressure variation was observed. In these tests, the highest pressure reached in the cell was around 5.6 GPa under 3.45 kN load with no sign of failure (e.g. cleavage or radial fracture). While applying higher load is possible, the risk of damaging the cell substantially increases as indicated by the previously discussed FEA stress analysis of the thread, and thus this force was considered a safe upper load limit. At the highest pressure point (5.6 GPa), the cell was left for two days with no pressure loss observed. This gasket behaviour shows that pre-compression of the cell allows the epoxy resin in the gasket to flow out of the pressurised culet area. A denser diamond and Al_2O_3 powder remains packed in the culet area which makes the pressure generated more stable. The highest attainable pressure (5.6 GPa) in the composite gasket is close to the one achieved using BeCu gasket. However, this requires extra 1 kN of force, which shows once again that the composite gasket is harder than the conventional BeCu gasket. The pressure was released and the cell was disassembled for examination, from which both cell body and the end-nut were found to be

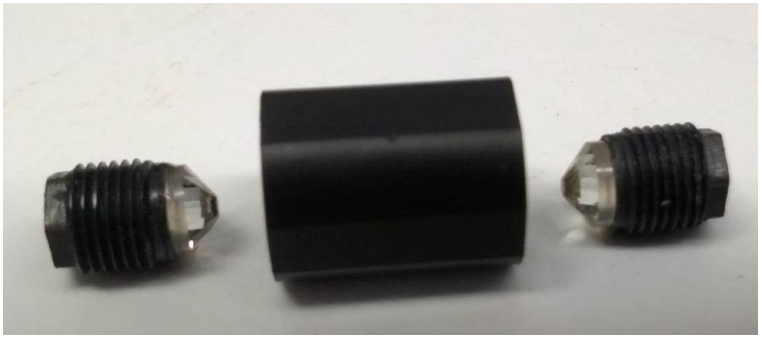

Figure 8.14: *The picture of disassemble of PTM-DAC (Final design).*

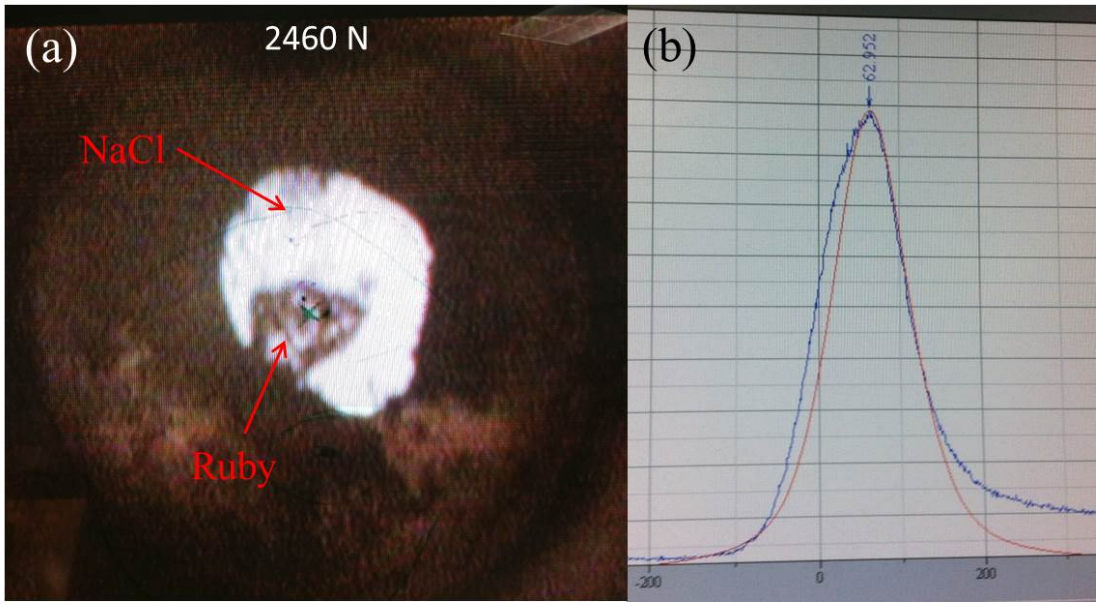

Figure 8.15: *(a) BeCu gasket with NaCl and Ruby under 2460 N compression load; (b) Snap shot of the pressure reading from Raman spectrometer, the peak shows that the pressure has reaches 62.95 Kbar (6.29 GPa)*

intact.

Alignment of the diamond anvils is the key for a successful pressurisation. The previous TM-DAC can maintain anvil alignment with the precise machining of the thread and an entering counter bore to aid diamond mounting. As there is no counter bore in the final PTM-DAC design, the diamonds are glued on the end-nut manually. Hence, the alignment of the two diamond anvils is still not perfect. It was found that the sample would usually flow out of the culet area and loose pressure (blow out) if too much sample was loaded. After a couple of tests, a sample hole smaller than 250 μm was found to be the optimal size to compensate for the misalignment.

Load (N)	Attainable pressure measured from the Ruby marker after clamping (GPa)
980	0.4
1480	1
2210	2
2500	2.4
3000	3
The cell is left overnight, sample pressure drop to 2.3GPa. Re-pressurisation	
2460	3.48
2800	4.16
3100	4.64
3450	5.58

Table 8.3: *Load and attainable pressure of the final design in the testing with the composite gasket.*

Noticeable permanent deformations as shown in Figure 8.17 was found when the cell was loaded to 5 GPa with the composite gasket after several cycles. Figure 8.17(a) shows that the anvil becomes inclined and (b) shows the hex head of the end-nut is deformed, which is most mainly caused by the anvil misalignment and material strength issue. As the cell still maintained pressure despite these deformations, they should not be considered as failures. Instead, it suggests a replacement schedule of the end-nut is needed. As the cost of plastic end-nut is low and can be mass-produced, this is an acceptable compromise.

8.8 Magnetic background of the pressure cell

In order to estimate the background of the assembled cell, it was loaded with Dy_2O_3, which is often used as a reference material for calibrating magnetic ac susceptometers since its χ' is frequency independent. The cell can be accommodated in a standard plastic straw used in MPMS magnetometer, as shown in Figure 8.18. The cell is initially assembled without the sample. The magnetic susceptibility of the empty cell was measured as a function of temperature using the MPMS at three frequencies (1, 744 and 1488 Hz). The sample was then loaded using the the procedure described above and the measurement was repeated.

Figure 8.19 shows that χ' magnetic ac susceptibility of the sample for the three different frequencies (χ'' was below the sensitivity of the MPMS for the loaded amount of Dy_2O_3). The data show that the signal is frequency independent as expected. The inset shows the background signal from the empty cell, from the cell with the sample and the difference, which is the sus-

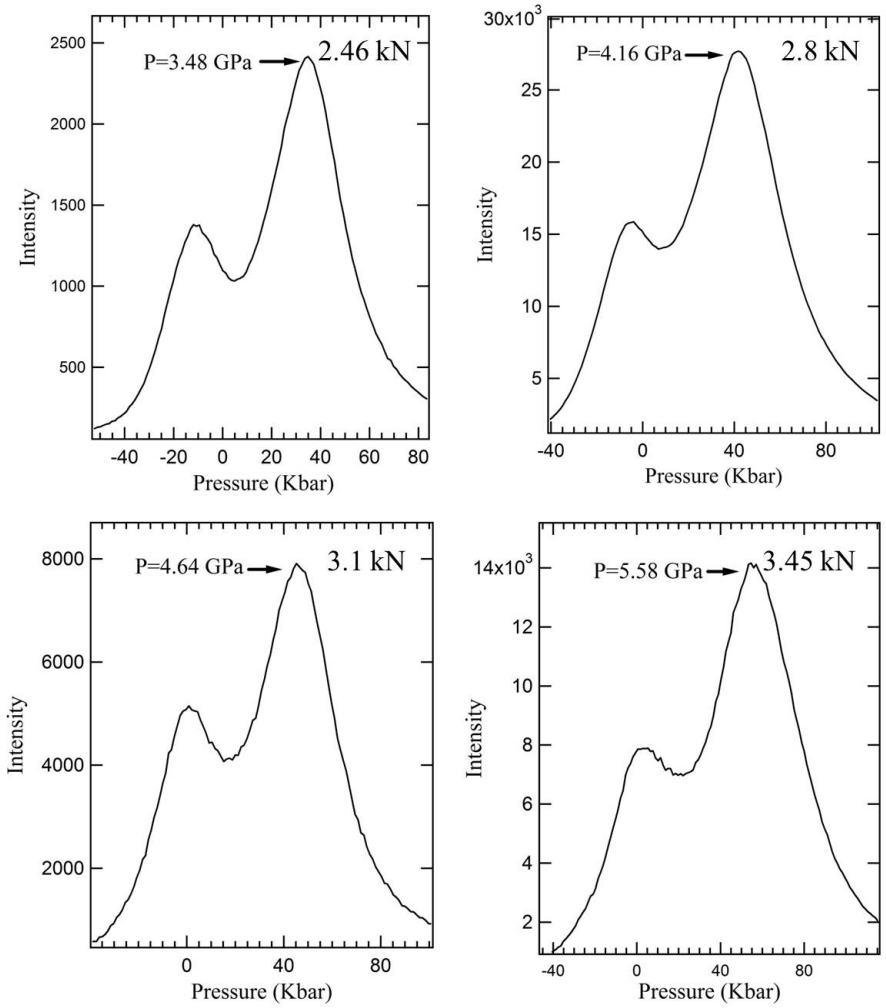

Figure 8.16: *The ruby fluorescence R_1 peak shift which is associated with pressure reading from Raman spectrometer at each load increment in Table 8.3*

ceptibility of the sample after correction for the background. The data in the inset are presented for the measurements conducted at 1 Hz, but are representative of the other two frequencies. The measurement shows that the background from the cell is smooth and featureless which makes it easy to extract the susceptibility of the sample. It also demonstrates feasibility of the measurements in the pressure cell.

8.9 Ac magnetic measurement of U_6Fe

The high pressure, ac magnetic measurement data of U_6Fe sample is demonstrated in this section to show the data quality of the PTM-DAC. Figure 8.20 shows the ac measurement of the

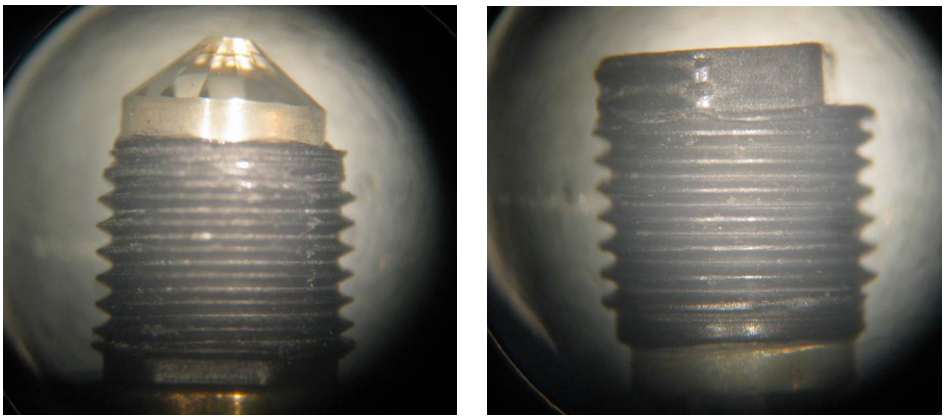

(a) the anvil become incline (b) Hex head deformation

Figure 8.17: *Unrecoverable deformation on the end nut appears after several loading cycles at 3.45 KN*

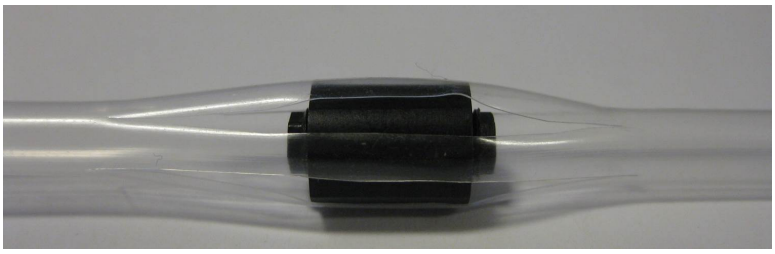

Figure 8.18: *The PTM-DAC can be loaded into a standard straw by expanding the slits. After that, the straw needs to be mounted on the sample rod of the MPMS magnetometer.*

U_6Fe at ambient pressure without the PTM-DAC. The T_C of this material is at 3.8 K and the material was found almost frequency independent. PTM-DAC was used to investigate the pressure dependence to the T_c as shown in Figure 8.21. In the experiment, the loaded cell was measured at two pressure points, 0.1 GPa and 3.4 GPa in the MPMS SQUID magnetometer. With applied 37 Hz ac field, the signal from the U_6Fe is legible even without cell background correction. The measurement result shows that the critical temperature of the material is clearly shift to lower temperature with increasing pressure. At 3.4 GPa pressure, the T_c is reduced to around 2.5 K from 3.8 K at ambient pressure.

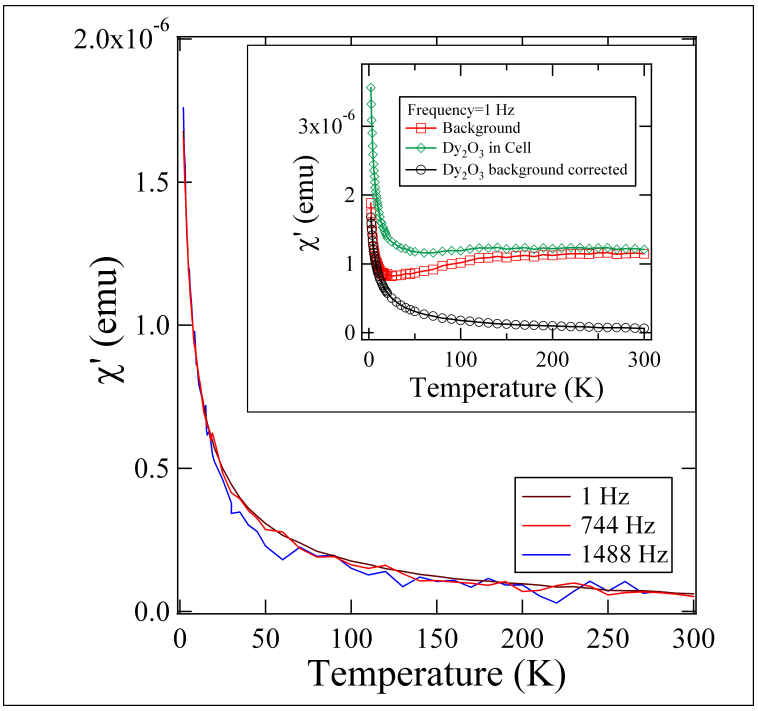

Figure 8.19: *$\chi'(T)$ of Dy_2O_3 loaded into the plastic DAC and measured at various frequencies at ambient pressure. The inset shows the characteristic background curve for the cell assembled without the sample.*

8.10 Future work

We assessed the mechanical and magnetic properties of several candidate composite materials for construction of non-metallic high-pressure cells. Finite element analysis models were constructed to evaluate stresses and deformation of various components of the pressure cell and to establish the modes of failure. These models were evaluated using experimental test data. It was found that in order to prevent failure of the cell a large area support for the anvil is required. The models were then used to optimise the design of the cell given the constraints imposed by the sample space available in MPMS. A pressure of 5.6 GPa was reached for a load of 3.45 kN, which we believe to be the highest to date for non-metallic pressure cells. The magnetic background of the cell was evaluated using Dy_2O_3 at several frequencies and no screening effect from the cell on the sample was observed. The high-pressure ac magnetic measurement data of U_6Fe demonstrated the high quality measurement signal can be retrieved from the PTM-DAC. Thus, this cell is expected to provide a new and useful method for the scientific community to study the magnetic susceptibility of materials through use of ac techniques under pressure in the commercial magnetometers.

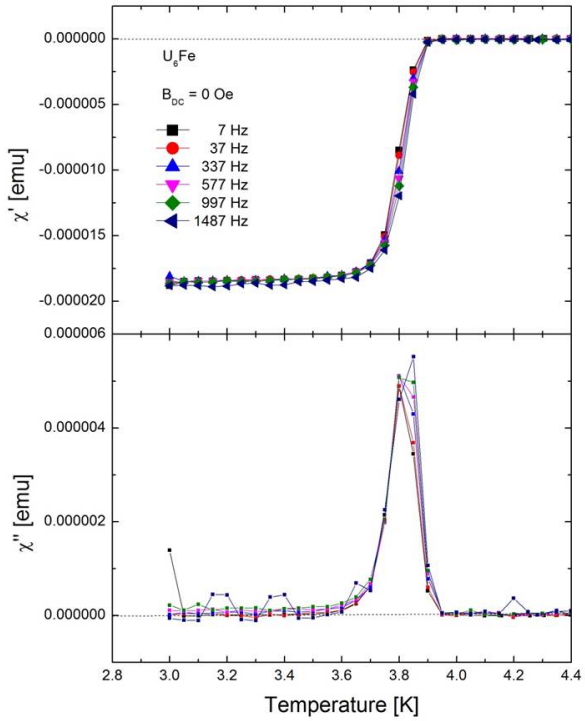

Figure 8.20: *χ'(T) and χ''(T) of superconductor U_6Fe at ambient pressure.*

There are two possible improvements that can be made in future. First, the strength of thread is the main weak point of the final design as shown in Figure 8.12. With the thread cutting machine process, the grain of the carbon fibre and peek would be inevitably disturbed and the strength would be compromised. One alternative is developing 3D printing technologies, which provide a way for improvement. 3D printing has been used to create a plastic prototype cell through a 3D printer available in campus as shown in Figure 8.22. The resolution of the current machine is obviously not high enough to produce a cell to be used. However, it shows a possible way to build a plastic cell through 3D printing when this technology is more mature to print strong plastic material such as Tecamax SRP or 90HMF40 with high accuracy.

Second, the alignment of the diamond anvils remains an issue as there is no alignment mechanism in the cell. Modifying the final design as shown in Figure 8.23 could be a solution. The cell body is drilled with a 4 mm diameter centre bore with high tolerance. The anvils can be centred by bore as the diameter of the anvil is 4 mm as well. The end nut is machined with a 4 mm diameter table to support the anvil and be centred by the bore too. In this way, the cell body needs to be extended extra 1 mm to provide enough space for the modification. The high centre tolerance of the diamond is the key for this mechanism to work.

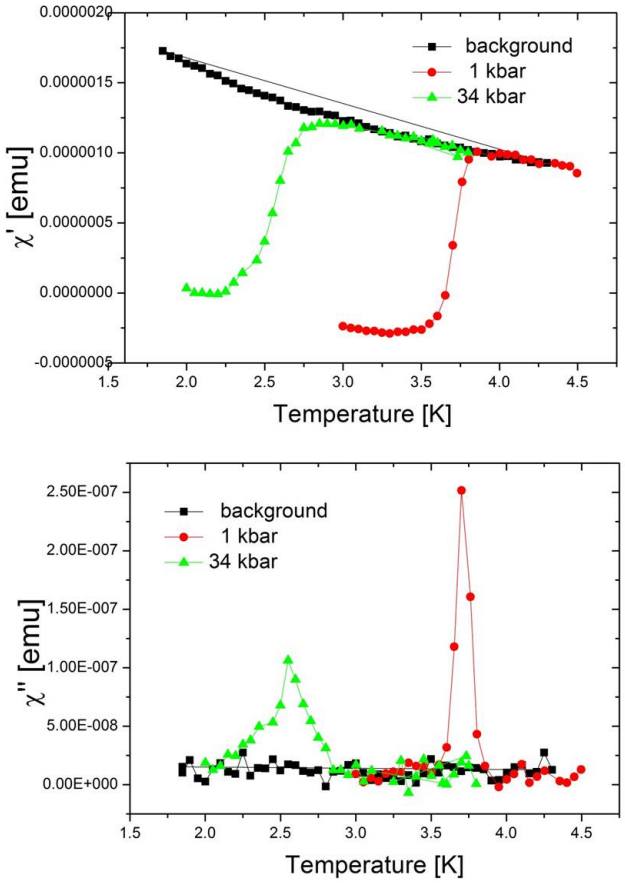

Figure 8.21: *χ'(T) and χ''(T) of superconductor U_6Fe at 0.1 GPa and 3.4 GPa pressure, the ac frequency is 37 Hz.*

For the current method of composite gasket preparation, liquid pressure media is difficult to use as liquid trend to leak during loading or pressurisation. The composite gasket is currently only able to contain Daphene 7373 and NaCl powder slurry as pressure medium to provide semi-hydrostatic pressure environment. How to improve the gasket is another major work in future.

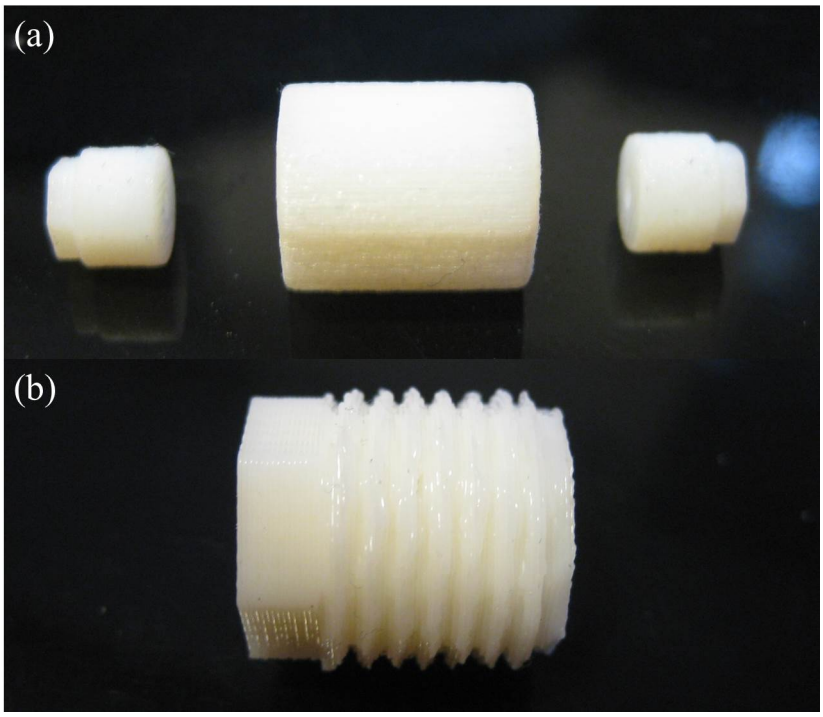

Figure 8.22: *(a) Prototype of 3D print with scale 1:1; (b) 1:2 scale end-nut print.*

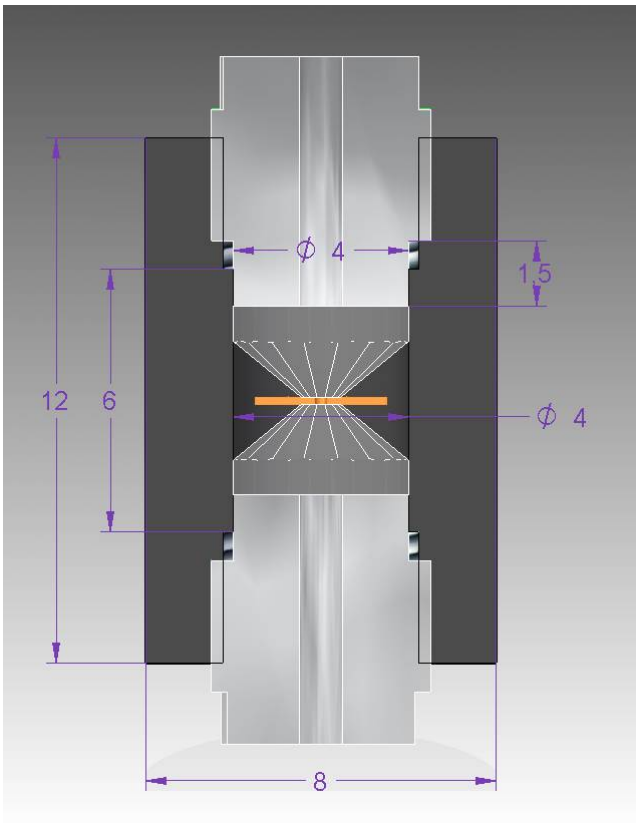

Figure 8.23: *An improved design concept of PTM-DAC.*

Chapter 9
Turnbuckle Sapphire Anvil Cell with Spherical Sapphire Anvils

This chapter presents a turnbuckle sapphire anvil cell for small angle neutron scattering. Commercial spherical sapphires were used in the cell as they are cost effectiveness and able to contain more sample volume. Two design concepts were tested experimentally and the second version was able to generate and maintain sample pressure above 6 GPa with a sample volume 6×10^{-2} mm^3 which is 6 times to conventional DAC. Failure analysis was performed on the sapphire anvil to gain a better understanding of the failure mechanism of spherical sapphire anvil. The cell had been used in measuring the crystal structure of signle crystal niobium at 1.6 GPa through SANS technique. The cell is less than 16 mm in length and 14 mm in diameter, it is the smallest sapphire anvil cell to date. The miniature feature allows it to fit into most cryostat of modern scientific instrument without difficulties.

9.1 Design motivation

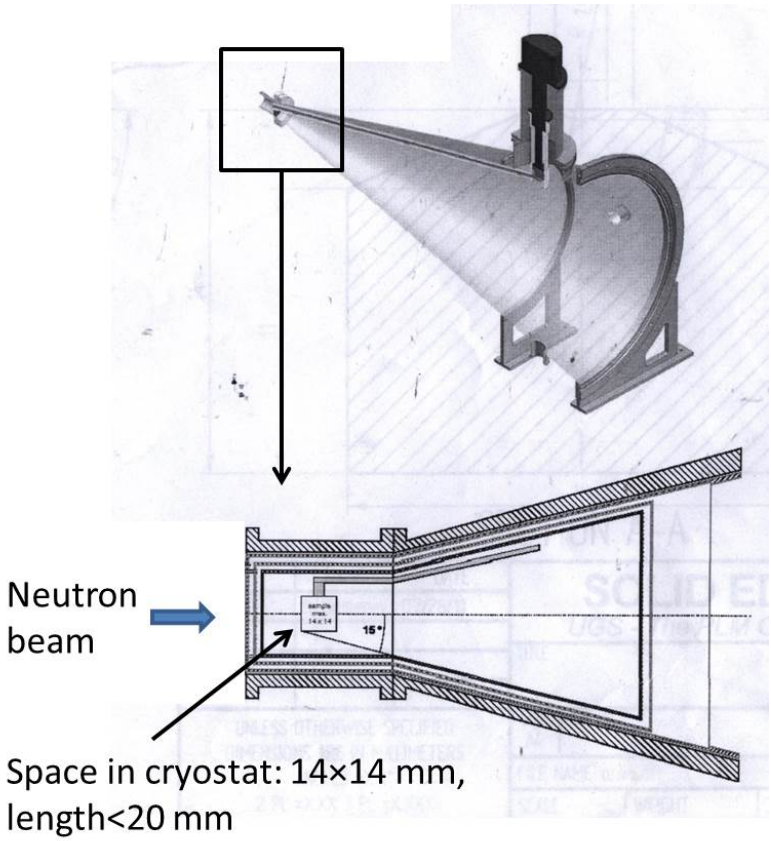

Figure 9.1: *SANS Diffractometer in HZB.*

The cell presented in this chapter is initially designed for small angle neutron scattering in the Extreme Environment Diffractometer (EXED) at Helmholtz-Zentrum Berlin (HZB), Germany. The main objective is to develop a high pressure instrument (pressure capability $>$ 3 GPa) to be used in the diffractometer as shown in Figure 9.1 without any modification of the device. The cell was required to function at low temperature and high magnetic field environment. The allowable space of the cryostat is the main restriction for incorporating high pressure conventional sapphire anvil cell and existing SANS cell reviewed in Chapter 2 are apparently oversized. Though DAC can be used as it can be made as miniature size. This type of cell is least favorable for neutron scattering because the limited sample volume results in excessive long counting time in the scattering. In last section, spherical sapphire anvils had been tried for the non-metallic cell, which inspired a possible solution to build an enlarged version of the turnbuckle cell with spherical sapphire anvil which allows more sample to be pressurized. To distinguish this cell from previous turnbuckle cells in this document, the cell presented in this

chapter is coded as T-SAC (turnbuckle sapphire anvil cell).

9.2 Design

In last chapter, 4 mm diameter spherical sapphire had been found difficult to be used as they were cracked easily. Two larger size of spherical sapphire anvils, 5 mm and 8 mm diameter sapphires (as shown in Figure 9.2 and Figure 9.3), were tried in this project respectively. As these two cells are the enlarged version of turnbuckle cell from previous design, the working mechanism of these cells are the same. The anvils are backing by two counter-thread end nuts. The end nuts are identical apart from having the external M10×0.5 threads cut in opposite direction, such as one end nut with left-hand external thread, the other one with right-hand thread. Correspondingly, left-hand internal thread on one side of the cell body and right-hand thread on the other side. In this setting, the sample pressure is generated by compressing two end nuts and locked by turning the cell body.

9.2.1 First design concepts

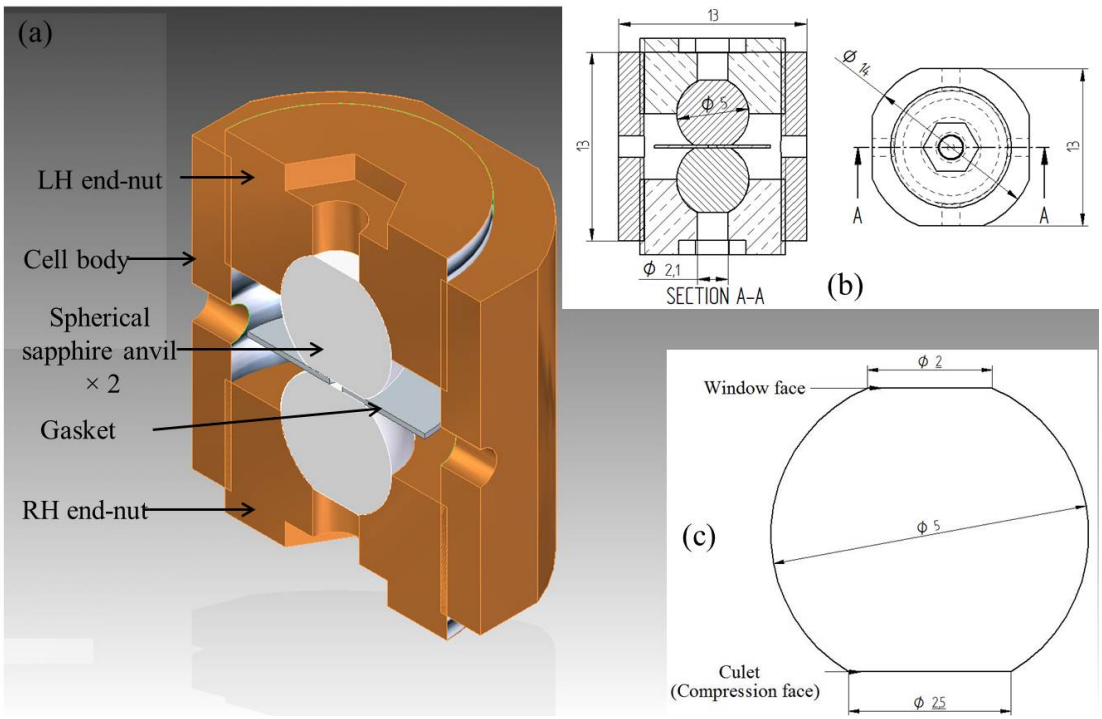

Figure 9.2: *(a) Section view of the first design concept of T-SAC; (b) CAD drawing with key dimensions; (c) The dimension of the spherical anvil.*

5 mm sapphire balls were used in the first concept as the overall dimension of the T-SAC can be minimal (as shown in Figure 9.2), which can be fit into the diffractometer easily. The central hole of the turnbuckle design is not only allow optical observation on the sample but also provide ports for the neutron beam. The spherical sapphire needs to be lapped with two parallel surfaces to be an anvil, one is the culet (pressurized surface) the other is for optical observation. Self-aligned feature is an advantage of the spherical anvil. One anvil is glued into the spherical support with approximate alignment, the other anvil is then inserted and culets were brought into contact. This will rotate the second anvil and the culets face will be self-aligned. The design drawing with key dimensions is shown in Figure 9.2, the key dimension of the cell body is 13×13×13 mm and the overall length of the assemble cell is less than 16 mm.

9.2.2 Second design concept

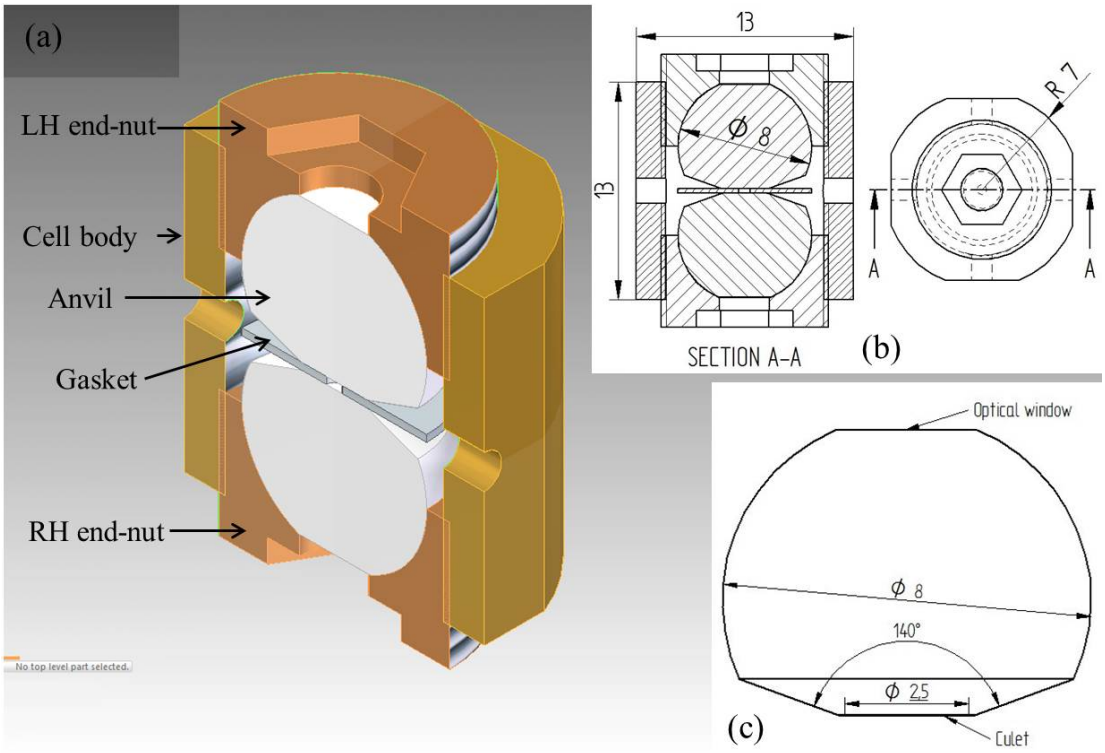

Figure 9.3: *(a) Section view of the second design concept of T-SAC; (b)CAD drawing with key dimensions; (c) The dimension of the spherical anvil.*

Larger size of anvil (8 mm diameter) is used in the second version of the T-SAC as show in Figure 9.3. In order to increase the anvil size without compromising the compactness, 8mm diameter spherical sapphire with 140° bevel angle is used in the second design. The overall

height of the anvil is around 6 mm and the culet can be polish to 2–3 mm diameter based on required sample volume. A parallel face is polished at the back for optical observation and incoming neutron beam. The length of the end-nut need to slightly increase with 0.5 mm, the diameter of sphere cutting is also needs to be increased to 8mm correspondingly to accommodate the anvil. As a result, the overall length of the cell is slightly longer than the first design. The optical hole on the end-nut is increased to 3 mm to provide a more transparent scattering angle.

9.2.3 Bracket

Similar to the TM-DAC, an enlarge version of a bracket and two supports are needed to apply load on the cell as shown in Figure 9.4. The pressurisation of the cell requires a hydraulic press. In addition, a load cell needs to be placed under the bracket to record the load. The operation of the cell is identical to the TM-DAC which has been described in Chapter 2.

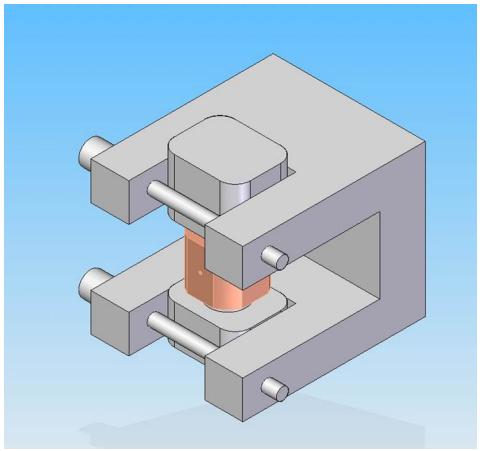

Figure 9.4: *Bracket for applying load on the T-SAC.*

9.3 FEA stress analysis

Finite element analysis is used to verify the design initially. The thread area and the anvil support area on the end-nut were firstly examined in FEA based on previous turnbuckle cell experience. The fully harden BeCu alloy (BERYLCO 25 from NGK [15]) was used to fabricate the entire cell as its properties are stable at low temperature and non-magnetic. Strain hardening effect was modeled in the FEA to obtain a better simulation result in FEA. This section start

with the followed descripton of the material behaviour.

9.3.1 Mechanical properties of BeCu alloy and sapphire

Diameter (mm)	Tensile strength S_{ut} (MPa)	Yield strength 0.2 % S_y (MPa)	Elongation (%)	Hardness (HV)
$\phi \leq 25$	1300-1500	1150-1400	1	390-440
$\phi > 25$	1200-1500	1050-1400	2	380-430

Table 9.1: *Mechanical properties of fully hardened BERYLCO 25 rods (Grade HT, 2hrs at 370°C) [15], E=130 GPa, ν=0.3.*

As shown in Table 9.1, the fully harden BERYLCO 25 rods are very brittle, The spec with diameter less than 25 mm would break at 1% elongation in tensile test. While the one with diameter larger than 25mm is with better plasticity, but only withstands 2% elongation. Using the lower bound of the strength value and the elongation percentages in Table 9.1, the stress-strain idealization of these two spec of BERYLCO 25 are plotted in Figure 9.5. It is clear that the first spec ($\phi \leq 25$) is hardly deformed plastically.

The cell was made out of the first spec of the fully harden BERYLCO 25, therefore the maximum principle stress needs to be examined in FEA simulation due to its brittleness feature. The maximum normal-stress theory is used as failure criterion, which states that failure would occur when the normal stress in the specimen reaches its normal tensile strength.

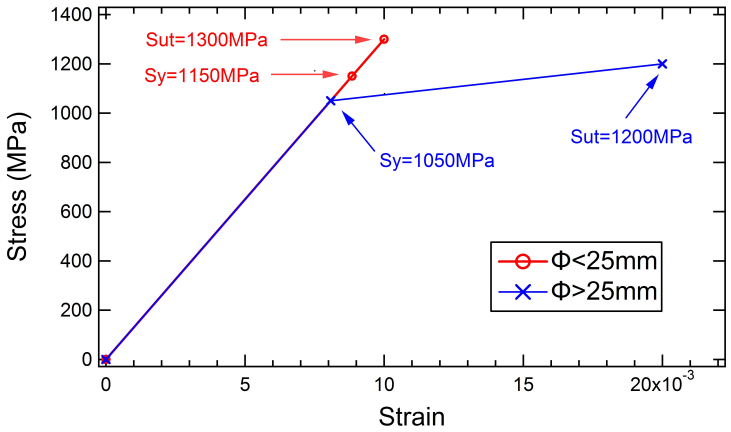

Figure 9.5: *Linear relation of stress and strain based on the mechanical properties of BeCu alloy shown in Table 9.1*

As described in Chapter 4, the mechanical properties of sapphire varies with its crystallographic direction because of the crystal structure. However, whether the actual anvil strength relate to

one particular crystal direction is still controversy. In our case, precisely controlling the crystal axis of the culet face in the lapping process is difficult. This article would not investigate this crystallographic strength problem of sapphire and all the sapphires in use are random-oriented. The sapphire is defined with linear isotropic characteristic, E=494 GPa and υ=0.3. The measured tensile strength of sapphire distributes between 275 to 400 MPa [103], the lower bound of tensile strength (S_{ut} =275 MPa) is considered the failure point of the sapphire anvil. However, the maximum normal-stress theory was found not applicable to explain the failure of the sapphire anvil, a full detail analysis would be introduced in the last part of this Chapter.

9.3.2 FEA model

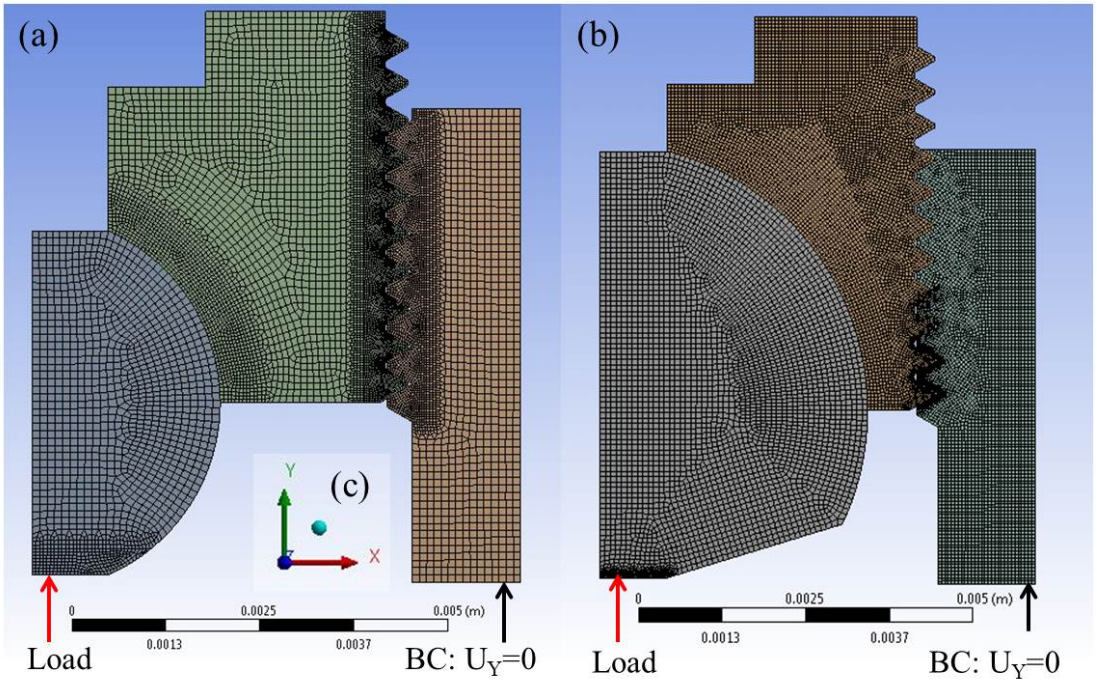

Figure 9.6: *FEA model of (a) first design concept and (b) second design concept; (c) the direction of the coordination in FEA model.*

To assess the strength of the structure of both designs, two similar axisymmetric models are created in ANSYS workbench [114] as shown in Figure 9.6. These models are suitable to simulate the cell at pressure clamped stage when the threads are engage and take entire load. The only boundary condition in these models is located at the section of the cell body (depicted in the Figure 9.6), where the vertical movement is constrained. A remote force is applied on the culet (compression face) of the spherical sapphire, which represents the reaction force from the

compressed sample and gasket. The mesh density of following interested areas, the sapphire contact region on the end-nut and the threaded region, are increased as demonstrated.

9.3.3 Stress analysis

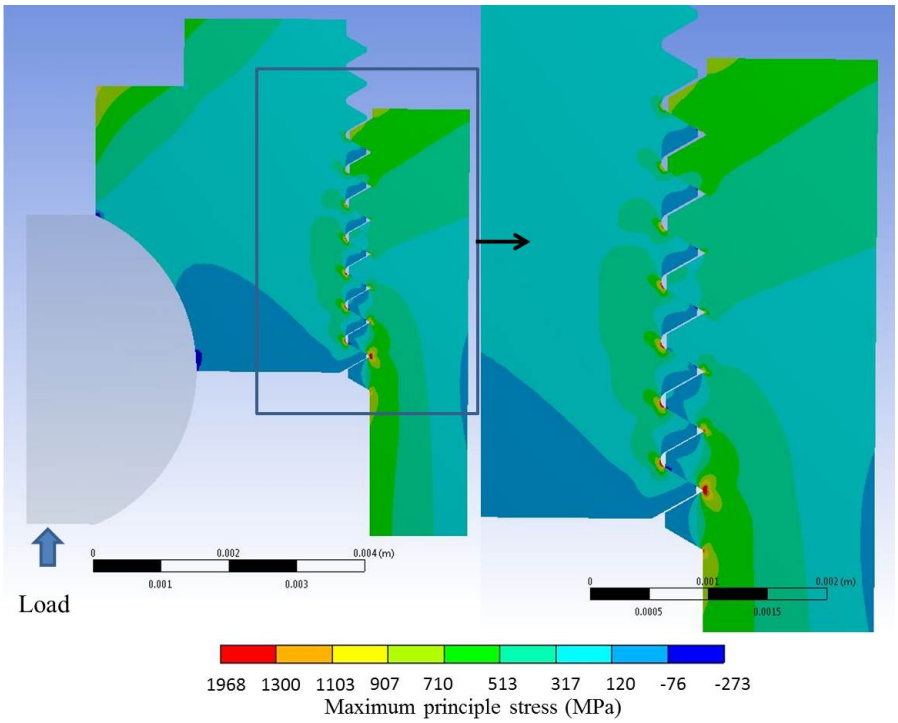

Figure 9.7: *Maximum principle stress distribution of the first design when subjected to 20 kN load; The areas with red colour is with tensile stress higher than 1300 MPa, where could be the origin of cracking failure.*

The maximum normal-stress theory are use as failure criterion in these brittle alloy and the area with highest tensile stress is the most concerned area. The simulation results shown in Figure 9.7 and Figure 9.8 demonstrates that 20 kN load can be the critical load of the thread because there are high tensile stress concentrate on the few turns of the threaded profile. The red areas in the figures have tensile stress value above 1300 MPa which is the material strength of the BERYLCO 25. The probability of cracking in these area is very high.

FEA result in Figure 9.8 shows that the strength of the thread is not sensitive to the profile of the anvil, because the maximum principle stress pattern of the second design under 20 kN load is almost identical with the first design. Based on the simulation result, the cell should not load higher than 20 kN to avoid failure. This load had been proved enable to generate sample pressure higher than 5 GPa based on the testing data of the existing spherical sapphire anvil

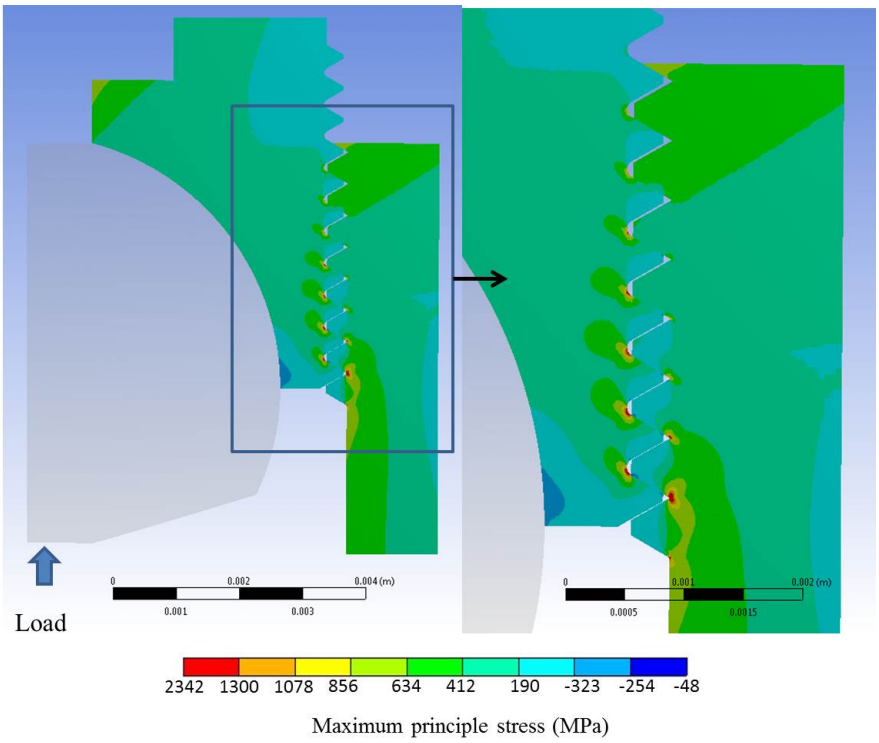

Figure 9.8: *Maximum principle stress distribution of the second design when subjected to 20 kN load.*

cell [45].

9.4 Manufacturing

This section focus on introducing the shaping process of the anvil from the standard sapphire ball. The lapping process can be carried out in the DIAMANTE polisher shown in Figure 9.9. The sapphire ball is mounted on the swing arm and rub on the spinning disk. Slurry which contains diamond powder was dropped on the disk to improve the lapping quality. The lapping process on the small size sapphire in the first design only takes less than 5 minutes. Because there is a 20° anvil bevel on the anvil of the second design, more sapphire material needed to be removed and the preparation time can be much longer. To form the bevel, modification was made on the original polisher. An motor was installed on the arm to rotate the sapphire, which allows the bevel can be lapped. A secondary manual polishing is needed after the lapping process. Because the surface finish after lapping was not satisfactory and scratches are visible on the culet as shown in Figure 9.10. These scratches could compromise the sapphire strength

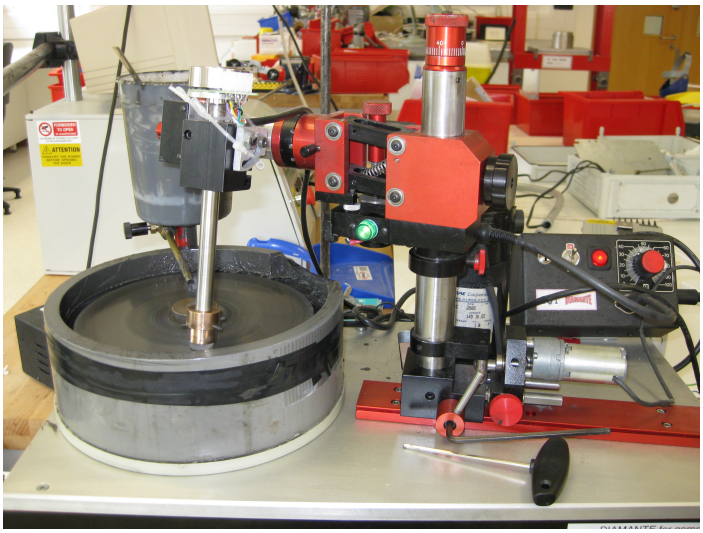

Figure 9.9: *DIMANTE polisher*

significantly as the culet is subjected with complex stress condition during pressurisation. The surface finish on the culet can be improved to a better grade by rubbing the culet of the anvil on a soft mat which contains 1 μm grain diamond powder.

9.5 Loading test

To assess the performance of both designs, prototypes were manufactured for pressurisation testing as shown in Figure 9.11. Soft metal gaskets were used in these tests, such as copper or unhardened BeCu. Harder gasket material was found to cause early anvil failure frequently. This phenomenon is in consistence with the existing result of the sapphire anvil cell [45, 47–50]. High strength gasket can induce shear stress on the culet, which usualy lead to surface damages (e.g. crack, scratches and chippings). All the gasket were indented before pressursation (initial thickness less than 300 μm). The indent gaskets were drilled with a central hole around 0.6 mm diameter to accommodate NaCl powder pressure medium and ruby marker. With these parameters, the initial sample volume is more than 0.06 mm^3 which is 6 times to the sample volume of the conventional DAC. A load cell was placed at the bottom of the cell to record the load applied on to the cell.

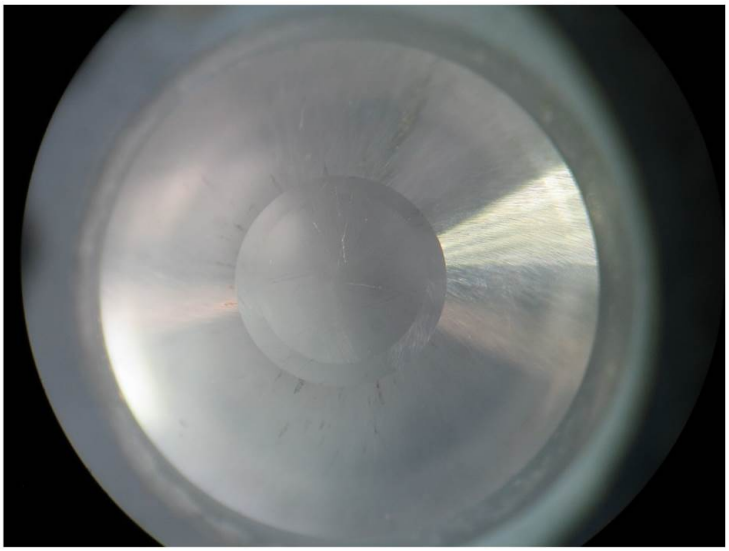

Figure 9.10: *The surface finished of the lapping area by the DIAMENTA polisher.*

9.5.1 Loading test of the first design

The first design was testing with both soften BeCu and copper gasket. The culet of the spherical anvils were polished to 2∼2.3 mm diameters. The experimental results of both cases are not satisfactory as the sapphire anvil failed earlier before the maximum allowable load (20 kN) of the cell. In the test with BeCu gasket, the highest attainable pressure was close to 3 GPa with 11 kN load. Further pressurisation resulted in the anvil cracking catastrophically as demonstrated in Figure 9.12.

In the test with copper gasket, the anvils were failed at lower load (8.61 kN) in the test as shown in Figure 9.13. The highest attainable pressure is 2.5 GPa with 7.83 kN load. Due to the lower strength of the gasket, the final thickness of the copper gasket is thinner and the final shape of sample hole was distorted significantly.

9.5.2 Loading test of the second design

For the testing of second design, the culet of the anvil was polished to around 2.5 mm diameter. Indented cooper gasket with 220 μm initial thickness and 0.6 mm diameter sample hole was used. As shown in Figure 9.14, the pressure performance of the second design was much better than the first design. The cell was tested close to the maximal allowable load of the cell and no anvil failure appear. The highest accessible pressure was 6.4 GPa with 19.6 kN

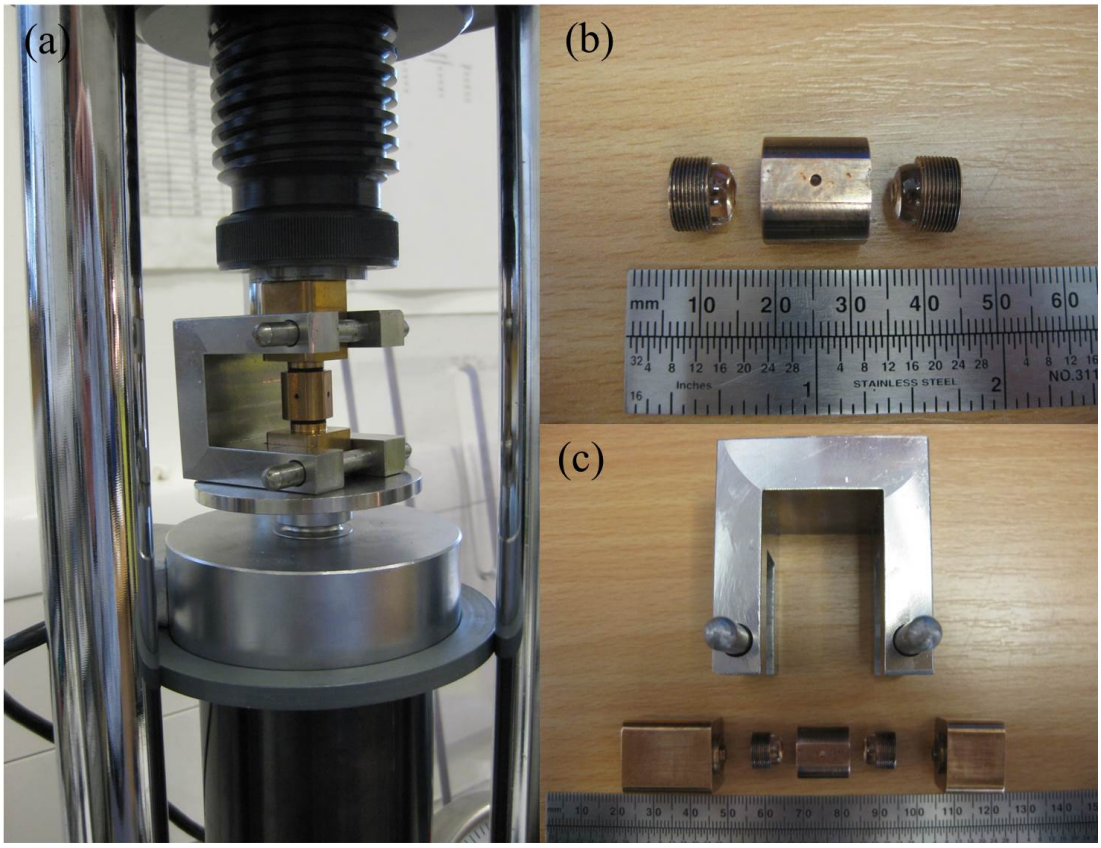

Figure 9.11: *(a) Figure of the cell in a loading test, a load cell is placed beneath the bracket to record the compressive force from the press; The prototype of the second design; (a) key parts of the cell (second design); (c) All the disassemble parts including the bracket.*

load. Figure 9.14 shows the deformation of the sample hole with increasing pressure. The sample hole start to expand and distort at 1.4 GPa, but the 2.5 mm compression surface manage to hold the sample pressure up to 6.4 GPa. The final gasket thickness was between 40$\sim$ 60 μm. The pressurisation test was not proceed any further as the risk of thread failure becomes higher. Nonetheless, the attainable pressure of the second design meet the requirements for high-pressure SANS experiment.

When the pressure was released, an unexpected surface damage occurred as shown in Figure 9.15. This kind of surface damage had been reported by Eremet [17] on diamond anvil which usually occurred at the pressure release stage after high pressure experiment with pressure above 100 GPa. Eremet believed that the surface crack at unloading stage is mainly due to the gasket becomes very thin and nearly flat during the increase of pressure. As the anvil culet subjects to cupping deformation at high pressure, when the load is decreased the edge of

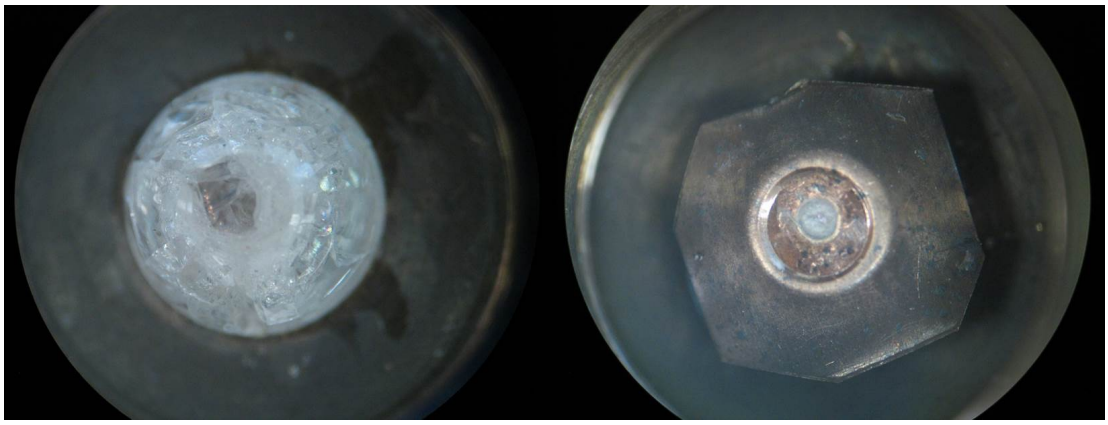

Figure 9.12: *Loading test with BeCu gasket which was pre-indented 200 μm thick (first design). The highest attainable pressure was 2.9 GPa with 11.08 kN load. The anvil broke at 12.33 kN load and the final gasket thickness is around 150 μm.*

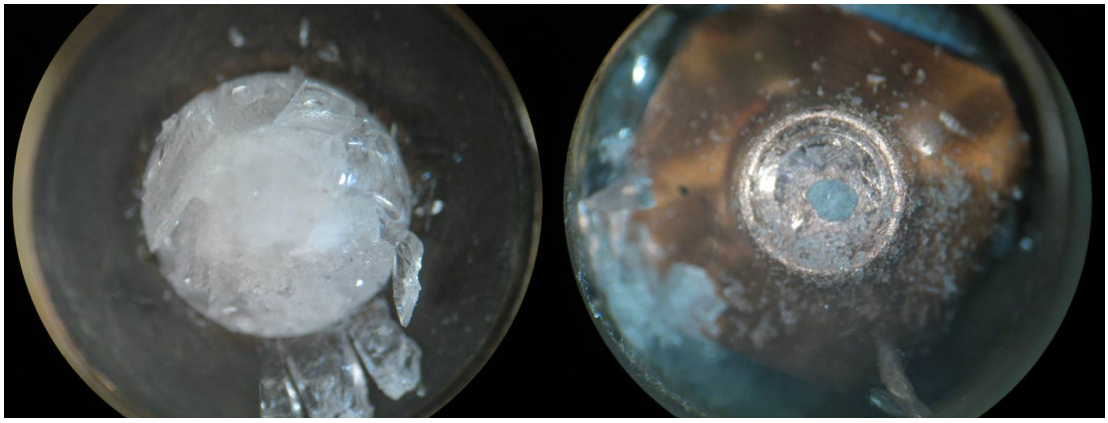

Figure 9.13: *Loading test with copper gasket which was pre-indented to 300 μm thick (first design). The highest attainable pressure was 2.5 GPa with 7.83 kN load. The anvil broke at 8.61 kN load and the final gasket thickness is between 100–112 μm.*

the contact surface is clear first. However, the gasket thickness is irreversible, the remaining contact surface become less than the working face which is resulting in tensile stress appear at the culet face. In our case, the final thickness of the copper gasket is only $40 \sim 60\ \mu m$, which could lead to similar stress condition. This damage shows that the anvil might needs to be replaced regularly after every successful high pressure experiment.

9.5.3 Discussion

This failure mode of the T-SAC is clearly different to the previous turnbuckle cells (TM-3He-DAC in Chapter 7 and PTM-DAC in Chapter 8). The anvils are the most important parts in

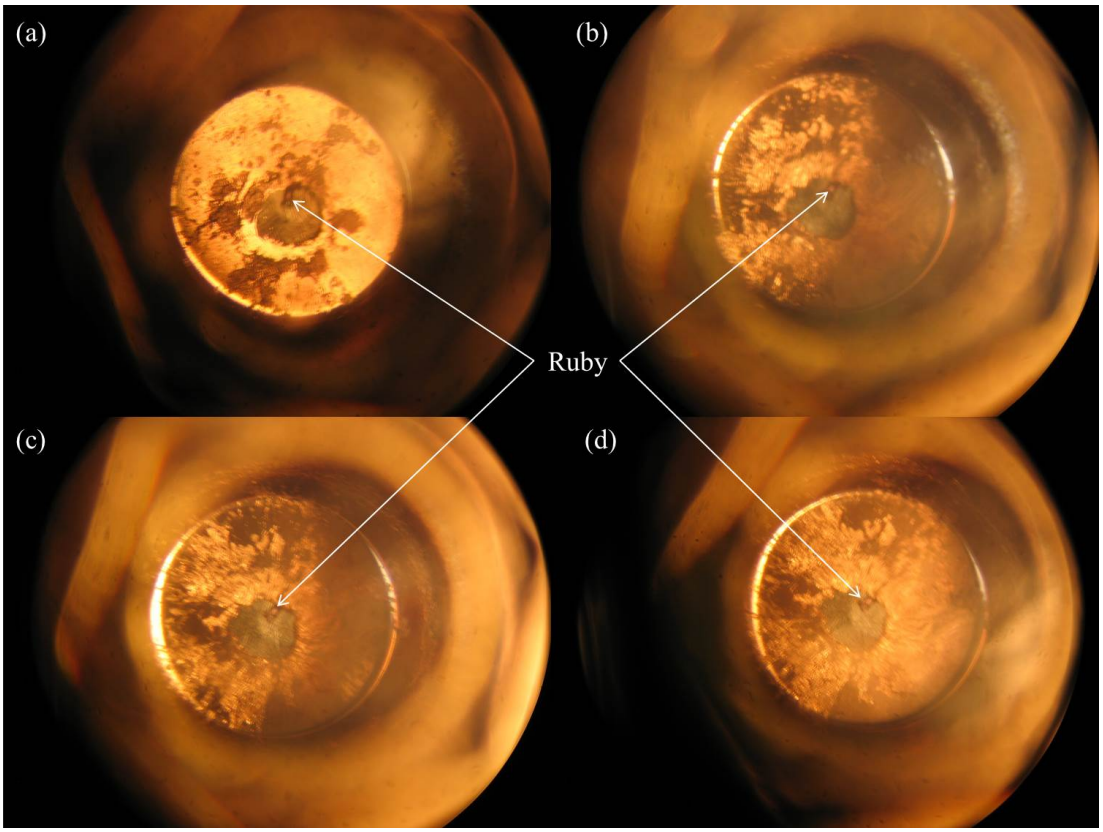

Figure 9.14: *Loading test of the second design with a copper gasket which was pre-indented to 220 μm thick; the final thickness varies from 60–80 μm; (a) 1.4 GPa with 9.84 kN load; (b) 4.2 GPa with 13.58 kN load; (c) 5.8 GPa with 17.33 kN load; (d) 6.4 GPa with 19.6 kN load.*

the designs as the tests show that they trend to fail easily. Since sapphire is much weaker than diamond, the shape of the sapphire anvil plays an important role in a successful pressurisation. The first concept was disappointing as the anvils were failed catastrophically before reaching a desired pressure. On the other hand, the second concept can generate and sustain higher sample pressure with the a load close to the maximum loading limit of the cell body. It is clear that the larger anvil is much more stronger for actual application and the final design should be settle on the second design concept. However, the probability of surface damage on the culet at the pressure releasing stage is difficult to reduce in this designing process. Nonetheless, the final design of T-SAC is settled on the second concept because the replacement of anvils is affordable with the cost effective feature of the commercial sapphire ball.

Massive support principle can explain the early anvil failure in the first design. The 5 mm diameter sapphire ball didn't provide enough massive support to the 2 mm cule which subjected

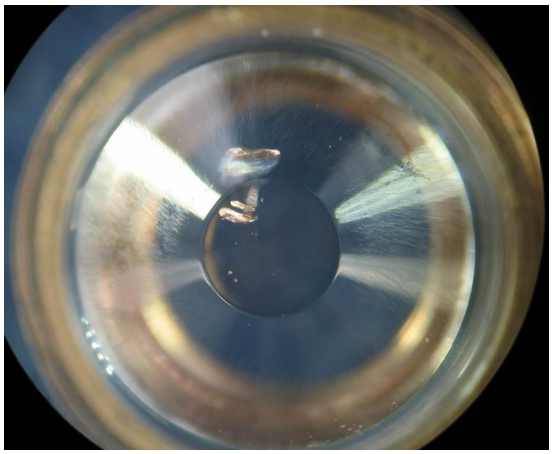

Figure 9.15: *Surface damage on the culet which occurred at the pressure release stage.*

to complex stresses condition. As a result, the anvil cannot withstand load higher than 8.61 kN. On the other hand, the anvils of second design survived with 19.6 kN load because its culet was surrounded by more sapphire material which enhanced the strength of the anvil. The stress pattern of the anvils under the final load is presented in next section to illustrate the effect of massive support.

9.6 Stresses analysis on anvils

9.6.1 FEA models

Despite the stresses pattern of the anvil can be retrieved from the FEA models shown in Figure 9.6, the shear stress analysis is not correct as the gasket was simplified by a direct load. The induced shear stress caused by gasket flowing did not exist in that model. Since shear stress is an important stress tensor which can lead to anvil failure [17, 46, 59]. In this section, the FEA models are mortified to include a gasket to obtain a better shear stress pattern. However, as gasket subjected to larger deformation and the simulation is highly non-linear, which usually creates convergence issue in the implicit solver in static structural analysis. To overcome this issue and reduce the computation time, the FEA models in this section are created in ABAQUS/CAE and solved by its explicit solver.

Two FEA models are created separately as shown in Figure 9.16 to analysis the stresses on the anvil when the final load was applied. Model 1 is based on the configuration in experimental testing in Figure 9.13 and Model 2 is based on Figure 9.14. Because copper gaskets were

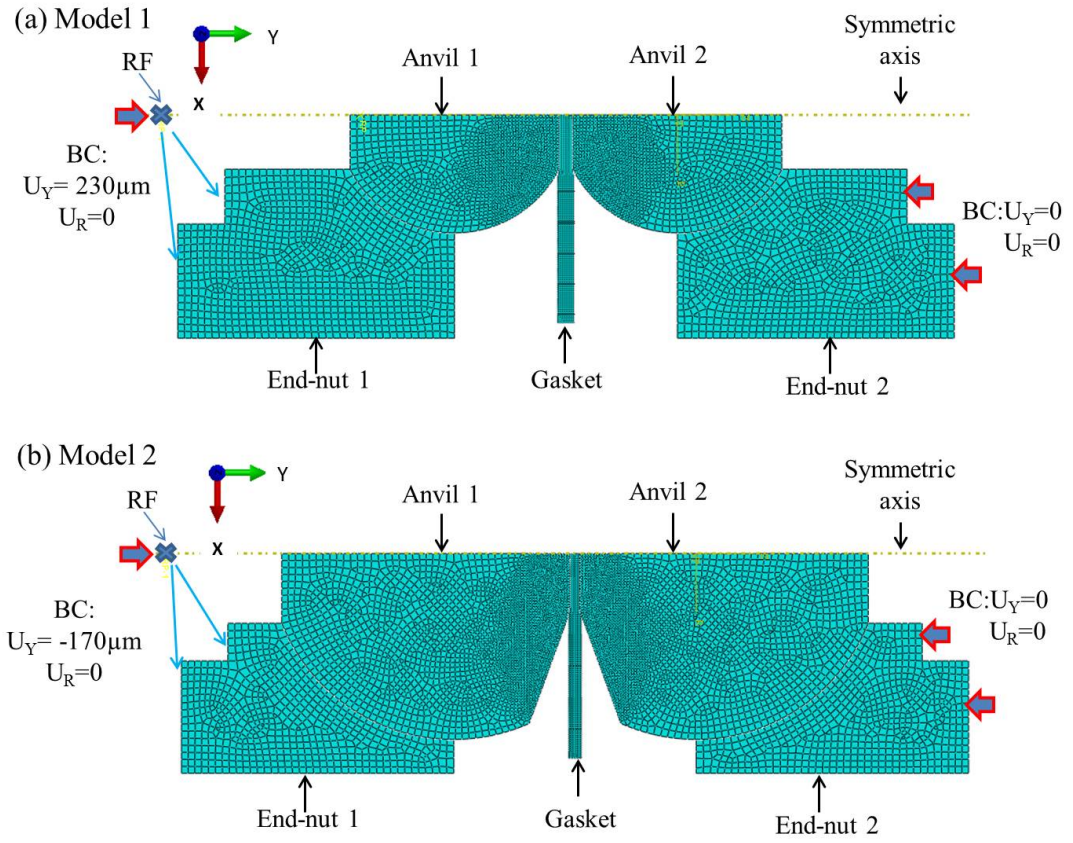

Figure 9.16: *(a) The FEA models used for stresses analysis of the anvil in (a) the loading test demonstrated in Figure 9.13 and (b) the loading test shown in Figure 9.14.*

used in both tests, the stress patterns on the anvils in both cases are comparable. The massive principle effect can be illustrated by comparing the stresses patterns of these two different anvil geometries. In the models, all the parts are modeled as axisymmetric and runs more close to the real working condition at anvil breaking point. The opposed anvils are supported by two end-nuts and controlled to squeeze the gasket by the applied boundary conditions. This layouts assure the gasket deforms close to reality and no loading and boundary conditions are applied directly on the anvils. Therefore, the stresses patterns on the anvils are much more reliable than the previous model.

Several simplifications are made in the FEA models to accelerate the computation and insure convergence. The cell body is not included in the model because it is irrelevant to the loading condition when sapphire failed. The sapphires have failed at the pressurised stage (before clamping) which means the thread between the end-nut and cell body was not engaged. Accordingly, the threaded profile of end-nut is insignificant and simplified. The sample is not modeled

based on the following reasons. NaCl powder sample is frictionless which means it would not induced shear stress on the culet of anvil. Furthermore, the mechanical properties of NaCl is difficult to defined in the model because its yield strength is too low (σ_Y=21 MPa [129]). The computation usually terminated when the sample part was over-distorted with large deformation. Therefore, the sample is presumed to be incompressible at the centre of the culet. This simplification of sample is the only uncertainty and pitfall in these FEA models. However, the effect should be minimal as the amount of sample is small if compare to the gasket.

Frictional contacts are defined between the anvil and end-nut, anvil and gasket. The friction coefficient of these frictional contacts is set to 0.15 which is based on available experimental data [130]. The degrees of freedom of the reference point is coupled to the edge of end nut, which are indicated by the blue arrows as shown in Figure 9.16. With this configuration, the movement of end-nut 1 can be controlled remotely by the boundary condition appointed on the reference point. The reaction force from the whole model can be calculated at each displacement, which is equivalent to the load applied to deform the gasket. The movement of end-nut 2 is constrained at the edges as shown in the figures. The mesh density near the culet area is increased as it is the most concerned area.

In addition, the gasket would experiences large deformation which can terminate the computation when some elements become over-distorted. Adaptive mesh function are defined to the meshes of the gasket to avoid such problem, which will be activated when some elements on the gasket start to collapse due to excessive deformation. The distorted elements will be re-meshed to an acceptable aspect ratio to keep the computation running.

The mechanical properties of copper is defined as tri-linear model as shown in Figure 9.17, which is based on the available material specification (No.102, cold drawn copper) [131]. With this idealised stress-strain lines, the yield stress σ_Y (322 MPa) can be hardened to the material tensile stress S_{ut} (345 MPa) when the plastic strain reach 0.167. On the other hand, the material properties of sapphire and BERYLCO 25 remain unchanged as in the previous FEA model (Figure 9.6).

The modified FEA model can be validated by comparing the final gasket thickness in the simulation and experimental test. As shown in Figure 9.18, the simulation is basically in line with the experimental loading test. The final gasket thickness in model 1 (103$\sim$116 μ) and the measured thickness (100$\sim$112 μm) in the experiential testing in Figure 9.13 are almost the same.

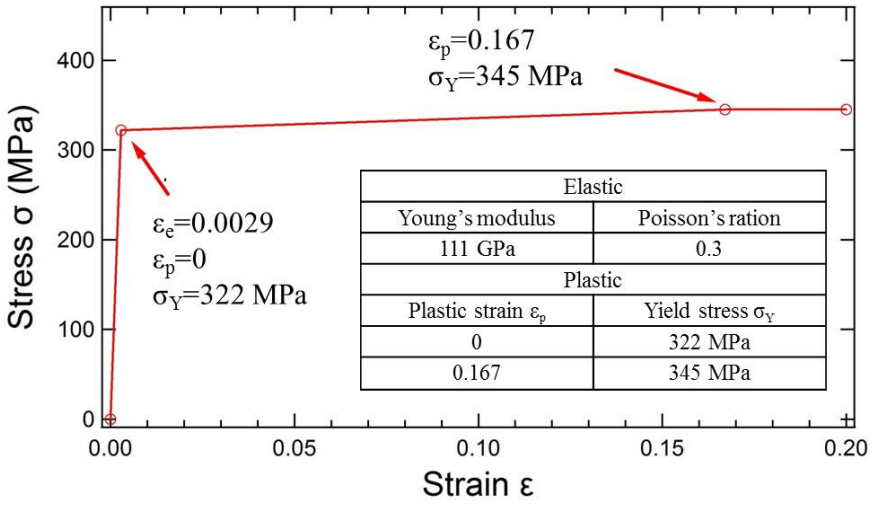

Figure 9.17: *Mechanical properties of copper material in FEA simulation. The parameters are based on the data sheet of No.102 copper [131].*

Accordingly, the final gasket thickness (58∼93 μm) in model 2 and the measured thickness (60∼80 μm) are largely the same. Apart from that, the cupping profile can be seen in the deformed gasket which shows that the culet area of the anvil is deformed with a 'cupping' manner. The level of the cupping deformation in model 2 is more conspicuous, which can explain why thin gasket is commonly perform better than thick gasket as the cupping profile can restrain the plastic flow of the gasket then the sample pressure can be generated more efficiently. This anvil deformation behaviour is consistence with the FEA analysis on the diamond anvil [65].

9.6.2 Stress analysis

The material strength of sapphire is firstly examined here and then compared to the stresses pattern to figure which stress tensor could be the major destructive stress. For sapphire material, the tensile strength is between 275 MPa to 400 MPa, the compressive strength is 2 GPa [103]. The shear strength of sapphire is roughly between 375 and 520 MPa in the view of the shear strength of hard brittle material is approximately 1.3 times larger than its tensile strength [132].

Figure 9.19 shows the three main stresses pattern of the anvil in first design concept when the cell is loaded with 8.6 kN final load. Theoretically, the tensile stress (positive maximum principle stress) is the most dangerous stress tensor for sapphire because as a brittle material it is weak in tension. However, the highest positive value in the maximum principle stress distribution is between 100∼150 MPa at the red contour, which is less then the lower bound

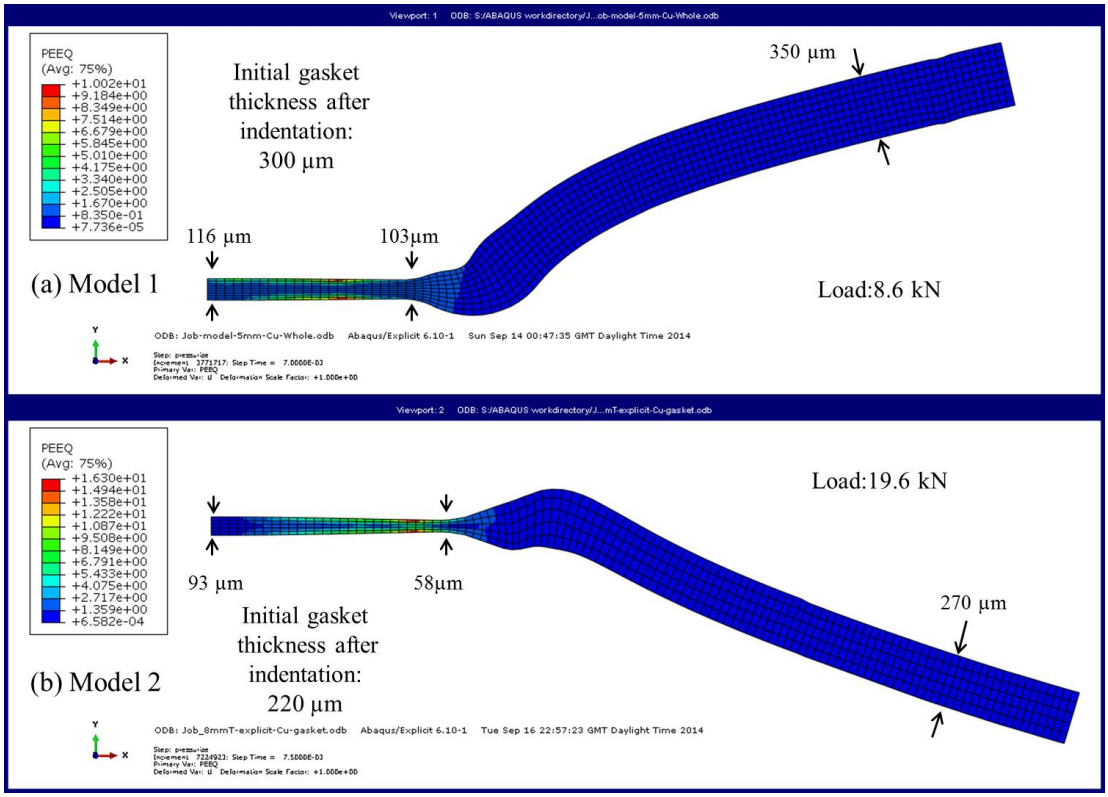

Figure 9.18: *The final gasket deformation with the corresponding final load in (a) model 1 and (b) model 2.*

of the material tensile strength (275 MPa). On the other hand, the compressive stress (negative minimum principle stress) is substantially high at the centre of the culet area and the highest compressive stress achieve 3.4 GPa. The area with compressive stress higher than the material compressive strength (2 GPa) is located with the blue to blue-green contour. The shear stress of the anvil is also exceed the upper bound of the material shear strength (520 MPa). The highest negative shear stress is located at the blue contour with the magnitude of 560∼630 MPa. The negative shear is mainly composed by the shear caused by the unsupported area and the outward plastic flow of the gasket.

Figure 9.20 shows the three main stresses pattern of the anvil in second design concept when the cell is loaded with final load 19.6 kN. As the load on the anvil is more than double of the first design, the high tensile stress area ($\geq$100 MPa) spreads across the anvil as shown in the red contour of the maximum principle stress distribution. However, the peak tensile value is only 170 MPa which is still lower than the material strength. The compressive stress increases dramatically up to 7.8 GPa, which is three times to the material compressive strength

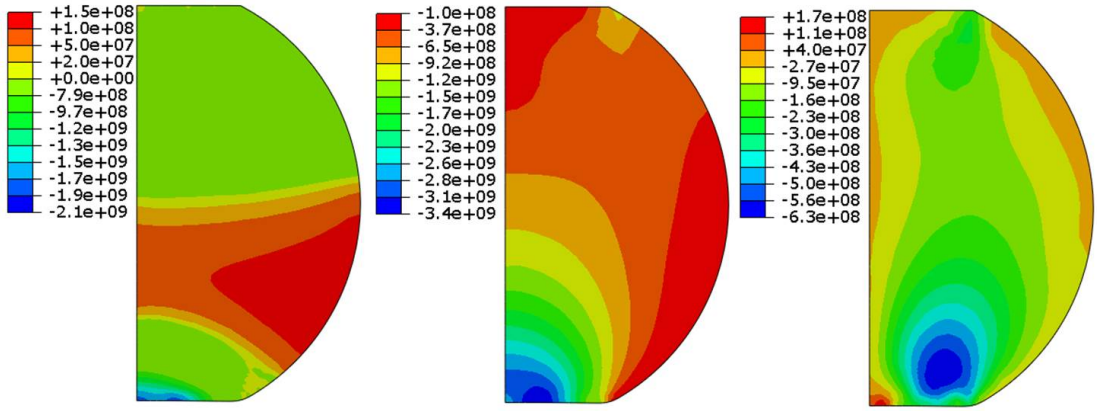

(a) Maximum principle stress (b) Minimum principle stress (c) Shear stress

Figure 9.19: *With 8.6 kN load applied in model 1, the (a) maximum principle stress, (b) minimum principle stress and (c) shear stress, the unit of the number is Pa.*

(2 GPa). The area with compressive stress higher than the material compressive strength is greater than the previous as well. Similar circumstances occur at the shear stress distribution, the highest shear reaches 1.3 GPa which is more than twice of the upper bound of the material shear strength (520 MPa) and the area with shear stress higher then the shear strength obvious larger (see the green contour). Despite the stresses condition is much more severe, the 8 mm anvil manage to undertake higher load and generate higher sample pressure without failure.

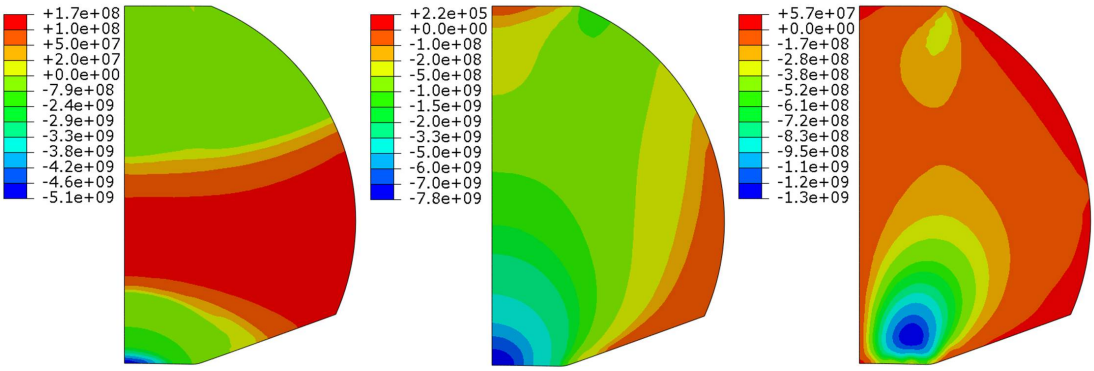

(a) Maximum principle stress (b) Minimum principle stress (c) Shear stress

Figure 9.20: *With 19.6 kN load applied in model 2, the (a) maximum principle stress, (b)minimum principle stress and (c) shear stress, the unit of the number is Pa.*

If comparing the magnitude of three stress tensors in the analysis, the compressive and shear are the most possible stress tensors which could lead to anvil failure. Apart from that, the analysis shows that the geometry shape of the sapphire anvil should be shape to provide massive support as much as possible to improve the pressure performance and anvil strength. However, it is

difficult to quantify the massive support at this point because there is little quantitative study of massive support for spherical sapphire anvil at present.

9.7 High pressure SANS experiment on single crystal Niobium

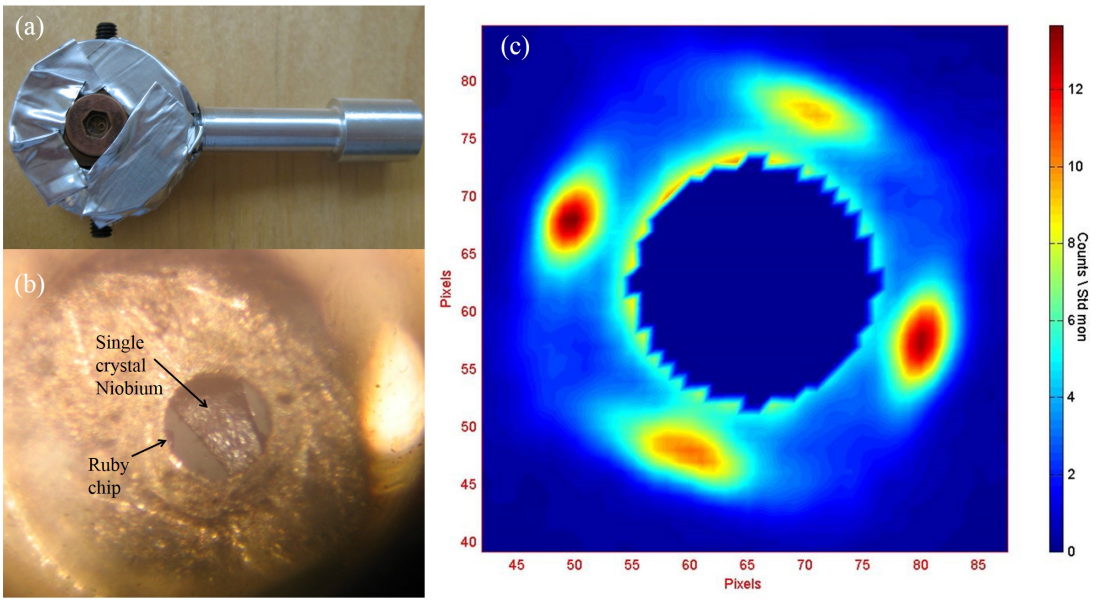

Figure 9.21: *Experimental set-up of the T-SAC for small neutron scattering; (a) the loaded T-SAC in a aluminium holder; (b) the single crystal Niobium in the gasket; (c) the collect data of sample when the cell was exposed to the neutron beam with 10 minutes. Note: figure (c) is unpublished, the author of this thesis is the main contributor of this SANS experiment.*

This section demonstrates an application of the T-SAC in high-pressure SANS experiment. A single crystal niobium was pressurised in this cell to study the pressure dependence of the flux line lattice (FLL) of the crystal through SANS technique. The sample piece was around 1 mm long and 0.3 mm thick as shown in Figure 9.21 (b). Accordingly, a thick gasket is needed for this experiment to cover the size of the sample. Copper gasket is unable to be used in this case due to its low strength and thin final thickness problem. To contain the sample, a BeCu gasket with 1 mm diameter sample hole and 0.5 mm thick was used. The initial sample volume is equivalent to 0.4 mm^3. Mixture of Flouriner (FC 72: FC 84) is used for pressure media to create a hydrostatic pressure environment. As the sample hole is larger than those in previous tests, the culets of the anvils were polished to 3 mm diameter accordingly to prevent the sample hole blowing out in the early presurisation stage.

In the experiment, the highest attainable pressure is 1.6 GPa with 17.33 kN. The pressurised cell was mount on the sample holder as shown in Figure 9.21 (a). To reduce the scattering background , the cell was covered with aluminum foil and the holder is made with aluminum alloy as well. The sample was pressurised to 1.6 GPa in the cell and the cell was loaded into a 17 T cryomagnet [133] in D22 beamline, Institut Laue-Langevin (ILL). The cell was cooled down to 1.8 K with the 17 T magnetic field. Figure 9.21 (c) shows the collect data when the cell was exposed to the neutron beam with 10 minutes. Further pressursation was not succeed, one anvil was failed when the cell was loaded to 18.4 kN and the remain gasket thickness is 0.3 mm. The relative high material strength and thick gasket restrict attainable pressure. Apart from that, liquid pressure media can lead to anvil failure as stated in Klotz's work [46]. Though the attainable 1.6 GPa pressure is rather low if compare to the loading test result, it still the highest record in the existing high pressure cell design for the SANS experiment.

9.8 Future work

We have designed and tested a compact sapphire anvil cell (T-SAC) based on combining spherical sapphire anvil and turnbuckle principle. Unlike to the traditional bulky sapphire anvil cells as shown in Figure 9.22, the T-SAC is much simpler in configuration and smaller, it is less than 16 mm in length and 14 mm in diameter. The size of T-SAC is even smaller than the 'egg' cell as shown in Figure 9.22, which was believed the smallest sapphire anvil cell. The miniature feature allow it can be fit into most cryostat of modern scientific instrument without difficulties and thermalised much faster. For pressure range below 6 GPa, the cost effectiveness of the T-SAC is much higher than conventional DAC. Sample volume of T-SAC can be 6 times to the diamond anvil cell while the cost almost negligible. Each 8 mm diameter sapphire ball costs less than 23 pounds which is much cheaper than diamond anvil (a standard 2.5 mm diamond is more than 800 euros). The compactness, non-magnetic body and large sample volume (up to 0.4 mm^3) facilitate the potential implementation in other scientific experiment such as resistivity, optical, magnetic measurement.

As the sapphire anvil is the most fragile part in the cell, future study can focus on investigating the methods to improve the anvil strength. For example, better polishing method and high temperature treatment are the potential improving method. Apart from that, the shape optimisation of the anvil hasn't been study, the relation of the anvil geometry (e.g. the flank angle, the culet bevel angle, the overall diameter) and massive support principle needs to be further

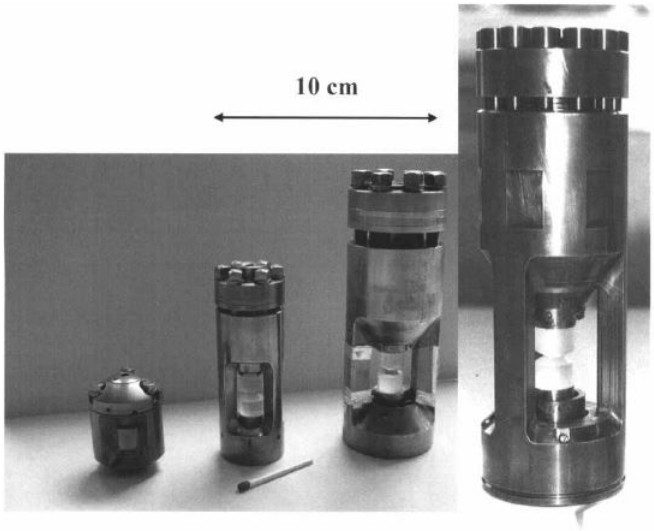

Figure 9.22: *Kurchatove-LLB high-pressure cells for low-temperature neutron diffraction. The left one is the "egg" cell which was claimed the smallest sapphire anvil cell.(Figure from [44])*

investigated.

Chapter 10
Large Volume Piston-Cylinder Pressure Cells

This chapter presents two piston-cylinder type high pressure cells for high-pressure chemistry studies. These cells were designed to pressurise large amount of liquid sample (particular for water-based sample) up to 800 MPa with controllable manner. Each design is presented separately with stress analysis in FEA and description of working mechanism. Hoop strain at the external surface of the cell were measured and then the internal pressure was calculated through Lamé equation. After that, the load and attainable internal pressure were calibrated for the users. The accessories tools for the liquid cells are introduced at last.

10.1 Introduction

High pressure method is popular in research interest such as substances reaction, decomposition, polymerization of organic substance, crystallization and synthesis ect. For this kind of research, large sample space and measurable pressure control are the two main basic requirements. The piston-cylinder type pressure cell is the most obvious experimental method to fulfill the requirements. Two piston cylinder cells were developed in this project for our research collaborators based on the above requirements. These cells are called liquid cell in this thesis as they are mainly used to pressurise large amount of liquid sample (particular for water-based sample). Some high pressure experiments performed in these cells require relatively high temperature (from room temperature to $150\,^{\circ}\mathrm{C}$). As the mechanical properties of BeCu alloy are stable for this temperature range [15], all the cell are made out of fully-harden BERYLCO 25 and the mechanical properties of the alloy have been demonstrated in Table 9.1 and Figure 9.5.

10.2 Type A liquid cell

10.2.1 Design and operation

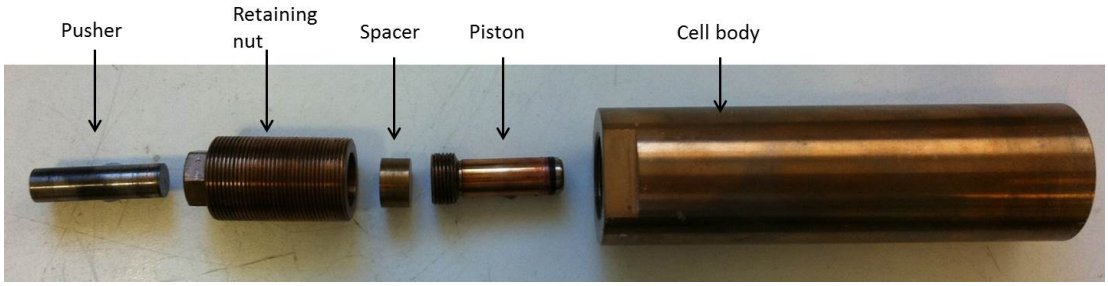

Figure 10.1: *Disassembly of the type A liquid cell*

This section present the type A liquid cell as shown in Figure 10.1 and Figure 10.2. It is a closed-end design which is effective to prevent leakage of water-based sample. The cell body is 35 mm in diameter and 118 mm long. The internal bore of the cell is 10.4 mm in diameter and 72 mm long which is equivalent sample volume around 5.3 mL. M22$\times$1 thread seats are machined on top of the cell body with 35 mm depth, which is used to clamp the pressure. Two seals, rubber seal and copper seal, are mounted on the piston to prevent leakage. The rubber seal works at low pressure range and the soft copper seal works at higher pressure range. The way of mounting the seals on the piston is demonstrated in the enlarge view in Figure 10.2.

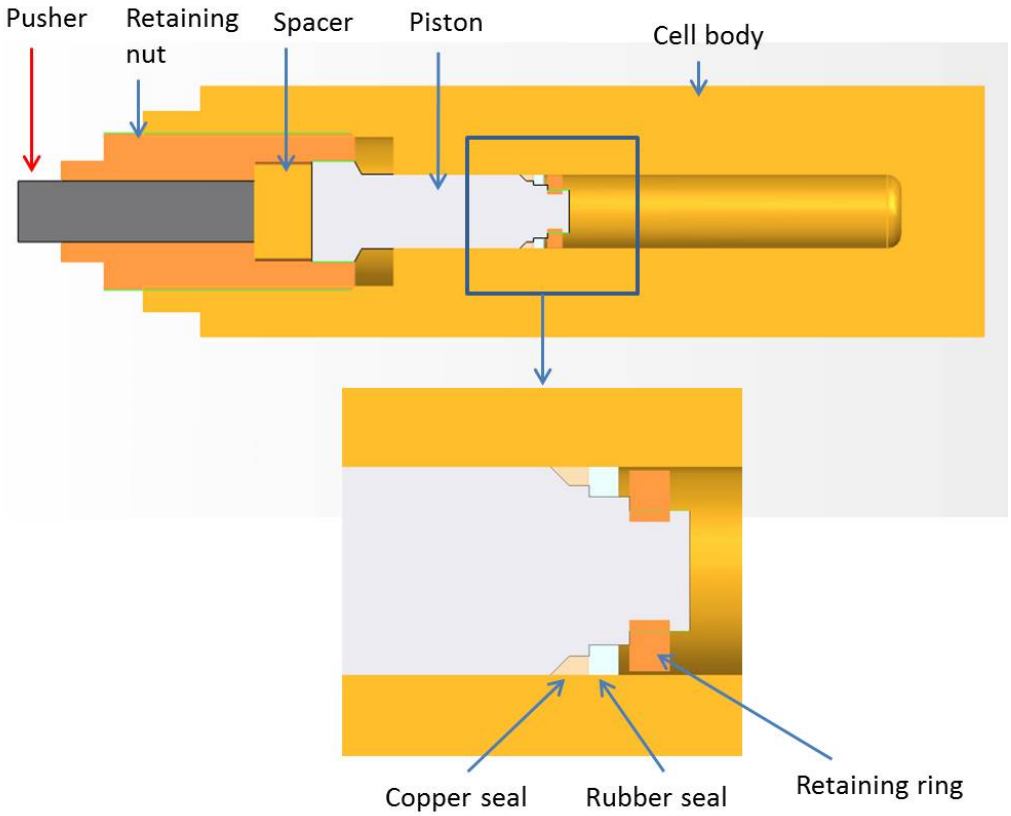

Figure 10.2: *Type A liquid cell*

A threaded retaining ring is used to fix the copper seal and rubber seal on the piston. All the parts except the pusher are made of fully harden BeCu alloy. The pusher is machined out from tungsten carbide (WC) which can effectively cope with the severe compressive load because it is with very high compressive strength (4 GPa). An external shield is needed to cover the whole cell during pressurization for safety measure which is presented later.

The operation of the cell is descbired as follows. Firstly, sample is filled into the bore of the cell as much as possible. Then the piston is mounted with seals and then inserted in to the sample bore. Vacuum grease needs to be smeared on top of the piston then the spacer is placed on the piston. This grease is used to create lubrication between the spacer and piston therefore rotation torque would not be transfer to the piston when users turn the retaining nut to lock the pressure. After all, the retaining nut and pusher are assembled to finish the installing procedure. Before applying pressure, the whole cell needs to be placed in the shield as shown in Figure 10.13 for user protection.

To pressurise the sample, the assembled cell is placed under the plunger of a hydraulic press.

The plunger presses directly on the tungsten carbide pusher and the load is then transferred to the sample by the piston advancing. Each movement of the piston is followed by an increase of the pressure inside the cell if those seals work. The applied load can be read from the gauge on the hydraulic press and pressure can be roughly estimated by dividing the force by the area. However, this pressure approximation can be over-estimated at high pressure stage, which is explained in detail later in this chapter. The retaining nut needs to be tighten after each advancement of piston to lock the pressure, this pressure locking mechanism is usually called self-clamping.

10.2.2 FEA stress analysis

10.2.2.1 FEA model

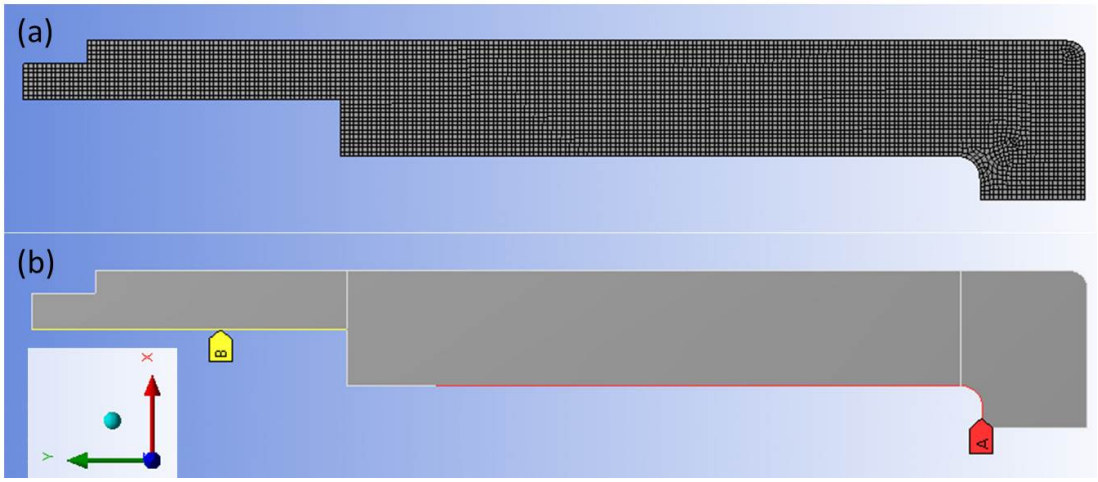

Figure 10.3: *FEA model of type A liquid cell (a) the mesh model (b) boundary and loading conditions, pressure is applied on region A and boundary condition U_y=0 is used to constrain the movement of the model on region B.*

The pressure limitation of the type A design is tested virtually through the FEA method as shown in Figure 10.3. 2D-axisymetric FEA model is used in the analysis with the boundary and loading conditions as demonstrated. The M22 thread is simplified in the model because of following reason. Any ISO threads with d$\leq$1 inch (25.4 mm), a thread length of at least 0.5d will have a strip strength in excess of the screw's tensile strength [92]. Based on the size and the length of thread the simplification is justified and the threaded part of the body is unlikely to be stripped off before the cell body was rupture axially in tensile.

Figure 10.3 (a) shows the model is meshed with quadrilateral elements which can provide high

accurate analysis result as described in Chapter 5. Figure 10.3 (b) demonstrates the boundary and loading condition of the FEA model. The axial movement of the top thread seat (marked as region B) is constrained throughout the simulation process. Furthermore, region A in Figure 10.3 was applied with pressure.

10.2.2.2 Stresses analysis

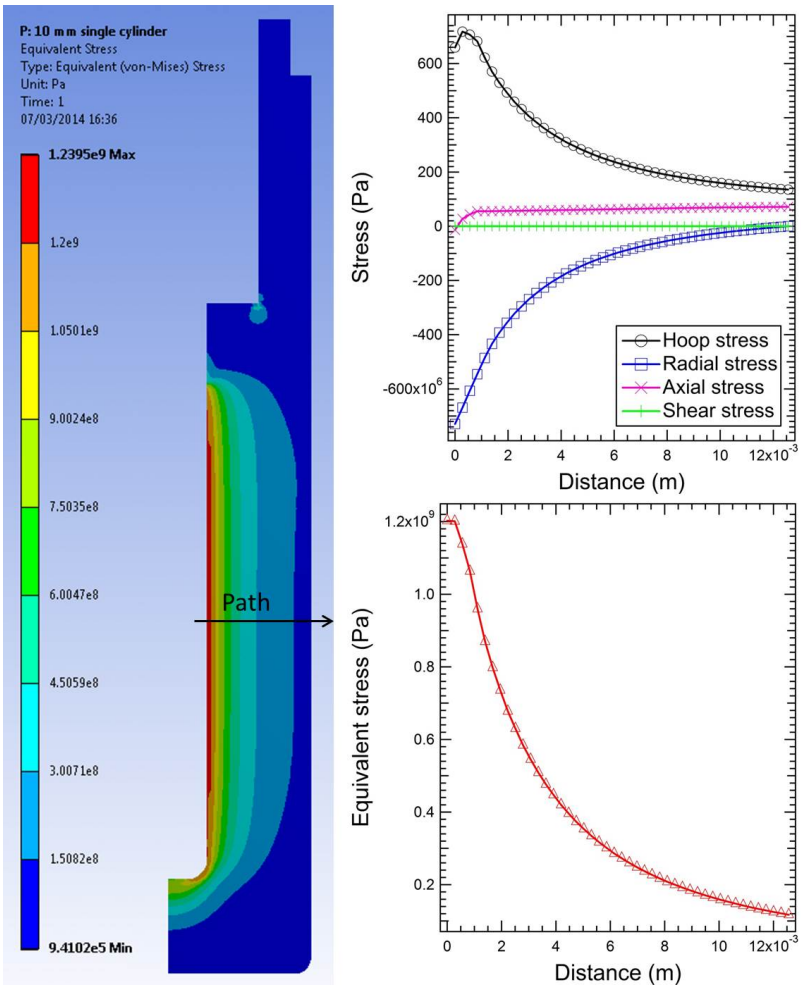

Figure 10.4: *Stress distribution of the type A liquid cell when subjects to 800 MPa internal pressure; equivalent stress distribution (left) and stresses distribution along the cross-section path (right)*

As the three main stress tensors (hoop, radial and axial stress) can be calculated conveniently with the aid of computer. Von Mises theory is used to assess the maximum allowable pressure for the type A design. The simulation result shows that the pressure limit of this design is 800 MPa (Figure 10.4). When pressure increases to 800 MPa, the internal bore starts to reach

the yield point of the material, further pressurisation would result in permanent plastic deformation on the bore which can reduce the working life time of the cell. Leakage would be the main issue if the cell was overloaded before. For safety consideration, the pressure in the cell must be smaller than 800 MPa to insure that the cell works in elastic deformation.

In addition, the stress distribution is highly uneven in the cell body. The two main stress tensors, hoop stress and radial stress, all peaks at the internal bore which results in the equivalent stress concentrates on the internal bore. This stress concentration agrees with the thick-walled cylinder theory. The axial stress is rather low if compare to other two stresses tensors. The shear stress is so trivial and can be neglected, which proof the assumption of hoop, radial and axial stress are the principle stresses. The analysis also points out that increasing the wall thickness is not an effective way to increase the pressure capability of a thick wall cylinder, because the material of thick wall cylinder has not been employed fully. The outer layer of the cylinder is hardly stressed, while all the main stresses (hoop and radial) concentrate on the internal bore where pressure is applied, resulting in high equivalent stress concentration on the bore. Pre-stressed methods can be used to increase the pressure capability but as these methods are beyond the range of this project, they would not be further discussed in this thesis.

10.3 Type B liquid cell

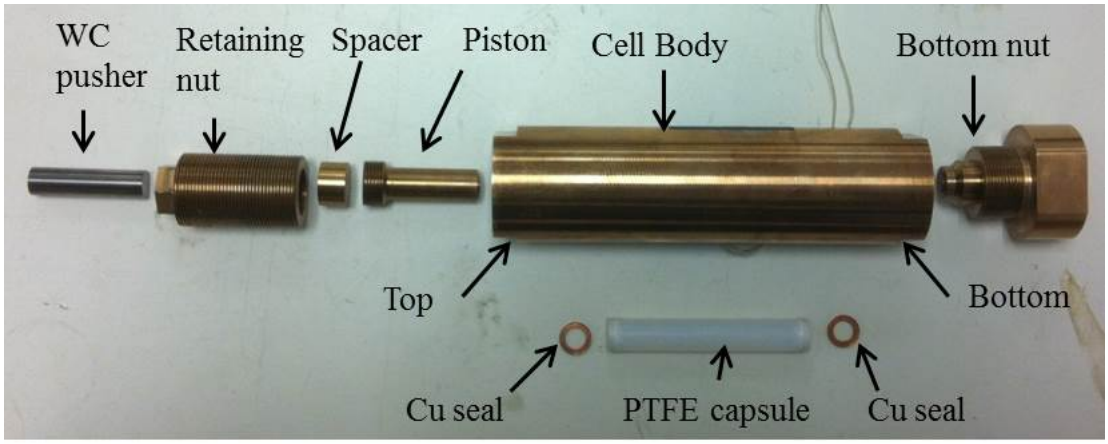

Figure 10.5: *Disassembly of the type B liquid cell.*

Liquid sample is loaded into the bore directly in the type A liquid cell, the direct contact of sample and cell body can caused contamination problem sometime particularly for those samples can react with the BeCu alloy. Sample encapsulation can solve this problem however retriev-

ing a capsuled sample from a close-end design after high pressure experiment is extremely inconvenient. To over come the problem, a open-end design (type B liquid cell) is presented in Figure 10.5 and Figure 10.6.

10.3.1 Design

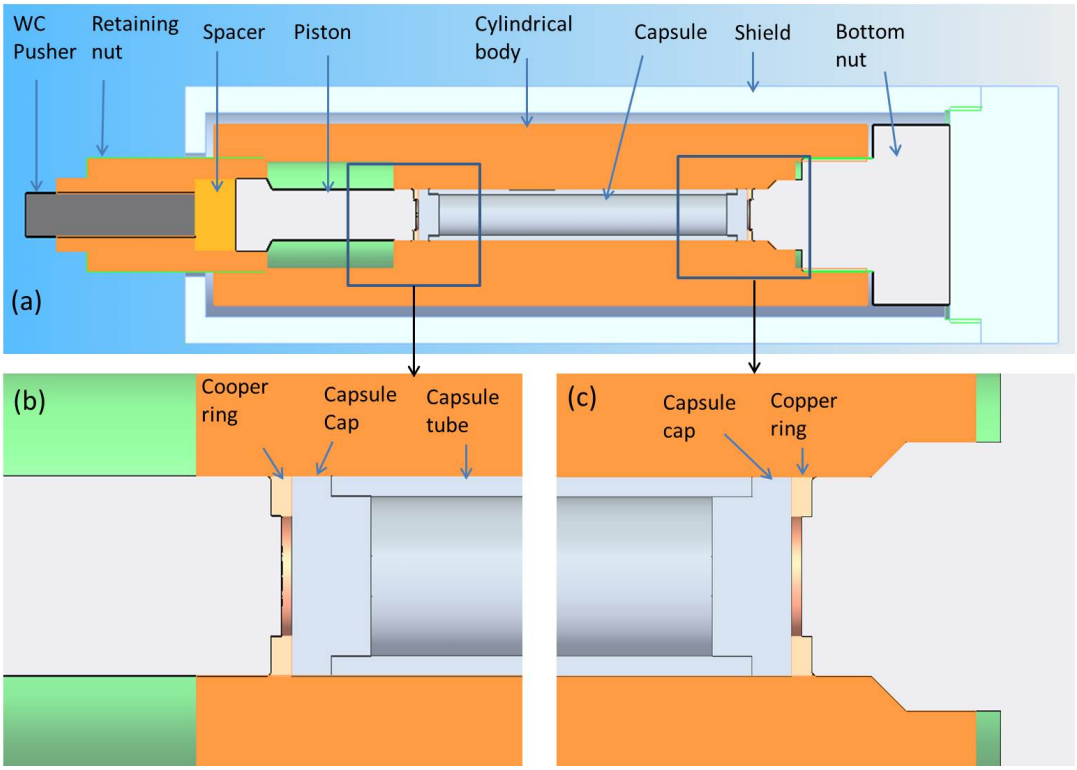

Figure 10.6: *Type B liquid cell, (a) the section view of the assembly; b enlarge view on the top seals; (c) enlarge view of the bottom seal.*

As shown in Figure 10.6, type B liquid cell is a single cylinder cell based on the type A design with modifications. The cell body is 35 mm in diameter and 127 mm long. The bore of the cell is set to 10 mm diameter to allow the standard capsule can be fitted in. The seals mechanism of the cell is re-designed to seal liquid sample contained in PTFE capsule, which consists of two caps and a tube. PTFE is an ideal material to be used for encapsulation because of its non-reactive and frictionless features. Apart from that, the PTFE cap acts as a first seal at low pressure range. At higher pressure, anti-extrusion cooper rings are placed on both ends of the capsule act as the secondary seal to prevent the PTFE caps over-extruded. Though the capsule can prevent contamination from the metallic body, it is with the cost of sample volume which reduced to 2.8 mL. The open end design enable the capsuled sample can be retrieved

conveniently after high-pressure experiment by pushing it out with a long rod. The pressure capability of the type B liquid cell should be no different to the type A liquid cell as the external diameters of the cells are identical, which is confirmed in the following section.

10.3.2 FEA stress analysis

10.3.2.1 FEA model

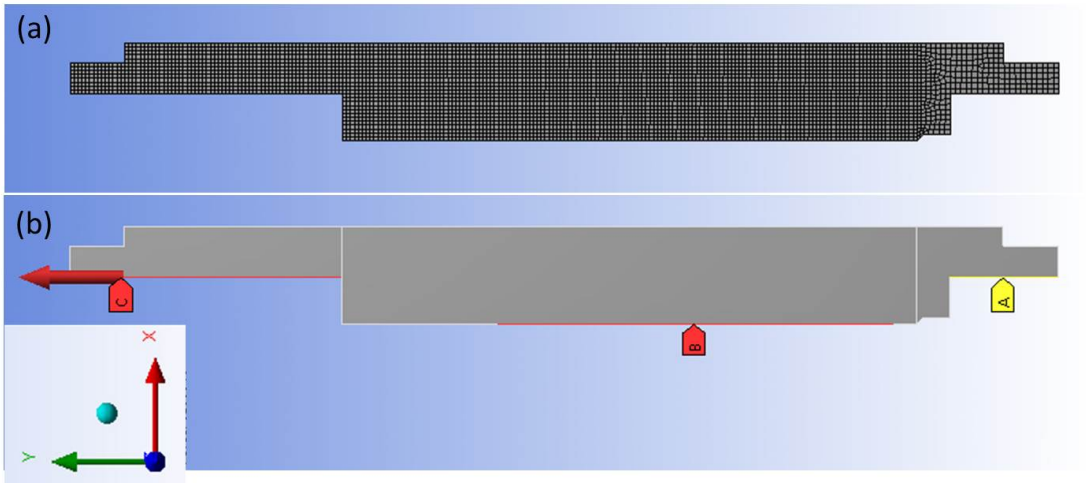

Figure 10.7: *FEA model of type B liquid cell; (a) the mesh model; (b) boundary and loading conditions, boundary condition U_y=0 is used to constrain the movement of the model on region A, pressure P is applied on region B and a equivalent axial force F_x=7.85×10^{-3}×P is applied on the region C.*

Similar to the analysis of type A liquid cell, a 2D-axisymetric FEA model with quadrilateral elements is used to assess the pressure limit of the type B cell as shown in Figure 10.7. The boundary and loading conditions are indicated in the figure. The vertical movement of the cell body is constrained at the bottom thread seat (region A) and the internal pressure is applied on the internal bore where marked as region B. Axial tension force is applied on the top thread seat (region C) to imitate the axial load when the cell is clamped at high pressure.

10.3.2.2 Stress analysis

The simulation result in Figure 10.8 shows that the pressure limit of the cell is identical to the previous design. The internal bore of the cell body starts to yield when the internal pressure reaches 800 MPa. Even though the equivalent stress distributions are slightly different due to the different of boundaries, the stresses along the middle cross-section of both designs are

fundamentally identical. Both hoop and radial stresses peaks at the surface of the bore and reduce gradually, as a result, the equivalent stress concentrates at the bore as well.

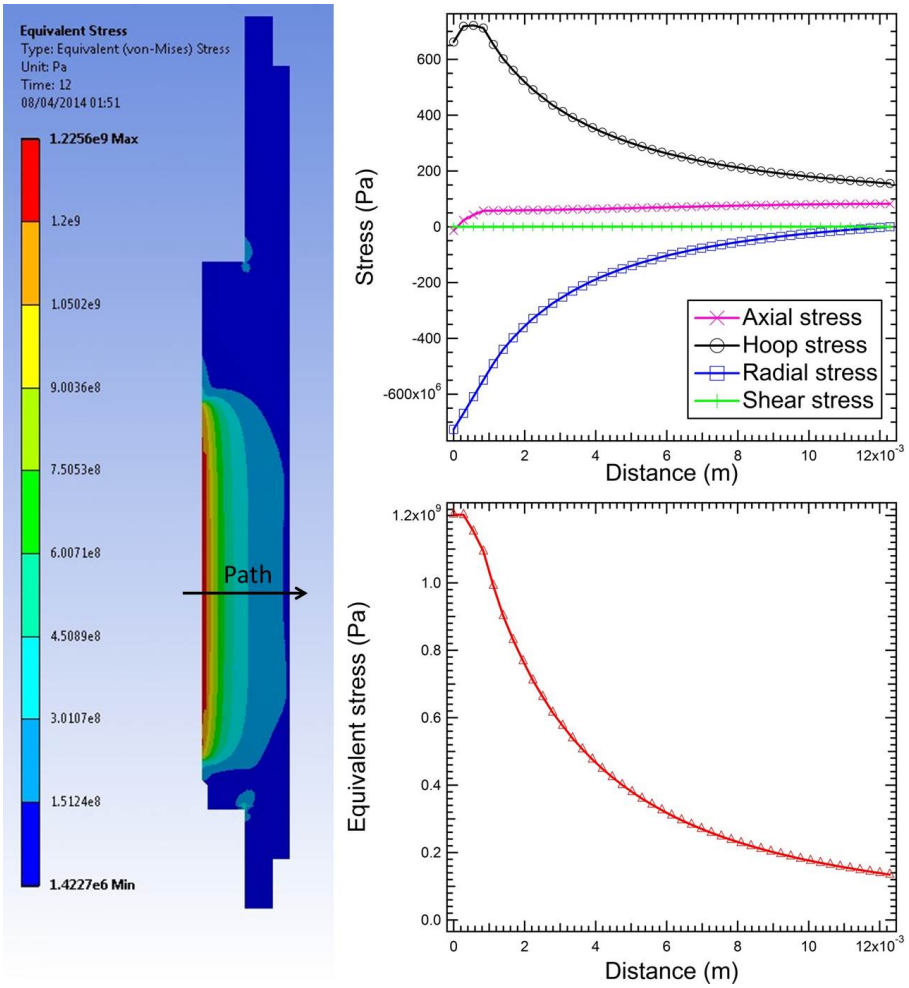

Figure 10.8: *Stress distribution of the type B liquid cell when subjects to 800 MPa internal pressure; equivalent stress distribution (left) and stresses distribution along the cross-section path (right).*

10.4 Pressure calibration

Since the load applied on the cell is available from the gauge on the hydraulic press, the internal pressure can be calibrated with the load by using P=F/A. However, this method is only applicable if users did not require accurate pressure information. From previous experience in using piston-cylinder cell, the friction can increased significantly to take part of the load from the hydraulic press at high pressure condition. The main reason is that the piston seals extrude to

fill the clearance between piston and sample bore and as a result the friction cannot be ignored. Therefore, the calibration could be over-estimated which is demonstrated later.

The high temperature environment is another factor needs to be considered. Once a pressurised cell is heating up in a furnace, internal pressure can increase substantially with the rising temperature, which could results the cell was overloaded at high temperature enviroment. This section presents the solutions to address these problems.

10.4.1 Pressure calibration with strain gauge

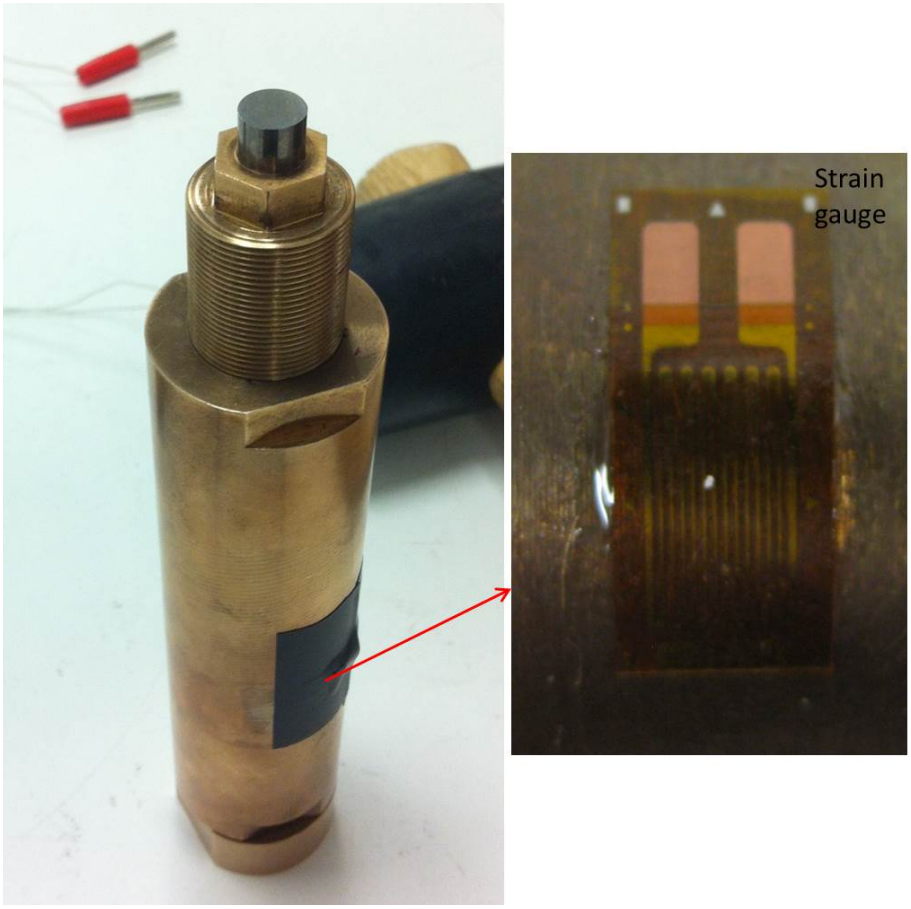

Figure 10.9: *Strain gage is attached on the type B liquid cell body.*

For piston cylinder cell, the most accurate way to measure pressure is using the pressure sensors such as manganin pressure gauge, which needs to be immersed in the pressurised liquid sample and measure the pressure directly. However, this method requires a feed-through wires to measure the resistivity of the manganin gauge and it is difficult to be implemented with the capsuled liquid sample. Chapter 2 has demonstrated that some piston-cylinder cell's design-

ers [26, 30, 31] can manage to be pressure calibrated with the geometry changes (axial elongation or radial expansion). In this section, we established the pressure calibration between load and attained pressure by using strain gauge method. A strain gauge was attached on the cell body (as shown in Figure 10.9) to measure the hoop strain on the external surface. Black tape was cover on the gauge to protect the gauge and wiring. The measured hoop strain was used to calculate the internal pressure based on the Lamé equations presented in Chapter 4. The hoop strain of the cell body can be measured by converting the resistance changes with the following equation from the gauge supplier [134],

$$GF = \frac{\Delta R/R}{\varepsilon} \tag{10.1}$$

Where GF is the gauge factor, $GF = 2.075$ for the model CEA-06-240UZ-120 from Vishay micro-measurement [134]; ΔR is the change in resistance caused by strain; R is the resistance of the undeformed gauge, $R = 120.71\ \Omega$; ε is the strain.

Load (Ton)	Hoop strain ε_t (before-clamped)	Hoop strain ε_t' (clamped)
1	0.000176707	0.000141203
1.5	0.00026506	0.000204819
2	0.000345382	0.000273092
2.5	0.000413655	0.000329317
3	0.000514056	0.000413655
3.5	0.000578313	0.000457831
4	0.000650602	0.000518072
4.5	0.000722892	0.000574297
5	0.000811245	0.00064257
5.5	0.000899598	0.000710843
6	0.000963855	0.000763052
6.5	0.001032129	0.000815261
7	0.001125674	0.000871486
7.5	0.001208654	N/A
8	0.001277152	N/A

Table 10.1: *Hoop strain data with load up to 8 ton.*

Capsuled water was used for the calibration. The gauge reading was recorded with every half-ton and then converted to strain as demonstrated in Table 10.1. The raw data of the measurment is attached in the Appendix F in this thesis. Clearly at each measure point, the hoop strain ε_t was reduce to ε_t' when the cell is clamped by the retaining nut and the load from the hydraulic

press is released . This strain difference of before-clamped and clamped is mainly caused by the different loading conditions. In the before-clamped condition, the cylinder body is only subject to two dimensional stress condition, the radial and hoop stress, and the axial stress is ignorable. Whereas, at clamped stage, the axial stress cannot be ignored (as shown in Figure 10.8) because the applied load is locked by its own thread. Apart from that, the internal pressure might drop at clamped condition as a result of the deformation of the thread and the piston might move back slightly.

Based on Lamé equations in Chapter 4, the pressure can be calculated with both before clamped and clamped conditions. For before-clamped condition, the axial stress is neglected and the Equation 4.14 below is used for the pressure calculation.

$$u = \frac{1-\nu}{E}\frac{P_i a^2 - P_o b^2}{b^2 - a^2} \cdot r + \frac{1+\nu}{E}\frac{a^2 b^2 (P_i - P_o)}{b^2 - a^2} \cdot \frac{1}{r}$$

As $\varepsilon_t = u/r$ and $P_o = 0$, then the equation is simplified as

$$P_i = \frac{\varepsilon_t E(b^2 - a^2)}{(1-\nu)a^2 + (1+\nu)a^2 b^2 \frac{1}{r^2}} \tag{10.2}$$

For clamped condition, Equation 4.13 below is used to calculated the pressure at this three dimensional stress conditions.

$$u = \frac{1-2\nu}{E}\frac{P_i a^2 - P_o b^2}{b^2 - a^2} \cdot r + \frac{1+\nu}{E}\frac{a^2 b^2 (P_i - P_o)}{b^2 - a^2} \cdot \frac{1}{r}$$

As $\varepsilon_t = u/r$ and $P_o = 0$, the equation is simplified as

$$P_i = \frac{\varepsilon_t E(b^2 - a^2)}{(1-2\nu)a^2 + (1+\nu)a^2 b^2 \frac{1}{r^2}} \tag{10.3}$$

For above equations, E=130$\times 10^9$ Pa, b=17.5$\times 10^{-3}$ m, a=5$\times 10^{-3}$ m, ν=0.3, r=b. Substitute the measured strain ε_t in to Equation 10.2 and substitute ε_t' into Equation 10.3, the calibrated pressure is obtained and listed in Table 10.2. The calibration pressures versus load is plotted in Figure 10.10 for a clearer demonstration of the friction effect. The nominal pressure (P=F/A) only agrees to the calibrated pressure P_b at before clamped condition up to 3 ton load. Above that, the nominal pressure is obviously overestimated and would be less reliable at higher loading condition. Furthermore, the pressure dropping effect needs to be considered as a result of

comparing the calibrated pressure P_b and P_c versus load. The slight pressure releasing cannot be neglected based on the significant difference which is mainly contributed by the deformation of thread. In most scenarios, the cell works at clamped condition as most high-pressure experiments need to be run for a long time period. Thus, the red curve (P_c versus load) in Figure 10.10 is the the optimal calibration for the users. With the Table 10.2, user can check the pressure inside the cell by looking the gauge reading (ton) on the hydraulic press.

Load (Ton)	Nominal pressure $P = F/A$ (MPa)	Calibrated pressure before clamped P_b (MPa)	Calibrated pressure clamped P_c (MPa))
1	125	129	121
1.5	187	193	176
2	250	252	235
2.5	312	302	283
3	374	375	356
3.5	437	422	394
4	500	475	446
4.5	562	528	494
5	624	593	552
5.5	687	657	612
6	750	704	656
6.5	812	754	701
7	874	816	749
7.5	937	874	N/A
8	999	931	N/A

Table 10.2: *Calibrated pressure with load, 1 ton=9807 N, A=78.5 mm^2.*

10.4.2 Pressure calibration for water-based sample at high temperature

Pressure, temperature and volume are the basic parameters in thermodynamics. In order to prevent the cell overloads at high temperature, this section provides an estimation of pressure change at high temperature environment (up to $150\,^{\circ}\mathrm{C}$) to users. The pressure estimation presented in this section only limits to water-based sample which are the most common sample pressurised within this cell at present. Apart form that, water had been studied extensively during last decades [135, 136] and the thermo-physical properties of water below 1000 MPa are available from the on-line data base in the national institute of standards and technology (NIST) [137]. The estimation is created by two following steps with two assumptions respectively, isothermal assumption and isochoric assumption.

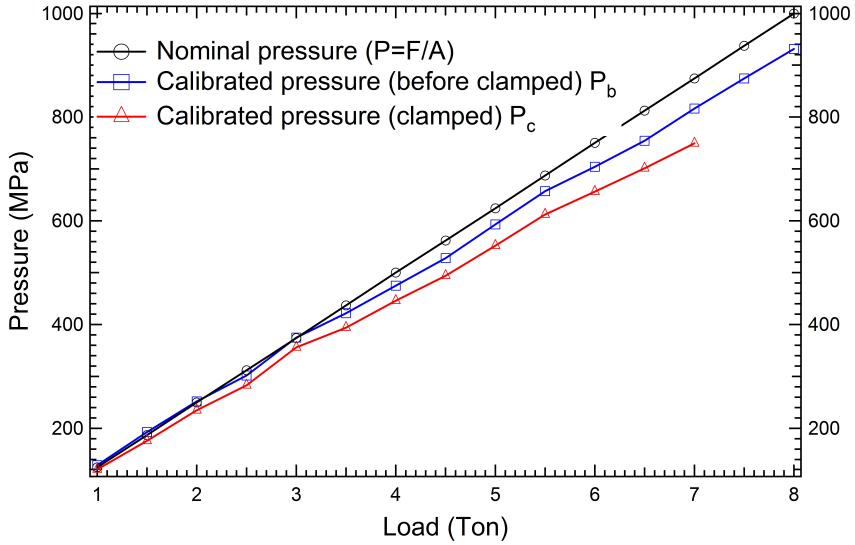

Figure 10.10: *Calibrated pressure at before-clamped and clamped condition.*

10.4.2.1 Isothermal

When the cell is pressurised at room temperature, we presume that the temperature variation during the pressurisation is ignorable. The relation of two isothermal properties, density and pressure, is plotted in Figure 10.11 based on the data from NIST [137]. It is clear that the density of water is increasing with the pressure and 7 data points are retrieved from the curve based on the 7 pressure point P_c listed in Table 10.2. These data points are listed in the Table 10.3 and used for the estimation of pressure change in next step.

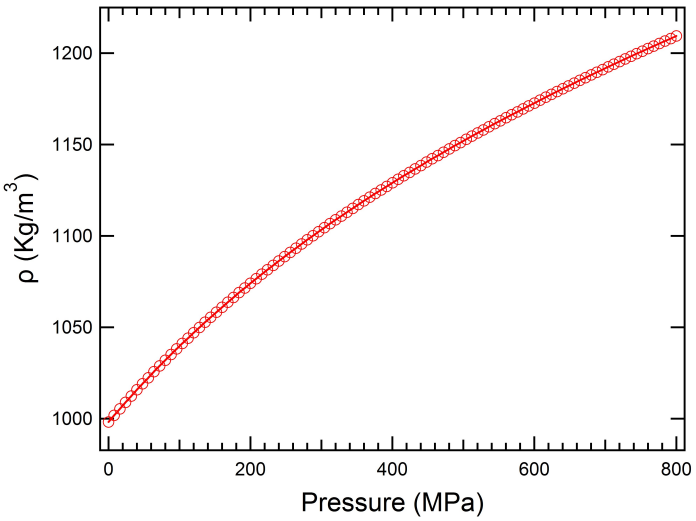

Figure 10.11: *Isothermal properties of water, density vs pressure*

Loading (Ton)	1	2	3	4	5	6	7
Pressure (MPa)	121	235	356	446	552	656	749
Density (Kg/m^3)	1047.8	1084.4	1118.2	1139.4	1163	1183.6	1200.4

Table 10.3: *7 pressure points of P_c in the Figure 10.11 and the corresponding load.*

10.4.2.2 Isochoric

When the pressurised cell is transfered into a furnace for heating, the sample is considered subjected to isochoric condition if the thermal expansion of the cell is negligible. based on this isochroic assumption, the pressure is rising up with temperature increase. At each density point listed in Table 10.3, pressure and temperature can be plotted in Figure 10.12 based on the available data [137]. For the user who intends to use the cell at high temperature, this graph provides an estimation of pressure change of the clamped cell at high temperature environment. The red dash line indicated the maximum limit of the cell, which also shows the upper bound temperature for pressure points above 552 MPa.

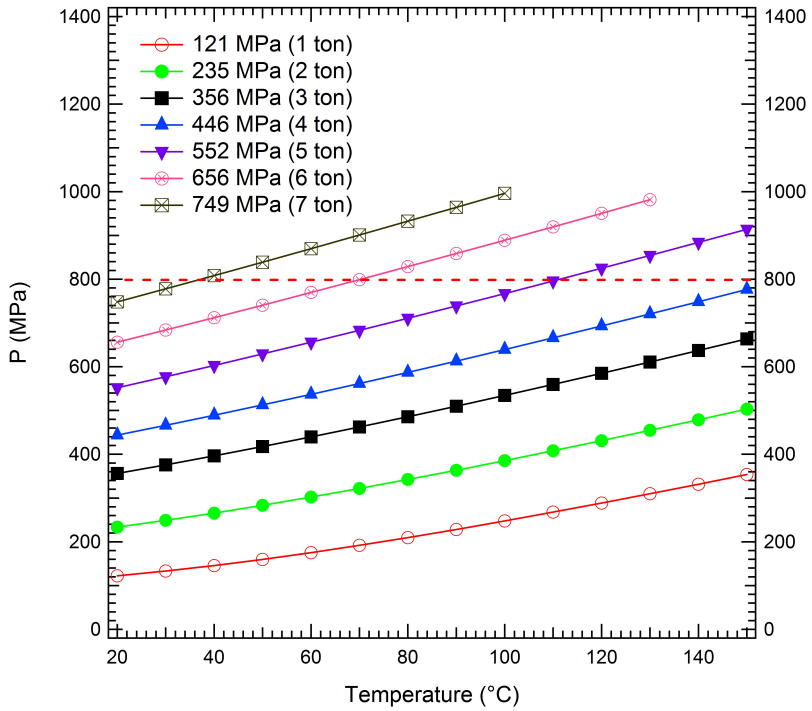

Figure 10.12: *Theoretical pressure change at high temperature.*

10.5 Accessories

Several auxiliary parts were developed/ordered for the operation of the liquid cells. This section provides brief information of these parts.

Shield

Unlike to the opposed anvil cell in previous chapters, the safety hazard of the liquid cells is much higher as these cells contain large amount of pressurised sample and store high energy accordingly. Protect element shield is needed to provide safety measure for the users. A set of protected shield which made of stainless steel are designed to cover the cell during the pressurisation as shown in Figure 10.13 (a). An open hole on the shield allows the cell to be operated within the shield in the press as shown in the Figure 10.13 (b). When the cell is clamped at high pressure, the tungsten carbide rod can be removed and the shield cap is screwed on top of the shield body to cover the cell entirely.

Hydraulic press

To pressurise the large amount of sample, a hydraulic press is an essential for the liquid cell system. Any standard hydraulic press with at least 10 ton capacity is capable to works with the liquid cells presented in this chapter. Figure 10.13 (b) shows a common workshop scale 10 ton hydraulic press which was used in testing.

Puller

When disassembling the liquid cell after a high pressure experiment, the piston usually jams in the bore due to the extrusion of the seal. A puller shown in Figure 10.14 is designed to pull out the piston when the jam occur. Both puller and piston heads are threaded with the same size of thread, internal thread for the puller and external thread for the piston. The piston head can be screwed in the puller with these fixture threads. Another long external thread is machined on the puller as well, which can be used to lift the piston by turning the handle.

Stirrer

For some high pressure experiments such as chemical reaction under high pressure, two different density of samples are pressurized in the cell. Sometimes it is essential to stir the pressurized liquid samples to accelerate the reaction. The PTFE coated magnetic alloy neodymium iron boron (NdFeB) as shown in Figure 10.15(a) is an ideal stirrer for our cell as it is the strongest

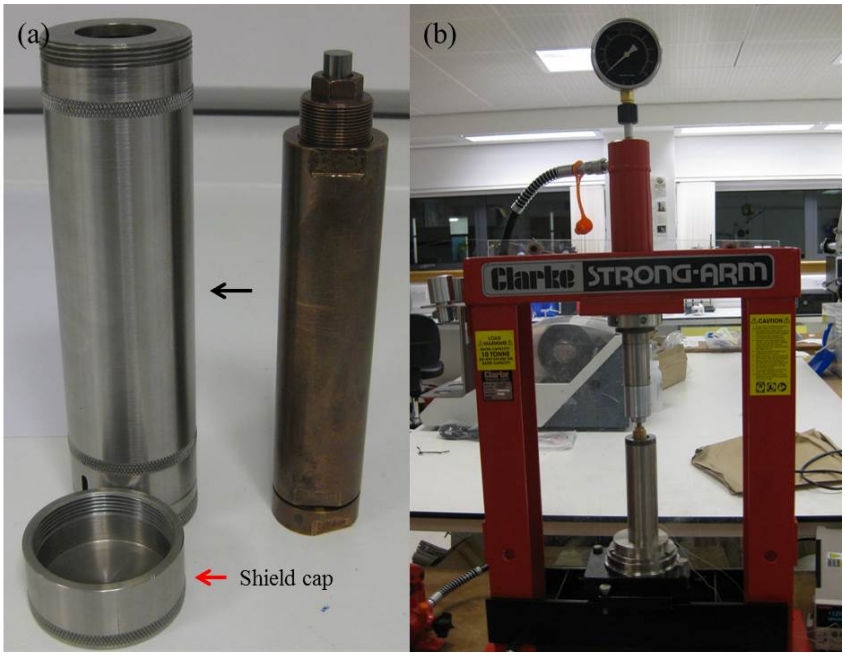

Figure 10.13: *(a) The steel shield and a assemble liquid cell. (b) The shielded liquid cell was pressed in a hydraulic press*

magnet so far. They can be implemented in our liquid cells conveniently as the PTFE coat can prevent contamination and the size fits the bore of the cell. The stirrer can spin or oscillate with external magnetic field. We have built and tested an electronic device 10.15(b) to drive current in four symmetrically positioned solenoids. The driver supplies alternating current to the solenoids, thus the oscillating magnetic field will be generated to drive the magnet inside the cell. However, this kind of setting cannot be used with the shield as shown in Figure 10.13 (a) as the shield reduce the magnetic field, a steel box is needed to cover the all the system to provide safety.

Anther simpler way to drive the magnet in the cell is using a single phase ac shaded pole motor as shown in Figure 10.16. The best advantage of the shaded pole motor is convenience. It is widely available from market with low cost. No wiring or controller is needed to operate the motor as it runs directly when connecting to 240 Volt ac power socket. The rotor of the motor can be removed as it is not needed. The remaining frame can generate high speed rotating field which are able to drive the magnet inside the cell.

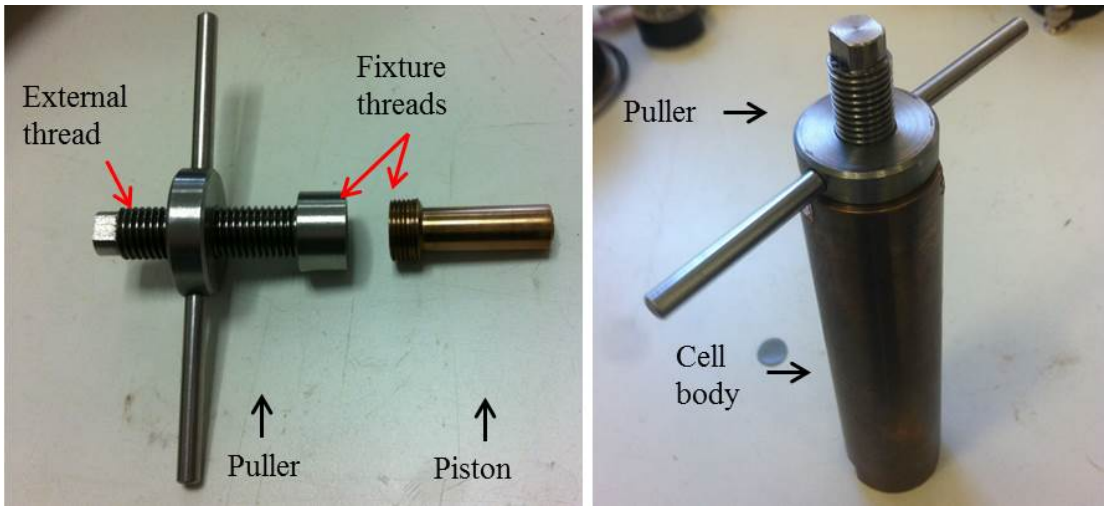

Figure 10.14: *Puller*

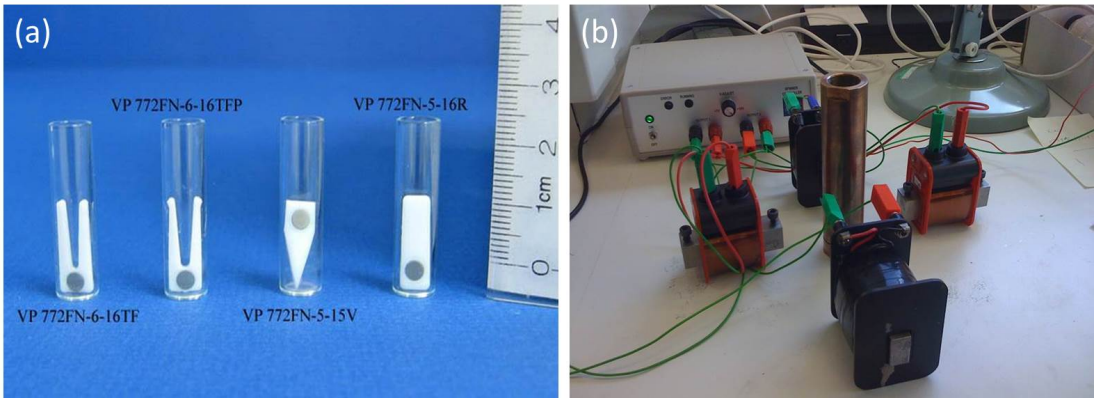

Figure 10.15: *(a) PTFE coated NdFeB magnets; (b) alternating current driver and solenoids*

10.6 Future work

This chapter presents two piston-cylinder type pressure cell with large sample volume capacity. FEA method was used to examine the pressure limit of the cell and analyse the stresses distribution. For convenience, the internal pressure of the cell was calibrated with the applied load through theoretical calculation. These cells have been used in the high-pressure study of salicylaldoximes process, bio-diesels decomposition and crystallization, material polymerisation and pharmaceutical experiments. In future, if higher pressure range is required, stronger alloy combined with pre-stressed techniques can be used to increase the pressure limit. The maximum pressure record of piston-cylinder type pressure cell is 4 GPa [16] at present, which is made of NiCrAl alloy and with interference fit pre-stressed technique.

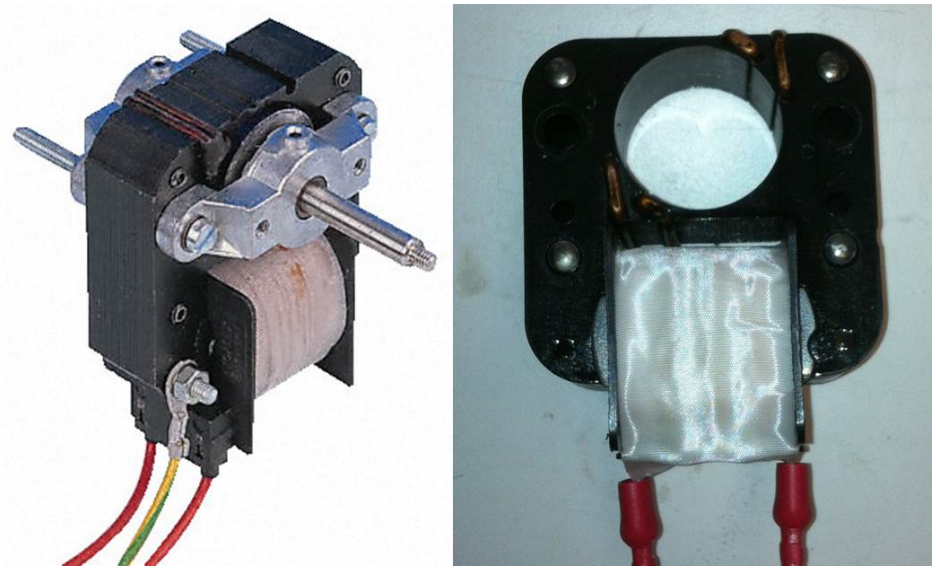

Figure 10.16: *Shaded pole motor*

Chapter 11
Conclusions and Future Developments

There are five types of high pressure cells have been successfully developed in this project to overcome the lack of experimental equipment. Three of them (Hellium gas pressure cell, TM-3He-DAC, PTM-DAC) are designed to be used with the MPMS SQUID magnetometer. To further develop the turnbuckle technique, the development of T-SAC added a new member to the series of turnbuckle opposed anvil cells. The last chapter presents two piston-cylinder cells which are able to provide large sample volume and measurable pressure control up to 800 MPa.This chapter summaries and outlines the conclusions and future development of each high pressure instrument developed in this project.

11.1 Helium gas pressure cell

A helium gas pressure cell has been developed for magnetic measurements on pressure sensitive materials. The design of the gas cell was optimised through commercial FEA package. The external gas driven design can provide precision pressure control inside the cell, which is particular suitable for pressure dependence magnetic study for pressure sensitive material. In addition, high quality data can be collected from the cell because of its large available sample volume.

A helium gas compressor with higher pressure output is needed if user requires higher gas pressures. The magnetic parts of the cell (the steel capillary, steel seal and steel nut) can be replaced by non-magnetic material to avoid interference and make the centering process of this cell easier. The pressure capability and safety of the cell can be increased by conventional piston-cylinder cell technique with compromising the available sample space, such as increased wall thickness, double-layers or autofrettage.

11.2 TM-3He-DAC

A miniature diamond anvil cell (TM-3He-DAC) has been developed for the 3He insert into MPMS SQUID magnetometer. The cell enables the measurement of magnetic susceptibility at high pressure (up to 5 GPa) and at extremely low temperatures (down to 0.05 K). The cell is probably the smallest diamond anvil cell to date, it is only 6 mm in diameter and 7 mm in length. The miniature feature and use of CuTi alloy allow the magnetic background signal from the cell to achieve lowest level. Even though further reducing the magnetic background signal is still possible and should be done in future by obtaining purer CuTi alloy.

Cold rolling of the CuTi alloy was reported can increase 30% of material strength. This material treatment is highly beneficial to improve the performance of the cell in future. With the currently available material, two available options can be used to improve the structure stability of the cell. First, enlarging the anvil support area by grinding off the sharp taper of the diamond or using a larger diamond. Alternatively, increasing the thickness of the anvil seat.

11.3 PTM-DAC

A miniature non-metallic diamond anvil cell (PTM-DAC) has been developed for high-pressure ac susceptibility measurement in MPMS SQUID magnetometer. The mechanical and magnetic properties of several candidate hgih strength polymer materials for construction of PTM-DAC were assessed. Finite element analysis models were constructed to evaluate stresses and deformation of various components of the pressure cell and to establish the modes of failure. These models were evaluated using experimental test data. It was found that in order to prevent failure of the cell a large area support for the anvil is required. The models were then used to optimise the design of the cell given the constraints imposed by the sample space available in MPMS. A pressure of 5.6 GPa was reached for a load of 3.45 kN, which is the highest to date for non-metallic pressure cells. The magnetic background of the cell was evaluated using Dy_2O_3 at several frequencies and no screening effect from the cell on the sample was observed. The high-pressure ac magnetic measurement data of U_6Fe further demonstrated the high quality data from the PTM-DAC. Thus, this cell is expected to provide a new and useful method for the scientific community to study the magnetic susceptibility of materials through use of ac techniques under pressure in the commercial magnetometers.

As mechanical machining process would inevitable disturb the structure of polymer, which can potentially compromise the material strength. 3D printing technology is a possible way to further developed the PTM-DAC when this technology is more mature to print strong plastic material with high accuracy. Apart from the material strength, the anvil alignment needs to be improved as demonstrated at the end of Chapter 8. Last, the composite gasket preparation method needs to be further improved to enable liquid pressure media can be used in PTM-DAC.

11.4 T-SAC

A compact turnbuckle sapphire anvil cell with spherical sapphire anvils (T-SAC) has been designed and tested. The T-SAC is less than 16 mm in length and only 14 mm in diameter. This cell is much simpler in configuration and smaller than the conventional sapphire anvil cell and SANS high pressure cell. The miniature feature allow it can be fit into most cryostat of modern scientific instrument without difficulties and to be thermalised much faster. The highest attainable pressure of T-SAC is 6.4 GPa with sample volume more than 0.06 mm^3. For pressure range below 6 GPa, if compare the T-SAC to the DAC, the cost effectiveness of the T-SAC

is impressive. The cell can provide more sample volume while the cost of the cell is almost negligible.

As the sapphire anvil is the most fragile part in the cell, future study can focus on investigating the methods to improve the anvil strength. For example, better polishing method and high temperature treatment are the potential improving method. Apart from that, the shape optimisation of the anvil hasn't been studied, the relation of the anvil geometry (e.g. the flank angle, the culet bevel angle, the overall diameter) and massive support principle needs to be further investigated.

11.5 Large volume piston-cylinder cells

Two large-volume piston-cylinder pressure cells have been developed in this project. The cells are the largest cells developed in this project and they are specially designed for compressing large amount of liquid sample up to 800 MPa. The sample volume of the type A liquid cell is 5.3 mL (5300 mm^3) and the type B liquid cell is 2.8 mL (2800 mm^3). These cells have been used in the high-pressure study of salicylaldoximes process, bio-diesels decomposition and crystallization, material polymerisation and pharmaceutical experiments. In future, if higher pressure range is required, stronger alloy such as NiCrAl combined with pre-stressed techniques can be used to increase the pressure limit.

Appendix A
Drawings of the Hellium Gas Pressure Cell

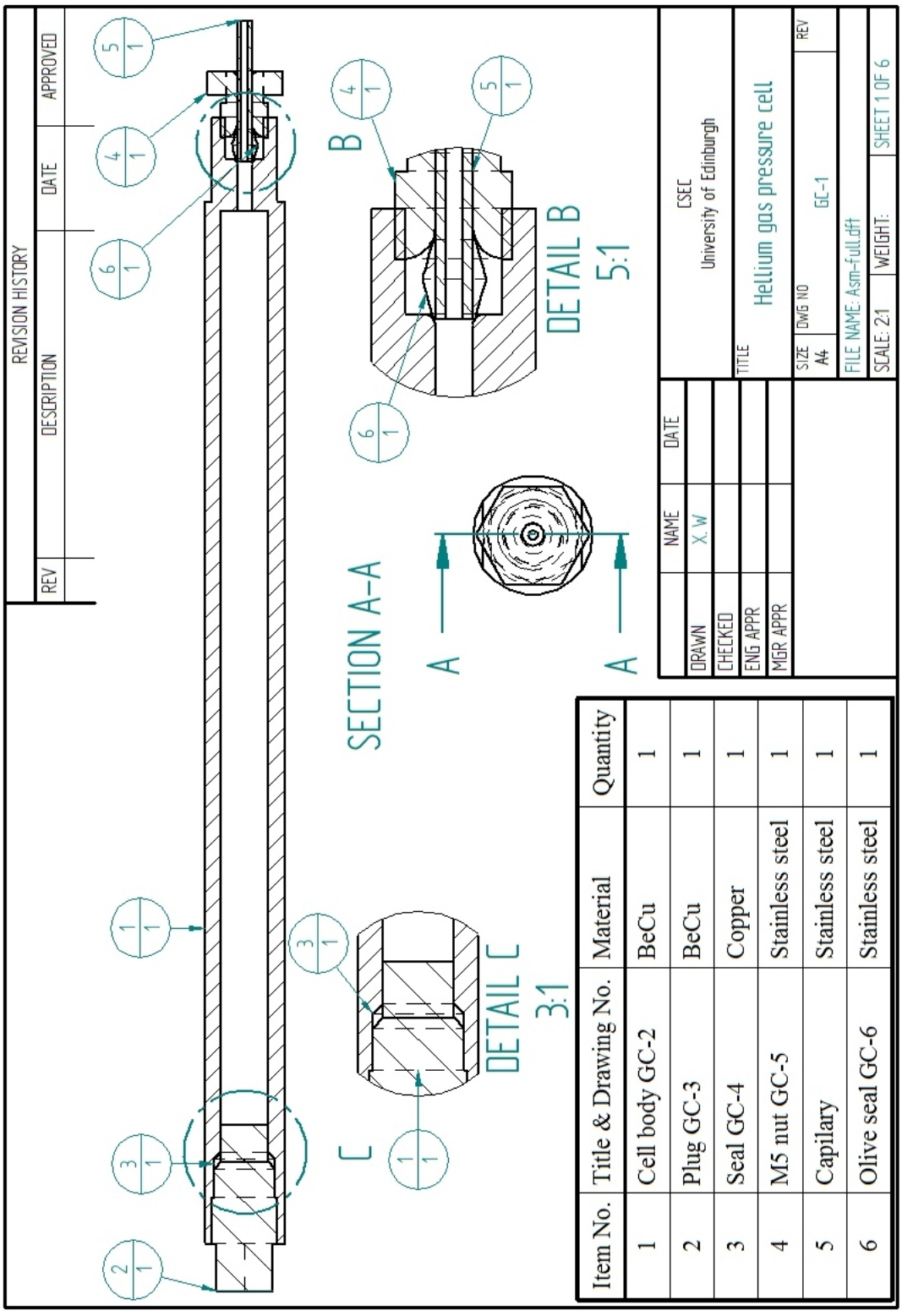

Figure A.1: *The assemble drawing of the helium gas pressure cell.*

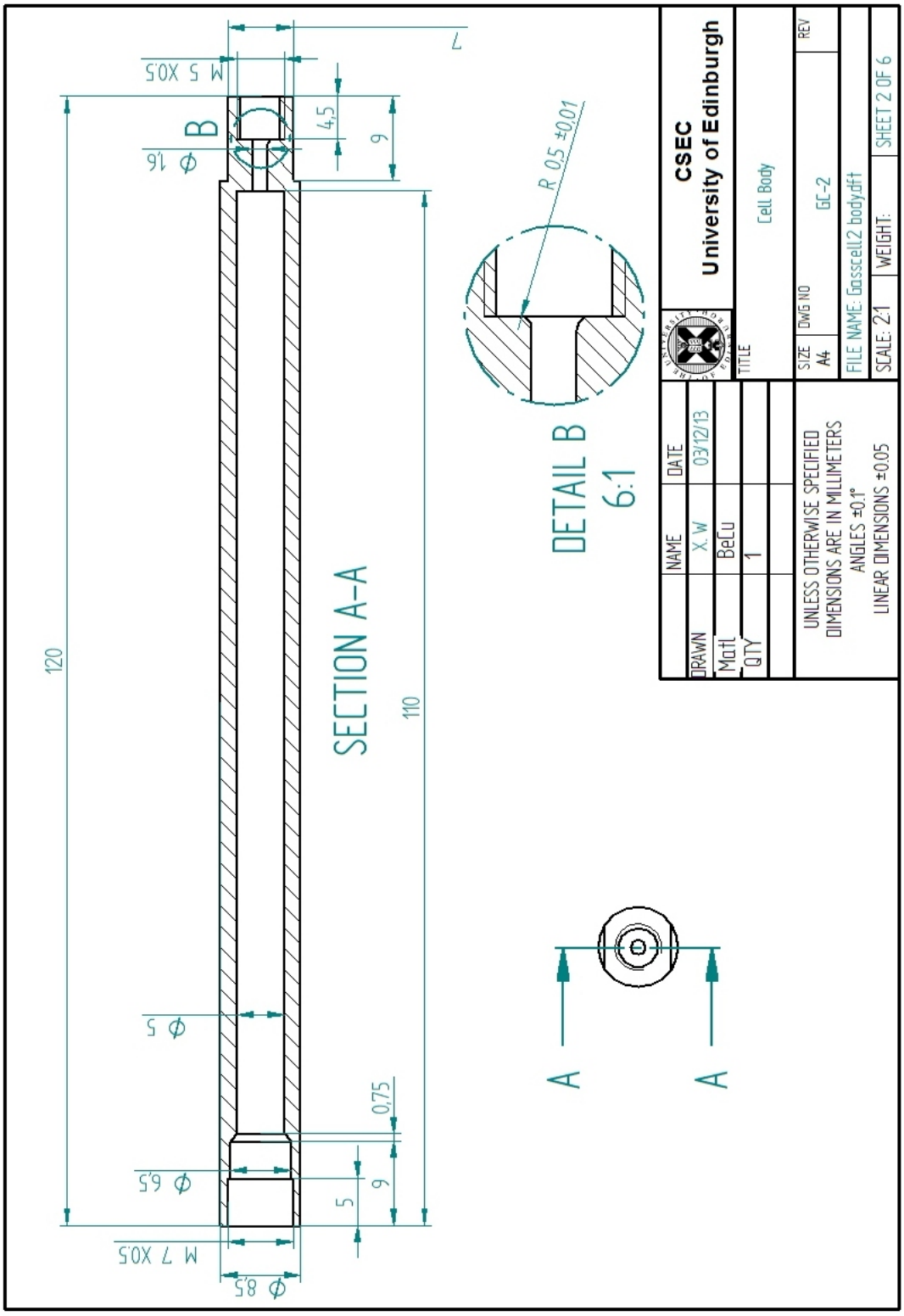

Figure A.2: *The drawing of the cell body.*

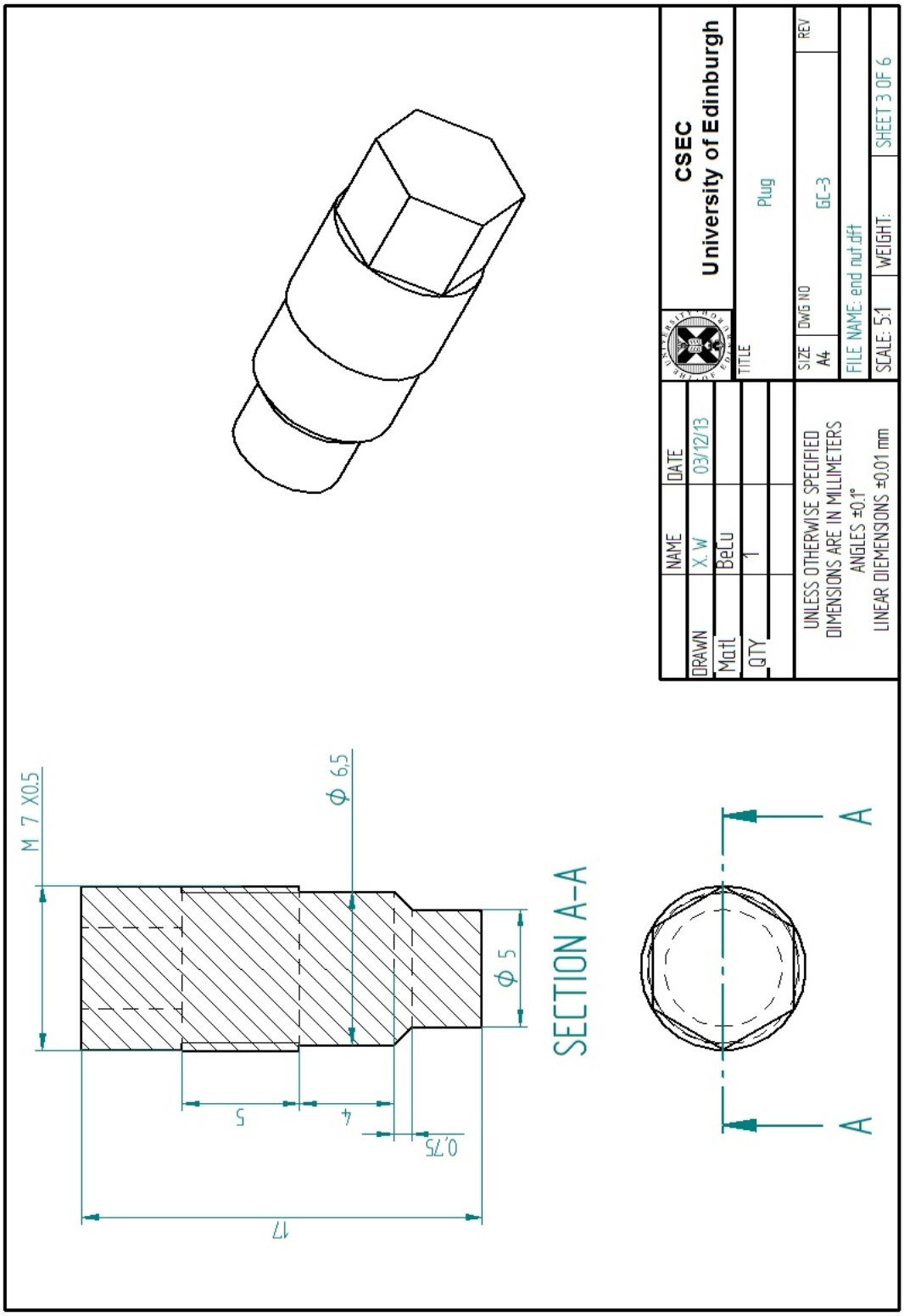

Figure A.3: *The drawing of plug.*

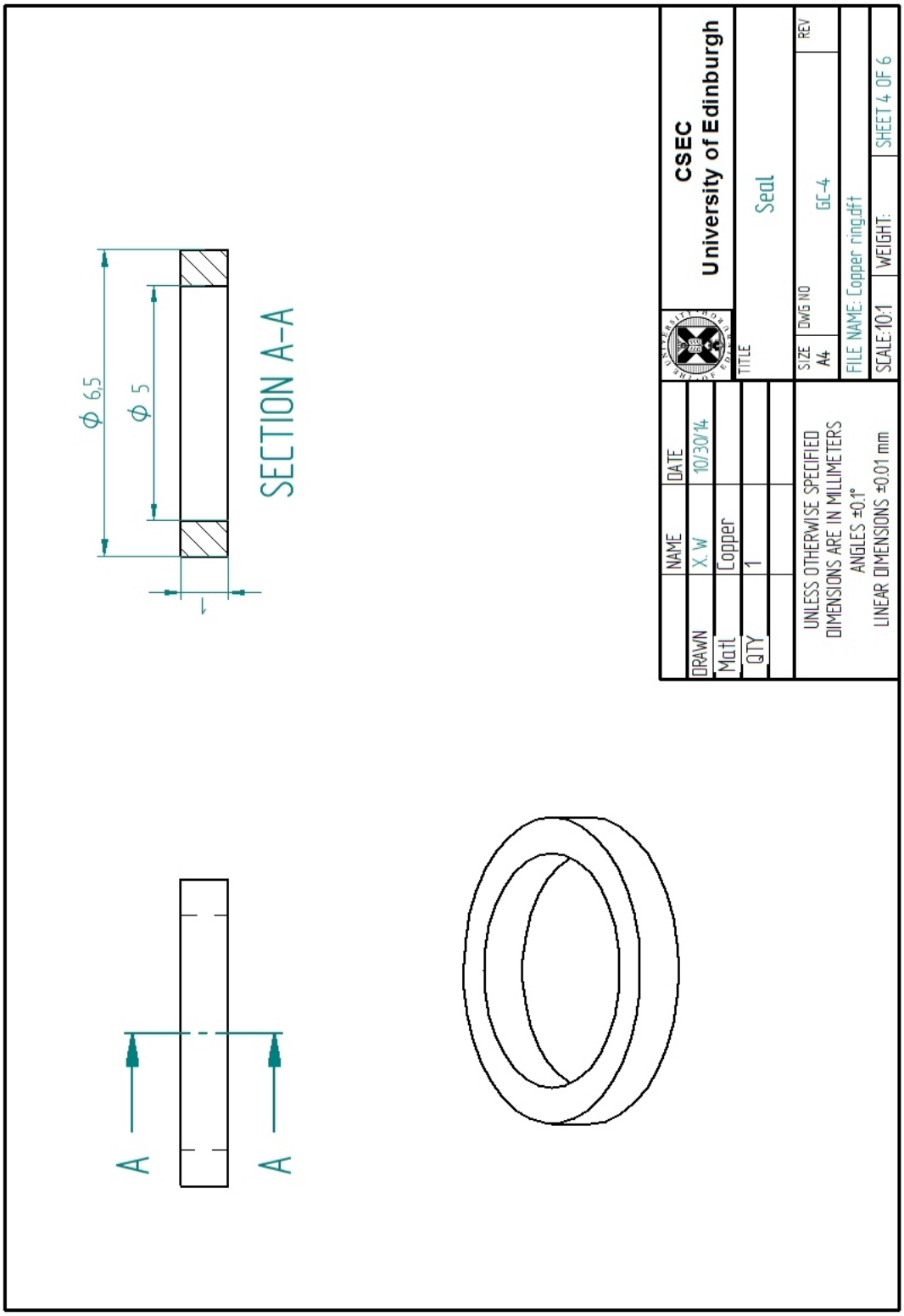

Figure A.4: *The drawing of copper seal.*

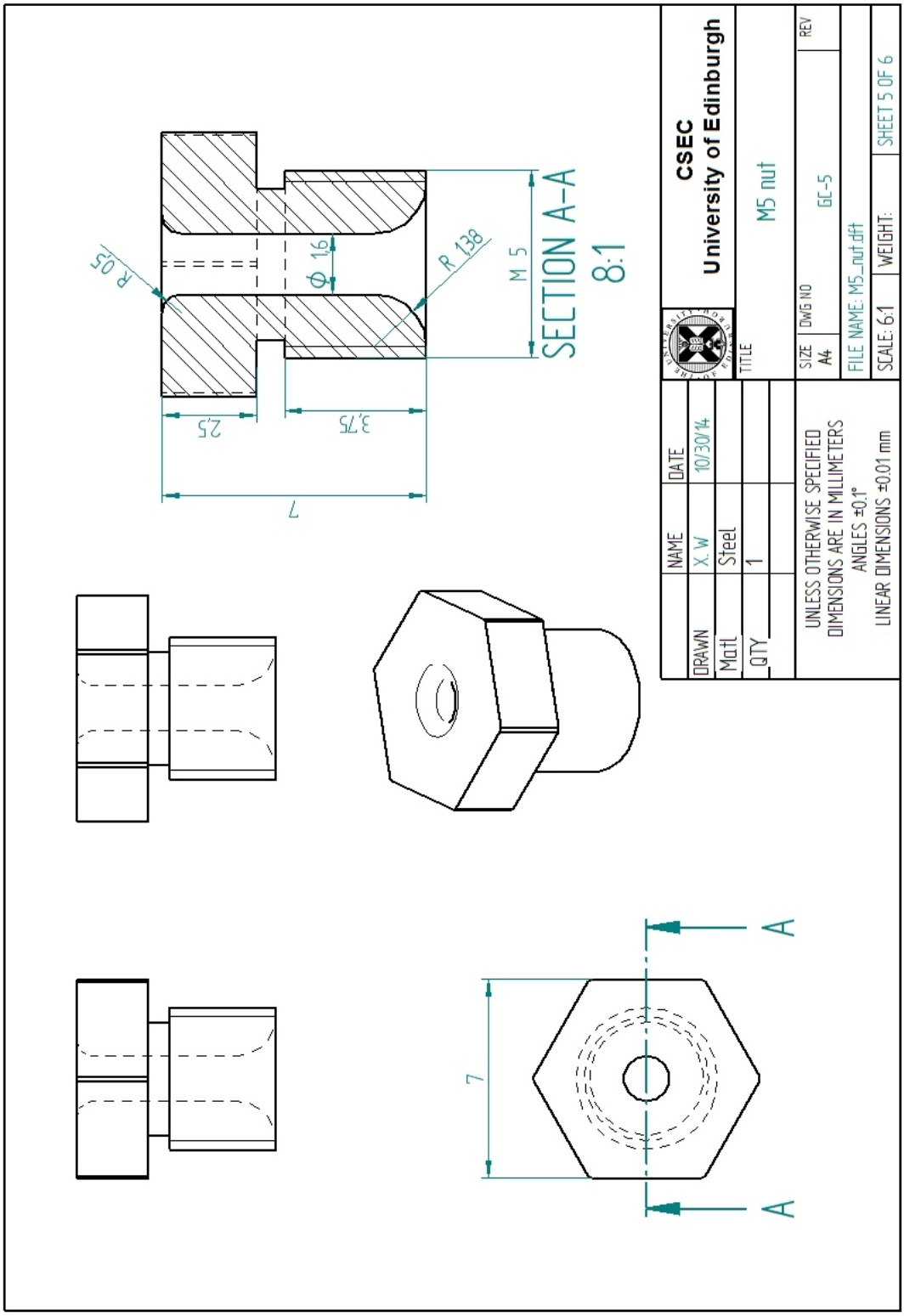

Figure A.5: *The drawing of M5 nut.*

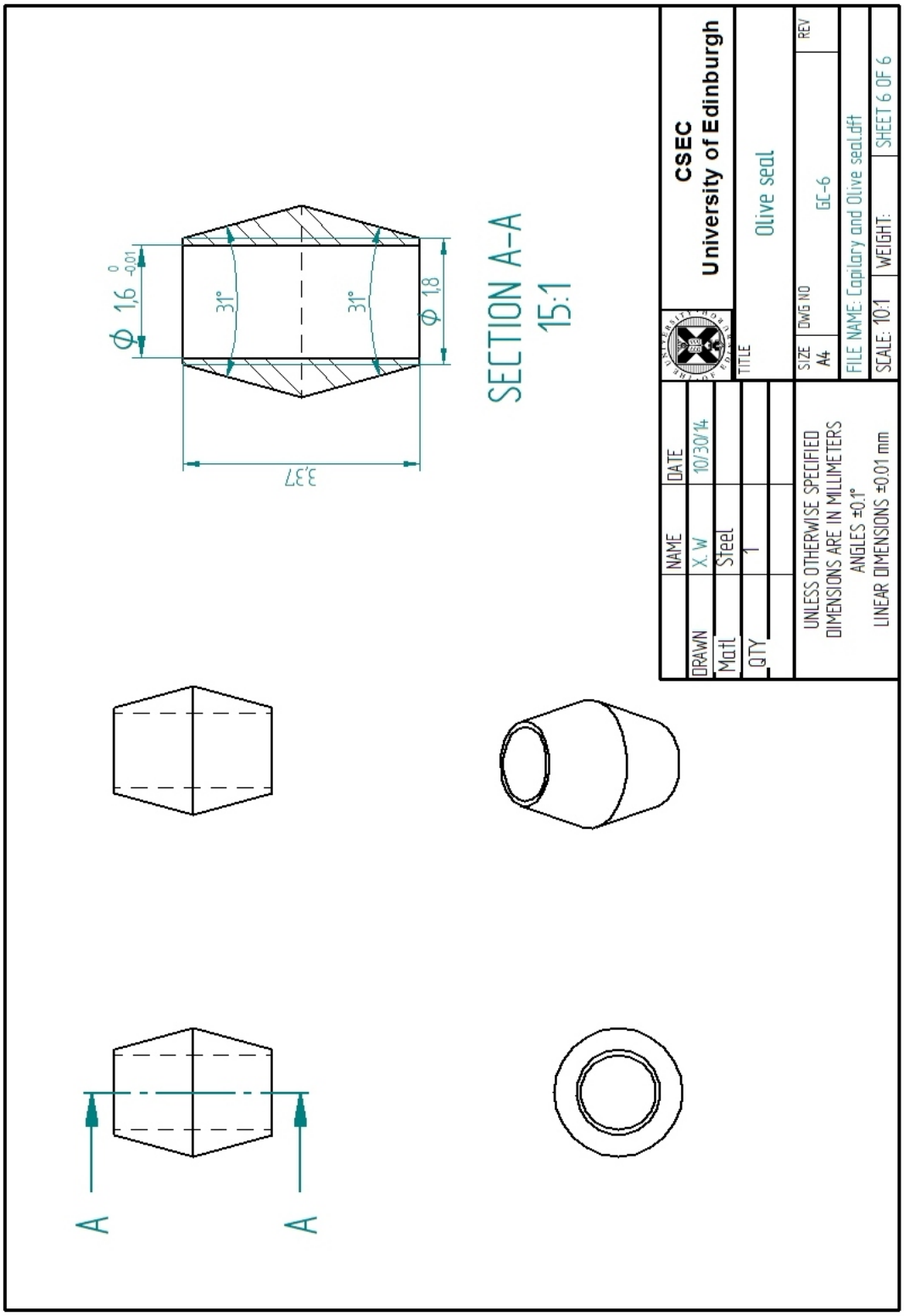

Figure A.6: *The drawing of olive seal.*

Appendix B
Drawings of TM-3He-DAC

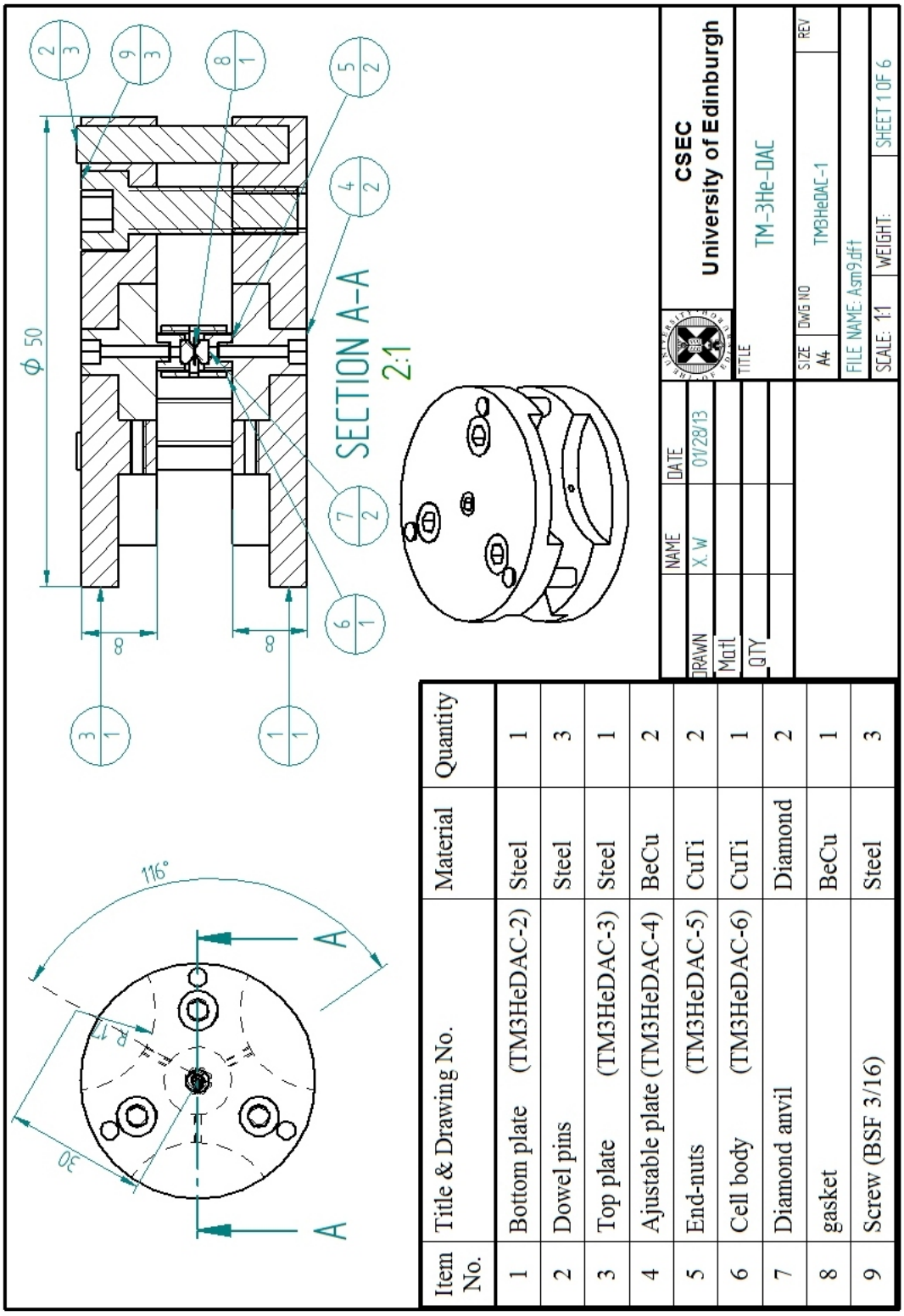

Item No.	Title & Drawing No.	Material	Quantity
1	Bottom plate (TM3HeDAC-2)	Steel	1
2	Dowel pins	Steel	3
3	Top plate (TM3HeDAC-3)	Steel	1
4	Ajustable plate (TM3HeDAC-4)	BeCu	2
5	End-nuts (TM3HeDAC-5)	CuTi	2
6	Cell body (TM3HeDAC-6)	CuTi	1
7	Diamond anvil	Diamond	2
8	gasket	BeCu	1
9	Screw (BSF 3/16)	Steel	3

Figure B.1: *The assemble drawing of the TM-3He-DAC.*

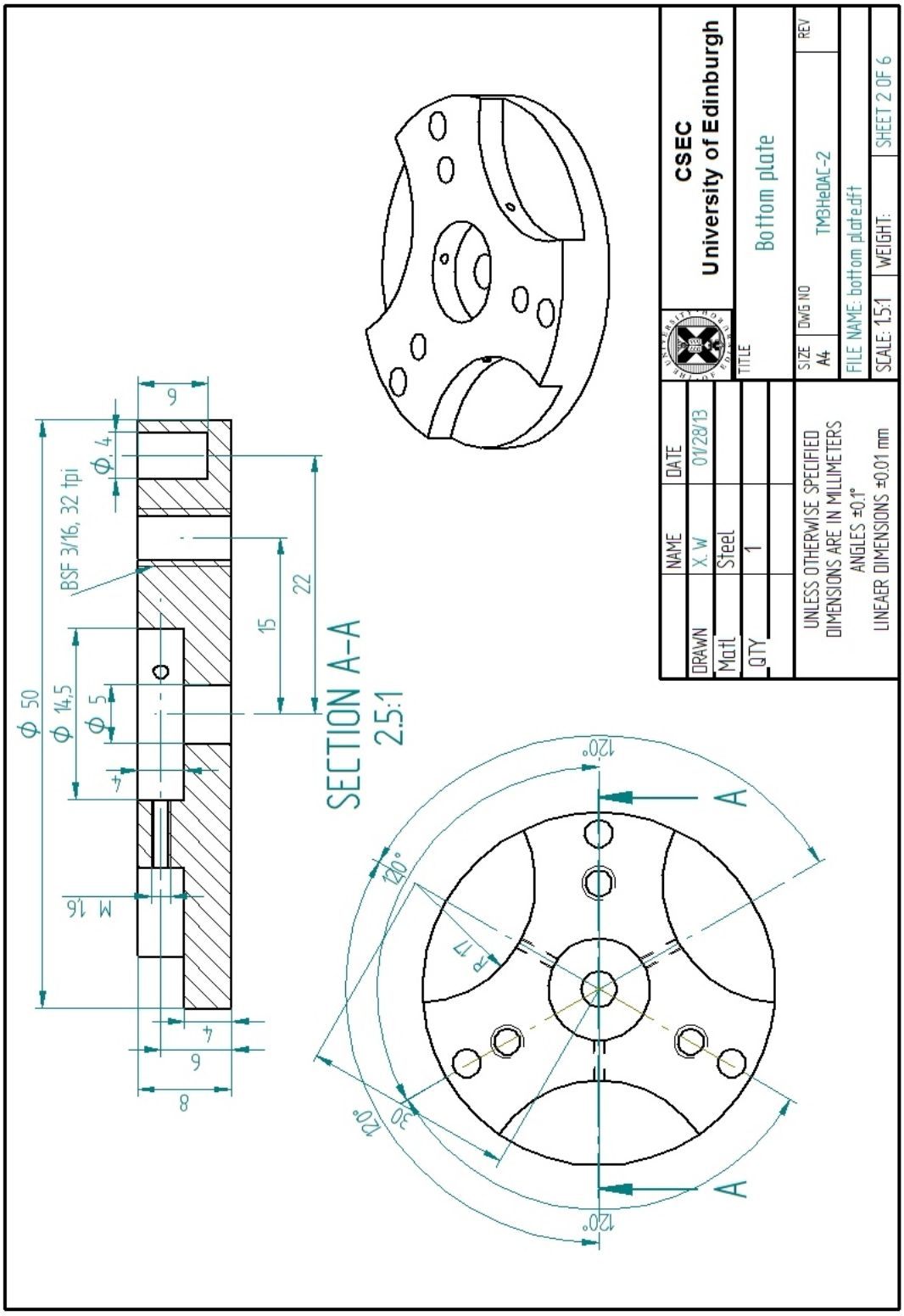

Figure B.2: *The drawing of the bottom plate.*

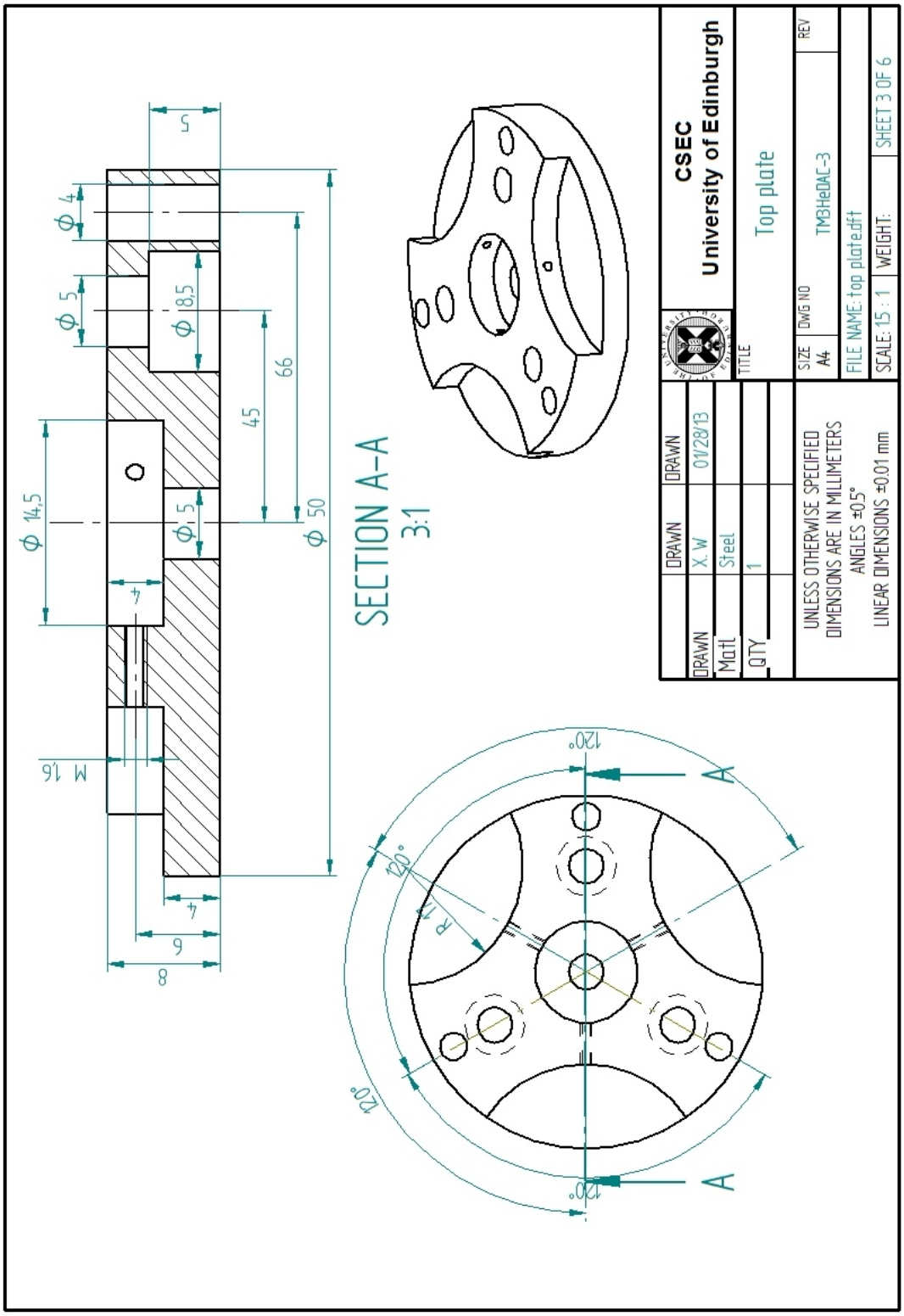

Figure B.3: *The drawing of the top plate.*

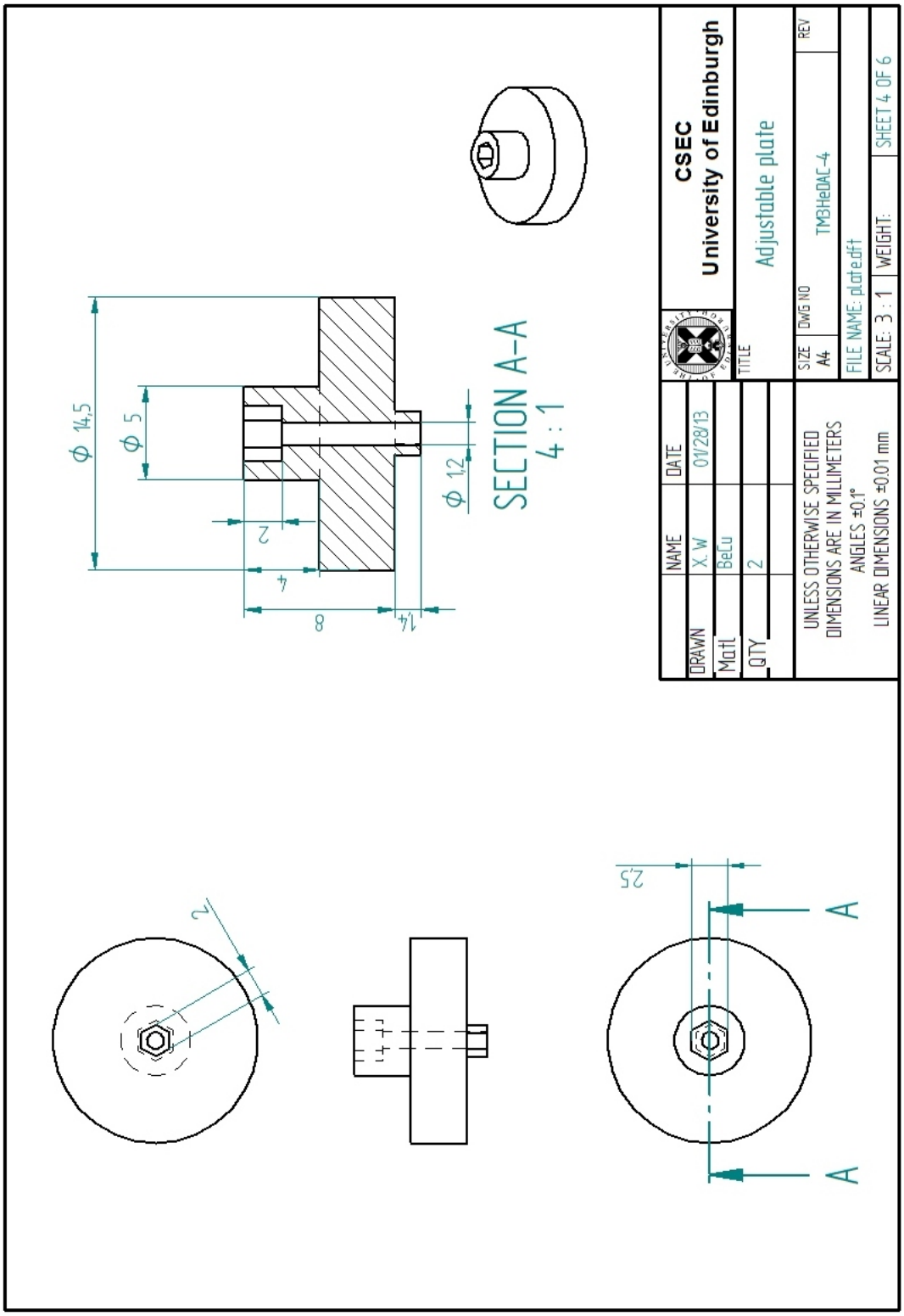

Figure B.4: *The drawing of the adjustable plate.*

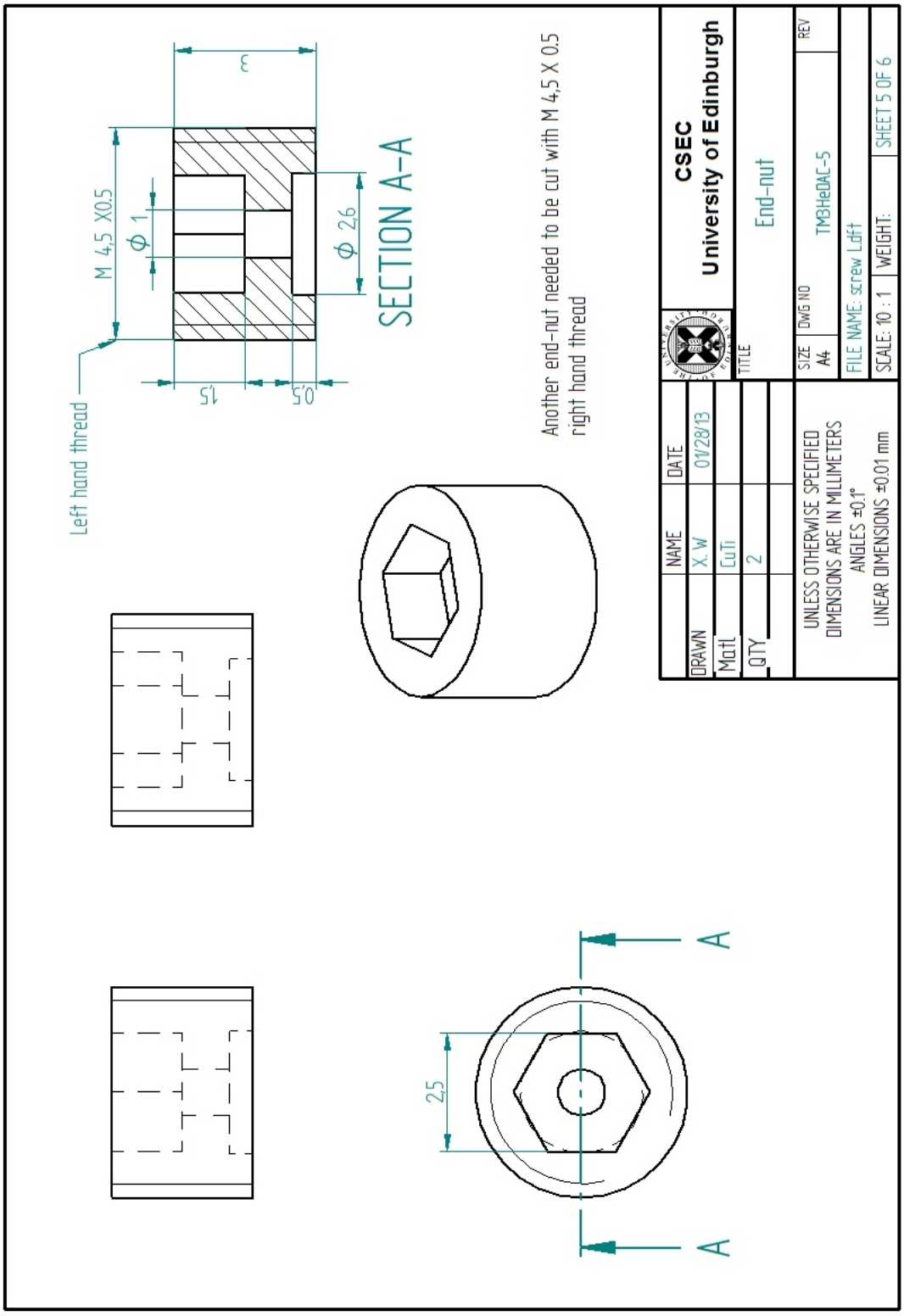

Figure B.5: *The drawing of the end-nut.*

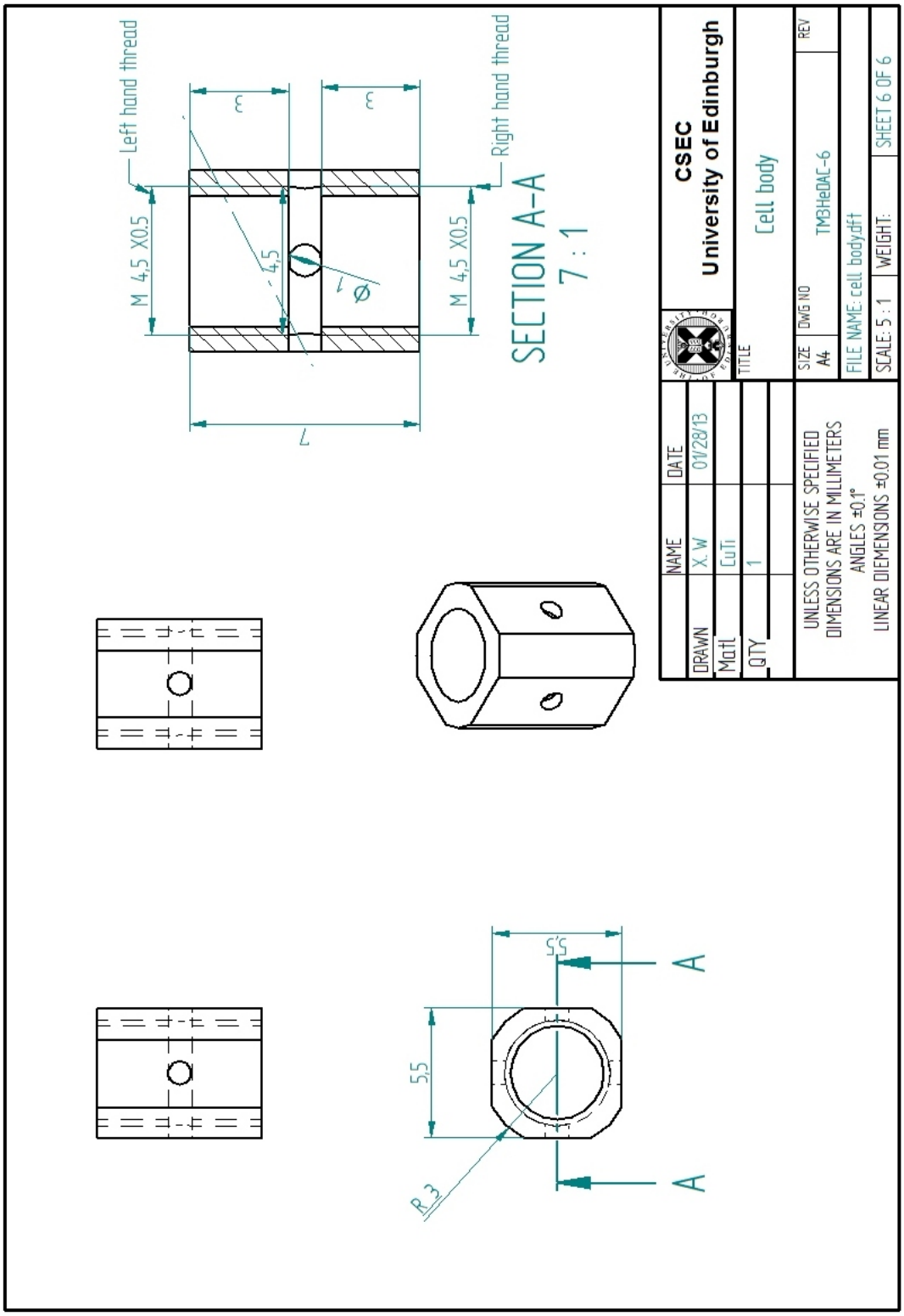

Figure B.6: *The drawing of the cell body.*

Appendix C
Drawings of PTM-DAC

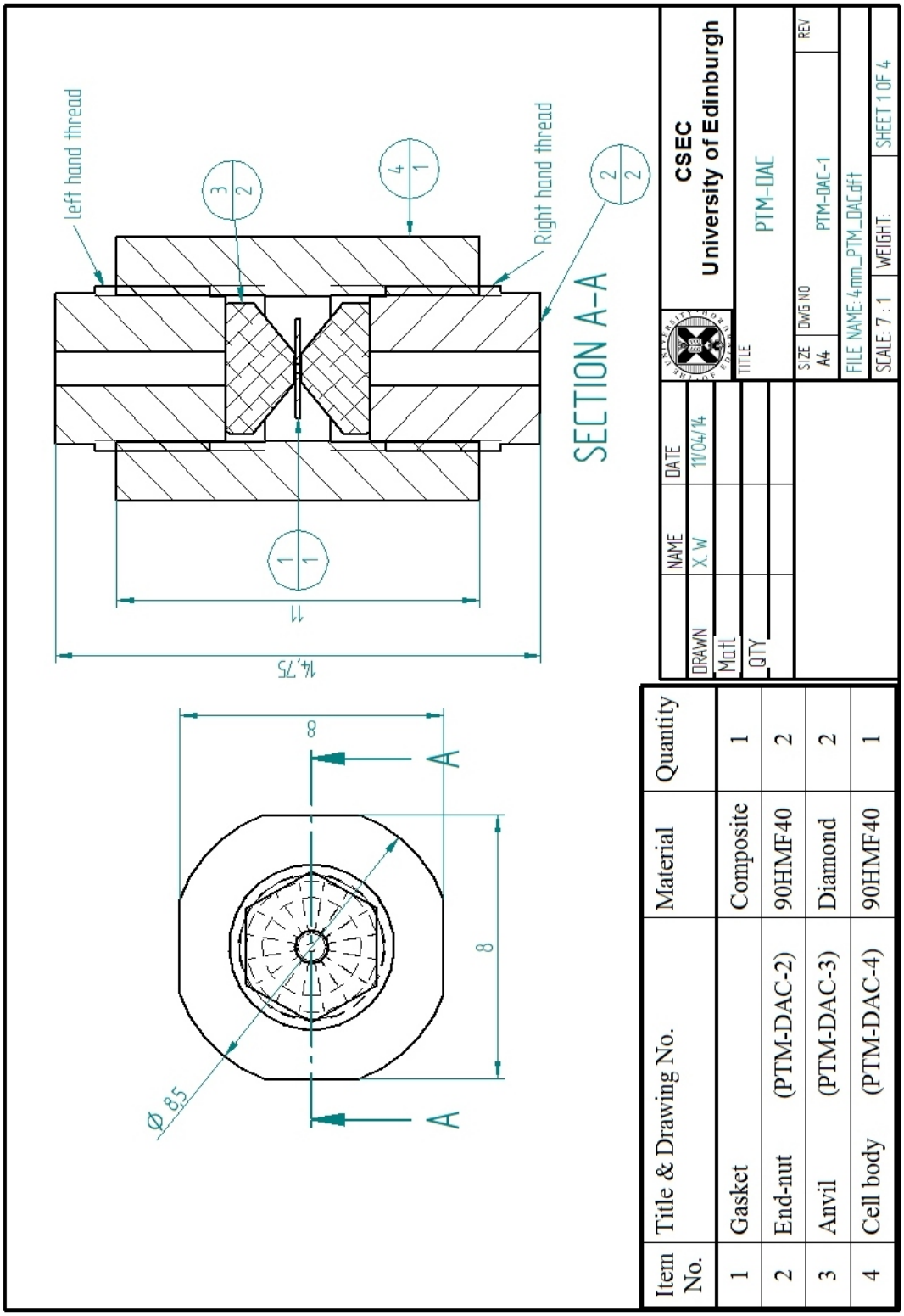

Figure C.1: *The assemble drawing of the PTM-DAC.*

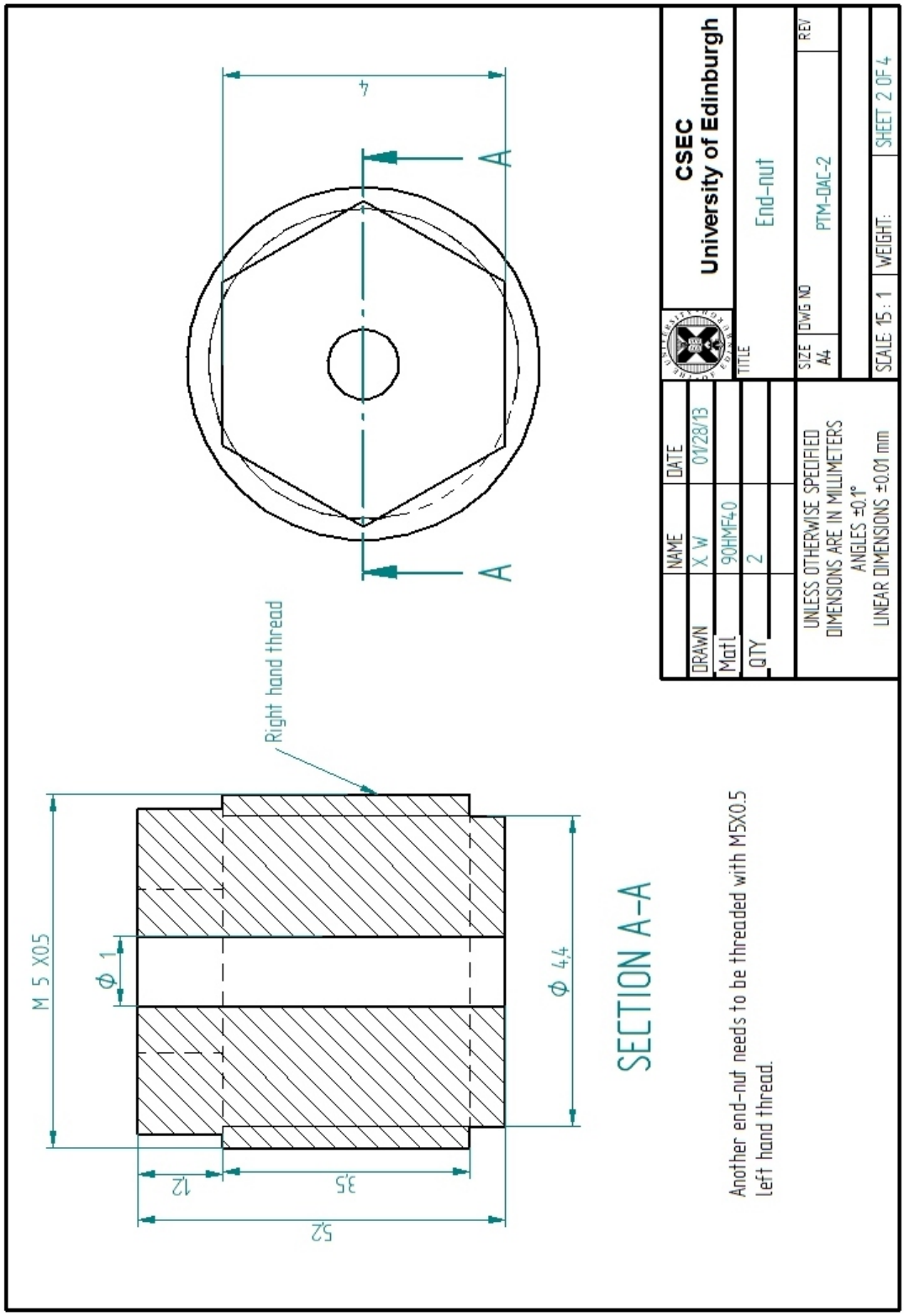

Figure C.2: *The drawing of end-nut.*

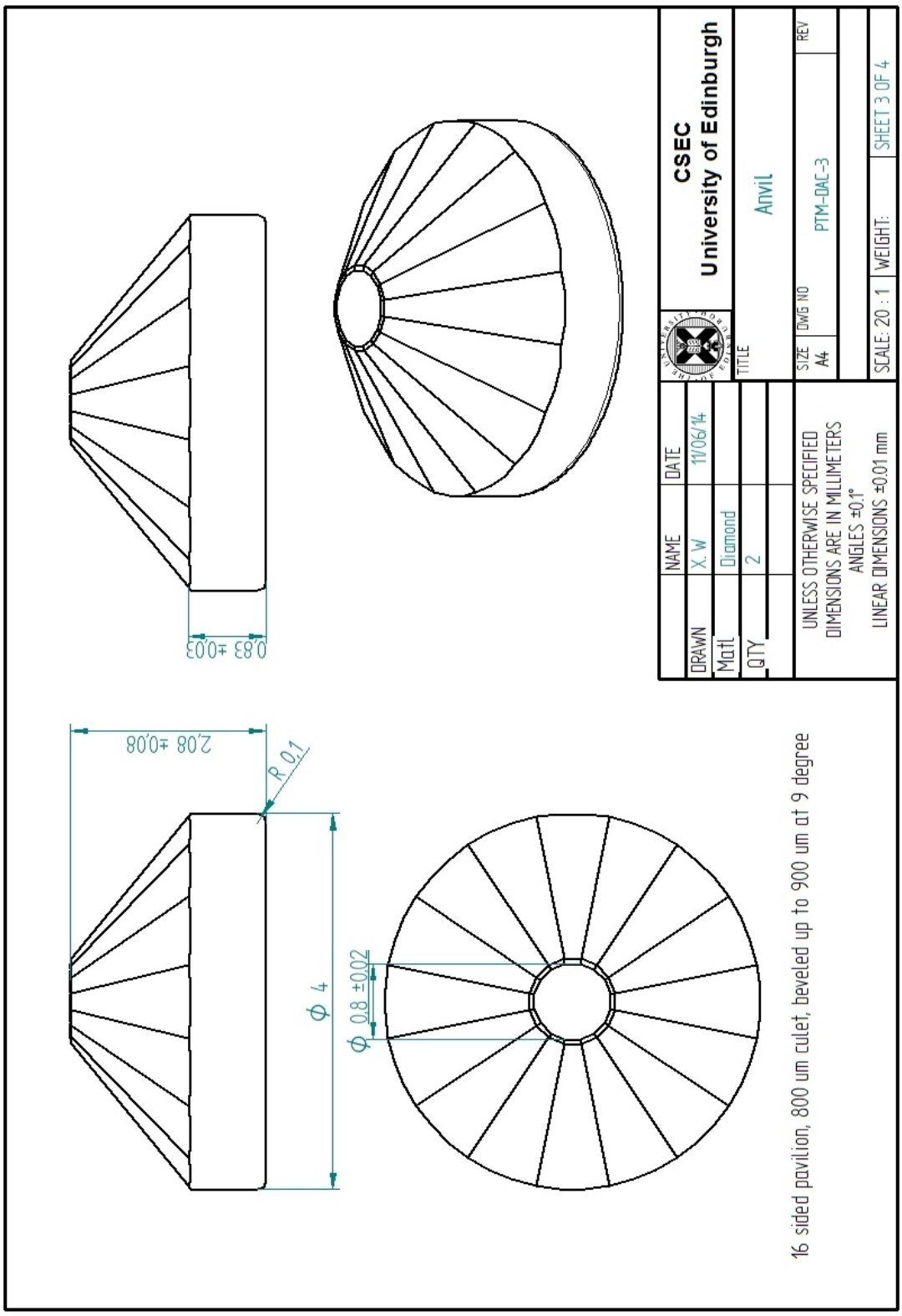

Figure C.3: *The drawing of anvil.*

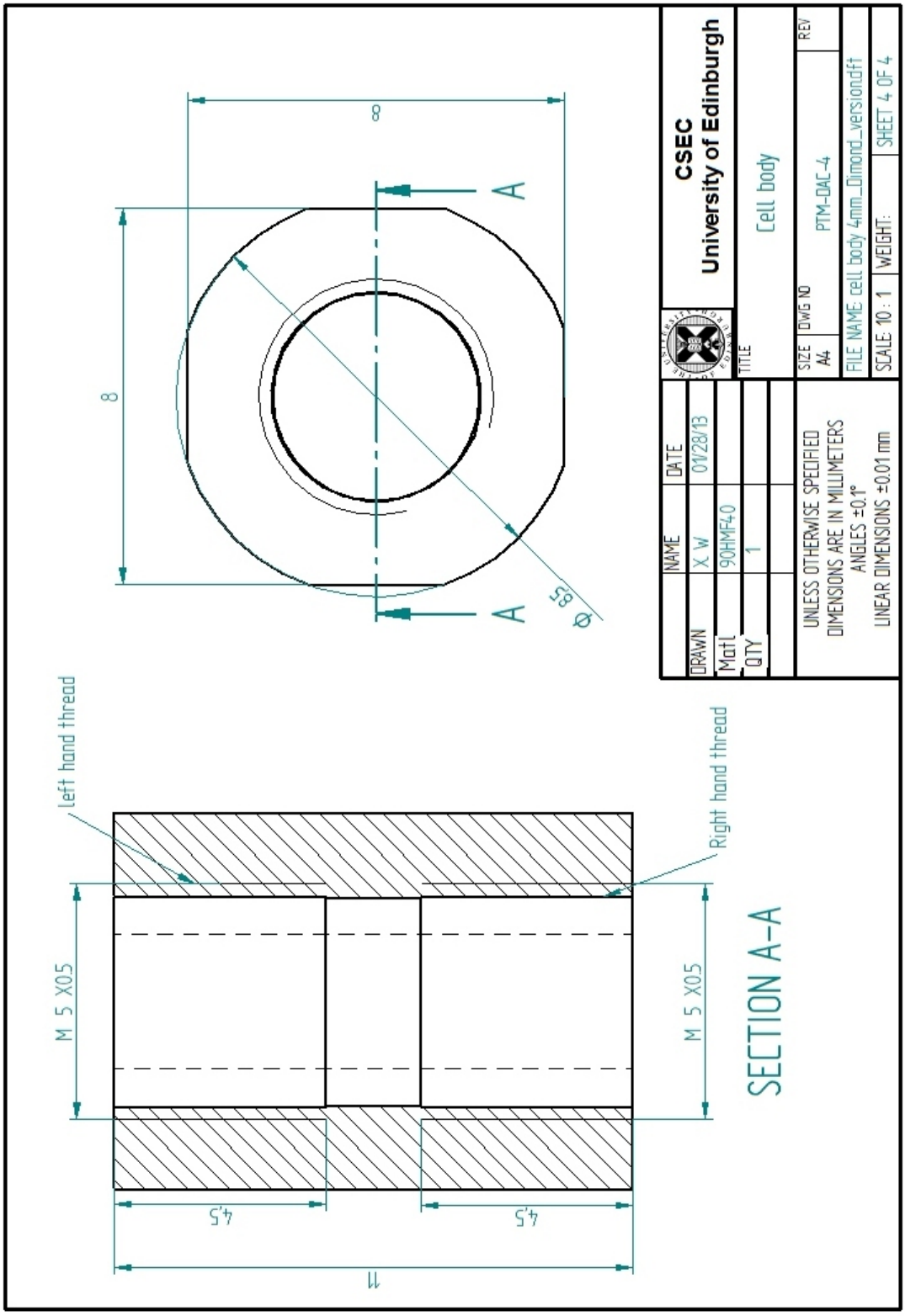

Figure C.4: *The drawing of cell body.*

Appendix D
Drawings of T-SAC

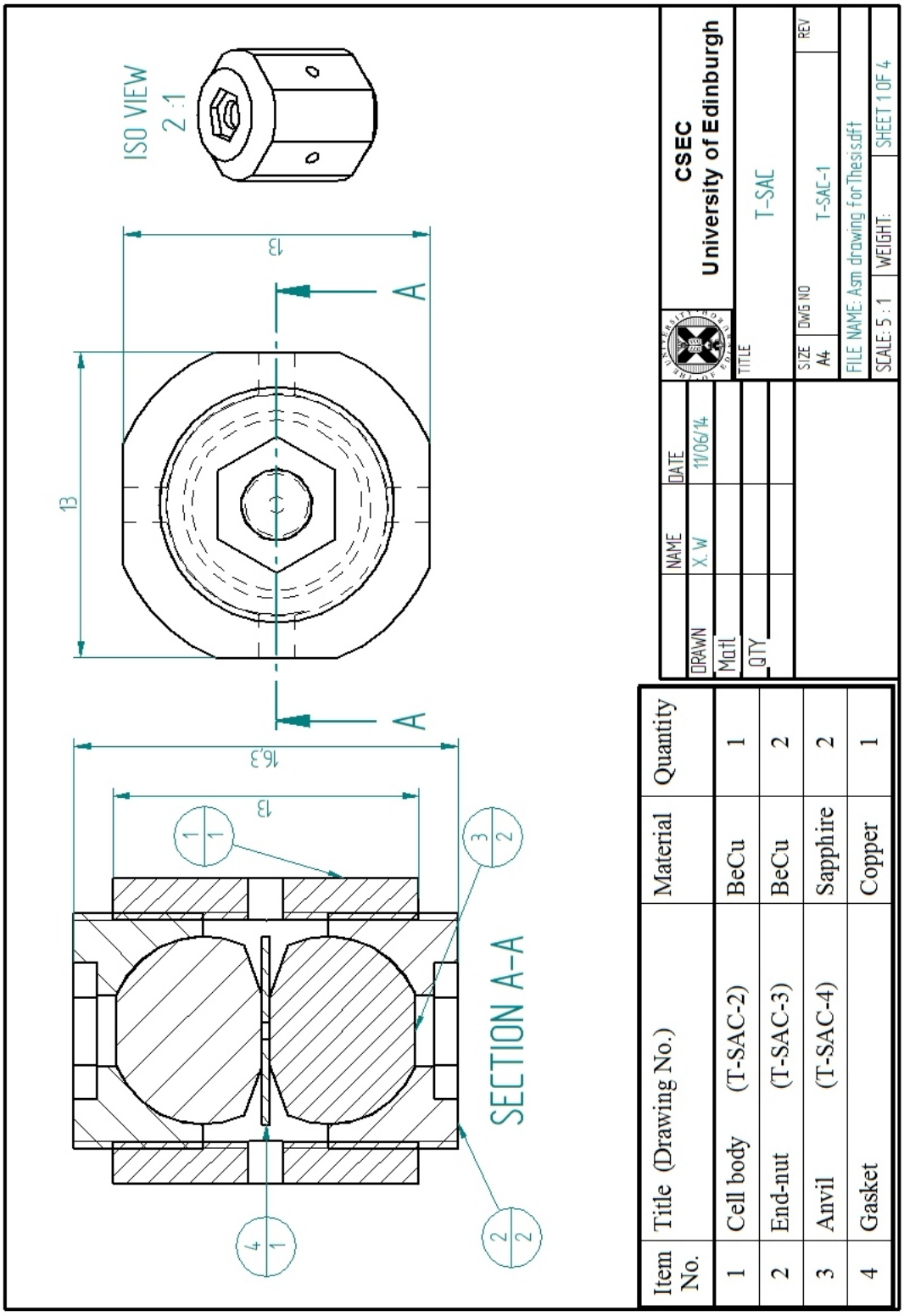

Figure D.1: *The assemble drawing of the T-SAC.*

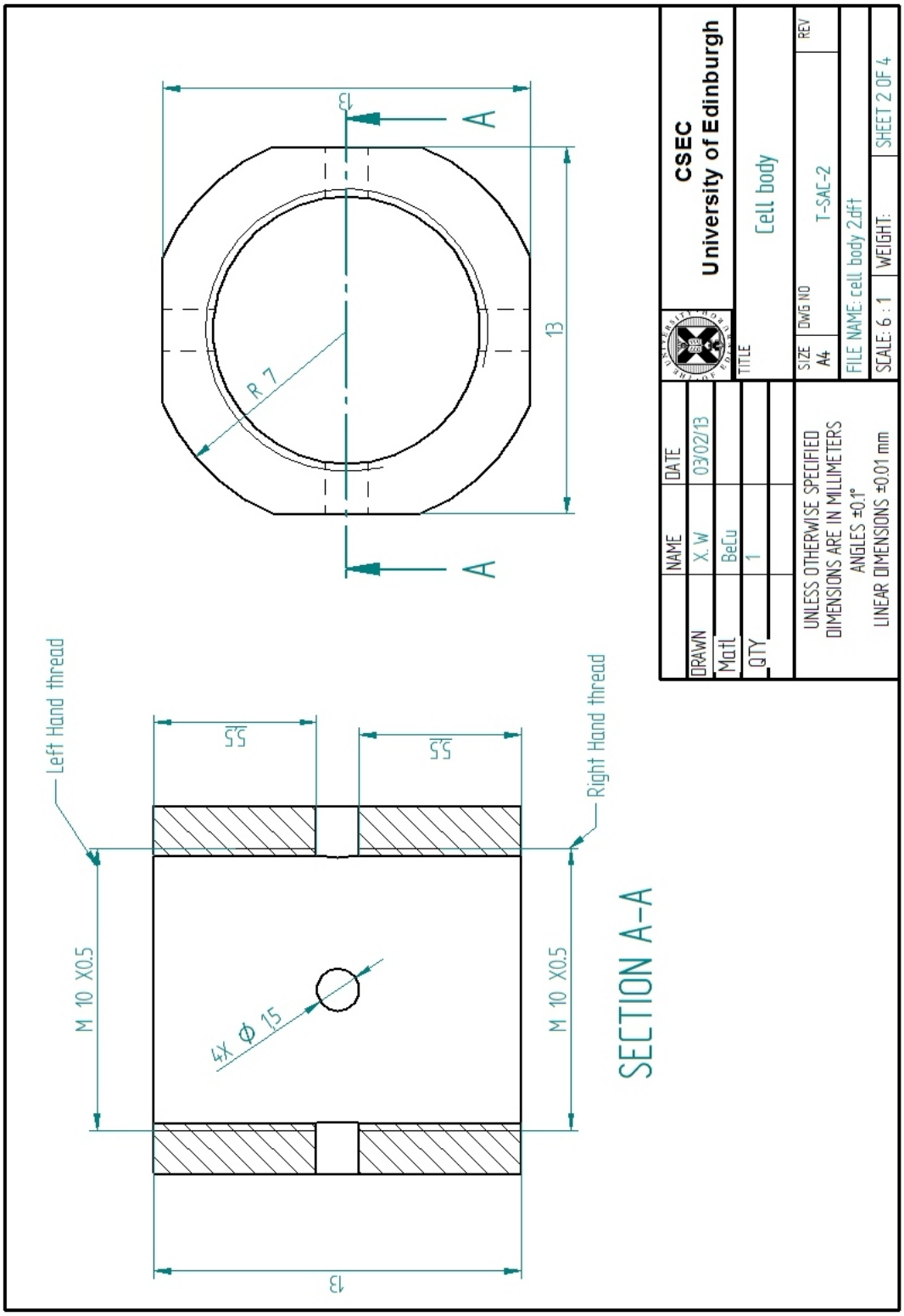

Figure D.2: *The drawing of the cell body.*

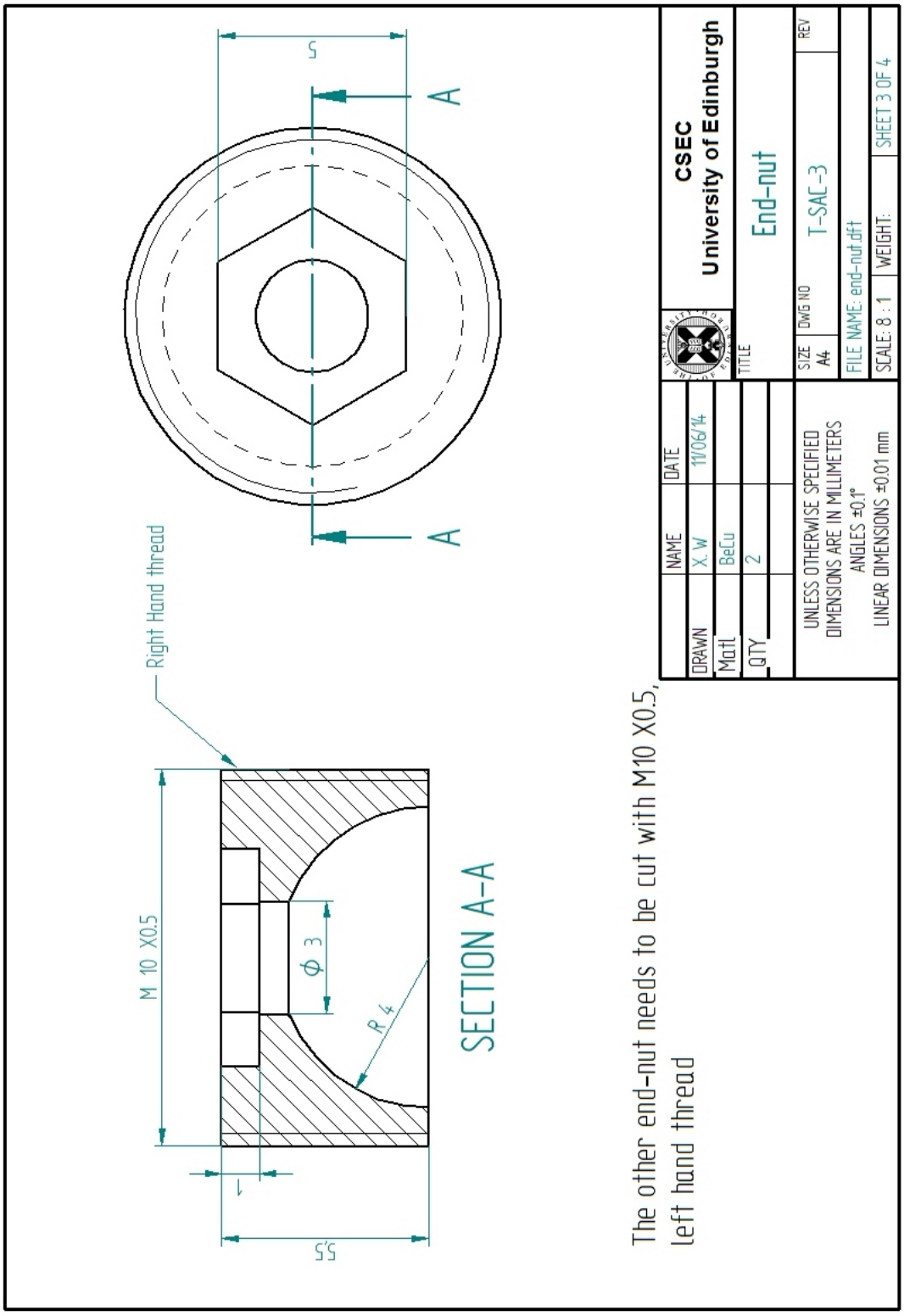

Figure D.3: *The drawing of the end-nut.*

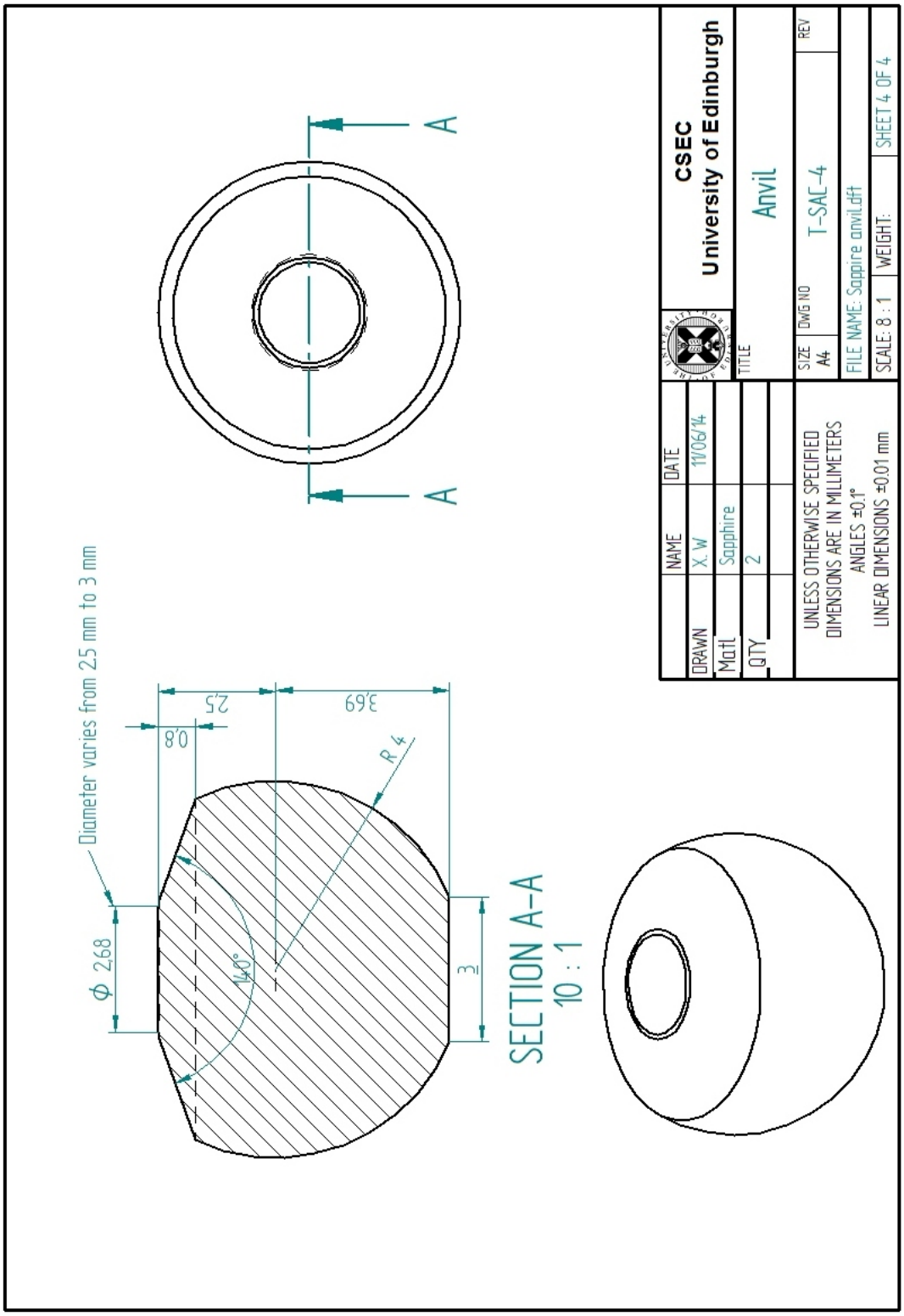

Figure D.4: *The drawing of the anvil.*

Appendix E
Drawings of Large Volumen Piston-cylinder Cell

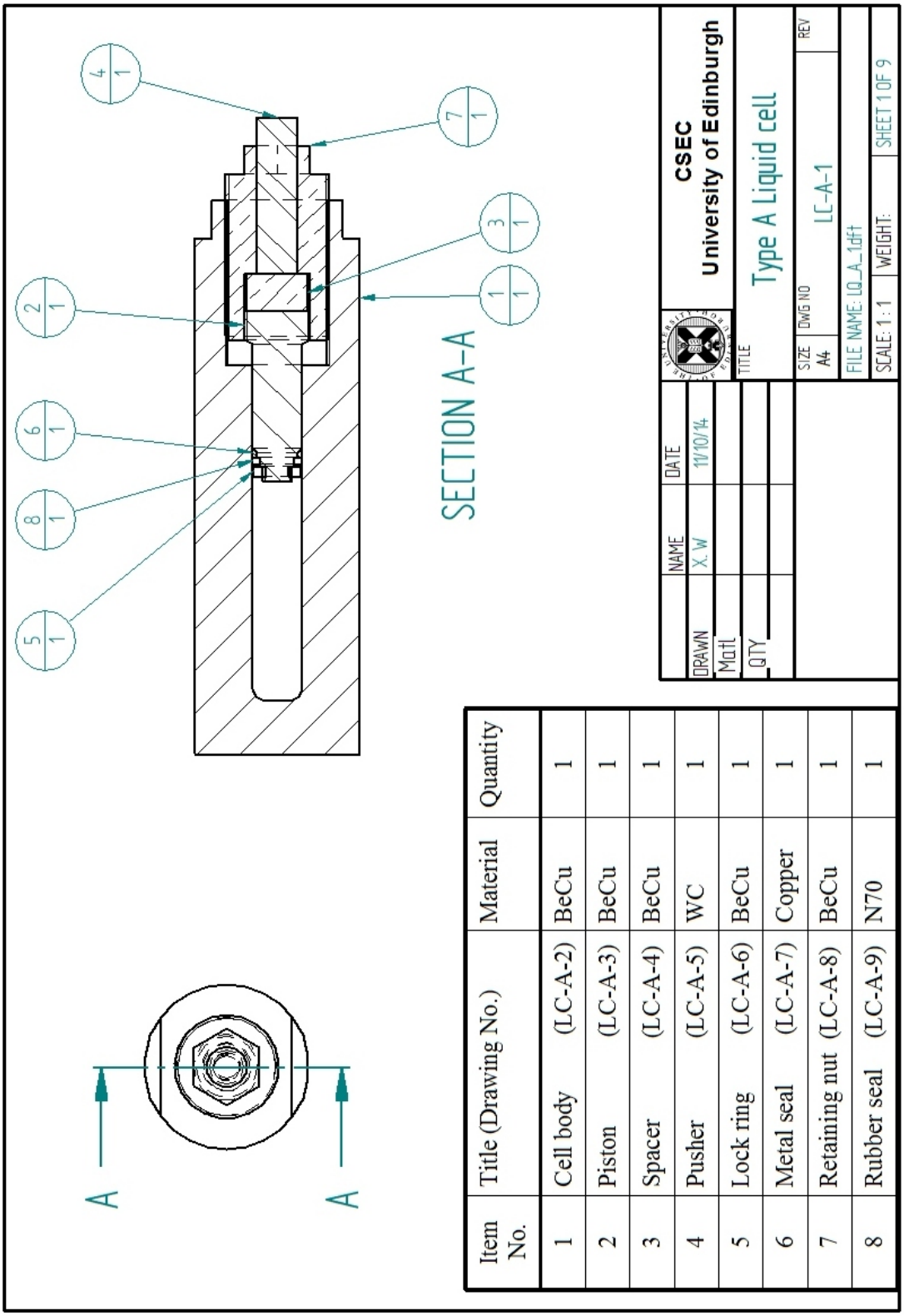

Item No.	Title (Drawing No.)	Material	Quantity
1	Cell body (LC-A-2)	BeCu	1
2	Piston (LC-A-3)	BeCu	1
3	Spacer (LC-A-4)	BeCu	1
4	Pusher (LC-A-5)	WC	1
5	Lock ring (LC-A-6)	BeCu	1
6	Metal seal (LC-A-7)	Copper	1
7	Retaining nut (LC-A-8)	BeCu	1
8	Rubber seal (LC-A-9)	N70	1

Figure E.1: *The assemble drawing of the type A liquid cell.*

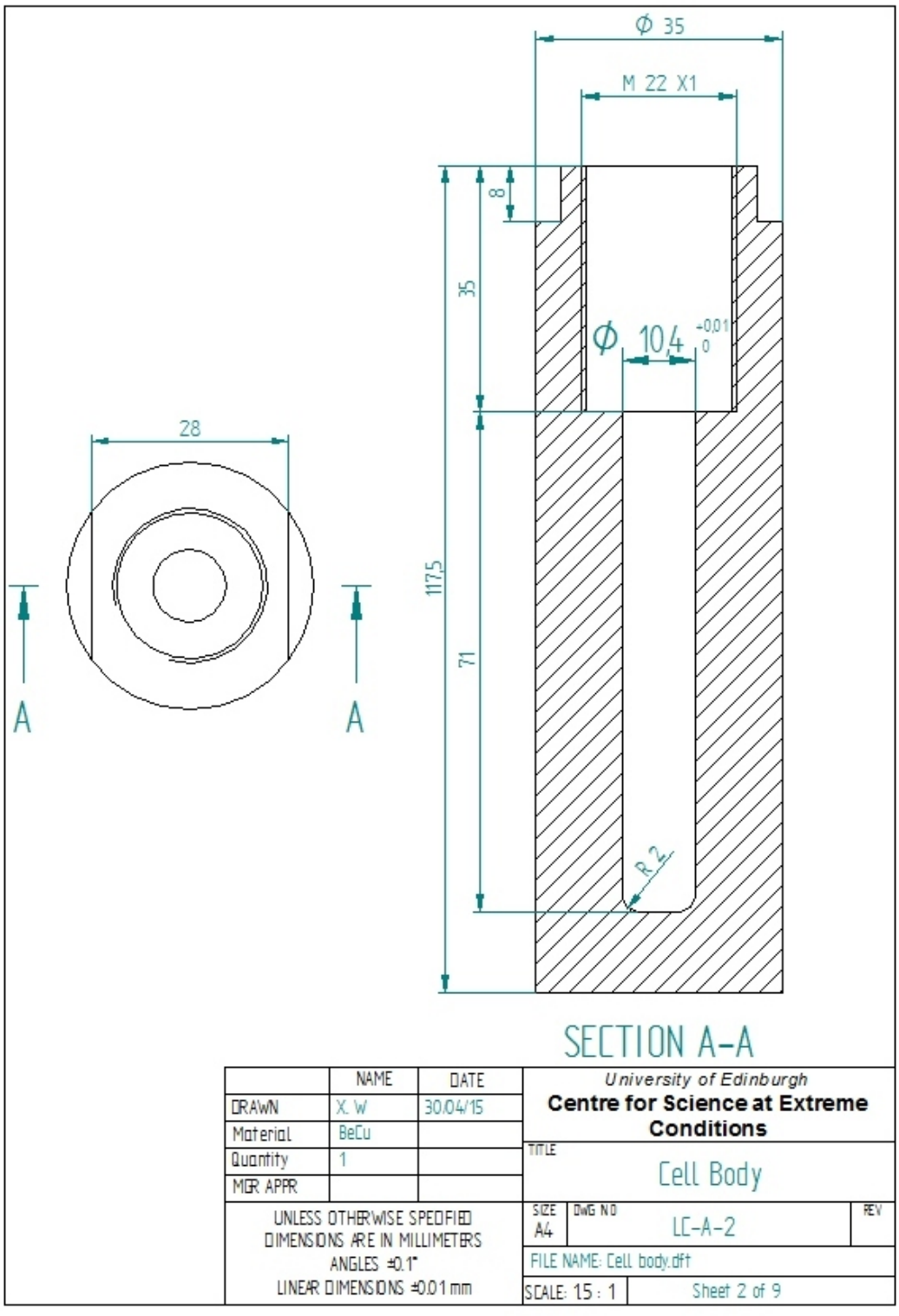

Figure E.2: *The drawing of the cell body (type A liquid cell).*

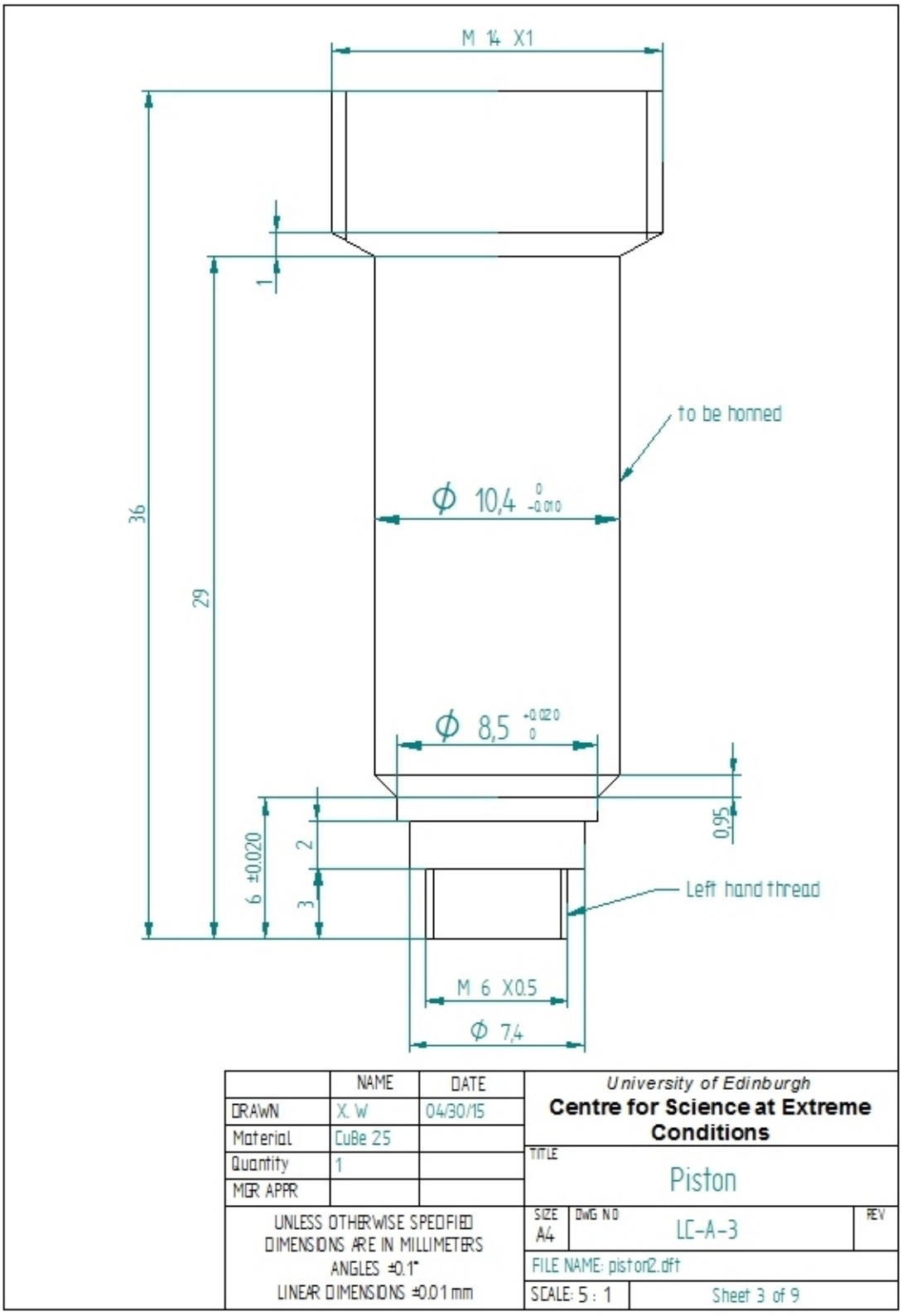

Figure E.3: *The drawing of the piston (type A liquid cell).*

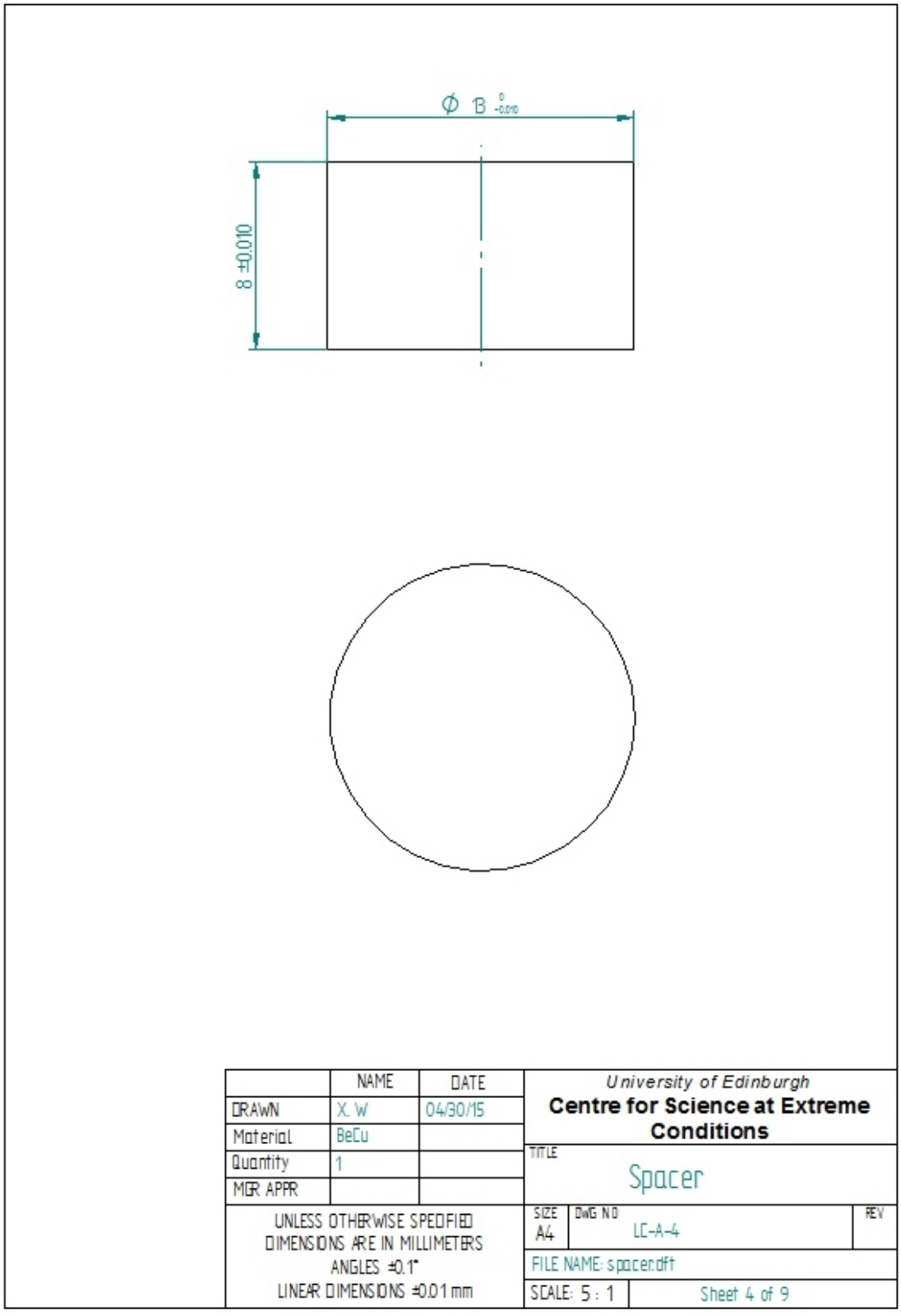

Figure E.4: *The drawing of the spacer.*

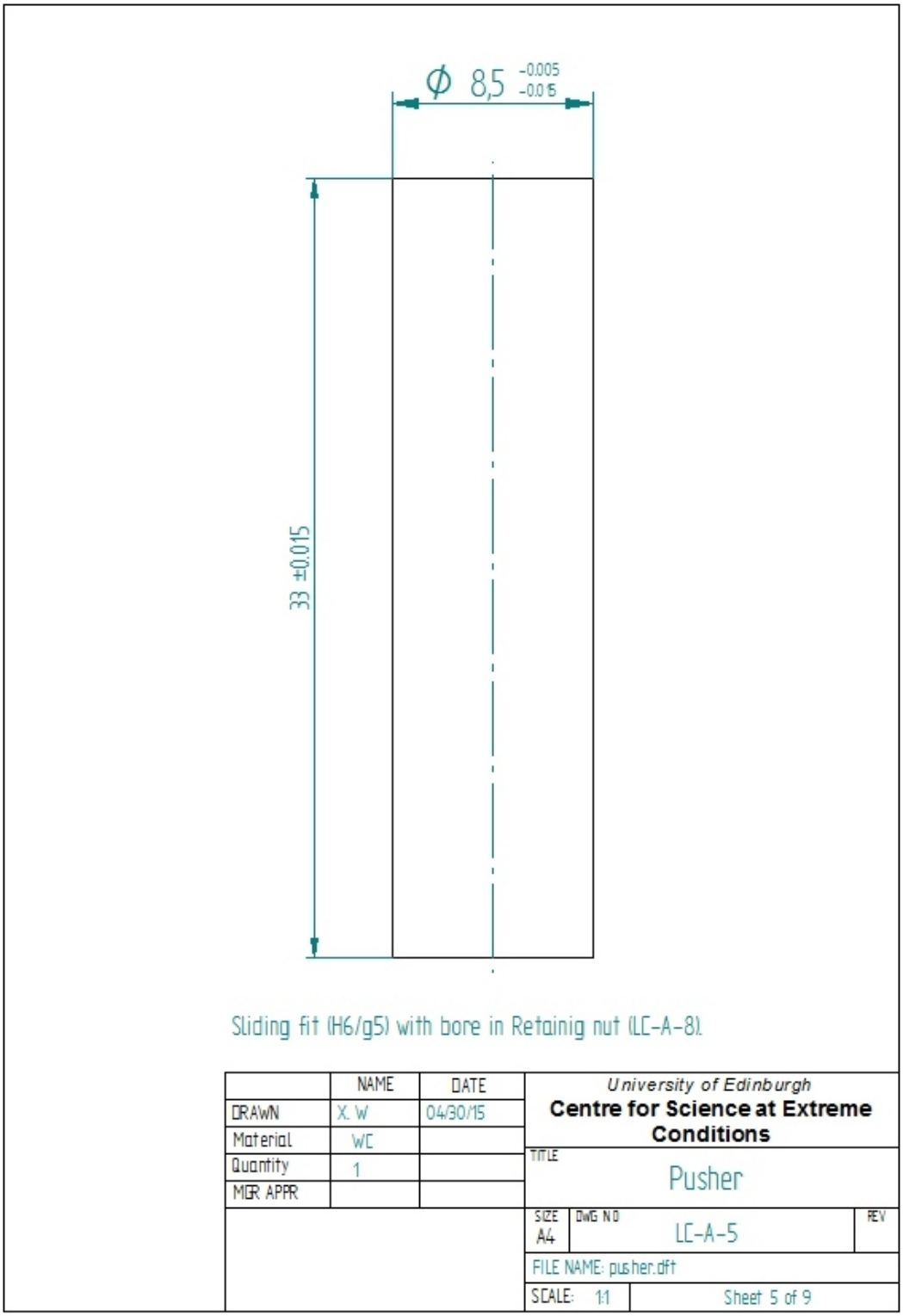

Figure E.5: *The drawing of the pusher.*

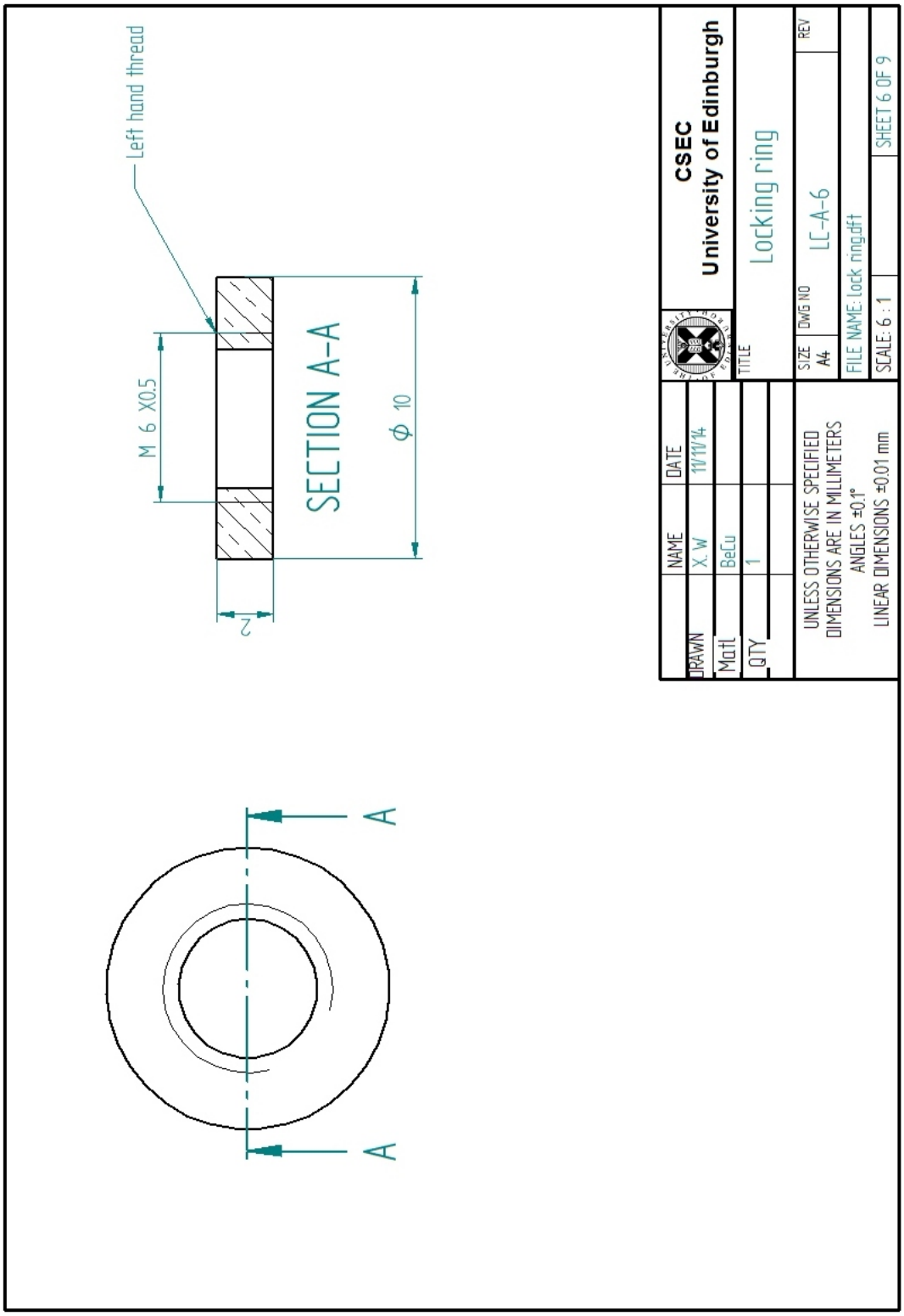

Figure E.6: *The drawing of the locking ring.*

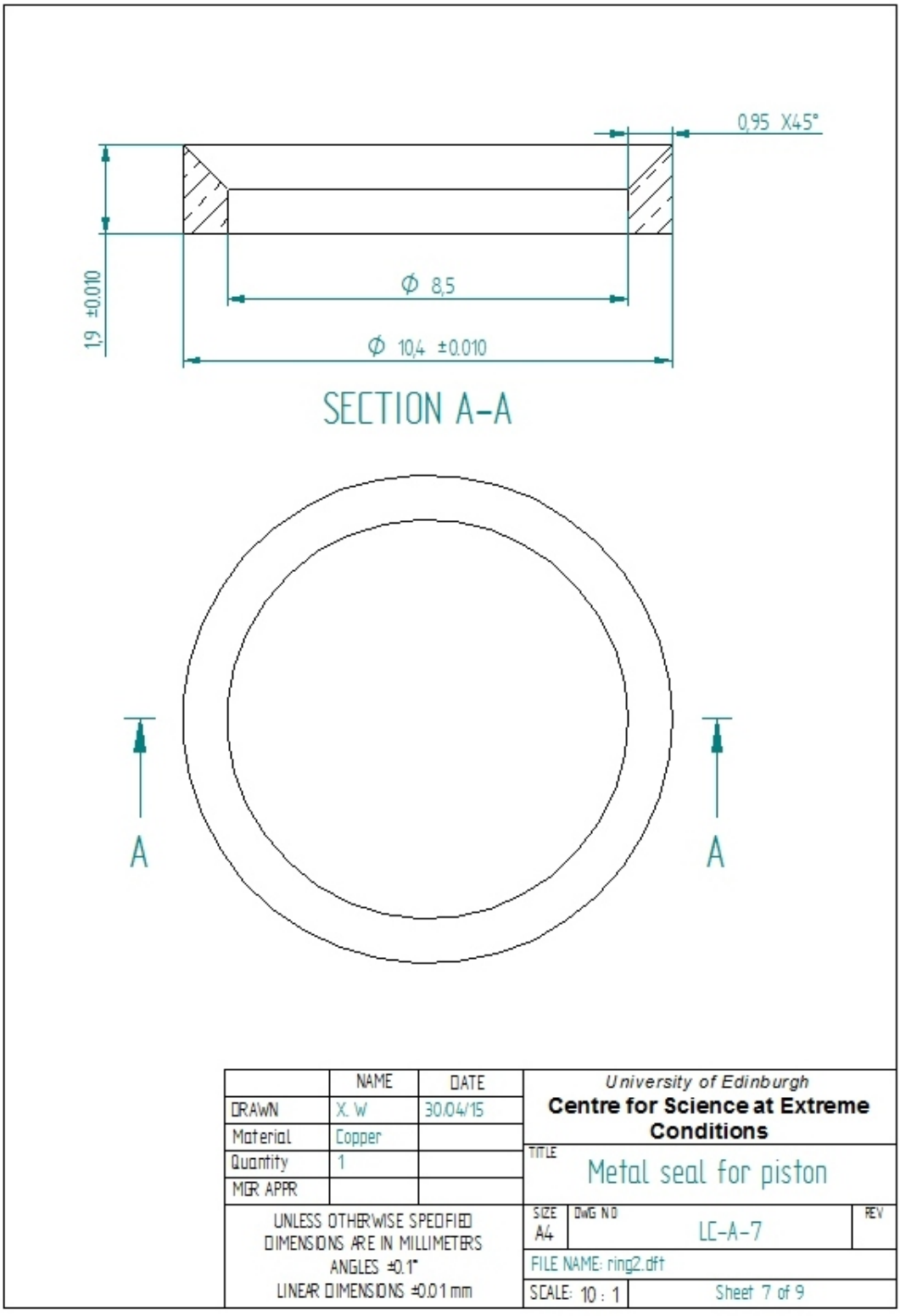

Figure E.7: *The drawing of the metal seal*

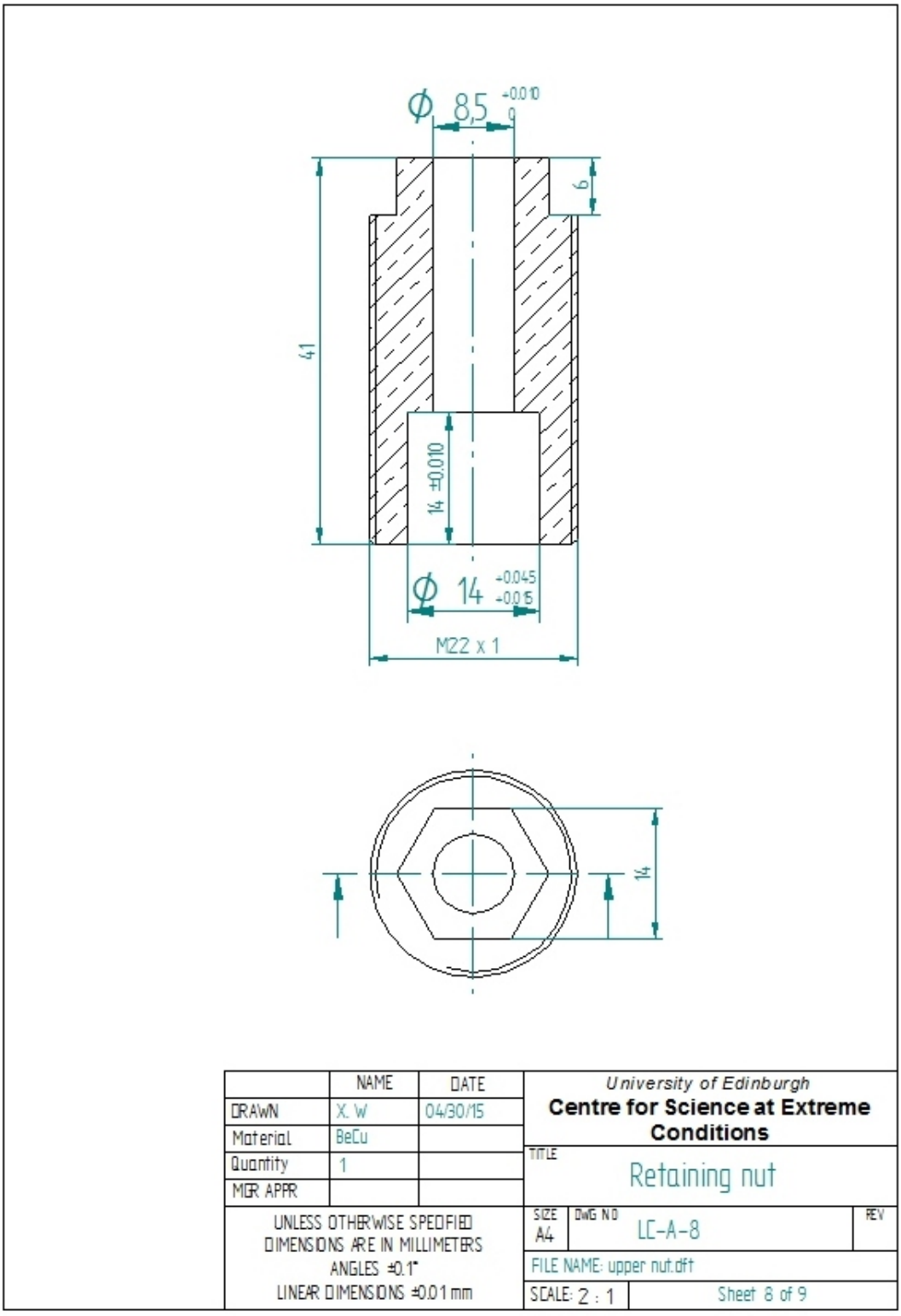

	NAME	DATE
DRAWN	X. W	04/30/15
Material	BeCu	
Quantity	1	
MGR APPR		

UNLESS OTHERWISE SPECIFIED
DIMENSIONS ARE IN MILLIMETERS
ANGLES ±0.1°
LINEAR DIMENSIONS ±0.01 mm

University of Edinburgh
Centre for Science at Extreme Conditions

TITLE: Retaining nut

SIZE A4 | DWG NO LC-A-8 | REV

FILE NAME: upper nut.dft

SCALE: 2 : 1 | Sheet 8 of 9

Figure E.8: *The drawing of the retaining nut.*

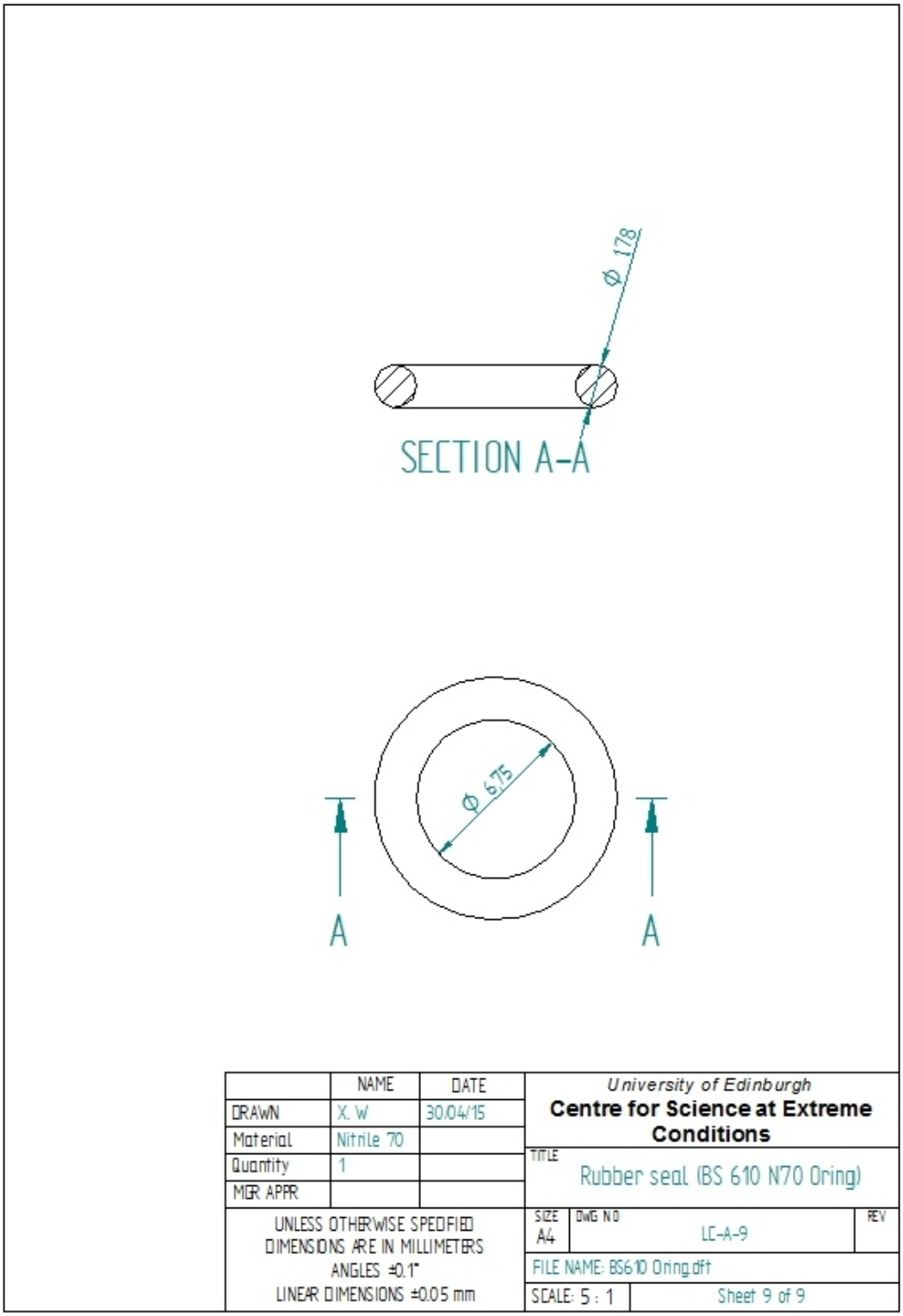

Figure E.9: *The drawing of the rubber seal.*

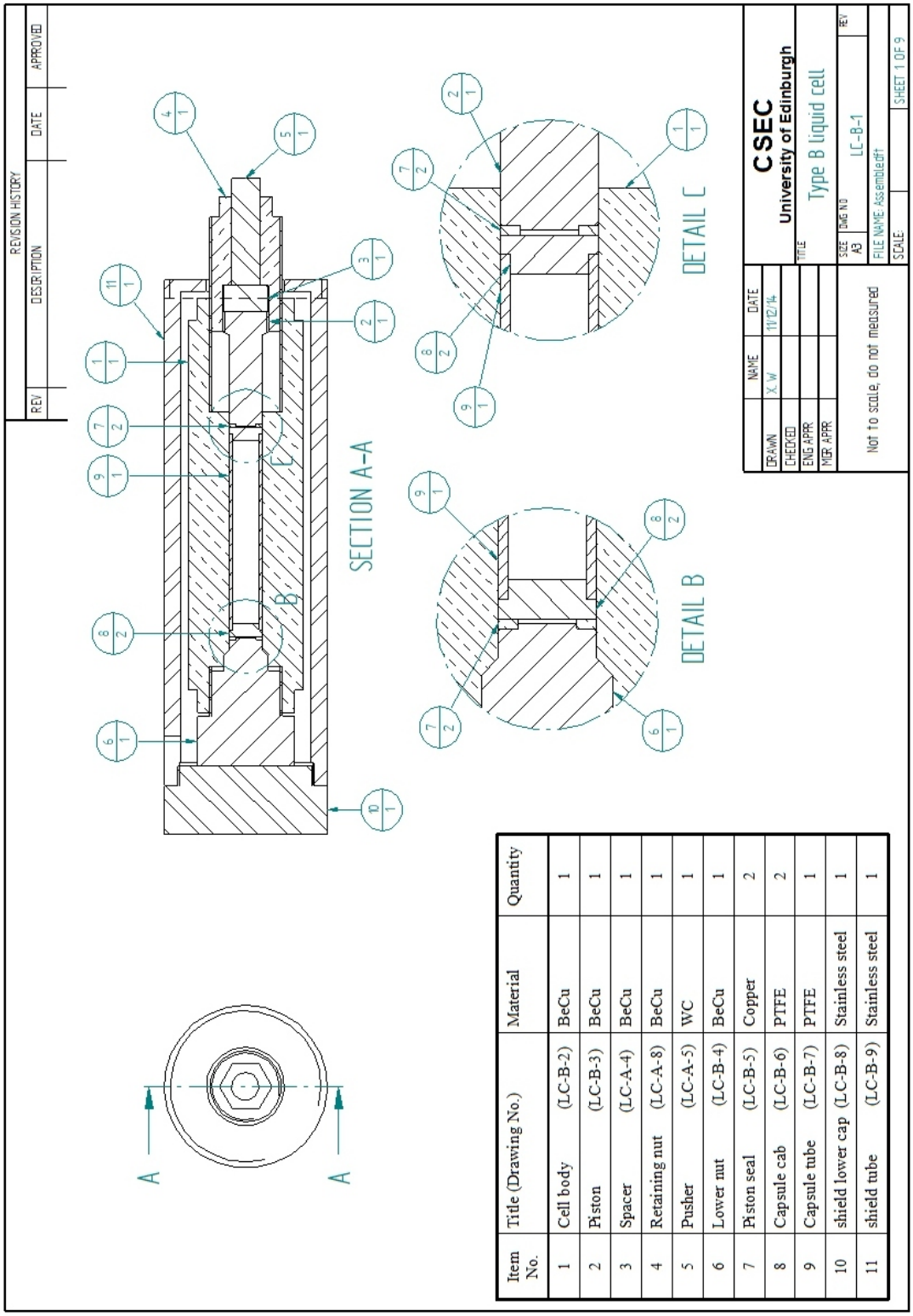

Item No.	Title (Drawing No.)		Material	Quantity
1	Cell body	(LC-B-2)	BeCu	1
2	Piston	(LC-B-3)	BeCu	1
3	Spacer	(LC-A-4)	BeCu	1
4	Retaining nut	(LC-A-8)	BeCu	1
5	Pusher	(LC-A-5)	WC	1
6	Lower nut	(LC-B-4)	BeCu	1
7	Piston seal	(LC-B-5)	Copper	2
8	Capsule cab	(LC-B-6)	PTFE	2
9	Capsule tube	(LC-B-7)	PTFE	1
10	shield lower cap	(LC-B-8)	Stainless steel	1
11	shield tube	(LC-B-9)	Stainless steel	1

Figure E.10: *The assemble drawing of the type B liquid cell.*

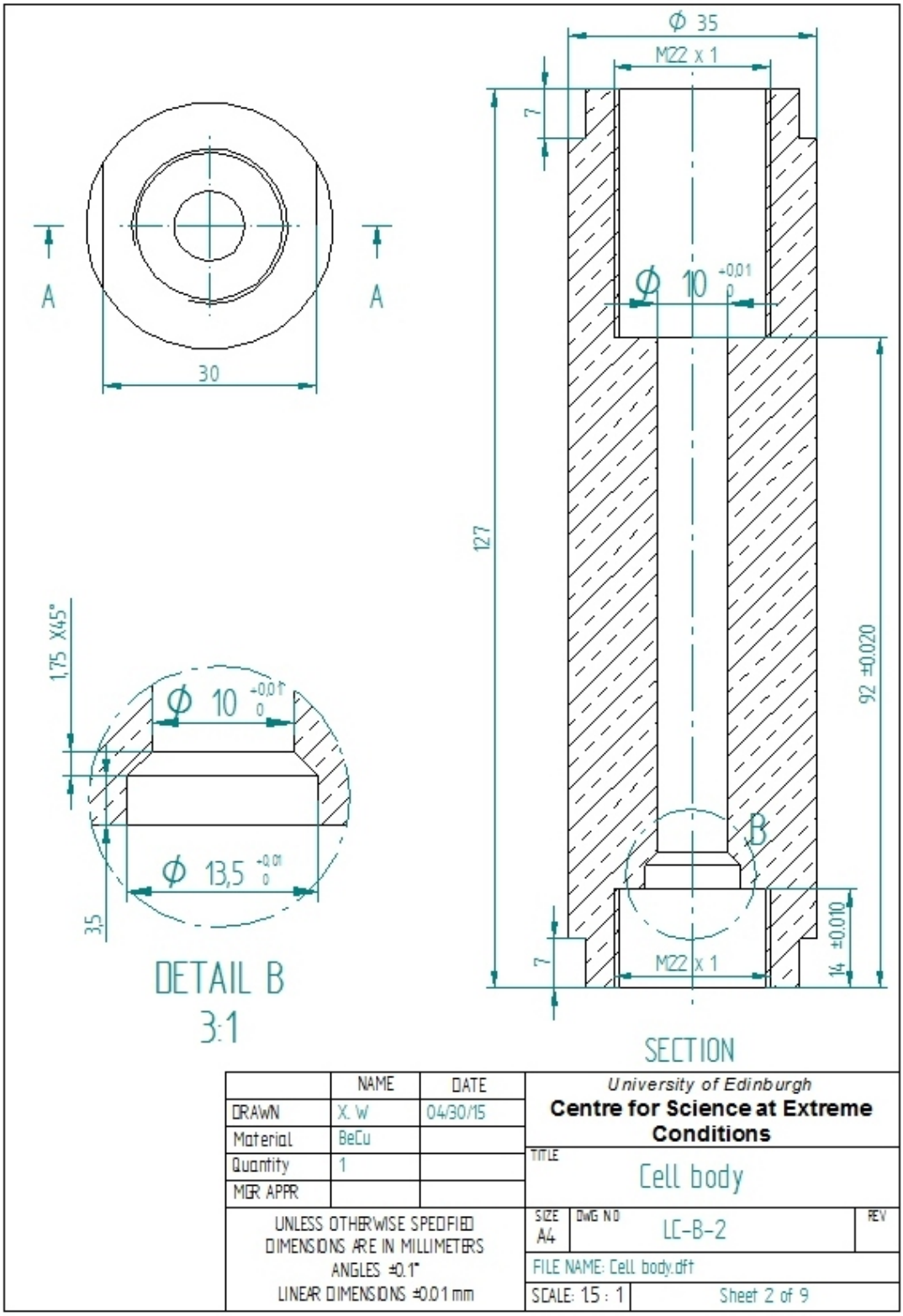

Figure E.11: *The drawing of the cell body (type B liquid cell).*

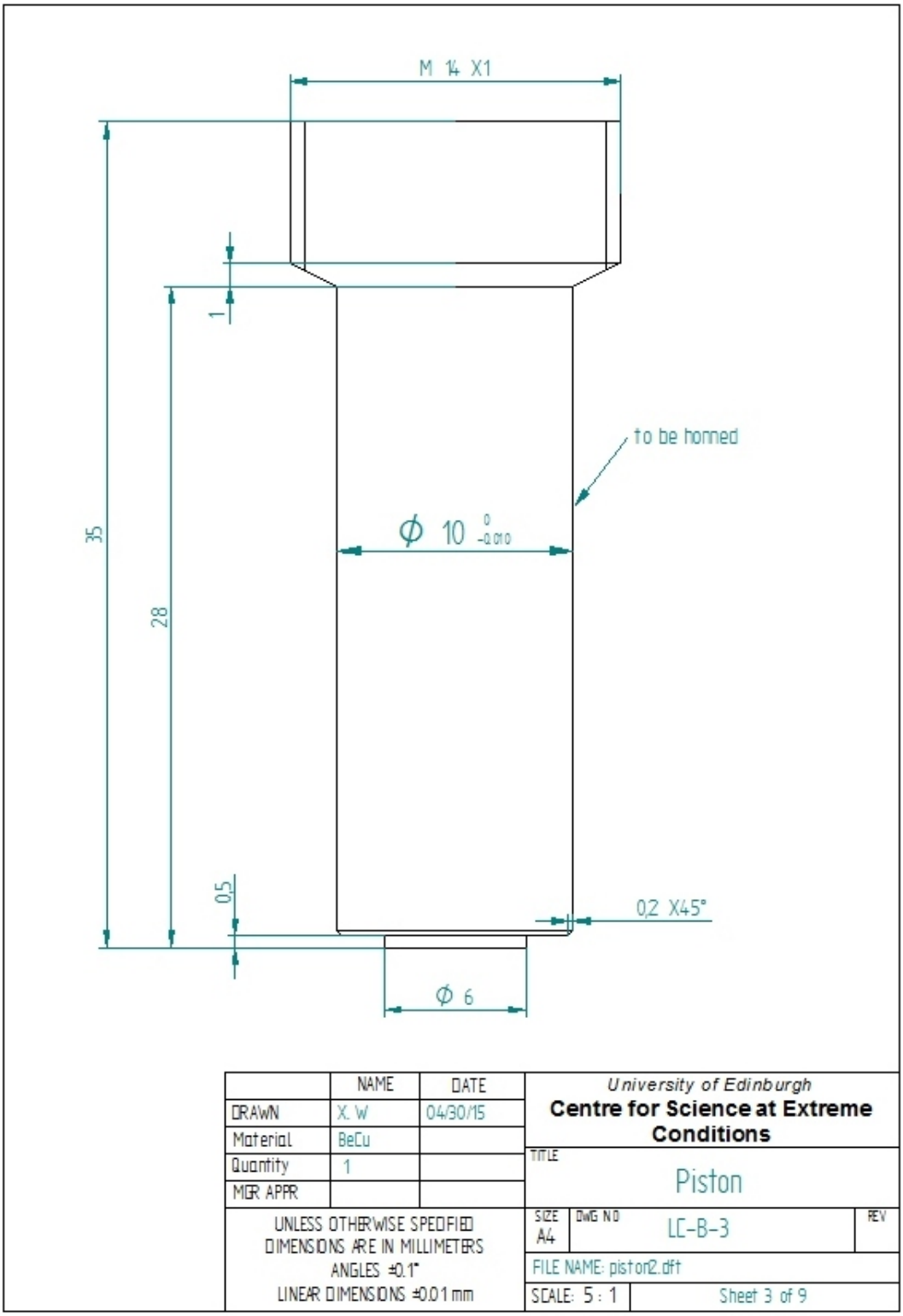

Figure E.12: *The drawing of the piston (type B liquid cell).*

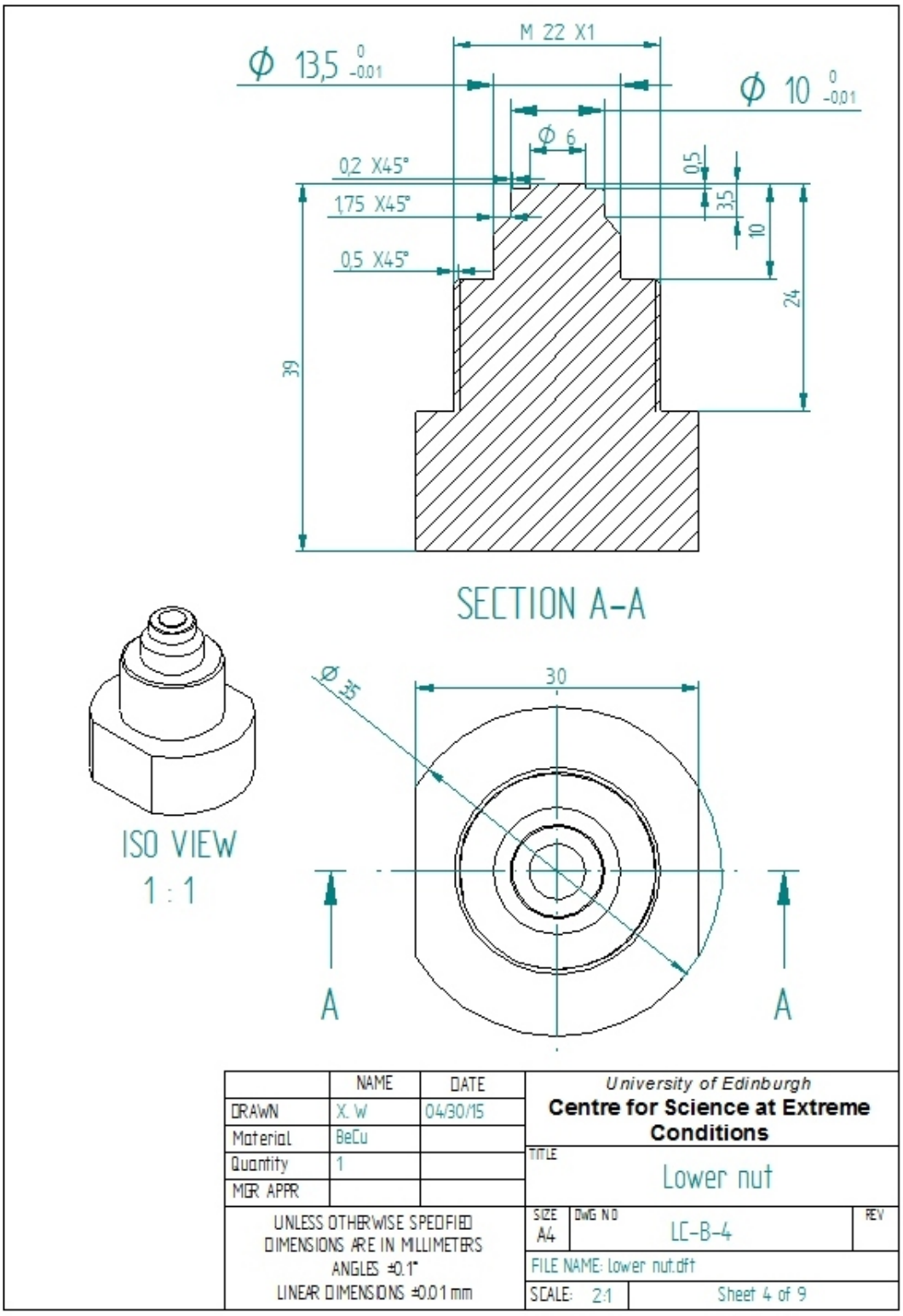

Figure E.13: *The drawing of the lower nut.*

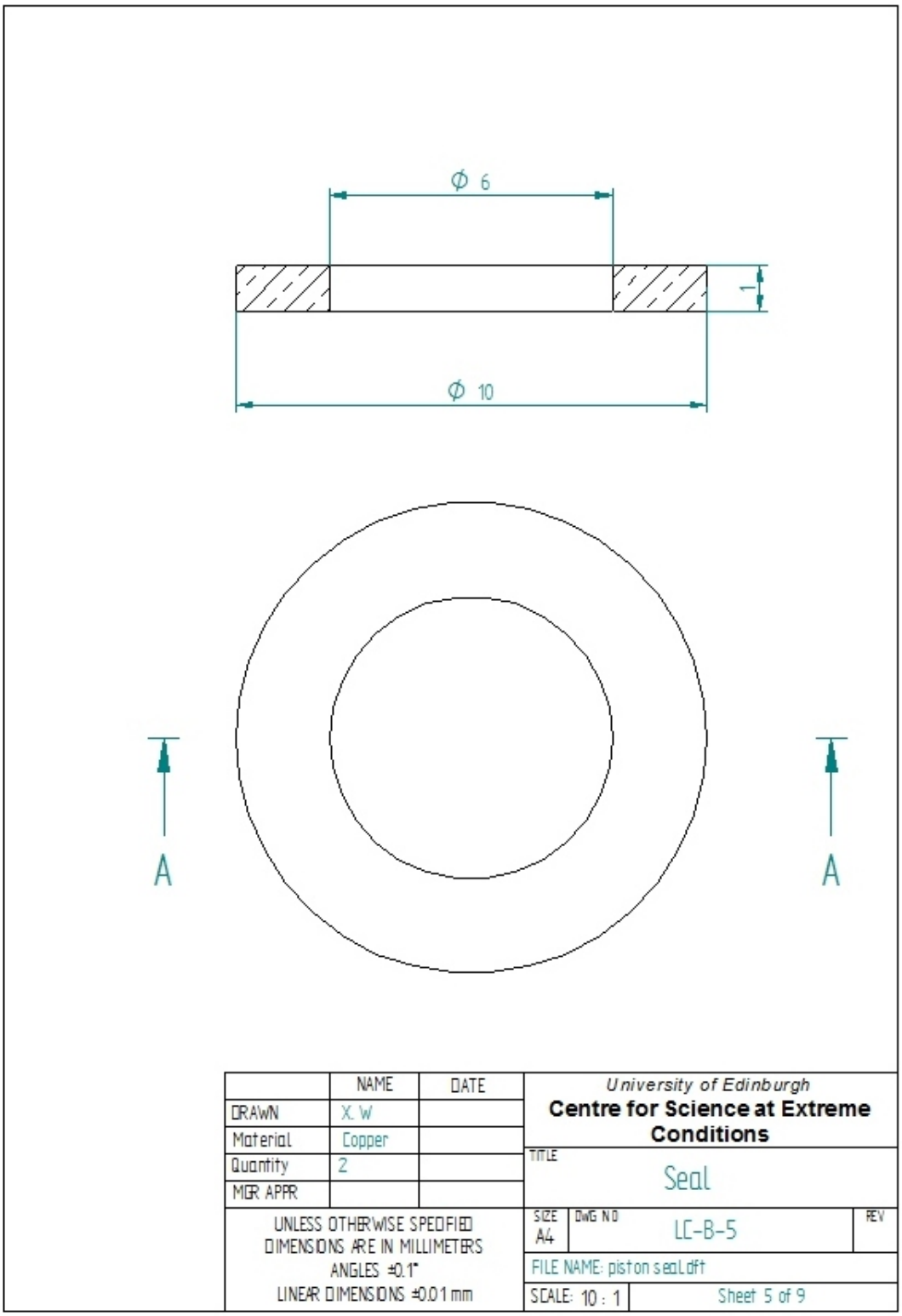

	NAME	DATE
DRAWN	X. W	
Material	Copper	
Quantity	2	
MGR APPR		

UNLESS OTHERWISE SPECIFIED
DIMENSIONS ARE IN MILLIMETERS
ANGLES ±0.1°
LINEAR DIMENSIONS ±0.01 mm

University of Edinburgh
Centre for Science at Extreme Conditions

TITLE: Seal

SIZE A4 | DWG NO: LC-B-5 | REV

FILE NAME: piston seal.dft

SCALE: 10 : 1 | Sheet 5 of 9

Figure E.14: *The drawing of the seal.*

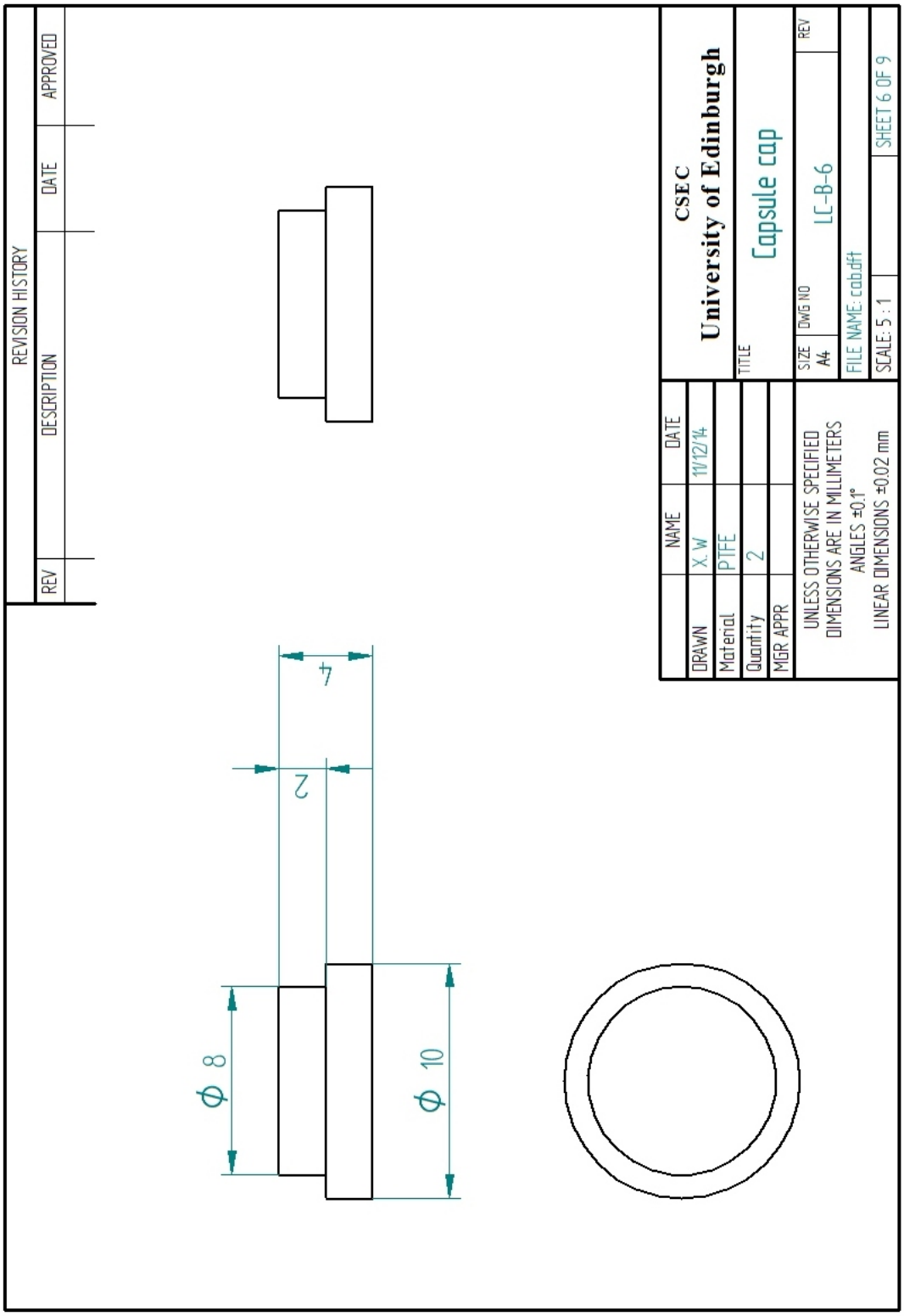

Figure E.15: *The drawing of the capsule cap.*

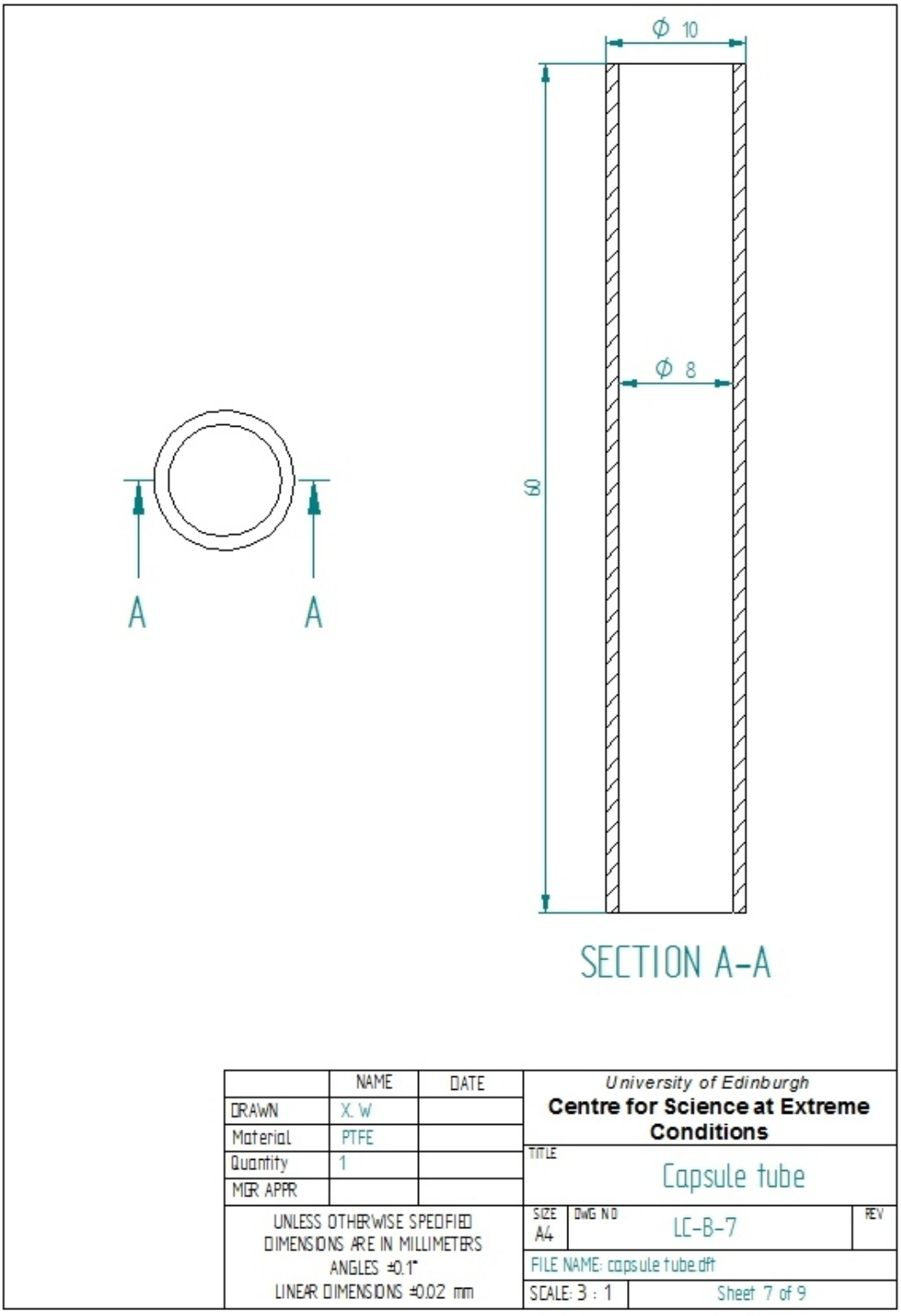

Figure E.16: *The drawing of the capsule tube.*

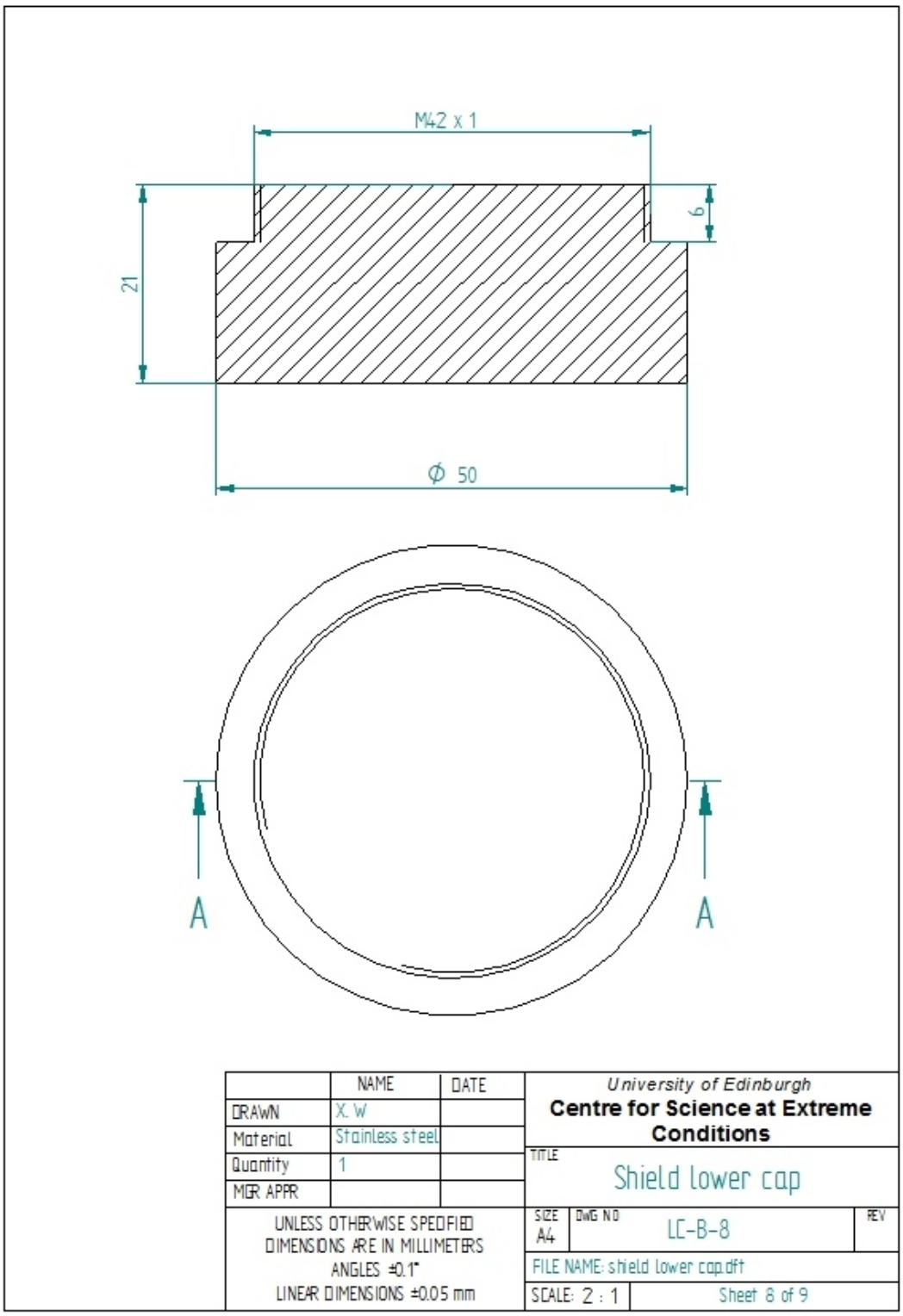

Figure E.17: *The drawing of the lower shield cap.*

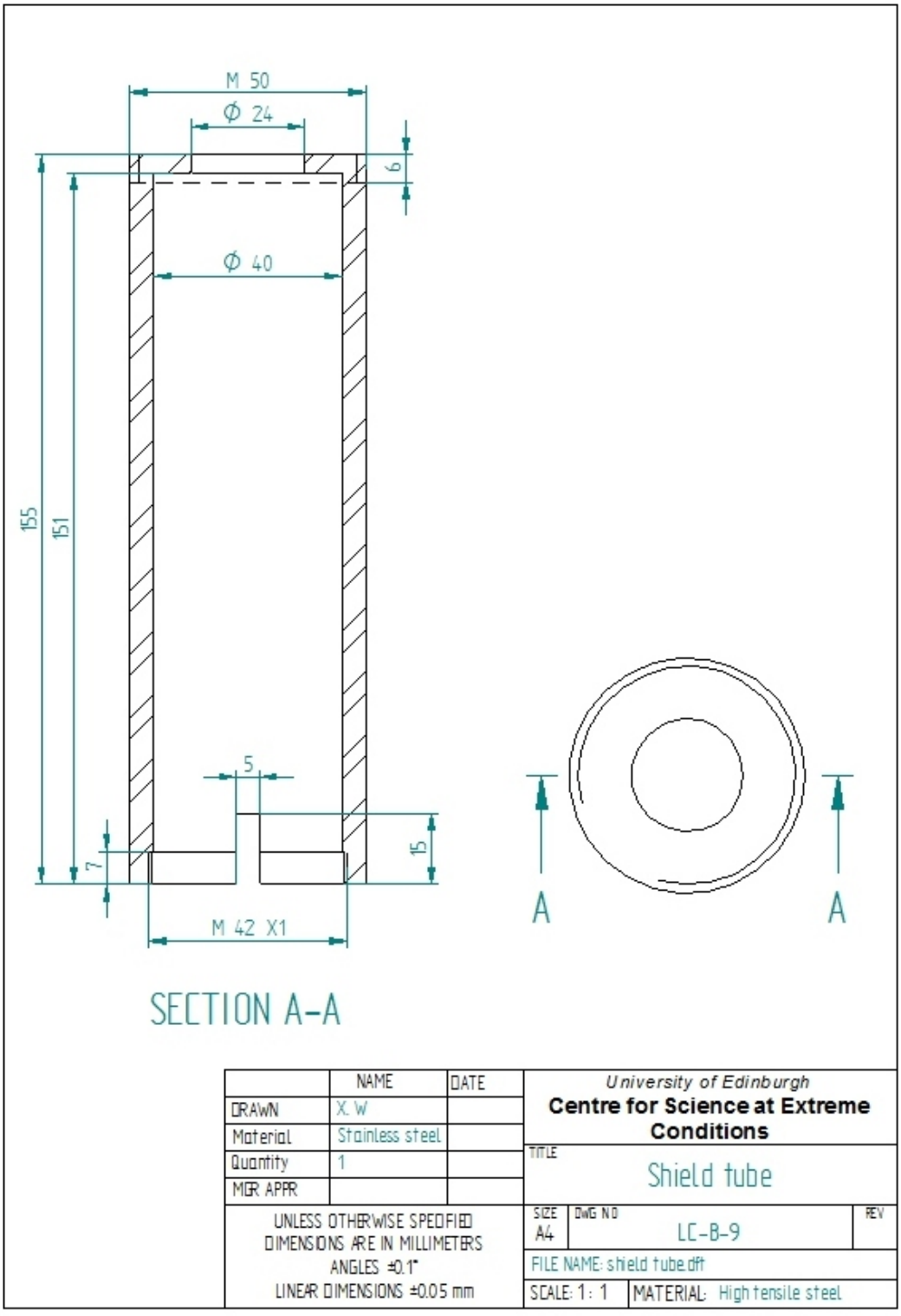

Figure E.18: *The drawing of the shield tube.*

Appendix F
Strain gauge measurment of type B liquid cell

Keithley 2700 multimeter was used to measure the resistence of the strain gauge, the measured resistence is acurate to three decimal places. The resistence of the undeformed straing gauge is R_o=120.710 Ω.

Gauge reading on the press (Ton)	Force (kN)	Measured resistence R_b (ohm)	Resistence change ΔR_b (ohm)	Measured resistence R_c (ohm)	Resistence change ΔR_c (ohm)
1	9.807	120.754	0.044	120.745	0.035
1.5	14.711	120.776	0.066	120.761	0.051
2	19.614	120.796	0.086	120.778	0.068
2.5	24.518	120.813	0.103	120.792	0.082
3	29.421	120.838	0.128	120.813	0.103
3.5	34.325	120.854	0.144	120.824	0.114
4	39.228	120.872	0.162	120.839	0.129
4.5	44.131	120.890	0.180	120.853	0.143
5	49.035	120.912	0.202	120.870	0.160
5.5	53.939	120.934	0.224	120.887	0.177
6	58.842	120.950	0.240	120.900	0.190
6.5	63.746	120.967	0.257	120.913	0.203
7	68.649	120.989	0.279	120.927	0.217
7.5	73.553	121.008	0.298		
8	78.456	121.026	0.316		

Table F.1: *Measured resistence of the strain gauge attached on the type B liquid cell; R_b was measured before the cell was clamped; R_c was measured after the cell was clamped and the load from the hydrulic press was released.*

Appendix G
Publications

- X. Wang and K. V. Kamenev, "Review of modern instrumentation for magnetic measurements at high pressure and low temperature," *Low Temperature Physics*, Vol. 40, no. 8, pp. 735-746, Aug. 2014.

- X. Wang, M. Misek, M. K. Jacobsen and K. V. Kamenev, "Use of an advanced composite material in construction of a high pressure cell for magnetic ac susceptibility measurements," *High Pressure Research*, Vol. 34, no. 4, pp. 371-384, Nov. 2014.

- I. B. Hutchison, A. Delori, X. Wang, K. V. Kamenev, A. J. Urquhart and D. H. Oswald, "Polymorphism of a polymer pre-cursor: metastable glycolide polymorph recovered *via* large scale high-pressure experiments ," *CrystEngComm*, Vol. 17, no. 8, pp. 1778-1782, Jan. 2015.

- J. M. Herrera, S. Titos-Padilla, S. J. A. Pope, I. Berlanga, F. Zamora, J. J. Delgado, K. V. Kamenev, X. Wang, A. Prescimore, E. K. Brechin and E. Colacio, "Studies on bifunctional Fe(II)-triazole spin crossover nanoparticles: time-dependent luminescence, surface grafting and the effect of a silica shell and hydrostatic pressure on the magnetic properties ," *Journal of Material Chemistry C*, Apr. 2015.

References

[1] W. C. Moss, J. O. Hallquist, R. Reichlin, K. A. Goettel, and S. Martin, "Finite element analysis of the diamond anvil cell: Achieving 4.6 Mbar," *Applied Physics Letters*, vol. 48, no. 19, p. 1258, 1986.

[2] D. R. Lide, *CRC handbook ofchemistry and physic*. CRC Press, 87th ed., 2006.

[3] "http://www.qdusa.com."

[4] M. McElfresh, "Fundamentals of magnetism and magnetic measurements featuring Quantum Design's magnetic property measurement system," *Quantum Design*, 1994.

[5] C. Martin, C. C. Agosta, S. W. Tozer, H. A. Radovan, T. Kinoshota, and M. Tokumoto, "Critical Field and Shubnikov-de Haas Oscillations of κ-(BEDT-TTF)$_2$Cu(NCS)$_2$ under Pressure," *Journal of Low Temperature Physics*, vol. 138, pp. 1025–1037, Mar. 2005.

[6] M. Kano, N. Kurita, M. Hedo, Y. Uwatoko, S. W. Tozer, H. Suzuku, T. Onimaru, and T. Sakakibara, "Electrical Resistivity Measurements on $PrPb_3$ under High Pressures," *Journal of the Physical Society of Japan suppl. A*, vol. 76, pp. 56–57, 2007.

[7] L. Chen, N. Kurita, M. Hedo, K. Nakazawa, I. Oguro, Y. Uwatoko, T. Matsumura, M. Tokumoto, and S. W. Tozer, "Magnetic Behavior of TmTe at High Pressure," *Journal of the Physical Society of Japan*, vol. 76, pp. 58–59, Jan. 2007.

[8] D. E. Graf, R. L. Stillwell, K. M. Purcell, and S. W. Tozer, "Nonmetallic gasket and miniature plastic turnbuckle diamond anvil cell for pulsed magnetic field studies at cryogenic temperatures," *High Pressure Research*, vol. 31, pp. 533–543, Dec. 2011.

[9] M. Kano, H. Mori, K. Matsubayashi, M. Itoi, M. Hedo, T. P. Murphy, S. W. Tozer, Y. Uwatoko, and T. Nakamura, "Anisotropy of Upper Critical Field in a One-Dimensional Organic System, $(TMTTF)_2PF_6$ under High Pressure," *Journal of the Physical Society of Japan*, vol. 81, p. 024716, Feb. 2012.

[10] W. A. Bassett, "Diamond anvil cell, 50th birthday," *High Pressure Research*, vol. 29, pp. 163–186, June 2009.

[11] G. Giriat, W. Wang, J. P. Attfield, A. D. Huxley, and K. V. Kamenev, "Turnbuckle diamond anvil cell for high-pressure measurements in a superconducting quantum interference device magnetometer.," *The Review of scientific instruments*, vol. 81, p. 073905, July 2010.

[12] M. J. Turner, R. W. Clough, H. C. Martin, and L. J. Topp, "Stiffness and Deflection Analysis of Complex Structures," *Journal of the aeronautical sciences*, vol. 23, no. 9, pp. 805–823, 1956.

[13] A. Galkin, E. A. Zavadskii, V. M. Smirnov, and V. I. Valkov, "Observation of ferromagnetic state in antiferromagnetic alloys of the MnFeAs system," *JETP letters*, vol. 20, no. 4, p. 111, 1974.

[14] "http://www.cryogenic.co.uk/products/s700x-squid-magnetometer."

[15] "http://www.ngkberylco.co.uk/."

[16] Y. Uwatoko, S. Todo, K. Ueda, A. Uchida, M. Kosaka, N. Mori, and T. Matsumoto, "Material properties of NiCrAl alloy and design of a 4 GPa class non-magnetic high-pressure cell," *Journal of Physics: Condensed Matter*, vol. 14, pp. 11291–11296, Nov. 2002.

[17] M. I. Eremets, *High Pressure Experimental Methods*. Oxford: Oxford University Press, 1996.

[18] K. Kamishima, M. Hagiwara, and H. Yoshida, "Investigation of a strong titanium alloy KS15-5-3 and the application to a high pressure apparatus for magnetization measurements," *Review of Scientific Instruments*, vol. 72, no. 2, p. 1472, 2001.

[19] D. Wohlleben and M. Maple, "Application of the Faraday Method to Magnetic Measurements under Pressure," *Review of Scientific Instruments*, vol. 42, no. 11, p. 1573, 1971.

[20] R. P. Guertin and S. Foner, "Application of a vibrating sample magnetometer to magnetic measurements under hydrostatic pressure," *Review of Scientific Instruments*, vol. 45, no. 6, p. 863, 1974.

[21] K. Koyama, S. Hane, K. Kamishima, and T. Goto, "Instrument for high resolution magnetization measurements at high pressures, high magnetic fields and low temperatures," *Review of Scientific Instruments*, vol. 69, no. 8, p. 3009, 1998.

[22] I. R. Walker, "Nonmagnetic pistoncylinder pressure cell for use at 35 kbar and above," *Review of Scientific Instruments*, vol. 70, no. 8, p. 3402, 1999.

[23] W. A. Coniglio, D. E. Graf, and S. W. Tozer, "Small plastic piston-cylinder cell for pulsed magnetic field studies at cryogenic temperatures," *High Pressure Research*, vol. 33, pp. 425–431, June 2013.

[24] S. Reich and T. Godin, "A miniature pressure cell for a SQUID magnetometer," *Measurement Science and Technology*, vol. 7, pp. 1079–1082, July 1996.

[25] A. Eiling and J. S. Schilling, "Pressure and temperature dependence of electrical resistivity of Pb and Sn from 1-300K and 0-10 GPa-use as continuous resistive pressure monitor accurate over wide temperature range; superconductivity under pressure in Pb, Sn and In," *Journal of Physics F: Metal Physics*, vol. 11, pp. 623–639, Mar. 1981.

[26] J. Diederichs, A. Gangopadhyay, and J. Schilling, "Pressure dependence of the electronic density of states and Tc in superconducting Rb_3C_{60}," *Physical Review B*, vol. 54, pp. R9662–R9665, Oct. 1996.

[27] I. Umehara, F. Tomioka, A. Tsuboi, T. Ono, M. Hedo, and Y. Uwatoko, "Design of micro pressure cell for measurements of specific heat and magnetization," *Journal of Magnetism and Magnetic Materials*, vol. 272-276, pp. 2301–2302, May 2004.

[28] Y. Uwatoko, T. Fujiwara, M. Hedo, F. Tomioka, and I. Umehara, "The development of a high pressure micro-cell for magnetization and specific heat measurements: the effect of pressure on the magnetism in CeAg," *Journal of Physics: Condensed Matter*, vol. 17, pp. S1011–S1016, Mar. 2005.

[29] "http://www.almax-easylab.com."

[30] J. Kamarad, Z. Machatova, and Z. Arnold, "High pressure cells for magnetic measurements-Destruction and functional tests," *Review of Scientific Instruments*, vol. 75, no. 11, p. 5022, 2004.

[31] K. V. Kamenev, S. Tancharakorn, N. Robertson, and A. Harrison, "Long symmetric high-pressure cell for magnetic measurements in superconducting quantum interference device magnetometer," *Review of Scientific Instruments*, vol. 77, no. 7, p. 073905, 2006.

[32] J. Sanchez-Benitez, S. Tancharakon, M. Hutchison, and K. V. Kamenev, "High-pressure cell for a SQUID magnetometer with a plug for in situ pressure measurements," *Journal of Physics: Conference Series*, vol. 121, p. 122001, 2008.

[33] M. Mito, M. Hitaka, and T. Kawae, "Development of Miniature Diamond Anvil Cell for the Superconducting Quantum Interference Device Magnetometer," *Japanese Journal of Applied Physics*, vol. 40, no. 11, pp. 6641–6644, 2001.

[34] P. Bridgeman, *Physics of High Pressure*. London: Bell, 1949.

[35] J. D. Barnett, S. Block, and G. J. Piermarini, "An Optical Fluorescence System for Quantitative Pressure Measurement in the Diamond-Anvil Cell," *Review of Scientific Instruments*, vol. 44, no. 1, p. 1, 1973.

[36] T. C. Kobayashi, H. Hidaka, H. Kotegawa, K. Fujiwara, and M. I. Eremets, "Nonmagnetic indenter-type high-pressure cell for magnetic measurements," *Review of Scientific Instruments*, vol. 78, no. 2, p. 023909, 2007.

[37] J. Kamarád, M. Mihalik, V. Sechovský, and Z. Arnold, "Miniature uniaxial pressure cells for magnetic measurements," *High Pressure Research*, vol. 28, pp. 633–636, Dec. 2008.

[38] P. L. Alireza and G. G. Lonzarich, "Miniature anvil cell for high-pressure measurements in a commercial superconducting quantum interference device magnetometer.," *The Review of scientific instruments*, vol. 80, p. 023906, Mar. 2009.

[39] N. Tateiwa, Y. Haga, Z. Fisk, and Y. $\bar{O}$nuki, "Miniature ceramic-anvil high-pressure cell for magnetic measurements in a commercial superconducting quantum interference device magnetometer.," *The Review of scientific instruments*, vol. 82, p. 053906, May 2011.

[40] N. Tateiwa, Y. Haga, T. D. Matsuda, and Z. Fisk, "Magnetic measurements at pressures above 10 GPa in a miniature ceramic anvil cell for a superconducting quantum interference device magnetometer.," *The Review of scientific instruments*, vol. 83, p. 053906, May 2012.

[41] N. Tateiwa, Y. Haga, T. D. Matsuda, Z. Fisk, S. Ikeda, and H. Kobayashi, "Note: Improved sensitivity of magnetic measurements under high pressure in miniature ceramic anvil cell for a commercial SQUID magnetometer.," *The Review of scientific instruments*, vol. 84, p. 046105, Apr. 2013.

[42] "http://www.fujidie.co.jp."

[43] "http://www.iquantum.co.jp/eng/pro.html."

[44] I. Goncharenko, "Neutron diffraction experiments in diamond and sapphire anvil cells," *High Pressure Research*, vol. 24, pp. 193–204, Jan. 2004.

[45] K. J. Takano and M. Wakatsuki, "An optical high pressure cell with spherical sapphire anvils," *Review of Scientific Instruments*, vol. 62, no. 6, p. 1576, 1991.

[46] S. Klotz, *Techniques in high pressure neutron scattering*. New York: CRC Press, 2012.

[47] W. Kuhs, H. Ahsbahs, D. Londono, and J. Finney, "In-situ crystal growth and neutron four-circle diffractometry under high pressure," *Physica B: Condensed Matter*, vol. 156-157, pp. 684–687, Jan. 1989.

[48] W. F. Kuhs, F. C. Bauer, R. Hausmann, H. Ahsbahs, R. Dorwarth, and K. Hölzer, "Single crystal diffraction with X-rays and neutrons: High quality at high pressure?," *High Pressure Research*, vol. 14, pp. 341–352, Jan. 1996.

[49] W. Kuhs, F. Bauer, H. Ahsbahs, and G. Mclntyre, "Neutron Single Crystal Diffraction on KDP at 20 K and 1.7 GPa," *The review of High Pressure Science and Technology*, vol. 7, pp. 307–309, 1998.

[50] W. B. Daniels, M. Lipp, D. Strachan, D. Winters, and Z. Yu, "Simple Sapphire ball cell for high pressure studies in the Ultraviolet," in *the XIII AIRAPT International Conference on High pressure Science and Technology* (A. Singh, ed.), (New Delhi), p. 809, Oxford & IBH publishing Co., 1992.

[51] D. K. Christen, H. R. Kerchner, S. T. Sekula, and P. Thorel, "Equilibrium properties of the fluxoid lattice in single-crystal niobium. I. Magnetization measurements," *Physical Review B*, vol. 21, no. 1, pp. 102–117, 1980.

[52] C. Pfleiderer, A. D. Huxley, and S. M. Hayden, "On the use of Cu:Be clamp cells in magnetization and neutron scattering studies," *Journal of Physics: Condensed Matter*, vol. 17, pp. S3111–S3120, Oct. 2005.

[53] N. Vennemann, M. Lechner, and R. Oberthür, "Thermodynamics and conformation of polyoxyethylene in aqueous solution under high pressure: 1. Small-angle neutron scattering and densitometric measurements at room temperature," *Polymer*, vol. 28, pp. 1738–1748, Sept. 1987.

[54] H. Takano, M. Nagao, Y. Nakayama, H. Hasegawa, T. Hashimoto, H. Seto, and M. Imai, "High pressure cell for small-angle neutron and light scattering studies of phase transitions in complex liquids," *polymer journal*, vol. 29, pp. 931–939, 1997.

[55] G. Pépy and P. Baroni, "A new high pressure cell with sapphire windows for small-angle neutron scattering," *Journal of Applied Crystallography*, vol. 36, pp. 814–815, Apr. 2003.

[56] M. Bonetti and P. Calmettes, "High-pressure cell for small- and medium-angle neutron scattering measurements up to 300 MPa," *Review of Scientific Instruments*, vol. 75, no. 2, p. 440, 2004.

[57] A. Gabke, J. Kraineva, R. Köhling, and R. Winter, "Using pressure in combination with x-ray and neutron scattering techniques for studying the structure, stability and phase behaviour of soft condensed matter and biomolecular systems," *Journal of Physics: Condensed Matter*, vol. 17, pp. S3077–S3092, Oct. 2005.

[58] J. Kohlbrecher, A. Bollhalder, R. Vavrin, and G. Meier, "A high pressure cell for small angle neutron scattering up to 500 MPa in combination with light scattering to investigate liquid samples.," *The Review of scientific instruments*, vol. 78, p. 125101, Dec. 2007.

[59] M. Bonetti and P. Calmettes, "Sapphire-anvil cell for small-angle neutron scattering measurements in large-volume liquid samples up to 530 MPa," *Review of Scientific Instruments*, vol. 76, no. 4, p. 043903, 2005.

[60] D. M. Adams and A. C. Shaw, "A computer-aided design study of the behaviour of diamond anvils under stress," *Journal of Physics D: Applied Physics*, vol. 1609, 1982.

[61] D. M. Adams, A. G. Christy, and A. J. Norman, "Optimization of diamond anvil cell performance by finite element analysis," *Measurement Science and Technology*, vol. 4, pp. 422–430, Mar. 1993.

[62] A. Love, *A treatise on the mathematical theory of ealsticity*. Cambridge University Press, 1927.

[63] M. S. Bruno and K. J. Dunn, "Stress analysis of a beveled diamond anvil," *Review of Scientific Instruments*, vol. 55, no. 6, p. 940, 1984.

[64] J. O. Hallquist, "NIKE2D-a Vetorized implicit finite deformation finite element code for analyzing the static and dynamic response of 2D solids," tech. rep., Lawrence Livermore National Laboratory, University of California, 1983.

[65] W. C. Moss and K. A. Goettel, "Finite element design of diamond anvils," *Applied Physics Letters*, vol. 50, no. 1, p. 25, 1987.

[66] R. J. Hemley, "X-ray Imaging of Stress and Strain of Diamond, Iron, and Tungsten at Megabar Pressures," *Science*, vol. 276, pp. 1242–1245, May 1997.

[67] S. Merkel, R. J. Hemley, and H. Mao, "Finite-element modeling of diamond deformation at multimegabar pressures," *Applied Physics Letters*, vol. 74, no. 5, p. 656, 1999.

[68] V. I. Levitas and G. V. Dushinskaya, "stress distribution in deformable gaskets of totoidal high pressure equipment," *Journal of superhard Materials*, vol. 5, no. 5, pp. 7–11, 1983.

[69] S. Klotz, G. Hamel, and J. Frelat, "A new type of compact large-capacity press for neutron and x-ray scattering," *High Pressure Research*, vol. 24, pp. 219–223, Jan. 2004.

[70] C. Bull, M. Guthrie, and S. Klotz, "Toroidal anvils for single-crystal neutron studies," *High Pressure Research*, vol. 25, no. 4, pp. 229–231, 2005.

[71] J. Fang, C. L. Bull, H. Hamidov, J. S. Loveday, M. J. Gutmann, R. J. Nelmes, and K. V. Kamenev, "A rotator for single-crystal neutron diffraction at high pressure," *Review of Scientific Instruments*, vol. 81, p. 113901, 2010.

[72] J. Fang, C. L. Bull, J. S. Loveday, R. J. Nelmes, and K. V. Kamenev, "Strength analysis and optimisation of double-toroidal anvils for high-pressure research.," *The Review of scientific instruments*, vol. 83, p. 093902, Sept. 2012.

[73] R. Li, H. A. Ma, Q. G. Han, Z. Z. Liang, B. H. Yin, W. Q. Liu, and X. Jia, "Simulation of pressure distribution in a pyrophyllite high-pressure cell by finite-element analysis," *High Pressure Research*, vol. 27, pp. 249–257, June 2007.

[74] Q. Han, X. Jia, J. Qin, and R. Li, "FEM study on a double-beveled anvil and its application to synthetic diamonds," *High Pressure Research*, no. June 2013, pp. 37–41, 2009.

[75] Q. Han, X. Jia, J. Qin, R. Li, C. Zhang, Z. Li, Y. Tian, and H. Ma, "Finite-element analysis on performance and shear stress of cemented tungsten carbide anvils used in the China-type cubic-anvil high-pressure apparatus," *High Pressure Research*, vol. 29, pp. 457–465, Sept. 2009.

[76] W. Wang, D. A. Sokolov, A. D. Huxley, and K. V. Kamenev, "Large volume high-pressure cell for inelastic neutron scattering.," *The Review of scientific instruments*, vol. 82, p. 073903, July 2011.

[77] Y. Ma, S. Y. Zhang, C. Goodway, R. Done, B. Evans, O. Kirichek, and Z. Bowden, "A non-destructive experimental investigation of elastic plastic interfaces of autofrettaged thick-walled cylindrical aluminium high pressure vessels," *High Pressure Research*, vol. 32, no. 3, pp. 364–375, 2012.

[78] D. Martien, "Introduction to: AC susceptibility," *Quantum Design*, 1994.

[79] N. Moulton, S. Wolf, E. Skelton, D. Liebenberg, T. Vanderah, A. Hermann, and H. Duan, "Pressure dependence of T_C in $Tl_2Ba_2CaCu_2O_8$ at hydrostatic pressures to 6 GPa," *Physical Review B*, vol. 44, pp. 12632–12634, Dec. 1991.

[80] J. Schilling, J. Diederichs, S. Klotz, and R. Sieburger, "Ac Susceptibility Studies of Superconducting Properties Under High Hydrostatic Pressure," *Magnetic Susceptibility of Superconductors and Other Spin Systems*, pp. 107–128, 1991.

[81] D. D. Berkley, E. F. Skelton, N. E. Moulton, M. S. Osofsky, W. T. Lechter, V. M. Browning, and D. H. Liebenberg, "Pressure dependence of the superconducting transition temperature in single crystals of $Tl_2Ba_2Ca_2Cu_3O_{10-x}$," *Physical Review B*, vol. 47, pp. 5524–5527, Mar. 1993.

[82] C. C. Kim, E. F. Skelton, M. S. Osofsky, and D. H. Liebenberg, "Pressure dependence of T_c in $NdBa_2Cu_3O_{7-\delta}$ to 6 GPa," *Physical Review B*, vol. 48, pp. 6431–6435, Sept. 1993.

[83] C. C. Kim, M. E. Reeves, M. S. Osofsky, E. F. Skelton, and D. H. Liebenberg, "A system for in-situ pressure and ac susceptibility measurements using the diamond anvil cell: T_c(P) for $HgBa_2CuO_{4+\delta}$," *Review of Scientific Instruments*, vol. 65, no. 4, p. 992, 1994.

[84] V. V. Struzhkin, Y. A. Timofeev, R. J. Hemley, and H. Mao, "Superconducting T_c and Electron-Phonon Coupling in Nb to 132 GPa: Magnetic Susceptibility at Megabar Pressures," *Physical Review Letters*, vol. 79, pp. 4262–4265, Nov. 1997.

[85] S. A. Gilder, M. LeGoff, J. Peyronneau, and J. Chervin, "Novel high pressure magnetic measurements with application to magnetite," *Geophysical Research Letters*, vol. 29, no. 10, pp. 30–1–30–4, 2002.

[86] Y. A. Timofeev, V. V. Struzhkin, R. J. Hemley, H.-k. Mao, and E. A. Gregoryanz, "Improved techniques for measurement of superconductivity in diamond anvil cells by magnetic susceptibility," *Review of Scientific Instruments*, vol. 73, no. 2, p. 371, 2002.

[87] P. L. Alireza and S. R. Julian, "Susceptibility measurements at high pressures using a microcoil system in an anvil cell," *Review of Scientific Instruments*, vol. 74, no. 11, p. 4728, 2003.

[88] D. D. Jackson, C. Aracne-Ruddle, V. Malba, S. T. Weir, S. A. Catledge, and Y. K. Vohra, "Magnetic susceptibility measurements at high pressure using designer diamond anvils," *Review of Scientific Instruments*, vol. 74, no. 4, p. 2467, 2003.

[89] S. Goh, P. Alireza, P. Mann, A.-M. Cumberlidge, C. Bergemann, M. Sutherland, and Y. Maeno, "High pressure de Haasvan Alphen studies of Sr_2RuO_4 using an anvil cell," *Current Applied Physics*, vol. 8, pp. 304–307, May 2008.

[90] N. Shirakawa, H. Horinouchi, and Y. Yoshida, "Measuring Sr_2RuO_4 down to with a commercial SQUID magnetometer combined with refrigeration," *Journal of Magnetism and Magnetic Materials*, vol. 272-276, pp. E149–E150, May 2004.

[91] N. Shirakawa and M. Tamura, "Low temperature static magnetization of an organic ferromagnet, β-p-NPNN," *Polyhedron*, vol. 24, pp. 2405–2408, Nov. 2005.

[92] R. L. Norton, *Machine Design An Integrated Approach*. New Jersey: Pearson, 2011.

[93] S. Timoshenko and J. Goodier, *Theory of elasticity*. New York: McGrawHill, 1970.

[94] E. Whalley, A. Lavergne, and P. T. T. Wong, "Hydrostatic optical cell with glass windows for 25 kilobar," *Review of Scientific Instruments*, vol. 47, no. 7, p. 845, 1976.

[95] L. H. Dmowski and E. Litwin-Staszewska, "The variation of the pressure coefficient of manganin sensors at low temperatures," *Measurement Science and Technology*, vol. 10, pp. 343–347, May 1999.

[96] A. Jayaraman, "Diamond anvil cell and high-pressure physical investigations," *Reviews of Modern Physics*, vol. 55, pp. 65–108, Jan. 1983.

[97] W. B. Holzapfel and N. S. Isaacs, eds., *High Pressure Techniques in Chemistry and Physics: A Practical Approach*. Oxford: Oxford University Press, 1997.

[98] D. J. Dunstan, "Theory of the gasket in diamond anvil high-pressure cells," *Review of Scientific Instruments*, vol. 60, no. 12, p. 3789, 1989.

[99] R. A. Forman, G. J. Piermarini, J. D. Barnett, and S. Block, "Pressure measurement made by the utilization of ruby sharp-line luminescence.," *Science (New York, N.Y.)*, vol. 176, pp. 284–5, Apr. 1972.

[100] G. J. Piermarini and S. Block, "Ultrahigh pressure diamond-anvil cell and several semiconductor phase transition pressures in relation to the fixed point pressure scale," *Review of Scientific Instruments*, vol. 46, no. 8, p. 973, 1975.

[101] H. K. Mao and P. M. Bell, "High-pressure physics: sustained static generation of 1.36 to 1.72 megabars.," *Science (New York, N.Y.)*, vol. 200, pp. 1145–7, June 1978.

[102] D. L. Decker, "High-Pressure Equation of State for NaCl, KCl, and CsCl," *Journal of Applied Physics*, vol. 42, no. 8, p. 3239, 1971.

[103] E. R. Dobrovinskaya, L. A. Lytvynov, and V. Pishchik, *Sapphire Material, Manufacturing, Applications*. New York: Springer, 2009.

[104] K. Furuno, A. Onodera, and S. Kume, "Sapphire-Anvil Cell for High Pressure Research," *Japanese Journal of Applied Physics*, vol. 25, pp. L646–L647, Aug. 1986.

[105] G. J. Piermarini, S. Block, and J. D. Barnett, "Hydrostatic limits in liquids and solids to 100 kbar," *Journal of Applied Physics*, vol. 44, pp. 5377–5382, Dec. 1973.

[106] K. Murata, H. Yoshino, H. O. Yadav, Y. Honda, and N. Shirakawa, "Pt resistor thermometry and pressure calibration in a clamped pressure cell with the medium, daphne 7373," *Review of Scientific Instruments*, vol. 68, no. 6, 1997.

[107] K. Yokogawa, K. Murata, H. Yoshino, and S. Aoyama, "Solidification of High-Pressure Medium Daphne 7373," *Japanese Journal of Applied Physics*, vol. 46, pp. 3636–3639, June 2007.

[108] R. G. Budynas and J. K. Nisbett, *Shigley's Mechanical Engineering Design*. New York: McGraw-Hill, ninth edit ed., 2011.

[109] *Abaqus 6.10 Analysis User's Manual, Volume 3*. SIMULIA DASSAULT SYSTEMES, 2010.

[110] S. Titos-Padilla, J. M. Herrera, X.-W. Chen, J. J. Delgado, and E. Colacio, "Bifunctional hybrid SiO_2 nanoparticles showing synergy between core spin crossover and shell luminescence properties.," *Angewandte Chemie (International ed. in English)*, vol. 50, pp. 3290–3, Mar. 2011.

[111] P. Gutlich and H. E. Goodwin, eds., *Spin Crossover in Transition Metal Compounds: Topics in Current Chemistry*. Berlin: Springer, 2004.

[112] O. Kahn and C. J. Martinez, "Spin-Transition Polymers: From Molecular Materials Toward Memory Devices," *Science*, vol. 279, pp. 44–48, Jan. 1998.

[113] "See http://www.plm.automation.siemens.com/ (Solid Edge)."

[114] "http://www.ansys.com/."

[115] L. Merrill and W. A. Bassett, "Miniature diamond anvil pressure cell for single crystal x-ray diffraction studies," *Review of Scientific Instruments*, vol. 45, no. 2, p. 290, 1974.

[116] S. Nagarjuna, K. Balasubramanian, and D. S. Sarma, "Effect of prior cold work on mechanical properties , electrical conductivity and microstructure of aged Cu-Ti alloys," *Journal of Materials Science*, vol. 34, no. 12, pp. 2929–2942, 1999.

[117] Testbourne Ltd, "http://www.testbourne.com/materials/alloys/."

[118] M. Özakça, E. Hinton, and N. V. R. Rao, "Shape optimization of axisymmetric structures with adaptive finite element procedures," *Structural Optimization*, vol. 5, no. 4, pp. 256–264, 1993.

[119] V. Toplosky, R. Walsh, S. W. Tozer, and F. Motamedi, *Advances in Cryogenic Engineering Materials*, vol. 46. Boston, MA: Springer US, 2000.

[120] A. L. Woodcraft, V. Martelli, and G. Ventura, "Thermal conductivity of Tecamax SRP from millikelvin temperatures to room temperature," *Cryogenics*, vol. 50, pp. 66–70, Feb. 2010.

[121] "See http://www.ensinger.co.uk/ (Ensinger Group Ltd)."

[122] "See http://www.quadrantplastics.com/eu-en/ (QUADRANT)."

[123] "See http://www.victrex.com/ (Victrex plc.)."

[124] J. Rice, "The localization of plastic deformation," in *Proceedings of the 14th international Congress on Theoretical and Applid Mechanics* (W. Koiter, ed.), (Delft), pp. 207–220, North-Holland Publishing Co., 1976.

[125] J. Desrues, J. Lanier, and P. Stutz, "Localization of the deformation in tests on sand sample," *Engineering Fracture Mechanics*, vol. 21, pp. 909–921, Jan. 1985.

[126] M. Ortiz, Y. Leroy, and A. Needleman, "A FINITE ELEMENT METHOD FOR LOCALIZED," *Computer Methods in Applied Mechanics and Engineering*, vol. 61, pp. 189–214, 1987.

[127] Y. Leroy and M. Ortiz, "Finite element analysis of transient strain localization phenomena in frictional solids," *International Journal for Numerical and Analytical Methods in Geomechanics*, vol. 13, pp. 53–74, Mar. 1990.

[128] C. Poirier, M. Ammi, D. Bideau, and J. Troadec, "Experimental study of the geometrical effects in the localization of deformation," *Physical Review Letters*, vol. 68, pp. 216–219, Jan. 1992.

[129] Z. Mi, S. R. Shieh, and High Pressure Mineral Physics Group, "High Pressure Strength Study on NaCl," *AGU Fall Meeting Abstracts*, p. C1891, Dec. 2010.

[130] E. P. Bowden and D. Tabor, *The Friction and lubrication of solids*. Oxford: Clarendon, 1964.

[131] "http://www.copper.org."

[132] A. D. Deutschman, W. A. Michels, and C. E. Wilson, *Machine design Theory and Practice*. MacMillan Publishing, machinery' ed., 1975.

[133] A. T. Holmes, G. R. Walsh, E. Blackburn, E. M. Forgan, and M. Savey-Bennett, "A 17 T horizontal field cryomagnet with rapid sample change designed for beamline use," *Review of Scientific Instruments*, vol. 83, no. 2, p. 023904, 2012.

[134] "www.vishay.com/ref/straingages."

[135] A. Saul and W. Wagner, "A Fundamental Equation for Water Covering the Range from the Melting Line to 1273 K at Pressures up to 25 000 MPa," *Journal of Physical and Chemical Reference Data*, vol. 18, no. 4, p. 1537, 1989.

[136] W. Wagner and A. Prub, "The IAPWS Formulation 1995 for the Thermodynamic Properties of Ordinary Water Substance for General and Scientific Use," *Journal of Physical and Chemical Reference Data*, vol. 31, no. 2, p. 387, 1999.

[137] "http://webbook.nist.gov/chemistry/fluid/."